



Minnesota
Department of
Transportation

**RESEARCH
SERVICES**

Office of
Policy Analysis,
Research &
Innovation

Development of Design Guide for Thin and Ultra-Thin Concrete Overlays of Existing Asphalt Pavements, Task 2: Review and Selection of Structural Response and Performance Models

Julie M. Vandebossche, Principal Investigator
Department of Civil and Environmental Engineering
University of Pittsburgh

December 2011

Research Project
Final Report 2011-25

Your Destination... Our Priority



All agencies, departments, divisions and units that develop, use and/or purchase written materials for distribution to the public must ensure that each document contain a statement indicating that the information is available in alternative formats to individuals with disabilities upon request. Include the following statement on each document that is distributed:

To request this document in an alternative format, call Bruce Lattu at 651-366-4718 or 1-800-657-3774 (Greater Minnesota); 711 or 1-800-627-3529 (Minnesota Relay). You may also send an e-mail to bruce.lattu@state.mn.us. (Please request at least one week in advance).

Technical Report Documentation Page

| | | | |
|---|--|---|-----------|
| 1. Report No. MN/RC 2011-25 | 2. | 3. Recipients Accession No. | |
| 4. Title and Subtitle Development of Design Guide for Thin and Ultra-Thin Concrete Overlays of Existing Asphalt Pavements, Task 2: Review and Selection of Structural Response and Performance Models | | 5. Report Date December 2011 | |
| | | 6. | |
| 7. Author(s) Feng Mu and Julie M. Vandebossche | | 8. Performing Organization Report No. | |
| 9. Performing Organization Name and Address Department of Civil and Environmental Engineering University of Pittsburgh Benedum Hall 3700 Ohara St. Pittsburgh, PA 15261 | | 10. Project/Task/Work Unit No. | |
| | | 11. Contract (C) or Grant (G) No. (c) 92965 | |
| 12. Sponsoring Organization Name and Address Minnesota Department of Transportation Research Services Section 395 John Ireland Boulevard, MS 330 St. Paul, MN 55155 | | 13. Type of Report and Period Covered Final Report | |
| | | 14. Sponsoring Agency Code | |
| 15. Supplementary Notes http://www.lrrb.org/pdf/201125.pdf | | | |
| 16. Abstract (Limit: 250 words) The existing ultra-thin whitetopping (UTW) and thin whitetopping (TWT) design methods are reviewed so that any gaps in the design process can be identified. Four design methods are included, namely the Colorado Department of Transportation (CDOT) method, the New Jersey Department of Transportation method, the Portland Cement Association (PCA) method, and the Illinois Centre for Transportation (ICT) method. The structural response and performance models used in these methods are evaluated using field data from the whitetopping sections at MnROAD. Based on these evaluation, the PCA structural model developed for the calculation of stress in the corner and at the top of the overlay seems more suitable for the prediction of the structural response of UTW and the CDOT structural model developed for the calculation of stress at the lane/shoulder edge and at the bottom of the overlay is more suitable for TWT. It is also found that the use of a temperature-dependent asphalt modulus of elasticity results in significantly higher fatigue damage in the overlay, which is ignored by all four methods. Finally, the asphalt fatigue analysis incorporated in some of these design procedures is does not result in fatigue failure of the hot mix asphalt and therefore need not be considered when designing these overlays. | | | |
| 17. Document Analysis/Descriptors Whitetopping, Ultra-thin, Thinness, Structural models, Stresses, Performance Model, Performance tests, Fatigue (Mechanics), Evaluation, MnROAD, Temperature-dependent asphalt, Asphalt, Modulus, Concrete overlays, Bonded concrete overlay | | 18. Availability Statement No restrictions. Document available from: National Technical Information Services, Alexandria, Virginia 22312 | |
| 19. Security Class (this report) Unclassified | 20. Security Class (this page) Unclassified | 21. No. of Pages 153 | 22. Price |

Development of Design Guide for Thin and Ultra-Thin Concrete Overlays of Existing Asphalt Pavements, Task 2: Review and Selection of Structural Response and Performance Models

Final Report

Prepared by:

Feng Mu
Julie M. Vandenbossche

Department of Civil and Environmental Engineering
University of Pittsburgh

December 2011

Published by:

Minnesota Department of Transportation
Research Services Section
395 John Ireland Boulevard, Mail Stop 330
St. Paul, Minnesota 55155

This report represents the results of research conducted by the authors and does not necessarily represent the views or policies of the Local Road Research Board, the Minnesota Department of Transportation, or the University of Pittsburgh. This report does not contain a standard or specified technique.

The authors, the Local Road Research Board, the Minnesota Department of Transportation, and the University of Pittsburgh do not endorse products or manufacturers. Any trade or manufacturers' names that may appear herein do so solely because they are considered essential to this report.

ACKNOWLEDGMENTS

The authors gratefully acknowledge the joint financial support provided by the departments of transportation of the following states: Minnesota, Missouri, New York, Texas and Pennsylvania.

The authors would also like to acknowledge the assistance of Mr. Luis Ramirez in generating this report.

TABLE OF CONTENTS

- 1 Introduction..... 1
- 2 Review of current design guides..... 4
 - 2.1 CDOT method..... 4
 - 2.1.1 Traffic 4
 - 2.1.2 Material characterization 5
 - 2.1.3 Geometry..... 6
 - 2.1.4 Environmental conditions 6
 - 2.1.5 Structural model..... 6
 - 2.1.6 Performance model 9
 - 2.1.7 Reliability..... 10
 - 2.1.8 Surface preparation 10
 - 2.1.9 Advantages and disadvantages 11
 - 2.2 NJDOT method 11
 - 2.2.1 Traffic 11
 - 2.2.2 Material characterization 12
 - 2.2.3 Geometry..... 13
 - 2.2.4 Environmental conditions 13
 - 2.2.5 Structural model..... 14
 - 2.2.6 Performance model 18
 - 2.2.7 Reliability..... 18
 - 2.2.8 Surface preparation 18
 - 2.2.9 Advantages and disadvantages 18
 - 2.3 PCA method 19
 - 2.3.1 Traffic 19
 - 2.3.2 Material characterization 19
 - 2.3.3 Geometry..... 20
 - 2.3.4 Environmental conditions 20
 - 2.3.5 Structural model..... 21
 - 2.3.6 Performance model 24
 - 2.3.7 Reliability..... 24
 - 2.3.8 Surface preparation 24
 - 2.3.9 Advantages and disadvantages 24

| | | |
|-------|--|-----|
| 2.4 | ICT method | 25 |
| 2.4.1 | Traffic | 25 |
| 2.4.2 | Material characterization | 25 |
| 2.4.3 | Geometry..... | 27 |
| 2.4.4 | Environmental conditions | 27 |
| 2.4.5 | Structural model..... | 27 |
| 2.4.6 | Performance model..... | 30 |
| 2.4.7 | Reliability..... | 31 |
| 2.4.8 | Surface preparation | 31 |
| 2.4.9 | Advantages and disadvantages | 31 |
| 2.5 | Summary of current design guides..... | 32 |
| 2.5.1 | Input determination..... | 32 |
| 2.5.2 | Structural models | 32 |
| 2.5.3 | Boundary of each method..... | 33 |
| 2.5.4 | Performance model..... | 33 |
| 3 | Evaluation of current design guides..... | 39 |
| 3.1 | MnROAD data | 39 |
| 3.2 | Evaluation of the NJDOT method..... | 44 |
| 3.2.1 | Conclusion for the NJDOT evaluation | 71 |
| 3.3 | Evaluation of the ICT method..... | 72 |
| 3.3.1 | Conclusion for the ICT evaluation..... | 88 |
| 3.4 | Evaluation of the PCA method..... | 88 |
| 3.4.1 | Conclusion for the PCA evaluation | 105 |
| 3.5 | Evaluation of the CDOT method | 105 |
| 3.5.1 | Conclusion for the CDOT evaluation | 121 |
| 3.6 | Conclusions made base on the evaluations | 121 |
| 4 | Recommendation for new guide | 128 |
| | References..... | 130 |

Appendix A: Load spectrum for single and tandem axles at the MnROAD cell

LIST OF FIGURES

| | |
|--|----|
| Figure 1. Flowchart for the review of the UTW/TWT design methods. | 2 |
| Figure 2. Illustration of the development of the structural response models..... | 3 |
| Figure 3. Pavement structure used in the finite element modeling of the CDOT method..... | 7 |
| Figure 4. Pavement structure used in the finite element modeling of the NJDOT method..... | 14 |
| Figure 5. Conversion of a concrete section to an equivalent asphalt section (Gucunski, 1998). . | 15 |
| Figure 6. Development of the PCA structural response model. | 21 |
| Figure 7. Pavement structure used in the finite element modeling of the PCA method..... | 22 |
| Figure 8. Comparison between parameters used in the ICT equations and those in the PCA equations. | 29 |
| Figure 9. Comparison between PCC fatigue models..... | 38 |
| Figure 10. Layout of test cells at the MnROAD facility..... | 39 |
| Figure 11. Transverse cracking history of MnROAD cells..... | 41 |
| Figure 12. IRI history of MnROAD cells. | 41 |
| Figure 13. Monthly average temperatures for various slabs..... | 42 |
| Figure 14. Average monthly temperatures for various years..... | 43 |
| Figure 15. Observed transverse cracking vs. fatigue damage predicted for the PCC of Cell 60 using the NJDOT method. | 46 |
| Figure 16. Observed transverse cracking vs. fatigue damage predicted for the HMA of Cell 60 using the NJDOT method. | 46 |
| Figure 17. Observed IRI vs. fatigue damage predicted for the PCC of Cell 60 using the NJDOT method..... | 47 |
| Figure 18. Observed IRI vs. fatigue damage predicted for the HMA of Cell 60 using the NJDOT method..... | 47 |
| Figure 19. Observed transverse cracking vs. fatigue damage predicted for the PCC of Cell 61 using the NJDOT method. | 49 |
| Figure 20. Observed transverse cracking vs. fatigue damage predicted for the HMA of Cell 61 using the NJDOT method. | 50 |
| Figure 21. Observed IRI vs. fatigue damage predicted for the PCC of Cell 61 using the NJDOT method..... | 50 |
| Figure 22. Observed IRI vs. fatigue damage predicted for the HMA of Cell 61 using the NJDOT method..... | 51 |
| Figure 23. Observed transverse cracking vs. fatigue damage predicted for the PCC of Cell 62 using the NJDOT method. | 52 |
| Figure 24. Observed transverse cracking vs. fatigue damage predicted for the HMA of Cell 62 using the NJDOT method. | 52 |

| | |
|--|----|
| Figure 25. Observed IRI vs. fatigue damage predicted for the PCC of Cell 62 using the NJDOT method..... | 53 |
| Figure 26. Observed IRI vs. fatigue damage predicted for the HMA of Cell 62 using the NJDOT method..... | 53 |
| Figure 27. Observed transverse cracking vs. fatigue damage predicted for the PCC of Cell 63 using the NJDOT method. | 54 |
| Figure 28. Observed transverse cracking vs. fatigue damage predicted for the HMA of Cell 63 using the NJDOT method. | 55 |
| Figure 29. Observed IRI vs. fatigue damage predicted for the PCC of Cell 63 using the NJDOT method..... | 55 |
| Figure 30. Observed IRI vs. fatigue damage predicted for the HMA of Cell 63 using the NJDOT method..... | 56 |
| Figure 31. Observed transverse cracking vs. fatigue damage predicted for the PCC of Cell 92 using the NJDOT method. | 57 |
| Figure 32. Observed transverse cracking vs. fatigue damage predicted for the HMA of Cell 92 using the NJDOT method. | 57 |
| Figure 33. Observed IRI vs. fatigue damage predicted for the PCC of Cell 92 using the NJDOT method..... | 58 |
| Figure 34. Observed IRI vs. fatigue damage predicted for the HMA of Cell 92 using the NJDOT method..... | 58 |
| Figure 35. Observed transverse cracking vs. fatigue damage predicted for the PCC of Cell 93 using the NJDOT method. | 59 |
| Figure 36. Observed transverse cracking vs. fatigue damage predicted for the HMA of Cell 93 using the NJDOT method. | 60 |
| Figure 37. Observed IRI vs. fatigue damage predicted for the PCC of Cell 93 using the NJDOT method..... | 60 |
| Figure 38. Observed IRI vs. fatigue damage predicted for the HMA of Cell 93 using the NJDOT method..... | 61 |
| Figure 39. Observed transverse cracking vs. fatigue damage predicted for the PCC of Cell 94 using the NJDOT method. | 62 |
| Figure 40. Observed transverse cracking vs. fatigue damage predicted for the HMA of Cell 94 using the NJDOT method. | 62 |
| Figure 41. Observed IRI vs. fatigue damage predicted for the PCC of Cell 94 using the NJDOT method..... | 63 |
| Figure 42. Observed IRI vs. fatigue damage predicted for the HMA of Cell 94 using the NJDOT method..... | 63 |
| Figure 43. Observed transverse cracking vs. fatigue damage predicted for the PCC of Cell 95 using the NJDOT method. | 64 |

| | |
|--|----|
| Figure 44. Observed transverse cracking vs. fatigue damage predicted for the HMA of Cell 95 using the NJDOT method. | 65 |
| Figure 45. Observed IRI vs. fatigue damage predicted for the PCC of Cell 95 using the NJDOT method..... | 65 |
| Figure 46. Observed IRI vs. fatigue damage predicted for the HMA of Cell 95 using the NJDOT method..... | 66 |
| Figure 47. Observed transverse cracking vs. fatigue damage predicted for the PCC of Cell 96 using the NJDOT method. | 67 |
| Figure 48. Observed transverse cracking vs. fatigue damage predicted for the HMA of Cell 96 using the NJDOT method. | 67 |
| Figure 49. Observed IRI vs. fatigue damage predicted for the PCC of Cell 96 using the NJDOT method..... | 68 |
| Figure 50. Observed IRI vs. fatigue damage predicted for the HMA of Cell 96 using the NJDOT method..... | 68 |
| Figure 51. Observed transverse cracking vs. fatigue damage predicted for the PCC of Cell 97 using the NJDOT method. | 69 |
| Figure 52. Observed transverse cracking vs. fatigue damage predicted for the HMA of Cell 97 using the NJDOT method. | 70 |
| Figure 53. Observed IRI vs. fatigue damage predicted for the PCC of Cell 97 using the NJDOT method..... | 70 |
| Figure 54. Observed IRI vs. fatigue damage predicted for the HMA of Cell 97 using the NJDOT method..... | 71 |
| Figure 55. Observed transverse cracking vs. fatigue damage predicted for Cell 60 using the ICT method..... | 73 |
| Figure 56. Observed IRI vs. fatigue damage predicted for Cell 60 using the ICT method. | 74 |
| Figure 57. Observed transverse cracking vs. fatigue damage predicted for Cell 61 using the ICT method..... | 75 |
| Figure 58. Observed IRI vs. fatigue damage predicted for Cell 61 using the ICT method. | 76 |
| Figure 59. Observed transverse cracking vs. fatigue damage predicted for Cell 62 using the ICT method..... | 77 |
| Figure 60. Observed IRI vs. fatigue damage predicted for Cell 62 using the ICT method. | 77 |
| Figure 61. Observed transverse cracking vs. fatigue damage predicted for Cell 63 using the ICT method..... | 78 |
| Figure 62. Observed IRI vs. fatigue damage predicted for Cell 63 using the ICT method. | 79 |
| Figure 63. Observed transverse cracking vs. fatigue damage predicted for Cell 92 using the ICT method..... | 80 |
| Figure 64. Observed IRI vs. fatigue damage predicted for Cell 92 using the ICT method. | 80 |

| | |
|--|-----|
| Figure 65. Observed transverse cracking vs. fatigue damage predicted for Cell 93 using the ICT method..... | 81 |
| Figure 66. Observed IRI vs. fatigue damage predicted for Cell 93 using the ICT method. | 82 |
| Figure 67. Observed transverse cracking vs. fatigue damage predicted for Cell 94 using the ICT method..... | 83 |
| Figure 68. Observed IRI vs. fatigue damage predicted for Cell 94 using the ICT method. | 83 |
| Figure 69. Observed transverse cracking vs. fatigue damage predicted for Cell 95 using the ICT method..... | 84 |
| Figure 70. Observed IRI vs. fatigue damage predicted for Cell 95 using the ICT method. | 85 |
| Figure 71. Observed transverse cracking vs. fatigue damage predicted for Cell 96 using the ICT method..... | 86 |
| Figure 72. Observed IRI vs. fatigue damage predicted for Cell 96 using the ICT method. | 86 |
| Figure 73. Observed transverse cracking vs. fatigue damage predicted for Cell 97 using the ICT method..... | 87 |
| Figure 74. Observed IRI vs. fatigue damage predicted for Cell 97 using the ICT method. | 88 |
| Figure 75. Observed transverse cracking vs. fatigue damage predicted for Cell 60 using the PCA method..... | 90 |
| Figure 76. Observed IRI vs. fatigue damage predicted for Cell 60 using the PCA method. | 91 |
| Figure 77. Observed transverse cracking vs. fatigue damage predicted for Cell 61 using the PCA method..... | 92 |
| Figure 78. Observed IRI vs. fatigue damage predicted for Cell 61 using the PCA method. | 93 |
| Figure 79. Observed transverse cracking vs. fatigue damage predicted for Cell 62 using the PCA method..... | 94 |
| Figure 80. Observed IRI vs. fatigue damage predicted for Cell 62 using the PCA method. | 94 |
| Figure 81. Observed transverse cracking vs. fatigue damage predicted for Cell 63 using the PCA method..... | 95 |
| Figure 82. Observed IRI vs. fatigue damage predicted for Cell 63 using the PCA method. | 96 |
| Figure 83. Observed transverse cracking vs. fatigue damage predicted for Cell 92 using the PCA method..... | 97 |
| Figure 84. Observed IRI vs. fatigue damage predicted for Cell 92 using the PCA method. | 97 |
| Figure 85. Observed transverse cracking vs. fatigue damage predicted for Cell 93 using the PCA method..... | 98 |
| Figure 86. Observed IRI vs. fatigue damage predicted for Cell 93 using the PCA method. | 99 |
| Figure 87. Observed transverse cracking vs. fatigue damage predicted for Cell 94 using the PCA method..... | 100 |
| Figure 88. Observed IRI vs. fatigue damage predicted for Cell 94 using the PCA method. | 100 |

| | |
|--|-----|
| Figure 89. Observed transverse cracking vs. fatigue damage predicted for Cell 95 using the PCA method..... | 101 |
| Figure 90. Observed IRI vs. fatigue damage predicted for Cell 95 using the PCA method..... | 102 |
| Figure 91. Observed transverse cracking vs. fatigue damage predicted for Cell 96 using the PCA method..... | 103 |
| Figure 92. Observed IRI vs. fatigue damage predicted for Cell 96 using the PCA method..... | 103 |
| Figure 93. Observed transverse cracking vs. fatigue damage predicted for Cell 97 using the PCA method..... | 104 |
| Figure 94. Observed IRI vs. fatigue damage predicted for Cell 97 using the PCA method..... | 105 |
| Figure 95. Observed transverse cracking vs. fatigue damage predicted for Cell 60 using the CDOT method..... | 107 |
| Figure 96. Observed IRI vs. fatigue damage predicted for Cell 60 using the CDOT method.... | 107 |
| Figure 97. Observed transverse cracking vs. fatigue damage predicted for Cell 61 using the CDOT method..... | 108 |
| Figure 98. Observed IRI vs. fatigue damage predicted for Cell 61 using the CDOT method.... | 109 |
| Figure 99. Observed transverse cracking vs. fatigue damage predicted for Cell 62 using the CDOT method..... | 110 |
| Figure 100. Observed IRI vs. fatigue damage predicted for Cell 62 using the CDOT method.. | 110 |
| Figure 101. Observed transverse cracking vs. fatigue damage predicted for Cell 63 using the CDOT method..... | 111 |
| Figure 102. Observed IRI vs. fatigue damage predicted for Cell 63 using the CDOT method.. | 112 |
| Figure 103. Observed transverse cracking vs. fatigue damage predicted for Cell 92 using the CDOT method..... | 113 |
| Figure 104. Observed IRI vs. fatigue damage predicted for Cell 92 using the CDOT method.. | 113 |
| Figure 105. Observed transverse cracking vs. fatigue damage predicted for Cell 93 using the CDOT method..... | 114 |
| Figure 106. Observed IRI vs. fatigue damage predicted for Cell 93 using the CDOT method.. | 115 |
| Figure 107. Observed transverse cracking vs. fatigue damage predicted for Cell 94 using the CDOT method..... | 116 |
| Figure 108. Observed IRI vs. fatigue damage predicted for Cell 94 using the CDOT method.. | 116 |
| Figure 109. Observed transverse cracking vs. fatigue damage predicted for Cell 95 using the CDOT method..... | 117 |
| Figure 110. Observed IRI vs. fatigue damage predicted for Cell 95 using the CDOT method.. | 118 |
| Figure 111. Observed transverse cracking vs. fatigue damage predicted for Cell 96 using the CDOT method..... | 119 |
| Figure 112. Observed IRI vs. fatigue damage predicted for Cell 96 using the CDOT method.. | 119 |

Figure 113. Observed transverse cracking vs. fatigue damage predicted for Cell 97 using the CDOT method..... 120

Figure 114. Observed IRI vs. fatigue damage predicted for Cell 97 using the CDOT method.. 121

LIST OF TABLES

| | |
|---|----|
| Table 1. Inputs used in the CDOT 2-D finite element analysis. | 7 |
| Table 2. Coefficients for the traffic-induced stresses in PCC (Gucunski, 1998). | 17 |
| Table 3. Coefficients for the traffic-induced stresses in HMA (Gucunski, 1998). | 17 |
| Table 4. Coefficients for temperature-gradient-induced stresses in PCC (Gucunski, 1998). | 18 |
| Table 5. Pavement parameters used in the PCA finite element analysis. | 21 |
| Table 6. Comparison between design methods. | 35 |
| Table 7. Pavement parameters used in the development, validation and sensitivity analysis of the design methods. | 37 |
| Table 8. Pavement parameters in MnROAD cells. | 40 |
| Table 9. Temperature dependency of the asphalt modulus of elasticity. | 44 |
| Table 10. Fatigue summary for Cell 60 using the NJDOT method. | 45 |
| Table 11. Example of stress predictions for Cells 60 and 62 using the NJDOT method. | 48 |
| Table 12. Fatigue summary for Cell 61 using the NJDOT method. | 49 |
| Table 13. Fatigue summary for Cell 62 using the NJDOT method. | 51 |
| Table 14. Fatigue summary for Cell 63 using the NJDOT method. | 54 |
| Table 15. Fatigue summary for Cell 92 using the NJDOT method. | 56 |
| Table 16. Fatigue summary for Cell 93 using the NJDOT method. | 59 |
| Table 17. Fatigue summary for Cell 94 using the NJDOT method. | 61 |
| Table 18. Fatigue summary for Cell 95 using the NJDOT method. | 64 |
| Table 19. Fatigue summary for Cell 96 using the NJDOT method. | 66 |
| Table 20. Fatigue summary for Cell 97 using the NJDOT method. | 69 |
| Table 21. Fatigue summary for Cell 60 using the ICT method. | 73 |
| Table 22. Stress predictions for Cell 60 using the ICT method. | 74 |
| Table 23. Fatigue summary for Cell 61 using the ICT method. | 75 |
| Table 24. Fatigue summary for Cell 62 using the ICT method. | 76 |
| Table 25. Fatigue summary for Cell 63 using the ICT method. | 78 |
| Table 26. Fatigue summary for Cell 92 using the ICT method. | 79 |
| Table 27. Fatigue summary for Cell 93 using the ICT method. | 81 |
| Table 28. Fatigue summary for Cell 94 using the ICT method. | 82 |
| Table 29. Fatigue summary for Cell 95 using the ICT method. | 84 |
| Table 30. Fatigue summary for Cell 96 using the ICT method. | 85 |
| Table 31. Fatigue summary for Cell 97 using the ICT method. | 87 |

| | |
|--|-----|
| Table 32. Fatigue summary for Cell 60 using the PCA method..... | 90 |
| Table 33. Stress predictions for Cell 60 using the PCA method. | 91 |
| Table 34. PCC fatigue predictions based on temperature-dependent asphalt modulus of elasticity for Cell 60 using the PCA method..... | 91 |
| Table 35. Fatigue summary for Cell 61 using the PCA method..... | 92 |
| Table 36. Fatigue summary for Cell 62 using the PCA method..... | 93 |
| Table 37. Fatigue summary for Cell 63 using the PCA method..... | 95 |
| Table 38. Fatigue summary for Cell 92 using the PCA method..... | 96 |
| Table 39. Fatigue summary for Cell 93 using the PCA method..... | 98 |
| Table 40. Fatigue summary for Cell 94 using the PCA method..... | 99 |
| Table 41. Fatigue summary for Cell 95 using the PCA method..... | 101 |
| Table 42. Fatigue summary for Cell 96 using the PCA method..... | 102 |
| Table 43. Fatigue summary for Cell 97 using the PCA method..... | 104 |
| Table 44. Fatigue summary for Cell 60 using the CDOT method..... | 106 |
| Table 45. Fatigue summary for Cell 61 using the CDOT method..... | 108 |
| Table 46. Fatigue summary for Cell 62 using the CDOT method..... | 109 |
| Table 47. Fatigue summary for Cell 63 using the CDOT method..... | 111 |
| Table 48. Fatigue summary for Cell 92 using the CDOT method..... | 112 |
| Table 49. Fatigue summary for Cell 93 using the CDOT method..... | 114 |
| Table 50. Fatigue summary for Cell 94 using the CDOT method..... | 115 |
| Table 51. Fatigue summary for Cell 95 using the CDOT method..... | 117 |
| Table 52. Fatigue summary for Cell 96 using the CDOT method..... | 118 |
| Table 53. Fatigue summary for Cell 97 using the CDOT method..... | 120 |
| Table 54. Summary of fatigue damage predictions at 3 million ESALs for MnROAD cells using a constant asphalt modulus of elasticity..... | 124 |
| Table 55. Summary of structural response predictions due to 18-kip single axle loading for MnROAD cells using a constant asphalt modulus of elasticity..... | 125 |
| Table 56. Summary of stress ratios due to 18-kip single axle loading for MnROAD cells using a constant asphalt modulus of elasticity. | 126 |
| Table 57. Summary of thermal stress/strain predictions for MnROAD cells using a constant asphalt modulus of elasticity..... | 127 |

EXECUTIVE SUMMARY

This report is the second of eight task reports as part of the Transportation Pooled Fund Project 5 (165): “Development of Design Guide for Thin and Ultra-thin Concrete Overlays of Existing Asphalt Pavements.”

In this task, the existing ultra-thin whitetopping (UTW) and thin whitetopping (TWT) design methods are reviewed with special attention paid to the modeling effort of the interface bonding. Four design methods are included, namely the Colorado Department of Transportation (CDOT) method, the New Jersey Department of Transportation method, the Portland Cement Association (PCA) method, and the Illinois Centre for Transportation (ICT) method.

The performance of the NJDOT, ICT, PCA and CDOT methods were evaluated using field observations. None of the methods yield perfect predictions for the fatigue development of the MnROAD test sections. The PCA and the CDOT methods seem to be able to yield the most reasonable predictions regarding fatigue in the Portland cement concrete (PCC) overlay. This might be due to the fact that there is consideration for partial bonding. The PCA structural model developed for calculating stress in the corner and at the top of the overlay is most suitable for the prediction of structural responses for UTWs and the CDOT structural model developed for calculating stress at the lane/shoulder edge and at the bottom of the overlay is more suitable for TWTs.

With respect to the concrete performance prediction model, the PCA model only employs the stress ratio as an input and yields an average fatigue prediction among the fatigue models. The modified American Concrete Pavement Association (ACPA) fatigue model not only considers the stress ratio but also takes into account the design probability and failure criterion. Nevertheless, the ACPA model and the PCA fatigue models yield similar predictions. Therefore, either one would be a sufficient for modeling the fatigue performance for PCC.

The Asphalt Institute fatigue model is used in the current whitetopping design methods, except for the ICT method where the asphalt fatigue is not considered as a failure criterion. However, it is worth noting that the Asphalt Institute model was not developed for a flexible layer beneath a concrete overlay and that the fatigue of the existing asphalt rarely dominates the failure of whitetopping during the evaluation. Therefore, it does not seem prudent to consider the fatigue of the existing asphalt in the design of whitetopping.

No model is currently available for characterizing the degradation of the interface bonding. Based on the review, more laboratory and field work is still needed to characterize interface debonding, which contributes greatly to the failure of whitetopping, especially for UTWs. This issue will be addressed in Task 3.

During the evaluation, it was also identified that the asphalt modulus of elasticity is such an important parameter in stress predictions that a monthly asphalt modulus of elasticity should be used. To achieve this goal, a nationwide characterization for climate in terms of ambient temperature and temperature gradient must be carried out. This issue will be addressed in Task 4. Furthermore, the condition of the existing asphalt layer has to be characterized so that the

regions where reflective cracking/distress could potentially develop can be identified. Guidance on when pre-overlay repairs should be performed will be provided in Task 5.

1 INTRODUCTION

The objective of this task is to review the existing ultra-thin whitetopping (UTW) and thin whitetopping (TWT) design procedures and evaluate their efficiency using field data in order to provide useful recommendations for the development of the new design procedure. In total, four design methods are reviewed and evaluated, namely the Colorado Department of Transportation (CDOT) method (Tarr et al., 1998), New Jersey Department of Transportation (NJDOT) method (Gucunski, 1998), Portland Cement Association (PCA) method (Wu et al., 1999), and the Illinois Centre for Transportation (ICT) method (Roesler et al., 2008).

The general framework under which each method is developed is illustrated in Figure 1. In most cases, three major modules are incorporated, namely the identification of inputs, the structure response models and the performance models.

Determining inputs is essential for the successful implementation of a UTW/TWT design method. The condition of the existing pavement has to be characterized first, e.g. the modulus of elasticity for the existing hot mix asphalt (HMA) layer, E_{HMA} , the depth of the HMA layer, H_{HMA} , and the modulus of subgrade reaction k -value. It is also important to predict the traffic loading and thermal loading during the design life of the overlay since they are the two major external factors that introduce stresses and strains into the pavement. During the design process, the Portland cement concrete (PCC) properties, i.e. the modulus of elasticity, E_{PCC} , the flexural strength, MOR_{PCC} , the coefficient of thermal expansion (CTE), and the use of fiber, should also be known beforehand for the structural response and performance models. The geometry of the PCC slab is typically established during the design process. It is common to establish the slab spacing, L , based on experience and the slab thickness through the design procedure.

An iterative process is often employed to design the slab thickness. In this process, a trial thickness is first assumed and inserted into the structural models to yield the design stress and strain. The allowable numbers of load repetitions in both PCC and HMA layers are then calculated using the performance models at the design stress or strain level. The final design thickness will be obtained by adjusting the trial thickness until the predicted allowable load repetitions is equal to the design traffic.

The structural response models are presented to the users as stress/strain prediction equations. The equations need to be fed with inputs defined in the first module and will yield the design stress or strain. In the CDOT, NJDOT and PCA structural models (the ICT method employs the PCA structural model), the stress prediction equations are developed following the same logic, as shown in Figure 2. A database is first populated based on the identified range of inputs. The finite element (FE) method is then employed to yield the critical stress/strain for the cases in the database. Finally, statistical correlations are established between the inputs used and the calculated stresses and strains, which are the structural prediction equations. The accuracy of each structural model in predicting the response of UTW/TWT highly depends on its assumption of the pavement structure, consideration of traffic and environmental loading, and consideration of bonding between the PCC and HMA layers. The suitability of applying each model in whitetopping design relies on its assumption of the location of the critical stress/strain, if it is at the top or the bottom of the slab, or whether it is at the corner or the midslab.

The final module within a design procedure includes the performance models for PCC and HMA. Here the predicted design stress and strain is used to determine the fatigue damage caused by a certain number of load repetitions. For the four methods reviewed, no PCC or HMA fatigue models were specially developed for UTW/TWT fatigue performance. Existing models for new PCC or HMA pavements are borrowed instead, which might introduce significant error.

Reliability is another important factor to be considered in design. Therefore, the use of reliability within each design method will be discussed.

After a review of the modules for each method and a discussion of their advantages and disadvantages, an evaluation will be carried out using field data to further compare the performance of these models. Finally, the most appropriate models for the development of the new design procedure will be recommended.

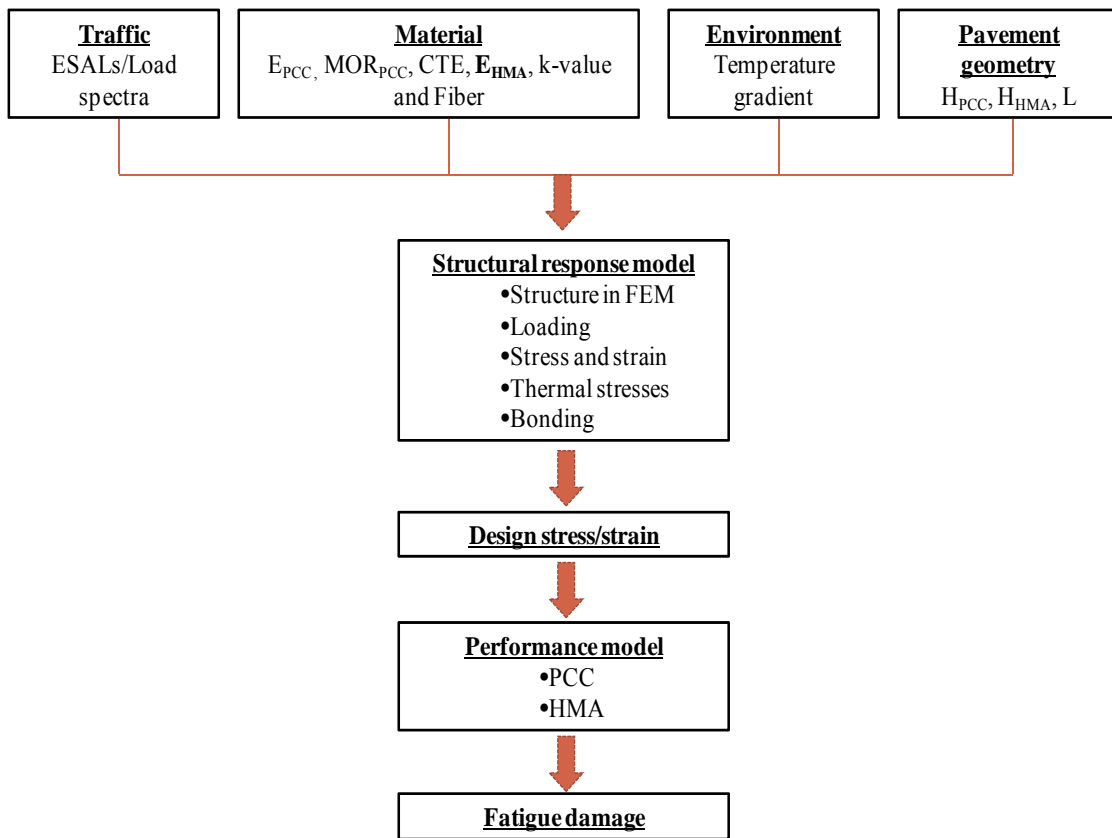


Figure 1. Flowchart for the review of the UTW/TWT design methods.

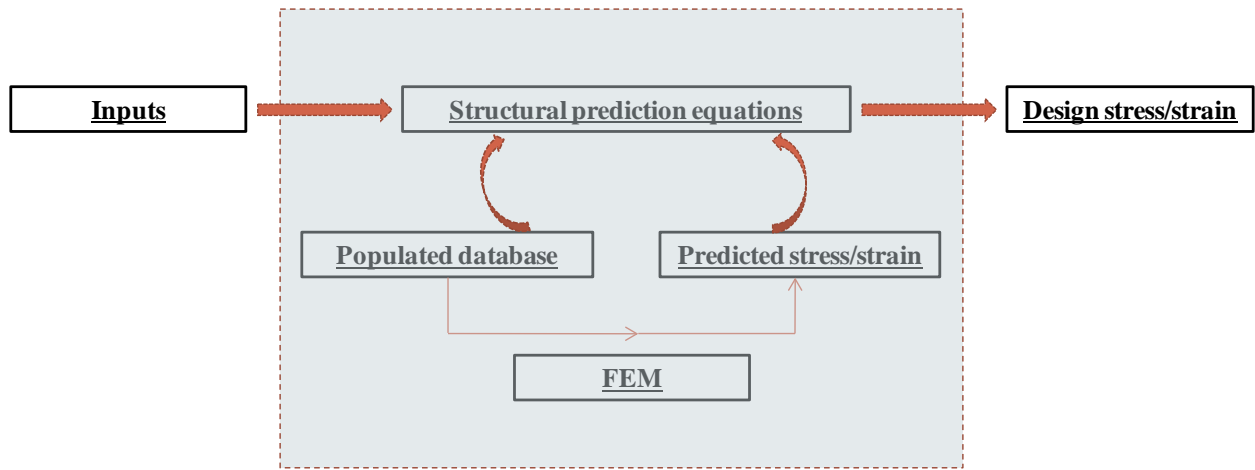


Figure 2. Illustration of the development of the structural response models.

2 REVIEW OF CURRENT DESIGN GUIDES

2.1 CDOT method

Tarr et al. (1998) proposed a whitetopping design method for the Colorado Department of Transportation (CDOT). In this method, the load-induced tensile stress and strain calculated for the TWT/UTW and HMA layers are adjusted to account for the temperature differential and partial bonding. Based on the stress and strain, the allowable number of load repetitions is determined using the performance model.

2.1.1 Traffic

Load spectra are used as the traffic input. However, design equations for PCC stress and HMA strain are only proposed for a 20-kip single axle load and a 40-kip tandem axle load. Stresses for the other single or tandem axle loads are computed as ratio of the 20-kip single axle load or 40-kip tandem axle load. Axles other than single axle and tandem axle are not considered.

A procedure using the 18-kip equivalent single axle loads (ESALs) is also proposed. The concept of ESALs in the Association of State Highway and Transportation Officials (AASHTO) 1993 Design Guide (AASHTO, 1993) was established based on the pavement performance data collected during the AASHTO road test in Ottawa, IL in the 1950's and 1960's, where the ESAL is a function of the pavement thickness and the minimum thickness is 6 in. Therefore, conversion factors were developed for UTW that has a thickness less than 4 in, based on the AASHTO load equivalency factors established for an 8-in thick concrete pavement and a terminal serviceability of 2.5. Two highway categories (primary and secondary) in Colorado were anticipated as typical recipients of whitetopping treatment and thus the conversions factors for them were proposed as shown in the following equations.

$$\text{Primary Highway: } F_{ESAL} = 0.985 + 10.057(h_{PCC})^{-3.456} \quad (1)$$

$$\text{Secondary Highway: } F_{ESAL} = (1.286 - 2.138/h_{PCC})^{-1} \quad (2)$$

where F_{ESAL} is the conversion factor from ESALs calculated assuming an 8-in concrete pavement and a terminal serviceability of 2.5 and h_{PCC} is the thickness of the whitetopping overlay.

It has been noted that using ESALs as traffic inputs results in a design thickness different from that using axle spectra as inputs. A correlation was then established between the design thicknesses based on the two kinds of traffic input as shown in Equation (3).

$$h_{ESAL} = -0.0728(h_{LS})^2 + 1.4675h_{LS} + 0.8638 \quad (3)$$

where h_{ESAL} is the concrete thickness using ESALs as traffic input, in and h_{LS} is the design thickness using load spectra, in.

2.1.2 Material characterization

2.1.2.1 PCC modulus of elasticity

Concrete cylinders were cast during the construction of two CDOT whitetopping test sites for the 28-day and 365-day PCC modulus of elasticity. The 28-day modulus was determined as 3.7 million and 3.28 million psi for the two sites, respectively. The 365-day modulus was 4.21 million and 4.0 million psi for the two sites, respectively. Based on these laboratory measurements, the PCC modulus of elasticity was assumed to be 4 million psi to develop the CDOT structural model. No further suggestion was specified with respect to how designers should define this input.

2.1.2.2 PCC flexural strength

During the CDOT field testing, concrete beams were tested at 28 days to determine their flexural strength. In the sensitivity analysis of the CDOT design method, 500, 650 and 800 psi were used for the flexural strength.

2.1.2.3 PCC coefficient of thermal expansion

The CTE input is not required in the CDOT design method, because the design stress is adjusted for the temperature gradient empirically, as discussed in Section 2.1.5.

2.1.2.4 HMA modulus of elasticity

The HMA resilient modulus was tested using cores from each of the three CDOT test sites and the results were 0.35 million, 0.8 million and 0.8 million psi. During the development of the CDOT structural model, 0.05 million, 0.5 million and 1 million psi were assumed for the HMA modulus of elasticity. In the design example, 0.6 million psi was used assuming 50 percent of remaining fatigue life and low-severity cracking for the existing HMA. There is no guidance to determine the HMA resilient modulus for design.

2.1.2.5 Modulus of subgrade reaction

In the development of the CDOT structural model, 75, 200 and 400 psi/in were employed for the modulus of subgrade reaction. This is mostly likely based on the field measurements, namely 150 psi, 225 psi and 340 psi for the three test sites. The design procedure provides no guidance on how to establish the modulus of subgrade reaction for design.

2.1.2.6 Fibers

The effect of fibers is not considered.

2.1.3 Geometry

2.1.3.1 PCC overlay thickness

The thickness of the CDOT test slabs ranged from 4 to 7 in. To develop the CDOT stress prediction equations, three PCC thicknesses were used in the finite element modeling, namely 4, 5 and 6 in.

2.1.3.2 HMA thickness

The HMA layers were 3 to 7.5 in thick for the test sections used in the development of the design procedure. During the development of the CDOT stress prediction equation, the HMA thickness was assumed to be 3, 6 and 9 in. In the design example, an HMA thickness of 7 in was used. No information is provided regarding the minimum HMA thickness for UTW/TWT applications.

2.1.3.3 Joint spacing

The joint spacing is 5 ft for the first CDOT whitetopping project. A 12-ft joint spacing was used for the second project, where dowel bars were applied at the joint. For the third project, random joint spacing, namely 4 ft, 6 ft or 12 ft, was employed and dowel bars were used for most of the joints. During the development of CDOT structural response models, square concrete slabs of 4, 6 and 12 ft were used. In the design example, a joint spacing of 6 ft was used.

2.1.4 Environmental conditions

The effect of temperature gradients on the stress was taken into account based on the measured temperature gradients, as will be discussed in Section 2.1.5. Temperature gradients were recorded for the test sections, which ranged from -1 to 5 °F/in. However, it is a disadvantage that no guidance was provided with respect to how to establish this input in the design procedure, especially considering the difficulty and expense in defining this input for design.

2.1.5 Structural model

Two-dimensional (2-D) FE software ILSL2 was employed to determine the tensile stresses at the bottom of each layer under 20-kip single axle loads and 40-kip tandem axle loads.

2.1.5.1 Structure

For the 2-D finite element modeling, the whitetopping structure was assumed to be as shown in the Figure 3. Several FE runs with the inputs presented in Table 1 were carried out to establish the empirical correlations, Equations 4 to 7, to predict the maximum stress and strain.

2.1.5.2 Loading

A 20-kip single axle or a 40-kip tandem axle loading condition was applied at the slab corner and edge in the FE model. It was found that the maximum tensile stress most frequently occurred at the bottom of the concrete layer due to edge loading. The corner loading would result in higher

stresses than the edge loading condition only when the effective radius of relative stiffness is high and thus, the magnitude of the maximum stress is small.

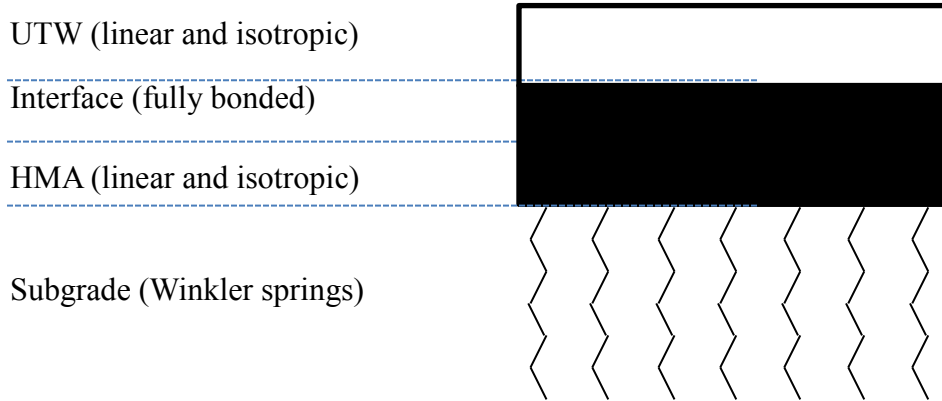


Figure 3. Pavement structure used in the finite element modeling of the CDOT method.

Table 1. Inputs used in the CDOT 2-D finite element analysis.

| Pavement parameters | Value |
|--------------------------------------|-------------------------|
| Concrete spacing, ft | 4, 6, 12 |
| Concrete thickness, in | 4, 5, 6 |
| Concrete modulus of elasticity, psi | 4 million |
| Asphalt thickness, in | 3, 6, 9 |
| Asphalt modulus of elasticity, psi | 0.05, 0.5 and 1 million |
| Modulus of subgrade reaction, psi/in | 75, 200, 400 |

2.1.5.3 Critical stress and strain

Based on the findings from the FE modeling, the maximum tensile stress was assumed to occur at the bottom of the PCC layer and its magnitude can be determined using Equations (4) and (5). The critical strain for the HMA layer was assumed to occur at the bottom of the layer, as described in Equations (6) and (7).

Concrete stress under 20-kip single axle loads:

$$\sigma_{PCC} = 919 + \frac{18492}{l_e} - 575.3 \log k + 0.000133 E_{HMA}, \quad R_{adj}^2 = 0.99 \quad (4)$$

Concrete stress under 40-kip tandem axle loads:

$$\sigma_{PCC} = 671.2 + \frac{15820}{l_e} - 437.1 \log k + 0.000099 E_{HMA}, \quad R_{adj}^2 = 0.99 \quad (5)$$

Asphalt strain under 20-kip single axle loads:

$$\frac{1}{\varepsilon_{HMA}} = 8.5114 \times 10^{-9} E_{HMA} + 0.008619 \frac{l_e}{L}, \quad R_{adj}^2 = 0.99 \quad (6)$$

Asphalt strain under 40-kip tandem axle loads:

$$\frac{1}{\varepsilon_{HMA}} = 9.61792 \times 10^{-9} E_{HMA} + 0.009776 \frac{l_e}{L}, \quad R_{adj}^2 = 0.99 \quad (7)$$

where σ_{PCC} is the maximum tensile stress at the bottom of the concrete slab, psi; ε_{HMA} is the maximum strain at the bottom of the asphalt layer, microstrain; E_{HMA} is the elastic modulus of the asphalt, psi; k is the modulus of subgrade reaction, psi/in; L is the joint spacing, in; and l_e is the effective radius of relative stiffness for fully bonded slabs as defined in Equation (8), in.

$$l_e = \frac{E_{PCC} h_{PCC}^3}{12 \cdot k(1 - \mu_{PCC}^2)^{1/4}} + \frac{E_{PCC} h_{PCC} (NA - h_{PCC}/2)^2}{k(1 - \mu_{PCC}^2)^{1/4}} + \frac{E_{HMA} h_{HMA}^3}{12 \cdot k(1 - \mu_{HMA}^2)^{1/4}} + \frac{E_{HMA} \cdot h_{HMA} (h_{PCC} - NA + h_{HMA}/2)^2}{k(1 - \mu_{HMA}^2)^{1/4}} \quad (8)$$

To determine the stress and strain due to 18-kip equivalent single axle loads, it was suggested that a reduction factor of 0.9 be applied to Equations (4) and (6), respectively.

2.1.5.4 Thermal stress

The effect of temperature gradients on the predicted maximum stress was taken into account through Equation (9). This equation should be used as long as the joint spacing exceeds 4 ft to account for the stress increment due to slab curling.

$$\sigma_{\%} = 4.56 \cdot \Delta_T \quad (9)$$

where $\sigma_{\%}$ is the percent change in stress, % and Δ_T is the temperature gradient, °F/in.

2.1.5.5 Bonding

The predicted PCC stress for the fully bonded condition was found smaller than the field observations. It was also identified that the measured HMA strain was on average 16 percent lower than the measured PCC strain at the PCC-HMA interface, as described by Equation (10). Both findings were considered to be evidence of partial interface bonding. Therefore, based on a statistical analysis, the increase in stress due to partial bonding at the interface can be accounted for through Equation (11).

$$\varepsilon_{HMA} = 0.842 \cdot \varepsilon_{PCC} \quad (10)$$

where ε_{HMA} is the measured strain at the top of the asphalt layer and ε_{PCC} is the measured strain at the bottom of the concrete layer.

$$\sigma_m = \alpha \cdot \sigma_p \quad (11)$$

where σ_m is the stress corrected for partial bonding at a zero temperature gradient, psi; σ_p is the predicted maximum stress at a zero temperature gradient either due to edge loading or corner loading, psi and α is the correction factor that is 1.65, 1.63 or 1.59 for 95 percent, 90 percent or 75 percent reliability of partial bonding, respectively.

2.1.5.6 Other considerations

The effect of load transfer, in terms of tied longitudinal joints, on the critical stress was studied based on the observations from the three projects. A reduction of 47 percent of the critical stress was suggested for slabs with tied longitudinal joints, as described by Equation ((12).

$$\sigma_{tied} = 0.53\sigma_{free} \quad (12)$$

2.1.6 Performance model

The allowable repetitions for each type of axle load were determined for the PCC layer according to the PCA fatigue model (PCA, 1984), Equations (13 and (14). The inputs required are the critical stress and the PCC flexural strength, of which the former can be obtained through the CDOT structural model and the latter one is left for users to define.

The asphalt fatigue model by the Asphalt Institute (1982) was used as shown in Equation (15). A correction factor to the equation was suggested to account for the consumed fatigue life of the HMA layer prior to the whitetopping construction. The factor can be determined by the designers as a percentage that represents the remaining fatigue life of the HMA layer.

$$N = \begin{cases} 10^{12.1(0.972-SR)} & SR > 0.55 \\ \left(\frac{4.258}{SR - 0.4325}\right)^{3.268} & 0.55 > SR > 0.45 \\ \infty & SR < 0.45 \end{cases} \quad (13)$$

$$SR = \frac{\sigma_{PCC}}{M_R} \quad (14)$$

where N is the fatigue life of the PCC; SR is the stress ratio; σ_{PCC} is the maximum flexural stress, psi and M_R is the PCC flexural strength, i.e. modulus of rupture, psi.

$$N_f = 18.4 \cdot (4.32 \times 10^{-3}) \cdot C \cdot (\varepsilon_{HMA})^{-3.291} \cdot (E_{HMA})^{-0.854} \quad (15)$$

where N_f is the number of load repetitions corresponding to 20 percent or greater asphalt fatigue cracking over the entire pavement area (or about 37 percent of the wheel path area); ε_{HMA} is the maximum tensile strain at the bottom of the asphalt layer; E_{HMA} is the asphalt modulus of elasticity, psi; C is a correction factor that is equal to 10^M where $M = 4.84[V_b/(V_b + V_v) - 0.69]$ and V_b and V_v are the percent volume of asphalt and air voids, respectively. C tends towards one for typical mixtures and thus the Asphalt Institute fatigue equation can be simplified as shown in Equation (16), which can be more readily used in design.

$$N_f = 0.0796(\varepsilon_{HMA})^{-3.291} \cdot (E_{HMA})^{-0.854} \quad (16)$$

2.1.7 Reliability

Reliability was considered when establishing the adjustment factors for partial bonding, as in Equation (11). However, there is no consideration regarding the overall reliability for design.

2.1.8 Surface preparation

Strain measurements were collected from gages instrumented at multiple depths of three locations, namely edge, center and corner. An analysis of all the strains showed that the strains were decreased by approximately 25 percent when milling was applied to the existing HMA layer. However, the strains were increased by approximately 50 percent when the newly placed HMA layer was milled. This might indicate that milling is a good surface preparation approach only for aged/distressed asphalt pavements. However, this finding was not considered valid or safe to be employed into design until it was verified by more tests. Therefore, no specific surface preparation was recommended to ensure a good interface bonding in the design procedure.

2.1.9 Advantages and disadvantages

2.1.9.1 Advantages

Primarily, the effect of partial bonding, joint load transfer and temperature gradients on the prediction of stress and strain is taken into account by calibrating the FE results to the field measurements at the three Colorado test sites. Additionally, the concept of reliability was employed when determining the partial bonding based on the field data. Finally, fatigue is considered for both PCC and HMA layers.

2.1.9.2 Disadvantages

The approach of adjusting stress and strain based on field measurements might not always be valid. For instance, the measured stress at the interface was found to be greater than the predicted stresses for a fully bonded condition, based on which the stress was adjusted for partial bonding. However, this may be caused by other factors besides the partial bonding, such as the poor quality of the underlying asphalt layer. Furthermore, the field measurements based on which the adjustments were made are localized and limited (only three projects in Colorado). Therefore, the adjustments might not be valid for applications in other states.

Little guidance is provided on how to establish the design inputs. Also, the temperature dependency of HMA stiffness is not considered and the effect of fibers is not discussed. More importantly, the critical stress is identified at the bottom of the slab edge. This may be more suitable for TWT whose dominant distress is transverse cracking. For UTW, which tend to develop corner cracks, the critical stress is mainly located at the top of the PCC corners.

2.2 NJDOT method

The New Jersey Department of Transportation (NJDOT) design method (Gucunski, 1998) firstly determines the design thickness of the overlay for a bonded and then for an unbonded pavement structure. The final design thickness is then linearly interpolated between the two thicknesses based on the degree of bonding assumed.

2.2.1 Traffic

The traffic loading is converted to equivalent 18-kip single axle loads (ESALs) by using the conversion factors as shown in Equations (17) and (18) for single and tandem axle loads, respectively.

For single axle loads,

$$W_{18} = \left(\frac{W_{SAL}}{18} \right)^{3.3} \quad (17)$$

where W_{18} is the factor to convert a single axle load W_{SAL} to the equivalent numbers of single 18-kip axle load.

For tandem axle loads,

$$W_{18} = \left(\frac{T \cdot W_{TAL}}{2 \times 18} \right)^{3.3} \quad (18)$$

where W_{TAL} is the weight of a tandem axle in kips and T is the tandem factor that indicates how much stress one axle introduces beneath the adjacent axle. The tandem factor depends on the tire configuration and the radius of relative stiffness of the pavement structure. It is suggested to be 1.25 for concrete pavements. The 18-kip equivalency factor can also be determined according to the AASHTO 1993 Design Guide if no details are available regarding the axle weights.

The design traffic, W_D in Equation (19), is then obtained by applying a safety factor to the equivalent 18-kip axle loads in order to account for the overall standard deviation of prediction errors and the required design reliability.

$$W_D = 10^{-Z_R S_0} W_{18} \quad (19)$$

where Z_R is the standard normal deviation depending on the design reliability and S_0 is the overall standard deviation of errors that is suggested to be 0.30 to 0.40 for rigid pavements according to the AASHTO 1993 Design Guide.

2.2.2 Material characterization

2.2.2.1 PCC modulus of elasticity

The PCC modulus of elasticity was assumed to be 3.4 million psi in the parametric study of the NJDOT structural model and 5 million in the design example. No guidance is provided on establishing this input for design.

2.2.2.2 PCC flexural strength

The flexural strength was determined based on laboratory testing or estimated based on the concrete elastic modulus using the correlation suggested in the AASHTO 1993 Design Guide as shown in Equation (20).

$$M_R = \frac{43.5 E_{PCC}}{1000000} + 448.5 \quad (20)$$

where E_{PCC} is the PCC modulus of elasticity, psi and M_R is the PCC flexural strength (i.e. modulus of rupture), psi.

2.2.2.3 PCC coefficient of thermal expansion

The PCC coefficient of thermal expansion was assumed to be $3.8 \times 10^{-6}/^{\circ}\text{F}$ in the parametric study of the NJDOT structural model and in the design example. No guidance is provided for determining this input for design.

2.2.2.4 HMA modulus of elasticity

In the parametric study of the NJDOT structural model, the HMA modulus of elasticity laid between 0.88 to 1.66 million psi. In the design example, 0.5 million psi was used. In-situ tests, such as the falling weight deflectometer (FWD) testing, were suggested for establishing this input.

2.2.2.5 Modulus of subgrade reaction

The modulus of subgrade reaction was assumed from 145 to 580 psi/in in the parametric study. In-situ tests, such as plate loading test, were suggested to obtain this input.

2.2.2.6 Fibers

The effect of fibers is not considered.

2.2.3 Geometry

2.2.3.1 PCC overlay thickness

The thickness of the PCC cores from the NJDOT test project at the I-295 ramp ranged from 2.9 to 4.6 in. During the parametric study of the NJDOT structural model, the PCC thickness was assumed to range from 3 to 5 in.

2.2.3.2 HMA thickness

The thickness of the HMA cores from the NJDOT tests ranged from 5.2 to 7.4 in. During the parametric study of the NJDOT structural model, the HMA thickness was assumed to range from 4 to 8 in. No further information is provided regarding the minimum HMA thickness for UTW/TWT applications.

2.2.3.3 Joint spacing

The slabs used in the NJDOT tests were 3, 4 and 6 ft long. During the parametric study of the NJDOT stress model, joint spacing of 3 or 4 ft was used. However, the stress prediction equation does not employ joint spacing as an input. Therefore, no information regarding this input is needed for design.

2.2.4 Environmental conditions

The temperature difference of the overlay is needed to calculate the thermal stress. In the design example, a temperature differential of $3^{\circ}\text{F}/\text{in}$ was used, which was multiplied by the trial

thickness of the PCC overlay as the temperature difference input for the design equation. No specification is suggested how to establish this input for design.

2.2.5 Structural model

Gucunski (1998) carried out a finite element study on whitetopping structures in an effort to develop the whitetopping design guide for NJDOT.

2.2.5.1 Structure

The PCC overlay, the existing HMA layer and the subbase layer were all simulated as linear, isotropic materials and the subgrade was represented by a set of Winkler springs, as shown in Figure 4. In order to investigate the effect of bonding on the induced stresses, the interface layer was simulated as an anisotropic layer that was 0.5 in thick (thin compared to the 3- to 5-in PCC overlay and the 4- to 8-in HMA layer used in the modeling).

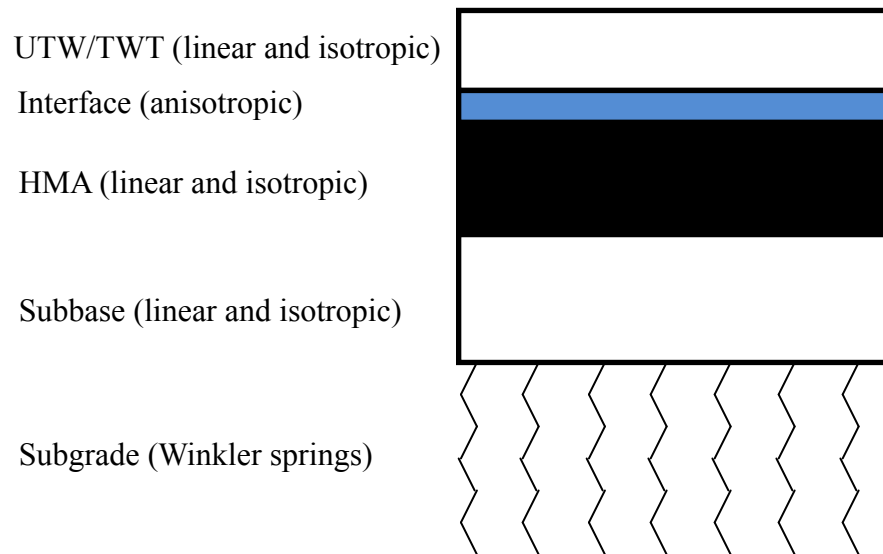


Figure 4. Pavement structure used in the finite element modeling of the NJDOT method.

2.2.5.2 Loading

The structural response of the abovementioned whitetopping structure was studied under four types of traffic and environmental loadings, namely the loadings due to a linear temperature gradient, 18-kip loads (single axle with dual tires) at slab corners, edges and centers, respectively. Center or edge loading was identified causing the maximum stresses in PCC and HMA layers.

2.2.5.3 Critical stress and strain

The maximum stress in the PCC layer was identified at the bottom of the layer, but the location of the maximum stress in the HMA layer was not documented. To correlate the FE calculated stresses with those based on the Westergaard's equations, the composite beam concept was used to convert the concrete overlay to an equivalent asphalt layer, considering two extreme bonding

conditions as shown in Figure 5. The new neutral axis and moment of inertia of the composite layers were therefore transformed to Equations (21) to (23).

$$I_B = \frac{nh_{PCC}^3}{12} + \frac{h_{HMA}^3}{12} + \frac{nh_{PCC}h_{HMA}(h_{PCC} + h_{HMA})^2}{4(nh_{PCC} + h_{HMA})} \quad (21)$$

$$I_U = \frac{nh_{PCC}^3}{12} + \frac{h_{HMA}^3}{12} \quad (22)$$

$$N.A. = \frac{nh_{PCC}^2 + h_{HMA}^2 + 2h_{HMA}h_{PCC}}{2(nh_{PCC} + h_{HMA})} \quad (23)$$

where I_B and I_U are the moments of inertia for fully bonded and unbonded sections, respectively, in³; $N.A.$ is the depth of the neutral axis from the top of the PCC overlay, in; h_{HMA} and h_{PCC} are the thicknesses of the HMA and the PCC layers, respectively, in, and n is the ratio of the elastic modulus between the PCC and the HMA, $n = E_{PCC}/E_{HMA}$.

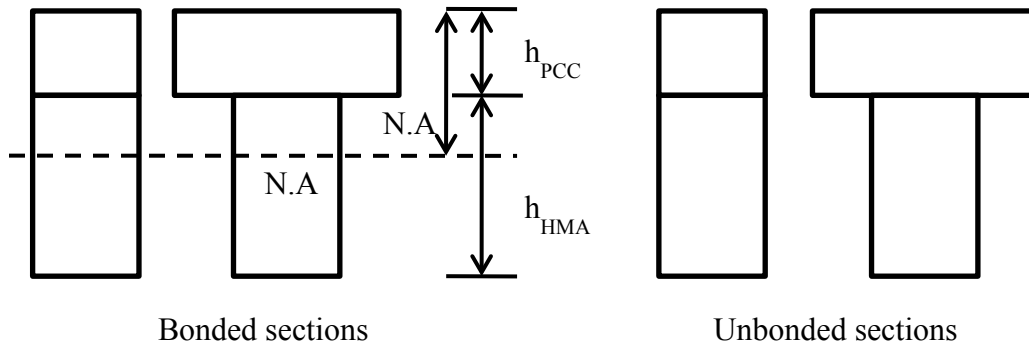


Figure 5. Conversion of a concrete section to an equivalent asphalt section (Gucunski, 1998).

The maximum stresses for the UTW layer and the HMA layer, namely σ^{PCC} and σ^{HMA} , induced by an 18-kip axle load, were calculated using 2-D finite element models and then expressed as a function of the parameters shown in Equations (24) to (27) for both fully bonded and unbonded conditions.

For bonded sections

$$\sigma_B^{PCC} = \frac{C \cdot P \cdot n(N.A. - h_{PCC})}{I_B} \left[C_1 \log\left(\frac{l}{b}\right) + C_2 \frac{N.A.}{h_{PCC}} + C_3 \right] \quad (24)$$

$$\sigma_B^{HMA} = \frac{C \cdot P(N.A. - h)}{I_B} \left[C_1 \log \left(\frac{l}{b} \right) + C_2 \frac{N.A.}{h_{HMA}} + C_3 \right] \quad (25)$$

For unbonded sections

$$\sigma_U^{PCC} = \frac{C \cdot P \cdot n \cdot h_{PCC}}{2I_U} \left[C_1 \log \left(\frac{l}{b} \right) + C_2 \frac{h_{PCC}}{h} + C_3 \right] \quad (26)$$

$$\sigma_U^{HMA} = \frac{C \cdot P \cdot h_{HMA}}{2I_U} \left[C_1 \log \left(\frac{l}{b} \right) + C_2 \frac{h_{HMA}}{h} + C_3 \right] \quad (27)$$

where P is the applied load, lbs; l is the radius of relative stiffness as shown in Equation (28), in; b is the effective contacting area of the wheel, as shown in Equation (29), in and C , C_1 , C_2 and C_3 are calibration coefficients shown in Table 2 and

Table 3.

$$l = \sqrt[4]{\frac{E \cdot I_{B/U}}{(1 - \mu^2)k}} \quad (28)$$

where E and μ are the elastic modulus, psi and Poisson's ratio of the slab, respectively and k is the modulus of subgrade reaction, psi/in.

$$b = \begin{cases} \sqrt{1.6r^2 + h^2} - 0.675h & \text{if } r < 1.724h \\ r & \text{if } r \geq 1.724h \end{cases} \quad (29)$$

where h stands for the total thickness of the composite layers, in and the radius of the contact area of the wheel r was suggested to be determined using Equation (30), in.

$$r = \sqrt{\frac{9kip}{3.14 \times \text{Tire pressure}}} \quad (30)$$

Moreover, Equation (31) was developed to determine the thermal stresses induced by temperature gradients.

$$\sigma_T = C \cdot E_c \cdot CTE \cdot \Delta T \left[C_4 \frac{c}{l} + C_5 \right] \quad (31)$$

where E_c and CTE are the concrete elastic modulus, psi and coefficient of thermal expansion, $10^{-6}/^{\circ}\text{F}$, respectively; ΔT is the temperature difference between the top and bottom of the concrete slab, $^{\circ}\text{F}$ and C , C_4 and C_5 are coefficients whose values can be obtained out of

Table 4.

The design stress was considered to be the sum of Equations (24) or (26) and (31) at the top of the concrete overlay.

2.2.5.4 Bonding

Only bonded and unbonded conditions were considered in the stress prediction equations. The stress corresponding to the actual partial bonding was suggested to be interpolated, based on the design engineer's judgment of the degree of bonding.

2.2.5.5 Other considerations

Whitetopping was only used for one lane of the two-lane ramp in the NJDOT field test. During construction, a longitudinal joint was formed along the centerline of the ramp. Concentrated distresses were found along the longitudinal construction joint. Therefore, the numerical modeling was modified accordingly in an effort to study the effect of the construction joint on the maximum stresses in both PCC and HMA layers. The modification consisted of a complete separation between UTW slabs along one longitudinal joint and crack propagation through the HMA below the longitudinal joint. Based on the numerical results, it was concluded that the construction joint increased the tensile stress in the HMA layer. If the HMA layer cracked, the stress relaxation in the HMA layer would result in higher PCC tensile stress. It was suggested the effect of the construction joint on the induced stresses should be taken into account by adjusting the coefficients in the design equations according to Table 2, Table 3 and Table 4.

Table 2. Coefficients for the traffic-induced stresses in PCC (Gucunski, 1998).

| | C | | C ₁ | C ₂ | C ₃ |
|----------|--------------------|-----------------------|----------------|----------------|----------------|
| | Construction joint | No construction joint | | | |
| Bonded | 1.25 | 1.1 | -0.2815 | 0.3479 | -0.2384 |
| Unbonded | 1.35 | 1.1 | 0.3152 | -0.096 | 0.035 |

Table 3. Coefficients for the traffic-induced stresses in HMA (Gucunski, 1998).

| | C | | C ₁ | C ₂ | C ₃ |
|----------|--------------------|-----------------------|----------------|----------------|----------------|
| | Construction joint | No construction joint | | | |
| Bonded | 1.25 | 1.1 | -0.2018 | -0.0075 | -0.0414 |
| Unbonded | 1.5 | 1.1 | 0.346 | -0.1767 | 0.1069 |

Table 4. Coefficients for temperature-gradient-induced stresses in PCC (Gucunski, 1998).

| | C | | C ₄ | C ₅ |
|----------|--------------------|-----------------------|----------------|----------------|
| | Construction joint | No construction joint | | |
| Bonded | 1.2 | 1 | -0.35 | 0.48 |
| Unbonded | 1.35 | 1 | 0.35 | -0.48 |

2.2.6 Performance model

The PCA fatigue model, Equations (13) and (14), were followed to obtain the allowable number of load applications for the TWT/UTW.

For HMA fatigue, the Asphalt Institute model, i.e. Equation (15), was borrowed and further simplified to Equation (32) based on the assumption of a linear stress-strain relationship, $M = 0$ and a HMA failure cracking criterion of 10 percent instead of 20 percent.

$$N = 0.058 \frac{E_{HMA}^{2.437}}{\sigma^{3.291}} \quad (32)$$

where N is the number of load repetitions before failure (10 percent cracking); E_{HMA} is the asphalt modulus of elasticity, psi and σ is the maximum tensile stress in asphalt, psi.

2.2.7 Reliability

It was suggested that the design ESALs be increased based on the standard deviation of errors in traffic prediction, pavement performance and the required design reliability, as shown in Equation (19).

2.2.8 Surface preparation

The surface of the existing HMA layer has to be milled and cleaned according to the NJDOT's UTW specification. These specifications have been documented by Gucunski (1998).

2.2.9 Advantages and disadvantages

2.2.9.1 Advantages

The fatigue for both PCC and HMA layers is considered. The effect of the construction joints at the adjacent lanes on the PCC stress is also addressed.

2.2.9.2 Disadvantages

The accuracy of predicting the design stress significantly relies on the engineer's judgment of the degree of bonding.

Little guidance is provided on how to establish the inputs. For example, the temperature dependency of HMA stiffness is not considered; the effect of fibers is not discussed and a means for establishing the temperature gradient is not suggested.

The critical stress is considered to occur at the bottom of the PCC overlay, with the exact location unknown. The critical stress at bottom of the PCC slab may be more suitable for TWT whose dominant distress is transverse cracking. For UTW, which presents more corner cracks, the critical stress is mainly located at the top of the concrete slab.

2.3 PCA method

The PCA whitetopping design method (Wu et al., 1999) was developed for whitetopping 4-in thick or thinner with a joint spacing of 4 ft or less and a low to medium traffic volume to complement the PCA rigid pavement design guide. In this method, the maximum tensile stress in the concrete overlay and the maximum tensile strain in the asphalt layer are determined first. Based on the calculated stresses and strains, the allowable number of load repetitions can then be calculated.

2.3.1 Traffic

Load spectrum was used as the traffic input. Design equations for PCC stress and HMA strain were proposed for an 18-kip single axle load and a 36-kip tandem axle load. Stresses and strains for the other axle loads are computed as ratios to the 18-kip single axle load or the 36-kip tandem axle load. Axle groups other than single axle and tandem axle were not considered.

2.3.2 Material characterization

The material property testing carried out for the projects at Missouri and Colorado was reviewed when developing the PCA structural model. Therefore, it might not be surprising to see that the properties used in the development of the PCA model are similar to those employed in the CDOT model development.

2.3.2.1 PCC modulus of elasticity

The PCC modulus of elasticity was assumed to be 4 million psi during the development of the PCA structural model and in the design example. No guidance was provided regarding how to determine this input for design.

2.3.2.2 PCC flexural strength

The flexural strength of concrete was assumed to be 650 psi in the design example. No guidance was provided regarding how to determine this input for design.

2.3.2.3 PCC coefficient of thermal expansion

The coefficient of thermal expansion of the concrete was assumed to be $5.5 \times 10^{-6}/^{\circ}\text{F}$ during the development of the PCA structural model and in the design example. No guidance was provided regarding how to determine this input for design.

2.3.2.4 HMA modulus of elasticity

During the development of the PCA stress prediction equation using 3-D FE, the asphalt modulus of elasticity was assumed to be 1 million psi. It was assumed 0.05 to 2 million psi when developing the stress prediction equation using 2-D FE. In the design example, 0.6 million psi was used. No further information was provided how to establish this input for design.

2.3.2.5 Modulus of subgrade reaction

During the development of the PCA stress prediction equation using 3-D FE, the modulus of subgrade reaction was assumed to be 100, 300 or 600 psi/in. The range was assumed to be 75 to 800 psi/in when using 2-D FE. In the design example, the modulus of subgrade reaction of 130 psi/in was used. No further information was provided how to determine this input.

2.3.2.6 Fibers

The effect of fibers was not considered.

2.3.3 Geometry

2.3.3.1 PCC overlay thickness

The PCA method is supposed to be developed for the design of PCC overlay thinner than 4 in. During the development of the PCA stress prediction equation using 3-D FE, the PCC thickness was assumed to be 2, 3 or 5 in. It was assumed to be 2, 3 or 4 in when developing the stress prediction equation using 2-D FE.

2.3.3.2 HMA thickness

It was suggested that the HMA layer should have a minimum of 2.5 to 3 in after milling as recommended by Speakman (1996) and Cown (1993). During the development of the PCA stress prediction equation using 3-D FE, the HMA thickness was assumed to be 3 or 6 in. The range was assumed to be 3 to 9 in when developing the stress prediction equation using 2-D FE. In the design example, a thickness of 5 in was used for the HMA.

2.3.3.3 Joint spacing

Based on the field data, it was concluded that the maximum joint spacing of 4 ft should be used. Square concrete slabs of 2 ft and 4 ft were used in the development of the PCA structural models (both 2-D and 3-D models). In the design example, a joint spacing of 4 ft was used.

2.3.4 Environmental conditions

Temperature differences were used to calculate the thermal stresses. Based on the temperature measurements made in Colorado and Missouri, three temperature differences in the slab, +15 °F, +5 °F, and -10 °F, were used for stress computations. No guidance was provided to determine this input for design.

2.3.5 Structural model

A structural model was proposed to predict the pavement response under traffic and temperature loads. First, a whitetopping pavement structure was modeled using 3-D FE method to calculate the stress at the top of the PCC layer and strain at the bottom of the HMA layer. In an effort to reduce the computational expense associated with 3-D FE analysis, 2-D FE analysis was then carried out to establish correlations between the 2-D and 3-D FE calculated stresses based on a multiple linear regression of the cases presented in Table 5. The flowchart in Figure 6 illustrates how the model was developed.

2.3.5.1 Structure

A total of nine slabs were modeled with connections between them made by 3-D spring elements to simulate the load transfer, as shown in Figure 7. In the vertical direction, spring elements were also used to model the subgrade. The interface bonding was modeled using two horizontal sets of 3-D spring elements that were placed perpendicularly. The spring stiffness represented the degree of the interface bonding.

Table 5. Pavement parameters used in the PCA finite element analysis.

| Pavement parameters | Conversion between 2-D and 3-D | 2-D analysis |
|--------------------------------------|--------------------------------|----------------|
| Concrete spacing, ft | 2, 4 | 2, 4 |
| Concrete thickness, in | 2, 3, 5 | 2, 3, 4 |
| Concrete modulus of elasticity, psi | 4 million | 4 million |
| Asphalt thickness, in | 3, 6 | 3-9 |
| Asphalt modulus of elasticity, psi | 1 million | 0.05-1 million |
| Modulus of subgrade reaction, psi/in | 100, 300, 600 | 75-800 |

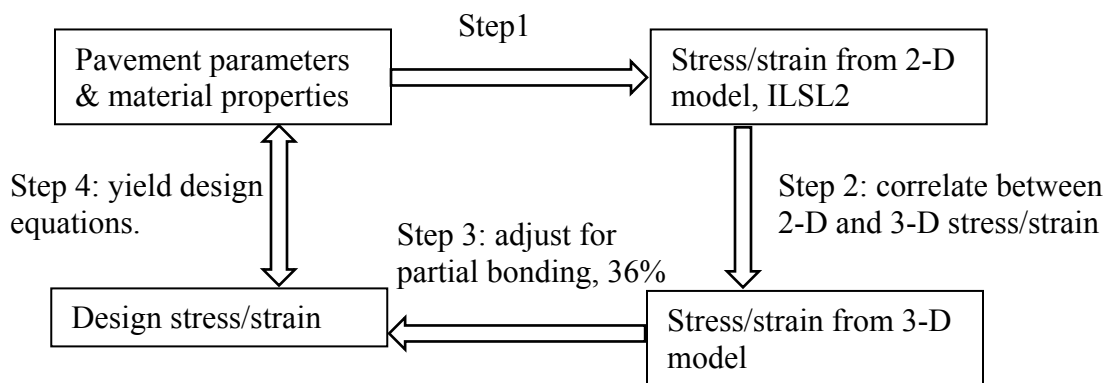


Figure 6. Development of the PCA structural response model.

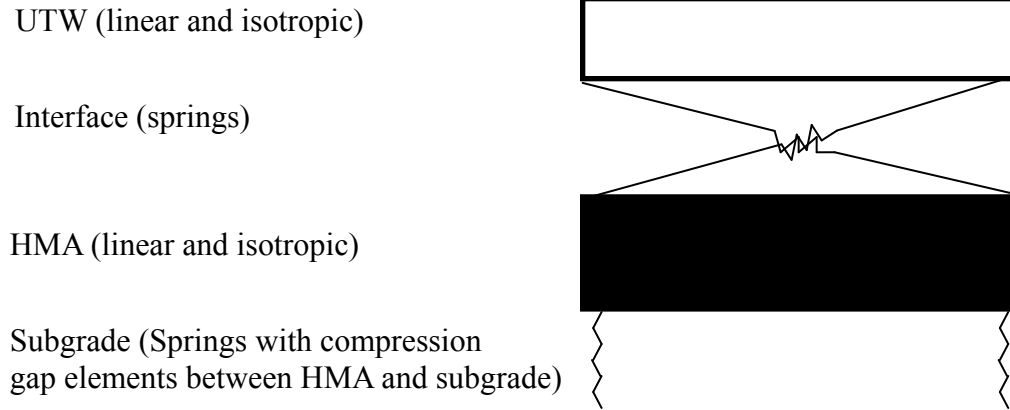


Figure 7. Pavement structure used in the finite element modeling of the PCA method.

2.3.5.2 Loading

The design was considered governed by either the edge or corner loading. Both 18-kip single axle loads and 36-kip tandem axle loads were used in the FE modeling. Stress prediction equations for other axle loads were interpolated linearly based on the equations for 18-kip single axle loads and 36-kip tandem axle loads. Maximum stresses were determined at the bottom of the HMA layer due to edge loading and at the top of the PCC layer for corner loading. Thermal stresses were also computed at the same locations as those due to traffic loading.

2.3.5.3 Critical stress and strain

The maximum stress due to traffic loading was found at the top of the concrete overlay under corner loading and the maximum strain was found at the bottom of the asphalt layer under edge loading. Therefore, prediction equations were established for the abovementioned critical stress and strain, as seen in Equations (33) to (38).

For strains at the bottom of the HMA layer due to 18-kip single axle joint loading,

$$\log \varepsilon_j = 5.267 - 0.927 \log k + 0.299 \log \left(12 \frac{8 - 24 / \left(\frac{L}{12} + 2 \right)}{l_e} \right) - 0.037 l_e, r_{adj}^2 = 0.892, N = 67 \quad (33)$$

For strains at the bottom of the HMA layer due to 36-kip tandem axle joint loading,

$$\log \varepsilon_j = 6.070 - 0.891 \log k + 0.786 \log l_e - 0.028 l_e, r_{adj}^2 = 0.870, N = 69 \quad (34)$$

For stresses at the top of the TWT/UTW due to 18-kip single axle corner loading,

$$\log \sigma_c = 5.025 - 0.465 \log k + 0.686 \log \left(12 \frac{8 - 24 / \left(\frac{L}{12} + 2 \right)}{l_e} \right) - 1.291 l_e, \quad (35)$$

$$r_{adj}^2 = 0.892, N = 80$$

For stresses at the top of the TWT/UTW due to 36-kip tandem axle corner loading,

$$\log \sigma_c = 4.898 - 0.559 \log k + 1.395 \log \left(12 \frac{8 - 24 / \left(\frac{L}{12} + 2 \right)}{l_e} \right) - 0.963 l_e$$

$$- 1.395 \left(12 \frac{8 - 24 / \left(\frac{L}{12} + 2 \right)}{l_e} \right), \quad r_{adj}^2 = 0.978, N = 80 \quad (36)$$

For strains at the bottom joint of the HMA layer due to temperature differences,

$$\varepsilon_j = -28.698 + 2.131(CTE \cdot \Delta T) + 17.692 \left(12 \frac{8 - 24 / \left(\frac{L}{12} + 2 \right)}{l_e} \right), \quad (37)$$

$$r_{adj}^2 = 0.788, N = 240$$

For stresses at the top corner of the TWT/UTW due to temperature differences,

$$\sigma_c = 28.037 - 3.496(CTE \cdot \Delta T) - 18.382 \left(12 \frac{8 - 24 / \left(\frac{L}{12} + 2 \right)}{l_e} \right), \quad (38)$$

$$r_{adj}^2 = 0.788, N = 240$$

where ε_j is the strain at the bottom of the HMA layer, microstrain; σ_c is the stress at the top of the PCC slab, psi; CTE is the coefficient of thermal expansion of the PCC, 10^{-6} in/in/°F; ΔT is the temperature difference between the top and the bottom of the PCC slab, °F; L is the joint spacing, in; l_e is the effective radius of relative stiffness for a fully bonded composite pavement as expressed in Equation (8), in; k is the modulus of subgrade reaction, psi/in; r_{adj}^2 is the adjusted coefficient of correlation and N is the number of runs carried out. It should be noted that the 36

percent stress increase for the partial bonding has already been inexplicitly taken into account in the above equations.

2.3.5.4 Bonding

The stress and strain obtained from the 3-D FEM analysis were compared with the field observations made in Missouri and Colorado to account for the effect of partial bonding. It was found that the measured stresses were 19 percent (standard deviation of 17 percent) and 57 percent (standard deviation of 32 percent) higher than the predictions at the top and bottom of the PCC overlay, respectively. However, it is interesting to notice that the difference is the same at the top as the bottom in terms of the absolute value. Based on the observed stresses at the top of the PCC layer, it was suggested that a stress increase factor of 36 percent (19 percent +17 percent) be applied to the 3-D FEM calculated stresses to account for the partial bonding.

2.3.5.5 Other considerations

No other factors were taken into account.

2.3.6 Performance model

Based on the calculated PCC stress and HMA strain, the allowable repetitions for each axle load can be determined according to the PCA fatigue model as presented in Equations (13) and (14). The asphalt fatigue model by the Asphalt Institute as presented in Equation (15) was employed to determine the allowable load applications for each axle load. Equation (16) instead of Equation (15) were suggested when no detail was available with respect to the HMA mixture.

2.3.7 Reliability

There was no overall reliability considered for design.

2.3.8 Surface preparation

Milling and cleaning, i.e. air blasting and cleaning to remove all laitance, dust, grit, and all foreign materials, were considered to be able to provide the most effective interface bonding. i.e. 100 psi of interface shear strength. Lower interface shear strength was measured for TWT/UTW on top of the newly placed asphalt layer. Therefore, milling was not suggested for newly placed asphalt. No discussion was made regarding the effect of various surface preparation techniques on the interface bonding.

2.3.9 Advantages and disadvantages

2.3.9.1 Advantages

The use of 3-D FE enables the structural model to predict more realistic pavement responses. The critical stress is identified at the top of the PCC overlay due to corner loading. Therefore, it is more appropriate for the prediction of corner cracking, which is the main distress for UTW. Furthermore, there was effort to take into account the effect of partial bonding in the modeling.

Field measurements were used to verify the results and the difference were attributed to partial bonding. Both PCC and HMA fatigue are predicted.

2.3.9.2 Disadvantages

The effect of partial bonding in increasing the stresses in the TWT/UTW layer was taken into account based on a statistical study of the field observations. However, the underestimation of stresses by the 3-D FEM compared with the field observations might not only be due to the interface debonding. Other factors may also have come into play, for example ‘the quality of the asphalt pavement underneath the concrete overlay’.

Little guidance is provided on establishing the inputs for the design. For example, the temperature dependency of the HMA stiffness is not considered; the effect of fibers is not discussed and the determination of the temperature gradient is not suggested.

2.4 ICT method

Roesler et al. (2008) proposed a method for UTW design in the research report for the Illinois Center for Transportation (ICT). In the ICT method, the allowable stress ratio was first determined by making the allowable load repetitions equal to the design traffic. Then, the design thickness of the TWT/UTW was determined as such that it yielded a stress ratio equal to the allowable one.

2.4.1 Traffic

It was suggested that ESALs be employed as the traffic input because no significant difference was found when comparing the damage caused by the load-spectrum loading with the damage caused by the ESALs. Furthermore, the wander in traffic was considered to reduce the fatigue damage and thus channelized traffic loading was assumed.

2.4.2 Material characterization

2.4.2.1 PCC modulus of elasticity

The average 14-day PCC compressive strength was obtained as 4,359 psi based on Illinois field data. For concrete with a 14-day compressive strength of 4,000 psi, the PCC modulus of elasticity could be calculated as 3.6 million psi using the ACI correlation seen in Equation (39).

$$E_{PCC} = 57,000 \sqrt{f'_c} \quad (39)$$

where f'_c is the 14-day PCC compressive strength, psi and E_{PCC} is the PCC modulus of elasticity, psi.

2.4.2.2 PCC flexural strength

A mean PCC flexural strength of 750 psi based on 3-point loading was recommended for design. Furthermore, if the whitetopping was open to traffic at or before 14 days, a minimum strength of 550 psi, based on 3-point loading, was required in the current design method used in Illinois.

2.4.2.3 PCC coefficient of thermal expansion

A typical CTE of $5.5 \times 10^{-6}/^\circ\text{F}$ for concrete in Illinois was suggested, which should be varied if the geology of the coarse aggregate dramatically changed.

2.4.2.4 HMA modulus of elasticity

Efforts were made to characterize the stiffness of the distressed HMA layer using the FWD, but it was not successful. Three primary categories were suggested. An elastic modulus of 0.1 million psi represented a fatigued asphalt pavement. An elastic modulus of 0.35 million psi was suggested for a moderate condition of the asphalt with some level of structural distresses. An elastic modulus of 0.6 million psi was used for a good asphalt pavement with only surface distresses such as rutting, shoving, or weathering that can be mostly eliminated by cold milling.

2.4.2.5 Modulus of subgrade reaction

The modulus of subgrade reaction (from 50 psi/in to 200 psi/in) was found to have negligible effects on the design of UTW and therefore a default value of 100 psi/in was employed to generate the design charts.

2.4.2.6 Fibers

The introduction of structural fiber was identified beneficial to the flexural resistance of the overlay. The contribution of the structural fiber was accounted for by enhancing the residual strength. The equivalent residual strength properties are dependent on the fiber type, the volume fraction or mass fraction of the fiber in the fiber reinforced concrete and the concrete mixture proportions. The residual strength can be determined based on 4-point bending flexural strength test following ASTM C1609.

$$R_{150,3} = \frac{f_{150,3}}{M_R} \times 100 \quad (40)$$

$$f_{150,3} = \frac{P_{150,3}S}{bd^2} \quad (41)$$

where $P_{150,3}$ is the residual load capacity at 1.2 in deflection, lbs and S , b , and d are the span, width, and depth of the beam, respectively, in. An average of 3 or 4 replicates are made to determine the equivalent and peak flexural strengths, i.e. $f_{150,3}$ and M_R , of the mixture.

It was recommended that the majority of UTW should use a residual strength ratio of 20 percent that is close to IDOT's currently specified value in their 2005 UTW special provisions.

2.4.3 Geometry

2.4.3.1 PCC overlay thickness

The PCA structural model was employed in the ICT stress prediction, where a PCC thickness of 2 to 4 in was used during the development. In the ICT method, 3-in to 5-in thicknesses were suggested for UTW design and a 3-in thickness was suggested to be the minimum. If a 3-in minimum was used, the PCC overlay essentially acted only as a wearing surface.

2.4.3.2 HMA thickness

It was considered that the minimum HMA thickness for each project would depend on the amount and severity of observed distresses and the expected loading conditions. It was recommended that the minimum asphalt thickness for a UTW project should be at least 2.5 in. In the design chart, HMA thicknesses of 2.5, 4 and 6 in were used.

2.4.3.3 Joint spacing

It was considered that 6x6-ft panels were out-performing the 4x4-ft slabs since 4x4-ft slabs resulted in a longitudinal joint located near the wheel path (Vandenbossche and Fagerness 2002; Vandenbossche 2003). However, for severely distressed HMA pavements where debonding was the concern, 4x4-ft slabs might be desired. In the proposed design charts, both 4 and 6 ft square slabs were employed.

2.4.4 Environmental conditions

The fatigue damage was calculated and multiplied by the percent of time of occurrence for each temperature gradient (at an interval of 0.1°F/in) of the temperature gradient frequency distribution for Champaign, Illinois. An equivalent temperature gradient of -1.4°F/in was obtained, which produced the same amount of fatigue damage as that due to all the individual negative temperature curling and traffic-induced stresses.

2.4.5 Structural model

It was suggested that the modified PCA structural response model for whitetopping should be adopted.

2.4.5.1 Structure

The same structure as in the PCA structural model was used.

2.4.5.2 Loading

The corner loading was considered the critical loading condition that produces a critical stress at top corner of the slab.

2.4.5.3 Critical stress and strain

With the assumption that the critical tensile stress due to traffic loading occurs at the top corner of the slab, the tensile stress σ_{18} (psi) due to an 18-kip single axle load was calculated using Equation (42).

$$\log(\sigma_{18}) = 5.025 - 0.465 \log(k) + 0.686 \log(L/l_e) - 1.291 \log(l_e) \quad (42)$$

where k is the modulus of subgrade reaction, psi/in; L is the length of a square slab, in and l_e is the effective radius of relative stiffness as determined by Equation (8), in.

The temperature induced stress σ_T (psi) at the top corner of the slab was calculated using Equation (43).

$$\sigma_T = 28.037 - 3.496(CTE * \Delta T) - 18.382 L/l_e \quad (43)$$

where CTE is the coefficient of thermal expansion of the concrete, $10^{-6}/^{\circ}\text{F}$; ΔT is the temperature difference, $^{\circ}\text{F}$. Tensile stresses due to the temperature difference were assumed to be at the top of the slab when negative temperature gradients were present, most likely at night.

Assuming that the slab remained in contact with the supports, the total stress σ_{TOTAL} was proposed to be the sum of the traffic and thermal stresses.

$$\sigma_{TOTAL} = \sigma_{18} + \sigma_T \quad (44)$$

As one may notice, the complicated third term in Equation (35), $12 \left[8 - 24 / \left(\frac{L}{12} + 2 \right) \right]$, was replaced by the slab length L in Equation (42). As shown in Figure 8, the use of slab length is a good approximation (less than 10 percent deviation) to the parameter used in the PCA equations for $L \in [24 \text{ in}, 60 \text{ in}]$. Beyond this range, the two parameters become increasingly farther apart from each other.

Since this structural model is a modified version of the PCA model, its stress predictions can be expected to be almost the same as the predictions by the PCA model, especially for slab joint spacing between 24 in and 60 in. The only difference is that the critical tensile stress was explicitly assumed at the top corner of the TWT/UTW. Therefore, the advantages and disadvantages for this structural model are expected to be the same as those for the PCA model.

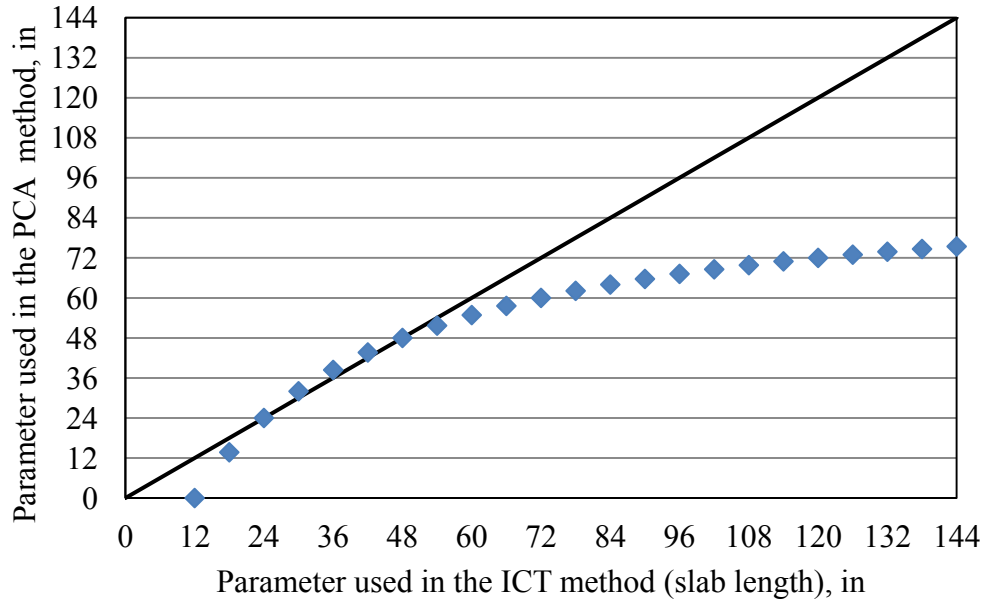


Figure 8. Comparison between parameters used in the ICT equations and those in the PCA equations.

2.4.5.4 Bonding

Following the work by Riley et al. (2005), the debonding potential was determined by comparing the bonding stress (Equation (45) and (46)) to the bonding shear limit (Equation (47)). The bonding plane limit (BL) as presented in Equation (48) indicates the likelihood of interface delamination. If the BL is greater than 100 percent, then debonding is likely to occur. However, this procedure was not incorporated into the design guide.

In the ACPA design guide (Riley et al., 2005), the maximum tensile stress σ_{max} in Equation (45) was identified at the top of the PCC overlay, as shown in Equations (35) and (42) where compensations were made to adjust the maximum tensile stress for partial bonding following the suggestions of the CDOT method. It was believed that the debonding stress σ_b should occur at the same location as σ_{max} , only at the PCC-HMA interface instead of at the top of the PCC overlay. Therefore, the stress at the bottom of the PCC should be calculated first based on the predetermined maximum tensile stress σ_{max} by Equation (42). After considering the contribution of temperature gradients, the debonding stress was proposed as Equation (45).

$$\sigma_b = (\sigma_{max} + \sigma_T) \cdot (1 - 0.36) \cdot \frac{h_c - NA}{h_c} \cdot (1.57 + 0.32 * Zscore) \quad (45)$$

where σ_b is the debonding stress at the PCC/HMA interface, psi; σ_{max} is the maximum tensile stress at the top of the PCC layer due to corner loading as can be calculated according to Equation (35), psi; σ_T is the tensile stress at the top of the PCC layer induced by temperature gradients as can be determined as per Equation (38), psi; h_c is the thickness of the PCC overlay,

in; NA is the depth of the neutral axis, in and Z score is defined as the absolute value of the inverse normal of one minus the reliability as shown in Equation (46).

$$Zscore = |\Phi^{-1}(1 - R)| \quad (46)$$

A bonding shear limit was proposed as a function of the reliability based on the data of Iowa shear tests from Colorado, Florida and Iowa, as shown in Equation (47).

$$\tau_b = -15032.412(1 - R)^4 + 17387.985(1 - R)^3 - 6642.377(1 - R)^2 + 1201.687(1 - R) \quad (47)$$

Finally, it was proposed that the likelihood of delamination should be represented by a bonding plane limit, BL , as shown in Equation (48). If BL was greater than 100 percent, debonding would likely occur.

$$BL = \frac{\sigma_b}{P_b * \tau_b} * 100 \quad (48)$$

where P_b is the percent bonding, with 1 for perfect bonding that is presumably achieved by milling and sweeping old asphalt and 0 for full debonding and it depends on the surface preparation of the distressed HMA layer. For example, a partially bonded case of $P_b = 80$ percent was suggested for a swept HMA surface. It is also noteworthy that a factor of safety of 2 was built in when the ACPA bond delamination equations were developed. Due to the lack of knowledge on the fatigue behavior of the bond plane, it was believed the magnitude of the design stresses should always be kept less than 50 percent of the shear limit.

2.4.5.5 Other considerations

No other factors were taken into account.

2.4.6 Performance model

The ACPA PCC fatigue model by Riley et al. (2005) was modified and used in the ICT design method, where the allowable number of load repetitions, N_{PCC} , was determined as a function of the stress ratio, reliability level and failure criterion in terms of cracking level, as shown in Equations (49) to (51).

$$\log N_{PCC} = \left[-\frac{SR^{-10.24} \log(R^*)}{0.0112} \right]^{0.217} \quad (49)$$

$$SR = \frac{\sigma_{TOTAL}}{M_R(1 + R_{150,3})} \quad (50)$$

$$R^* = 1 - \frac{(1 - R) \cdot P_{cr}}{0.5} \quad (51)$$

where N_{PCC} is the fatigue life in terms of the number of allowable repetitions; SR is the stress ratio; σ_{TOTAL} is the sum of the maximum stresses due to traffic and temperature difference, psi; M_R is the modulus rupture of the concrete, psi; $R_{150,3}$ is the residual strength ratio that characterizes the contribution of fiber reinforcement; R^* is the effective reliability at certain failure, P_{cr} , that stands for the percentage of slabs cracked. R^* would then be equal to R in Equation (51) when the failure is defined as 50 percent slabs cracked.

HMA fatigue was considered in the original ACPA models by using the AI fatigue model. However, it was doubted the suitability of using a fatigue model developed for new asphalt pavement in distressed and weakened asphalt. No HMA fatigue was considered in the ICT method.

2.4.7 Reliability

In the ICT design method, the failure criterion was defined as the percent of slabs cracked, P_{cr} , as shown in Equation (50). Then, a reliability factor, R , was applied in order to increase the level of confidence, which is a modification to the ACPA fatigue model. As R approaches 50 percent, Equation (49) becomes exactly the same as the ACPA fatigue equation. It was also recommended that $R = 85 \text{ percent}$ and $P_{cr} = 20 \text{ percent}$ for the UTW design based on the minimum reliability requirement for rural interstates ($R = 85 \text{ percent}$) in the AASHTO design guide.

2.4.8 Surface preparation

It was considered that milling and cleaning the surface were the best approaches for surface preparation. Milling helps improve the bond by exposing the porous asphalt surface and thus creating a rough surface. It also removes rutting and restores the proper grade and cross slope. Patching should be carried out before milling if the HMA surface is highly distressed. Cleaning can be performed by either a low pressure wash or a mechanical broom. Air cleaning may be required if the surface is cleaned more than a few hours prior to paving. Furthermore, the milled surface needs to be cleaned again before paving if traffic was allowed on it.

No discussion was available on the effect of different surface preparation on the interface bonding.

2.4.9 Advantages and disadvantages

2.4.9.1 Advantages

The PCA structural model is employed, where the critical stress is assumed at the top of the PCC overlay under corner loading. This facilitates the prediction of corner cracking that is the dominant distress for UTW.

Details are provided in determining the inputs. For example, an effective equivalent temperature gradient is established for Illinois based on a statistical analysis.

A criterion is established to determine the debonding potential. The criterion is defined as the ratio between the debonding tensile stress and the shear bonding limit at a certain level of reliability, where the shear bonding limit was established based on results from Iowa shear tests. Furthermore, the significance of structural fibers is taken into account by considering its improvement of the concrete flexural strength.

2.4.9.2 Disadvantages

This criterion in determining debonding potential is very empirical in nature, as is indicated by the fact that it is defined as the ratio between a **tensile** stress and a **shear** limit and the shear limit is determined only as a function of reliability. Because of such an empirical nature and also because of a lack of validation, this debonding potential criterion was not recommended for use in the ICT design method.

HMA fatigue is not considered in the ICT method, although it will accelerate and might in some circumstance dominate the failure of the whitetopping structure. The temperature dependency of the HMA stiffness is not taken into account during modeling, just like the PCA method. Finally, the effect of structural fiber is discussed only in terms of its improvement to PCC strength, but not its effect in providing better joint/crack performance.

2.5 Summary of current design guides

A summary is carried out on the characteristics of each method as shown in Table 6 and Table .

2.5.1 Input determination

The ICT method is the best method in providing a comprehensive guidance on establishing the inputs, such as the temperature gradient. It is also the only method that takes into account the effect of fibers.

The temperature dependency of the HMA stiffness is neglected by all the methods, which is believed to be significant to the fatigue of the PCC overlay.

With respect to traffic loading, ESALs are used in the ICT method based on the conclusion that the fatigue damage caused by ESALs is the same as the load spectrum loading. Furthermore, the application of load spectrum as traffic inputs in the CDOT and PCA methods is very weak, since only two typical loads are used to establish stress prediction equations. The stress due to other axles has to be linearly interpolated based on the axle weight.

2.5.2 Structural models

As identified in Task 1, transverse cracking is the most dominant distress for TWTs, while corner cracking is predominant for UTWs. In this sense, the PCA and ICT methods are more appropriate for UTW design, since they have the critical stress determined at the top of the PCC overlay under corner loading.

The issue of interface bonding is not taken into account well by the current design methods. The best practice so far is to adjust the predicted stresses for partial bonding based on field measurements.

The surface preparation is believed to be one of the factors affecting the bond strength. It seems common that milling and cleaning are suggested to ensure a good bond.

2.5.3 Boundary of each method

Structural-response equations developed based on numerical analysis are employed in most of the current whitetopping design methods, i.e. the NJDOT method, the ICI method, the PCA method and the CDOT method. During the development of these equations, many FE runs are involved, especially for the CDOT and PCA methods that were developed based on '2.5-D' FE analysis. In '2.5-D' FE analysis, FE runs were carried out not only to link the pavement parameters to the 2-D FE results, but also to correlate the 2-D FE results to the 3-D FE results. The quality of the correlation between the pavement parameters and the numerical results greatly depends on the number of FE runs made and more importantly the range of the pavement parameters used in the FE runs. For example, analytical solutions based on thousands of FE runs, but all with a whitetopping thickness of 15 in, would not be considered reliable in generating a reasonable design thickness. Therefore, it is important to know the inference space for which each method was developed and most likely beyond which its use may become unreliable. In Table 7, the inference space, in terms of the range of inputs used for the model development, validation and calibration, are summarized for each method.

2.5.4 Performance model

For PCC fatigue, the modified ACPA model is employed in the ICT method while the PCA model is used in the other three methods. Both models are presented in Figure 9 along with some other PCC fatigue models as shown in Equations (52) to (55), where ACPA and PCA models yield similar PCC fatigue performances while the prediction of the PCA model lies in the middle of all the predictions.

Darter (1988) proposed a single-logarithm concrete fatigue model, as shown in Equation (52), which was later known as the ERES/COE model. The model was developed based on the Corps of Engineering data from 51 full-scale field sections.

$$\log N = 2.13 \cdot S^{-1.2} \quad (52)$$

where N is the allowable number of load applications and SR is the stress to strength ratio.

Two other single-logarithm models are the NCHRP 1-26 model (Salsilli et al., 1993) and the Zero-Maintenance model (Darter and Barenberg, 1977), as presented in Equation (53) and (54), respectively. As one can see in Equation (53), the concrete fatigue life in the NCHRP 1-26 model is also a function of reliability along with the stress level. The NCHRP 1-26 model was developed based on AASHTO Road Test data and the Zero-Maintenance model was based on 140 sets of laboratory beam testing data.

$$\log N = \left[\frac{-SR^{-5.367} \log(1 - P)}{0.0032} \right]^{0.2276} \quad (53)$$

$$\log N = 17.61 - 17.61 \cdot SR \quad (54)$$

where N is the allowable number of load applications; SR is the stress to strength ratio and P is the probability of failure.

An example of the double-logarithm model is the ARE model (Treybig, 1977), as shown in Equation (55). This model was also developed based on the AASHTO Road Test data.

$$N = 23,440 \cdot SR^{-3.21} \quad (55)$$

The Asphalt Institute model is the only model used for HMA fatigue prediction by the current UTW/TWT design methods.

Table 6. Comparison between design methods.

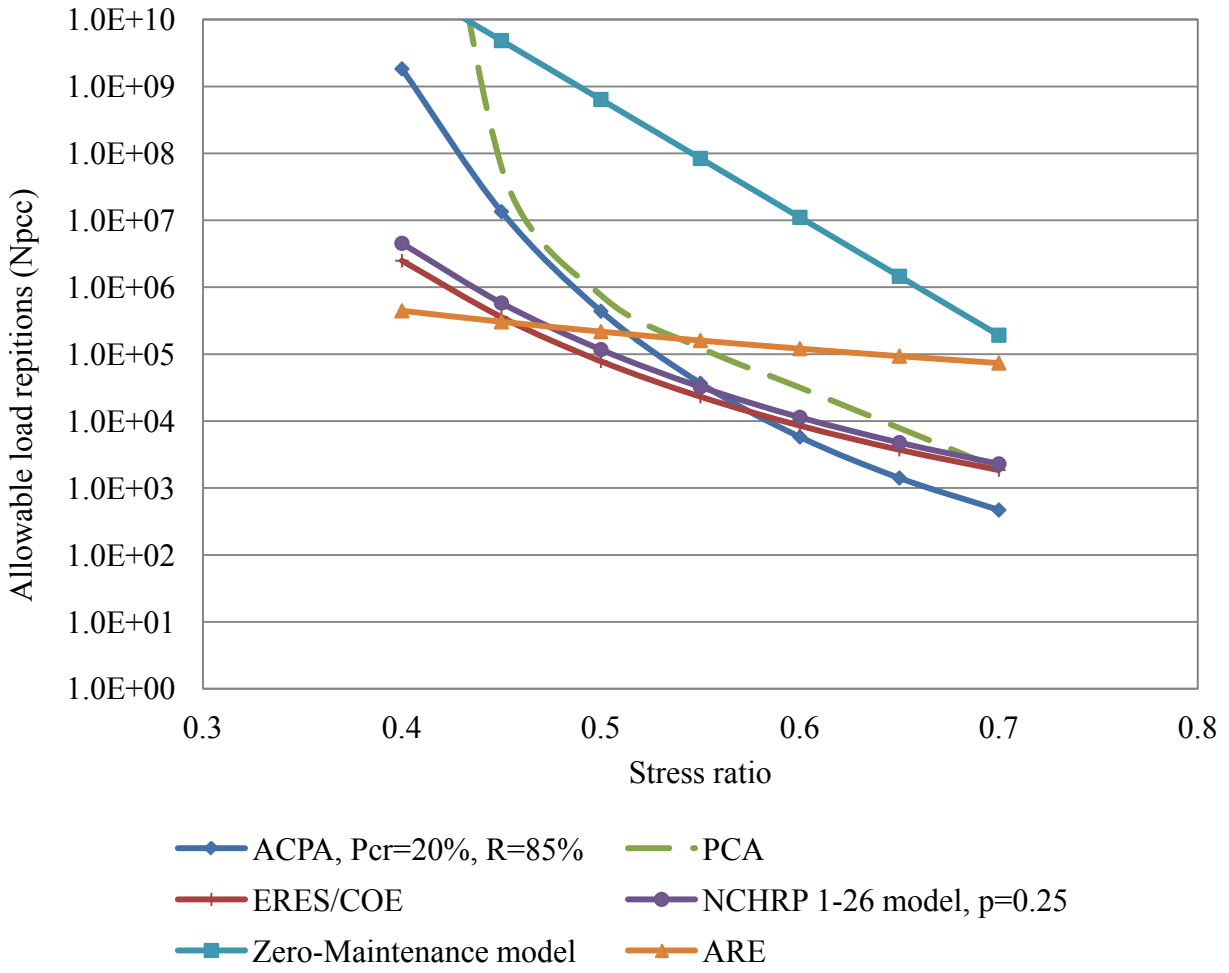
| Design Methods | CDOT | NJDOT | PCA | ICT |
|--|---|---|---|---|
| Application | UTW/TWT | UTW/TWT | UTW | UTW |
| Traffic | Load spectrum | ESAL | Load spectrum | ESAL |
| Temperature dependency of HMA modulus | Not considered | Not considered | Not considered | Not considered |
| Critical temperature difference considered | Positive, -1 to 5 °F/in based on CDOT test measurements | Positive, no guidance in determining this input | Negative, no guidance in determining this input | Negative, -1.4 °F/in for Illinois based on equivalent damage |
| Fiber | Not considered | Not considered | Not considered | 20 percent increase of flexural strength due to use of structural fiber extending the fatigue life of PCC |
| Minimum HMA thickness, in | N.A. | N.A. | 2.5-3 | 2.5 |
| Location of critical loading | Edge | Center/Edge | Corner | Corner |
| Location of critical stress in PCC | Bottom of PCC | Bottom of PCC | Top of PCC | Top of PCC |
| Location of critical stress in HMA | Bottom of HMA | Unknown | Bottom of HMA | HMA not considered |

Table 6. Comparison between design methods (continued).

| Design Methods | CDOT | NJDOT | PCA | ICT |
|-----------------------------|--|---|---|--|
| Distress predicted | Transverse and longitudinal cracks | Transverse and longitudinal cracks | Corner cracks | Corner cracks |
| Reflection crack prediction | Not considered | Not considered | Not considered | Not considered |
| Interface bonding | PCC stresses increased by 65%-59% for reliabilities of 95% to 75% based on Colorado data (3 sites) | Degree of Bonding based on Engineering Judgment | 36% increase in PCC stress to account for partial bonding based on Missouri and Colorado Data | Fully bonded |
| Reliability | Not considered | Considered when predicting design ESALs | Not considered | Overall reliability considered, 85% for UTW design |
| Surface preparation | Milling should not be applied for newly placed HMA | Milling and cleaning to ensure good bond | Milling and cleaning to ensure good bond; milling not appropriate for newly placed HMA | Milling and cleaning to ensure good bond |

Table 7. Pavement parameters used in the development, validation and sensitivity analysis of the design methods.

| Pavement parameters | NJDOT | ICT | PCA | | CDOT |
|---|--------------------------------------|---|----------------------|--------------|--|
| | | | 2-D and 3-D analysis | 2-D analysis | |
| Concrete spacing, ft | 3, 4 | 4, 6 | 2, 4 | 2, 4 | 4, 6, 12 |
| Concrete thickness, in | 3-5 | 3-6 | 2, 3, 5 | 2-4 | 4-6 |
| Concrete modulus of elasticity, million psi | 3.4 | 4 | 4 | 4 | 4 |
| Concrete Poisson's ratio | 0.15 | - | - | - | 0.15 |
| Concrete coefficient of thermal expansion, $10^{-6}/^{\circ}\text{F}$ | 3.8 | - | - | - | - |
| Asphalt thickness, in | 4-8 | 3-9 | 3, 6 | 3-9 | 3, 6, 9 |
| Asphalt modulus of elasticity, million psi | 0.88-1.66 | 0.05-1 | 1 | 0.05-1 | 0.05, 0.5, 1 |
| Asphalt Poisson's ratio | 0.35 | - | - | - | 0.35 |
| Subbase thickness, in | 12 | - | - | - | - |
| Subbase modulus of elasticity, psi | 4,200 to 16,800 | - | - | - | - |
| Subbase Poisson's ratio | 0.35 | - | - | - | - |
| Modulus of subgrade reaction, psi/in | 145-580 | 75-800 | 100, 300, 600 | 75-800 | 75, 200, 400 |
| Notes | Inputs were used in parametric study | The range of inputs was assumed to be the same as for the PCA guide, since the PCA equations were borrowed. | | | Inputs were used for developing design equations based on ILLSLAB. |



Note: markers are only for the convenience of readers, not indicating data points.

Figure 9. Comparison between PCC fatigue models.

3 EVALUATION OF CURRENT DESIGN GUIDES

3.1 MnROAD data

The MnROAD facility contains more than 50 pavement designs, each referred to as a cell. Each test cell is a 100 to 500-ft long roadway section. The layout of the MnROAD facility is illustrated in Figure 10. Six different whitetopping sections (Cells 92 to 97) were constructed in 1997, among which Cells 93, 94 and 95 were replaced by Cells 60 to 63 in 2004 because of an excessive drop in the serviceability.

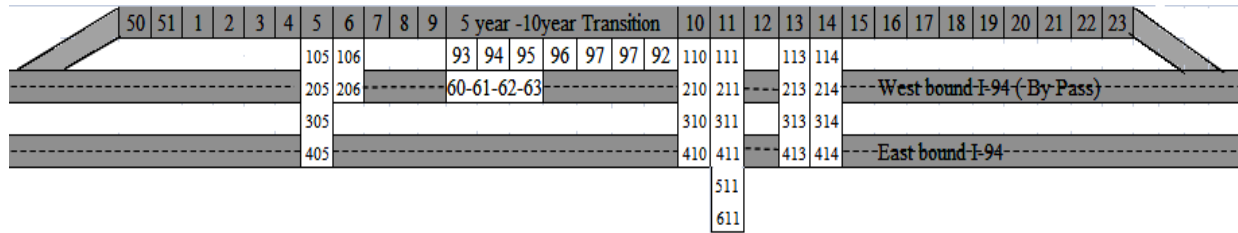


Figure 10. Layout of test cells at the MnROAD facility.

The pavement parameters that are of interest for this study are presented in Table 8. The asphalt modulus of elasticity E_{HMA} is an annual average value that is calculated using Equation (56) based on the mid-depth HMA temperature measurements. A typically value is assumed for Poisson’s ratio of the asphalt μ_{HMA} and it is assumed to be constant for each cell. The modulus of subgrade reaction k is also assumed to be the same for all the cells and it is obtained by defining the resilient modulus for each layer and using the procedure provided in the 1993 AASHTO Design Guide to determine the composite k -value. The concrete modulus of elasticity E_{PCC} , the modulus of rupture M_R , and Poisson’s ratio μ_{PCC} are obtained from Burnham (2006) for Cells 60 to 63 and Vandebossche and Rettner (1998) for Cells 93 to 97. The concrete properties for Cell 92 are assumed to be the same as its adjacent cell, Cell 97. The concrete CTE is only available for Cells 60 to 63 (Burnham, 2006) and therefore a CTE was defined as the average CTE obtained for Cells 92 to 97. Temperature gradients ΔT are determined based on the research by Vandebossche (2001), where the mean temperature gradients for 3-in, 4-in and 6-in MnROAD whitetopping cells were found to be -0.9 °F/in, -0.9 °F/in and -0.7 °F/in, respectively. The temperature gradient for 5-in cells is obtained based on linear interpolation. The last thing worth noting is that the longer edge of a rectangular panel is adopted as the joint spacing, L . For instance, 72 in is taken as the slab length for Cell 60 that has panels of 5 ft \times 6 ft. This is due to the limitation that all four design methods were developed for square panels. However, employing the dimension of the longer edge that is normal to the traffic direction is not an indication of predicting the fatigue damage resulting in longitudinal cracks. Instead, it is still aiming at predicting the fatigue damage that results in transverse cracking.

Figure 11 and Figure 12 present the distress development in terms of transverse cracking and International Roughness Index (IRI) with respect to the traffic load in ESALs for each cell, which is obtained in Task 1. Taking Cell 60 as an example, the legends in Figure 11 and Figure 12 can be interpreted in the following way, 5 in as the thickness of the PCC overlay, 5 ft x 6 ft as the slab size, ‘UD’ for undoweled joint and ‘S’ for sealed joint.

Table 8. Pavement parameters in MnROAD cells.

| Variable | Cell 60 | Cell 61 | Cell 62 | Cell 63 | Cell 92 | Cell 93 | Cell 94 | Cell 95 | Cell 96 | Cell 97 |
|--------------------------|---------|---------|---------|---------|---------|---------|---------|---------|---------|---------|
| $E_{HMA}, 10^6$ psi | 0.48 | 0.48 | 0.48 | 0.48 | 0.48 | 0.48 | 0.48 | 0.48 | 0.48 | 0.48 |
| $H_{HMA},$ in | 7 | 7 | 8 | 8 | 7 | 9 | 10 | 10 | 7 | 7 |
| μ_{HMA} | 0.35 | 0.35 | 0.35 | 0.35 | 0.35 | 0.35 | 0.35 | 0.35 | 0.35 | 0.35 |
| $E_{PCC},$ psi | 4.6 | 4.4 | 4.9 | 5.0 | 4.7 | 4.8 | 4.8 | 4.4 | 4.7 | 4.7 |
| $h_{PCC},$ in | 5 | 5 | 4 | 4 | 6 | 4 | 3 | 3 | 6 | 6 |
| $M_R,$ psi | 595 | 545 | 575 | 560 | 830 | 860 | 810 | 835 | 890 | 830 |
| μ_{PCC} | 0.18 | 0.11 | 0.13 | 0.11 | 0.20 | 0.19 | 0.18 | 0.19 | 0.2 | 0.2 |
| $\Delta T,$ °F/in | -0.8 | -0.8 | -0.9 | -0.9 | -0.7 | -0.9 | -0.9 | -0.9 | -0.7 | -0.7 |
| $L,$ in* | 72 | 72 | 72 | 72 | 144 | 48 | 48 | 72 | 72 | 144 |
| $CTE, 10^{-6}/^{\circ}F$ | 4.1 | 4.4 | 3.8 | 4.1 | 5.5 | 5.5 | 5.5 | 5.5 | 5.5 | 5.5 |
| $k,$ psi/in | 315 | 315 | 315 | 315 | 315 | 315 | 315 | 315 | 315 | 315 |

*L is defined by the longest dimension of the panel.

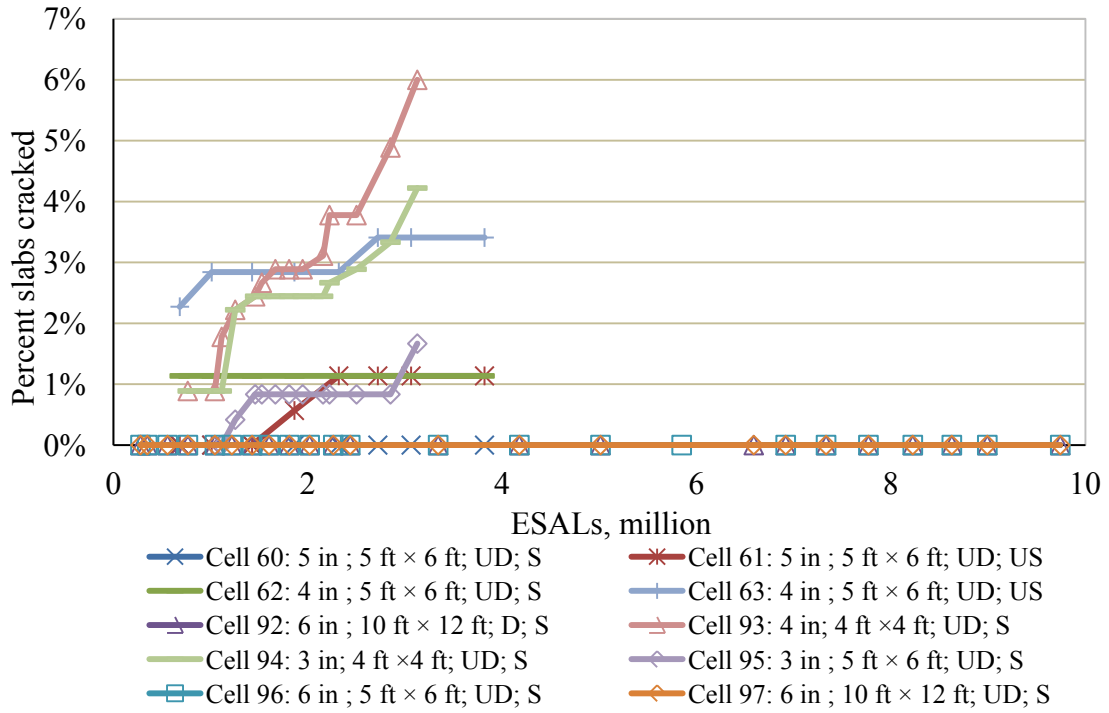


Figure 11. Transverse cracking history of MnROAD cells.

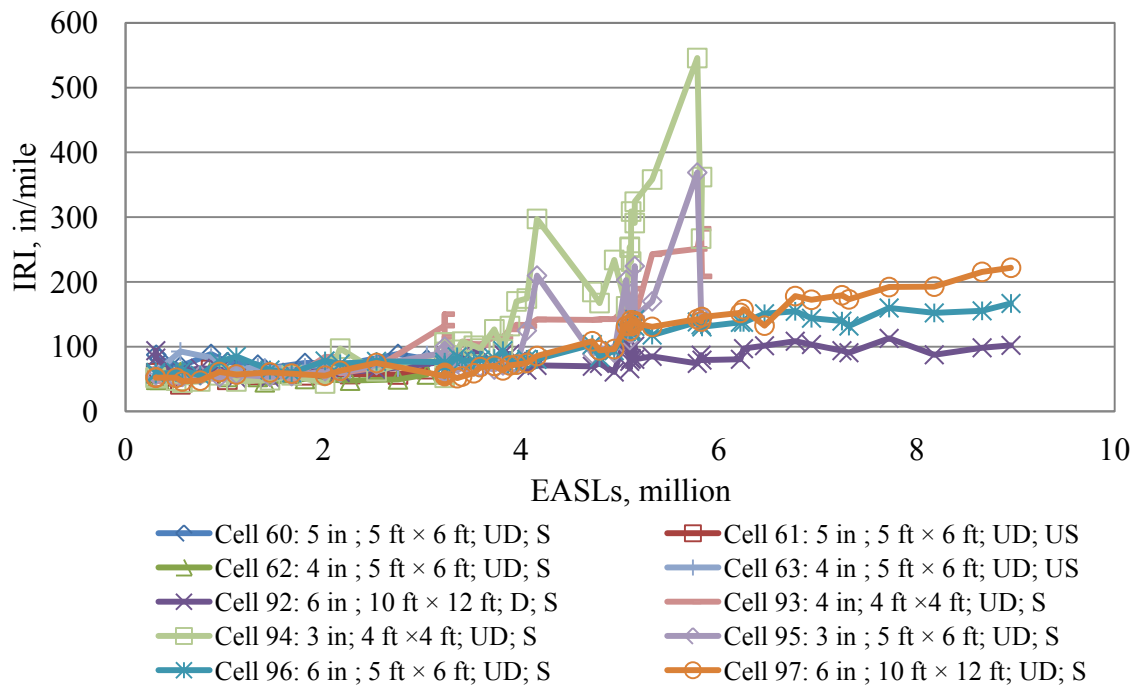


Figure 12. IRI history of MnROAD cells.

The mid-depth temperature of the asphalt layer is also part of the data recorded at MnROAD. For each whitetopping cell, temperature data is read every 15 minutes and such data has been

collected for Cells 93, 95 and 97 from 1998 to 2001. This allows for the monthly determination of the asphalt modulus of elasticity E_{HMA} . The monthly average temperature is determined by averaging all the temperature measurements for each month. As presented in Figure 13, no significant difference in monthly average temperature can be seen among the cells. Figure 14 shows the profiles of the monthly average temperatures for each year and again no significant difference can be found. Therefore, the same monthly average temperatures that are processed based on the four year measurements are used for all the MnROAD cells in this study.

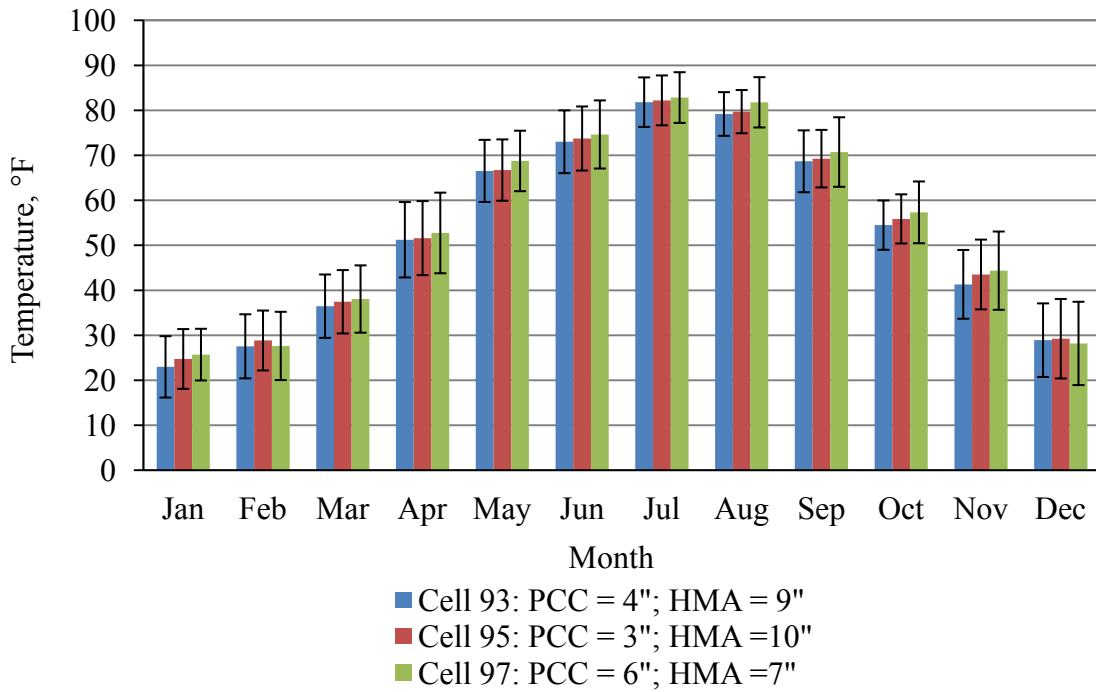


Figure 13. Monthly average temperatures for various slabs.

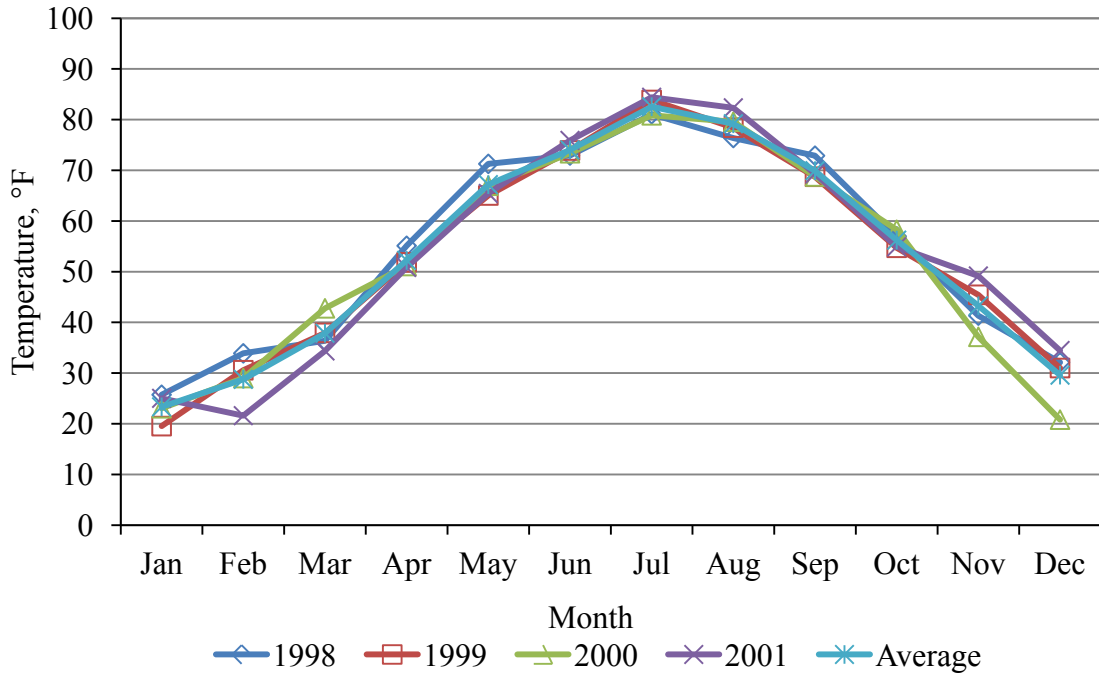


Figure 14. Average monthly temperatures for various years.

A correlation between the asphalt modulus of elasticity and temperature was established in the research work by Vandebossche and Fagerness (2002) based on the measured asphalt resilient modulus on cores taken after each lift and the measured temperatures at mid-depth of the asphalt layer. The correlation can be mathematically presented as shown in Equation (56).

$$E_{HMA} = 205.65 \cdot T^2 - 36132 \cdot T + 1730000 \quad (56)$$

where T is the interface temperature, °F and E_{HMA} is the asphalt modulus of elasticity, psi. The high dependency of the asphalt modulus on temperature is demonstrated in Table 9, which summarizes the predicted MnROAD monthly asphalt modulus of elasticity (to the nearest 1,000 psi) using Equation (56).

Table 9. Temperature dependency of the asphalt modulus of elasticity.

| Month | Temperature, °F | E _{HMA} , psi |
|-----------|-----------------|------------------------|
| January | 23 | 1,007,000 |
| February | 29 | 855,000 |
| March | 38 | 654,000 |
| April | 52 | 407,000 |
| May | 67 | 232,000 |
| June | 74 | 182,000 |
| July | 83 | 148,000 |
| August | 79 | 159,000 |
| September | 70 | 208,000 |
| October | 56 | 352,000 |
| November | 43 | 557,000 |
| December | 30 | 831,000 |

Four design methods, namely the NJDOT method, the ICT method, the PCA method and the CDOT method, are evaluated using the MnROAD pavement parameters and field observations as described previously. The distresses developed in the MnROAD cells are available based on survey results. However, none of these four methods is able to directly predict distresses due to the lack of transfer models that relates the fatigue damage to distresses. The transfer models are highly site dependent and such a transfer model has not been established for MnROAD, so additional errors might be introduced if the transfer models for other projects are employed. **In this study, the fatigue damage that results in transverse cracks will be predicted using each method and compared with the field observations, i.e. transverse cracking and IRI. The fatigue damage is expressed as the ratio between the applied and the allowable load repetitions in the following evaluation.** Even though this is not a direct comparison, it is believed that this is sufficient for evaluating the ability of each method in capturing the development of pavement fatigue damage that is comparable to distresses.

3.2 Evaluation of the NJDOT method

Fatigue damage for both the PCC and HMA layers are calculated using 18-kip ESALs as the traffic input in accordance with the NJDOT method. The predictions for all the MnROAD whitetopping cells are presented in this section, which are compared with the observed transverse cracking and IRI.

Using the predictions for Cell 60 as an example, the predicted fatigue damage for both the PCC and HMA layers are presented in Table 10 for its four years in service. The accumulated ESALs to the five specific months in Table 10 are 0.2, 1.1, 1.9, 2.7 and 3.6 million, respectively. As we can see, the fatigue damage based on the assumption of unbonded PCC and HMA layers is significantly higher than those for bonded layers and the difference between the two cases is more significant for PCC than HMA. This is because a greater majority of the load is carried by the concrete overlay when it is unbonded to the HMA layer, as can be shown in Table 11.

Table 10 also presents the comparison between predictions using a constant elastic modulus, 480,000 psi and those using monthly asphalt moduli of elasticity, which are determined from the discussion in Section 2.3.2. More fatigue damage is predicted using a temperature-dependent asphalt modulus of elasticity. As illustrated in Figure 15, most of the PCC fatigue damage occurs during the summer (for instance, June to August, which corresponds to 0.6- to 0.8-million ESALs in Figure 15) when the asphalt is softer and greater tensile stresses develop. The opposite is true for the development of HMA fatigue, which mostly occurs in winter when the asphalt is stiffer and thus takes more tensile stresses. Comparing Figure 15 and Figure 16, it can be seen that the periods when the most rapid fatigue development occurs are different for PCC and HMA.

The comparisons between the predicted fatigue damage and the observed transverse cracking are presented in Figure 15 and Figure 16 for PCC and HMA layers, respectively. Similar comparisons between the predicted fatigue damage and the observed IRIs are presented in Figure 17 and Figure 18. The observed IRI and transverse cracking suggest that Cell 60 consistently performed well from 2004 to 2008. This observed performance trend seems to agree better with the fatigue predictions for bonded conditions, indicating good bonding between the PCC and HMA layers.

Similar conclusions regarding Cell 60 can be drawn for Cells 61, 62 and 63 based on Table 12 to Table 14 and Figure 19 to Figure 30.

Compared with Cells 60 to 63, less fatigue damage is predicted for Cells 92 to 97, as shown in Table 15 to Table 20 and Figure 31 to Figure 54, mainly due to the higher concrete modulus of rupture. Cells 93, 94 and 95 present significantly greater fatigue predictions, which are believed to be due to the thinner slabs.

Table 10. Fatigue summary for Cell 60 using the NJDOT method.

| Date | Constant E_{HMA} | | | | Temperature-dependent E_{HMA} | | | |
|--------|--------------------|---------|----------|---------|---------------------------------|---------|----------|---------|
| | Bonded | | Unbonded | | Bonded | | Unbonded | |
| | PCC | HMA | PCC | HMA | PCC | HMA | PCC | HMA |
| Dec-04 | 0.0E+00 | 5.2E-02 | 1.3E+04 | 2.5E-01 | 0.0E+00 | 2.2E-01 | 2.0E+03 | 5.7E-02 |
| Dec-05 | 0.0E+00 | 2.5E-01 | 6.3E+04 | 1.2E+00 | 1.3E+01 | 2.2E-01 | 1.0E+09 | 1.6E+00 |
| Dec-06 | 0.0E+00 | 4.4E-01 | 1.1E+05 | 2.1E+00 | 2.5E+01 | 3.9E-01 | 2.0E+09 | 2.8E+00 |
| Dec-07 | 0.0E+00 | 6.3E-01 | 1.6E+05 | 3.0E+00 | 3.8E+01 | 5.6E-01 | 3.0E+09 | 4.1E+00 |
| Dec-08 | 0.0E+00 | 8.2E-01 | 2.1E+05 | 4.0E+00 | 5.0E+01 | 7.3E-01 | 4.0E+09 | 5.3E+00 |

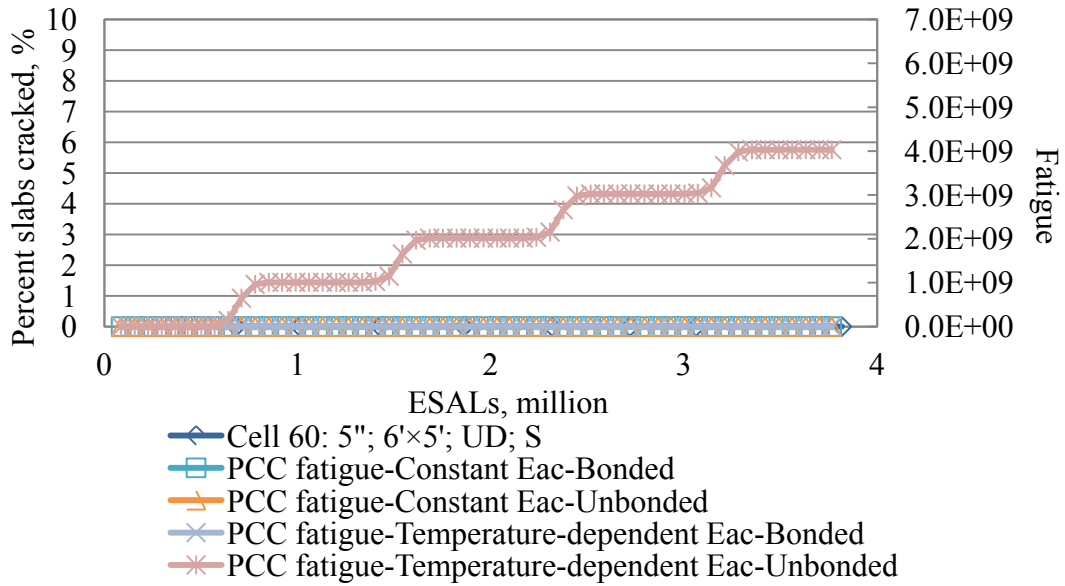


Figure 15. Observed transverse cracking vs. fatigue damage predicted for the PCC of Cell 60 using the NJDOT method.

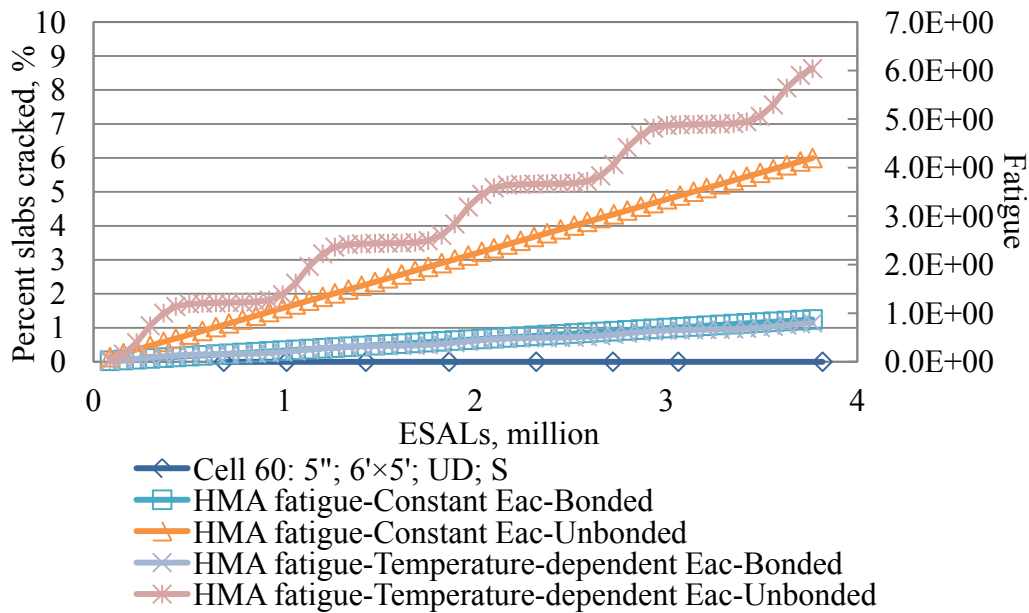


Figure 16. Observed transverse cracking vs. fatigue damage predicted for the HMA of Cell 60 using the NJDOT method.

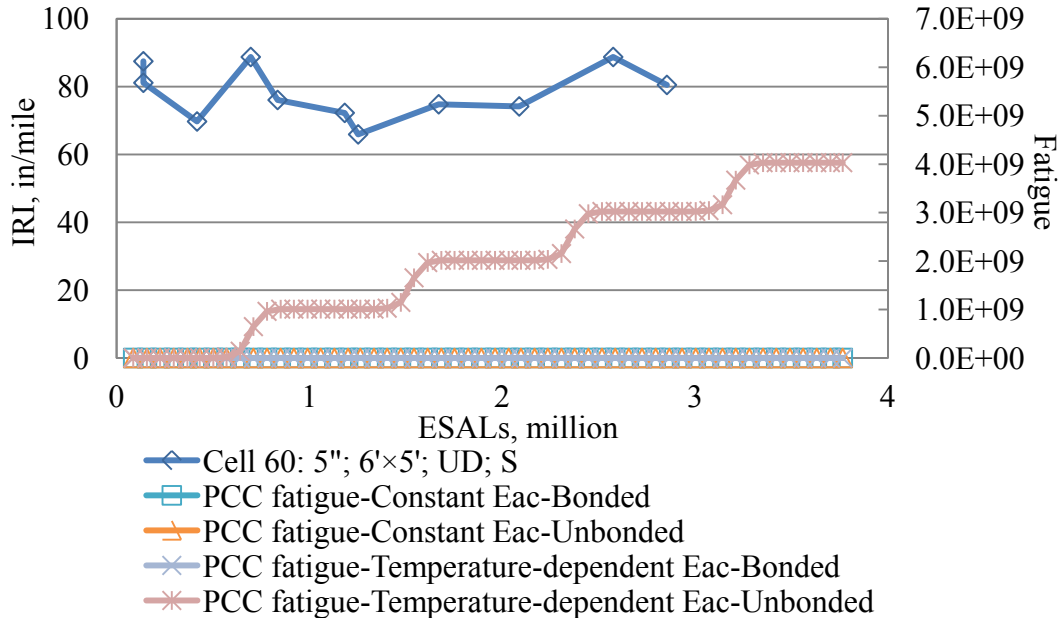


Figure 17. Observed IRI vs. fatigue damage predicted for the PCC of Cell 60 using the NJDOT method.

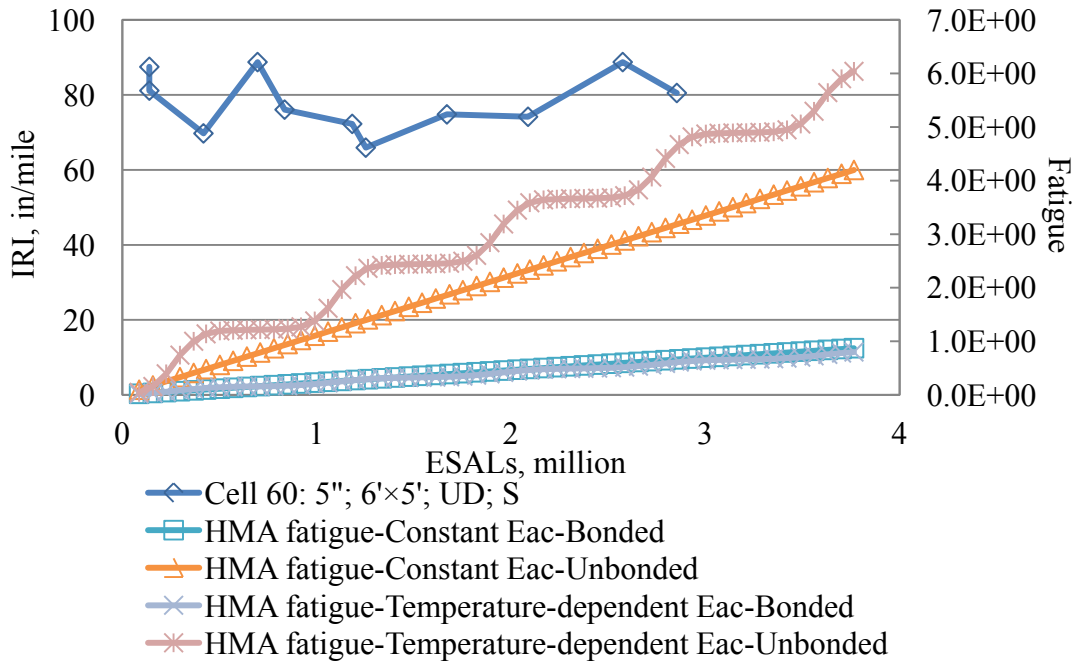


Figure 18. Observed IRI vs. fatigue damage predicted for the HMA of Cell 60 using the NJDOT method.

Table 11. Example of stress predictions for Cells 60 and 62 using the NJDOT method.

| | | Cell 60 | | | | Cell 62 | |
|--|-----|------------------|----------|------------------|----------|------------------|----------|
| | | HMA stress , psi | | PCC stress , psi | | PCC stress , psi | |
| | | Bonded | Unbonded | Bonded | Unbonded | Bonded | Unbonded |
| Temperature- dependent E_{HMA} | Jan | 77 | 165 | 46 | 427 | -28 | 407 |
| | Feb | 74 | 151 | 62 | 459 | -18 | 454 |
| | Mar | 70 | 129 | 96 | 512 | 6 | 535 |
| | Apr | 62 | 94 | 177 | 602 | 73 | 689 |
| | May | 52 | 62 | 305 | 699 | 201 | 873 |
| | Jun | 47 | 51 | 369 | 737 | 274 | 950 |
| | Jul | 42 | 43 | 427 | 769 | 346 | 1,014 |
| | Aug | 44 | 46 | 407 | 758 | 320 | 992 |
| | Sep | 50 | 57 | 333 | 716 | 233 | 908 |
| | Oct | 60 | 85 | 207 | 629 | 101 | 738 |
| | Nov | 68 | 116 | 121 | 544 | 25 | 586 |
| | Dec | 74 | 149 | 65 | 465 | -16 | 462 |
| Constant E_{HMA} | | 65 | 105 | 146 | 572 | 45 | 587 |

Table 12. Fatigue summary for Cell 61 using the NJDOT method.

| Date | Constant E_{HMA} | | | | Temperature-dependent E_{HMA} | | | |
|--------|--------------------|---------|----------|---------|---------------------------------|---------|----------|---------|
| | Bonded | | Unbonded | | Bonded | | Unbonded | |
| | PCC | HMA | PCC | HMA | PCC | HMA | PCC | HMA |
| Dec-04 | 0.0E+00 | 5.3E-02 | 5.8E+04 | 2.7E-01 | 0.0E+00 | 2.4E-01 | 7.2E+03 | 5.8E-02 |
| Dec-05 | 0.0E+00 | 2.5E-01 | 2.7E+05 | 1.3E+00 | 2.8E+01 | 2.3E-01 | 1.4E+10 | 1.7E+00 |
| Dec-06 | 0.0E+00 | 4.5E-01 | 4.9E+05 | 2.3E+00 | 5.7E+01 | 4.0E-01 | 2.8E+10 | 3.0E+00 |
| Dec-07 | 0.0E+00 | 6.4E-01 | 7.0E+05 | 3.3E+00 | 8.5E+01 | 5.7E-01 | 4.1E+10 | 4.3E+00 |
| Dec-08 | 0.0E+00 | 8.4E-01 | 9.2E+05 | 4.3E+00 | 1.1E+02 | 7.4E-01 | 5.5E+10 | 5.6E+00 |

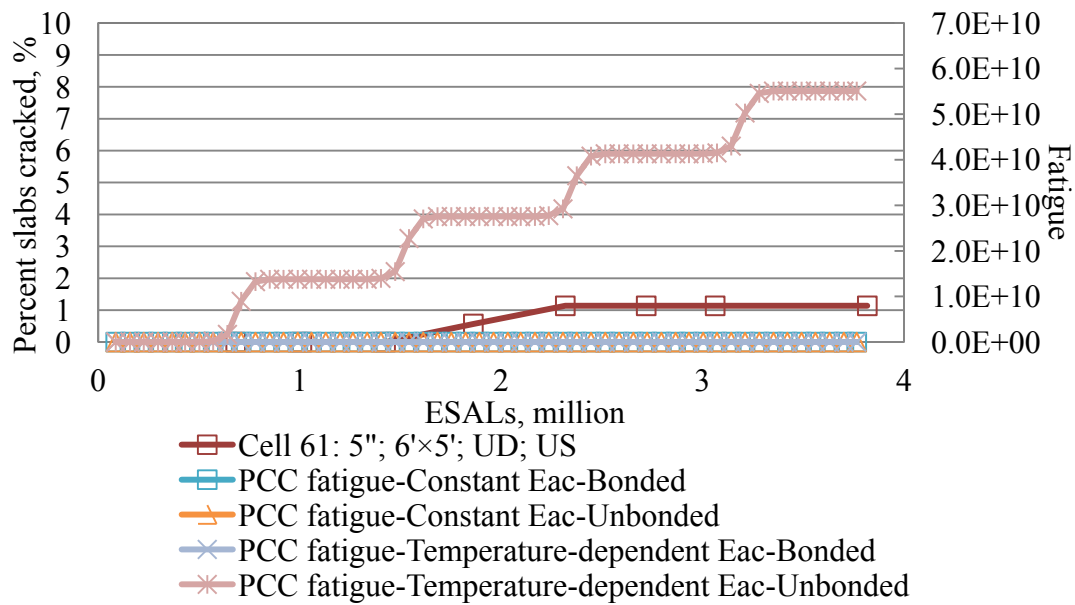


Figure 19. Observed transverse cracking vs. fatigue damage predicted for the PCC of Cell 61 using the NJDOT method.

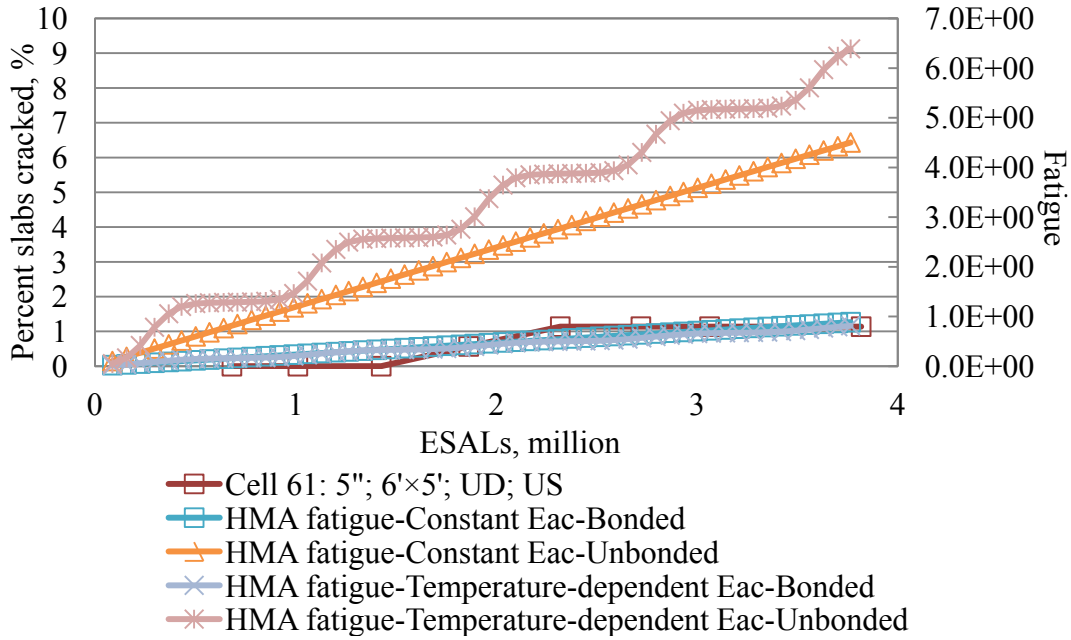


Figure 20. Observed transverse cracking vs. fatigue damage predicted for the HMA of Cell 61 using the NJDOT method.

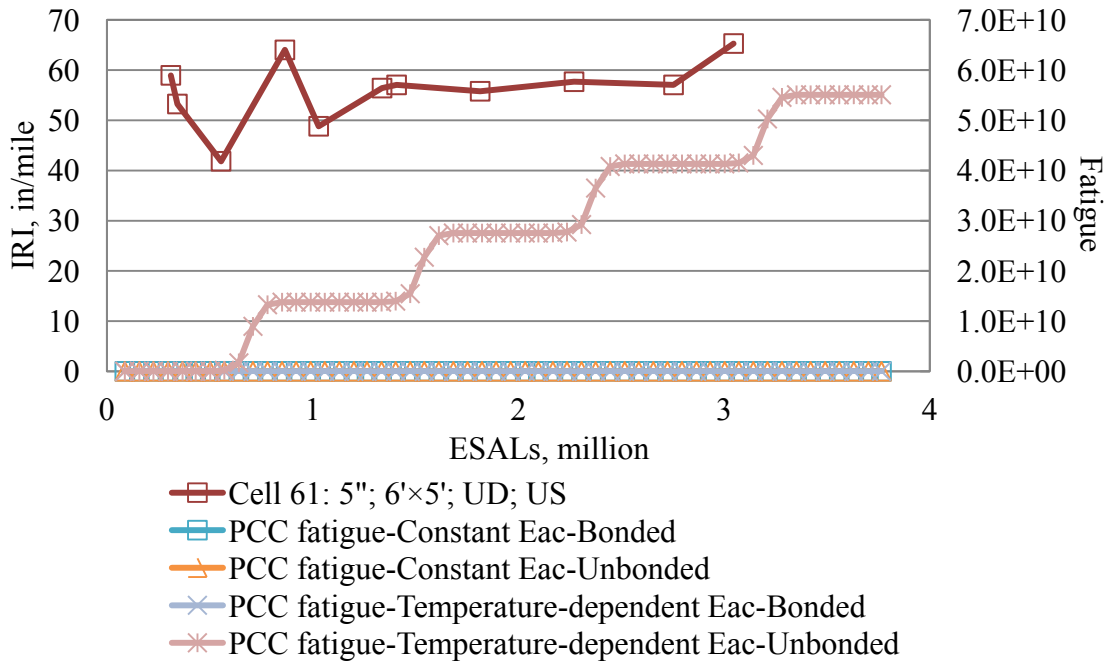


Figure 21. Observed IRI vs. fatigue damage predicted for the PCC of Cell 61 using the NJDOT method.

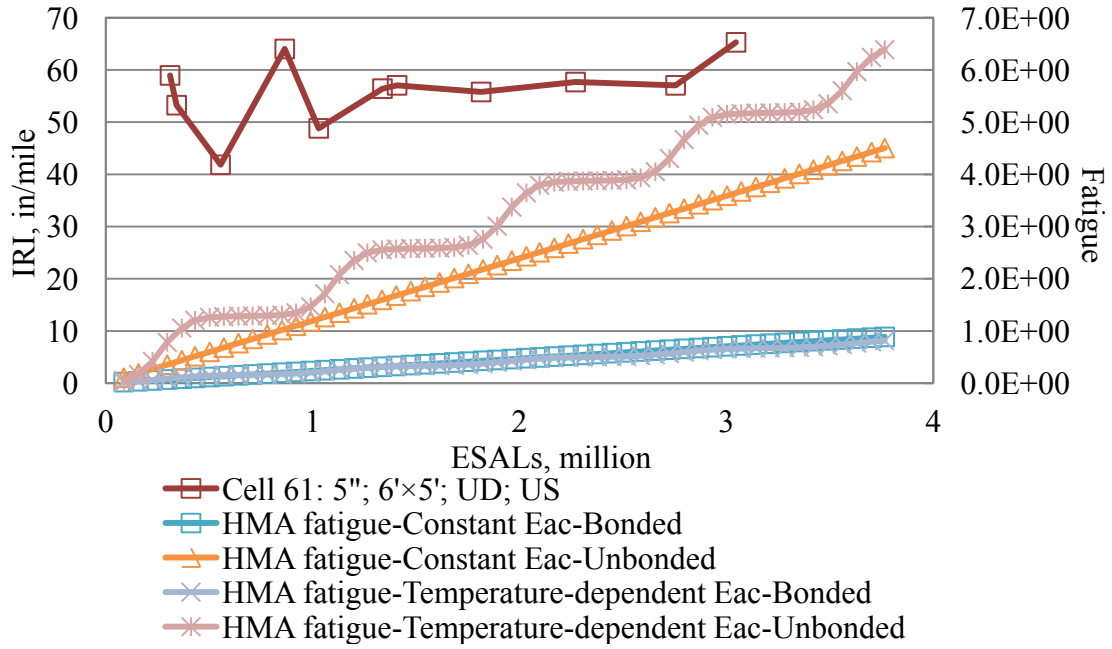


Figure 22. Observed IRI vs. fatigue damage predicted for the HMA of Cell 61 using the NJDOT method.

Table 13. Fatigue summary for Cell 62 using the NJDOT method.

| Date | Constant E_{HMA} | | | | Temperature-dependent E_{HMA} | | | |
|--------|--------------------|---------|----------|---------|---------------------------------|---------|----------|---------|
| | Bonded | | Unbonded | | Bonded | | Unbonded | |
| | PCC | HMA | PCC | HMA | PCC | HMA | PCC | HMA |
| Dec-04 | 0.0E+00 | 8.1E-02 | 1.2E+06 | 9.2E-01 | 0.0E+00 | 9.2E-02 | 5.0E+08 | 1.5E+00 |
| Dec-05 | 0.0E+00 | 2.9E-01 | 4.2E+06 | 3.3E+00 | 2.9E+00 | 2.7E-01 | 3.7E+14 | 3.5E+00 |
| Dec-06 | 0.0E+00 | 5.2E-01 | 7.5E+06 | 5.9E+00 | 5.9E+00 | 4.7E-01 | 7.4E+14 | 6.1E+00 |
| Dec-07 | 0.0E+00 | 7.4E-01 | 1.1E+07 | 8.5E+00 | 8.8E+00 | 6.7E-01 | 1.1E+15 | 8.6E+00 |
| Dec-08 | 0.0E+00 | 9.7E-01 | 1.4E+07 | 1.1E+01 | 1.2E+01 | 8.7E-01 | 1.5E+15 | 1.1E+01 |

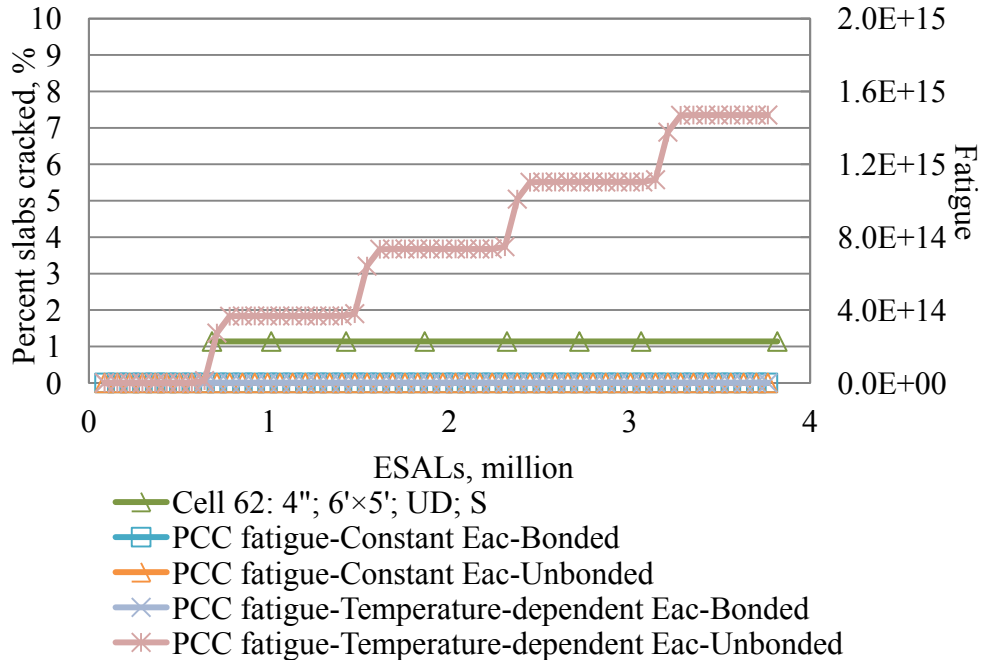


Figure 23. Observed transverse cracking vs. fatigue damage predicted for the PCC of Cell 62 using the NJDOT method.

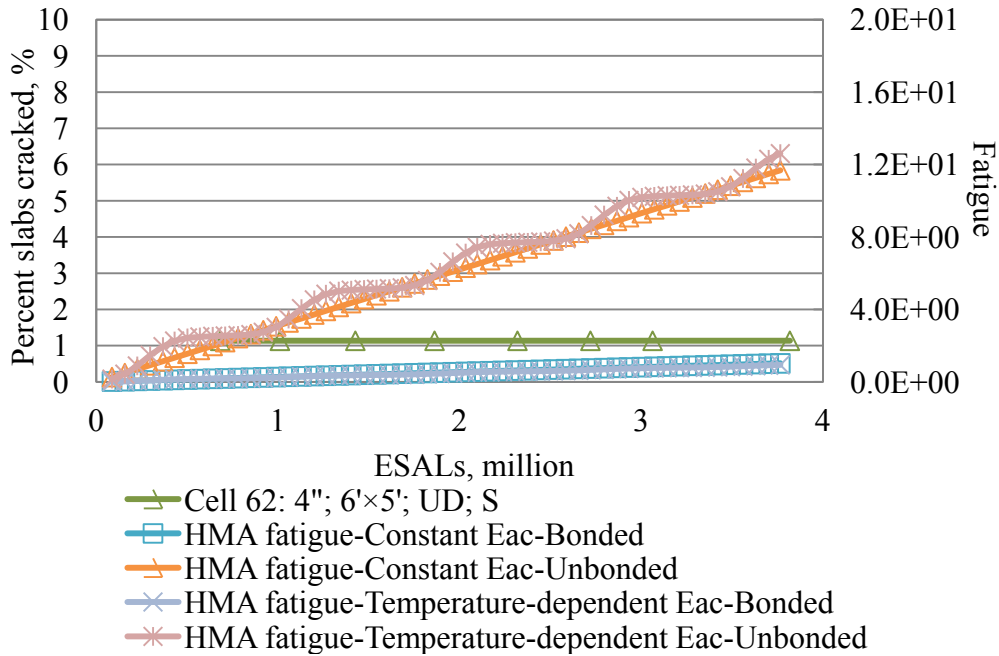


Figure 24. Observed transverse cracking vs. fatigue damage predicted for the HMA of Cell 62 using the NJDOT method.

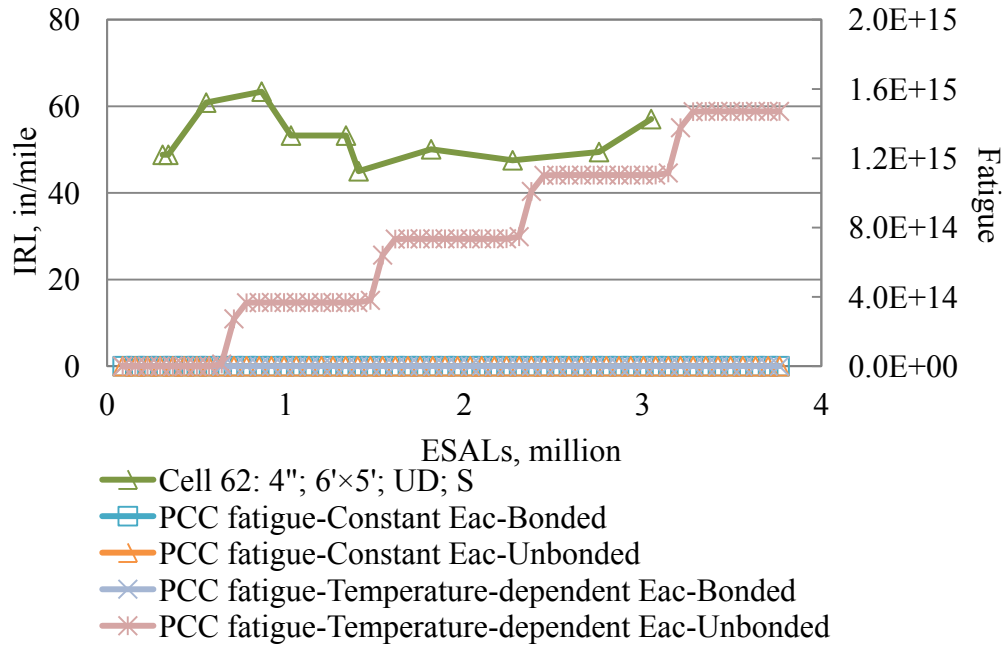


Figure 25. Observed IRI vs. fatigue damage predicted for the PCC of Cell 62 using the NJDOT method.

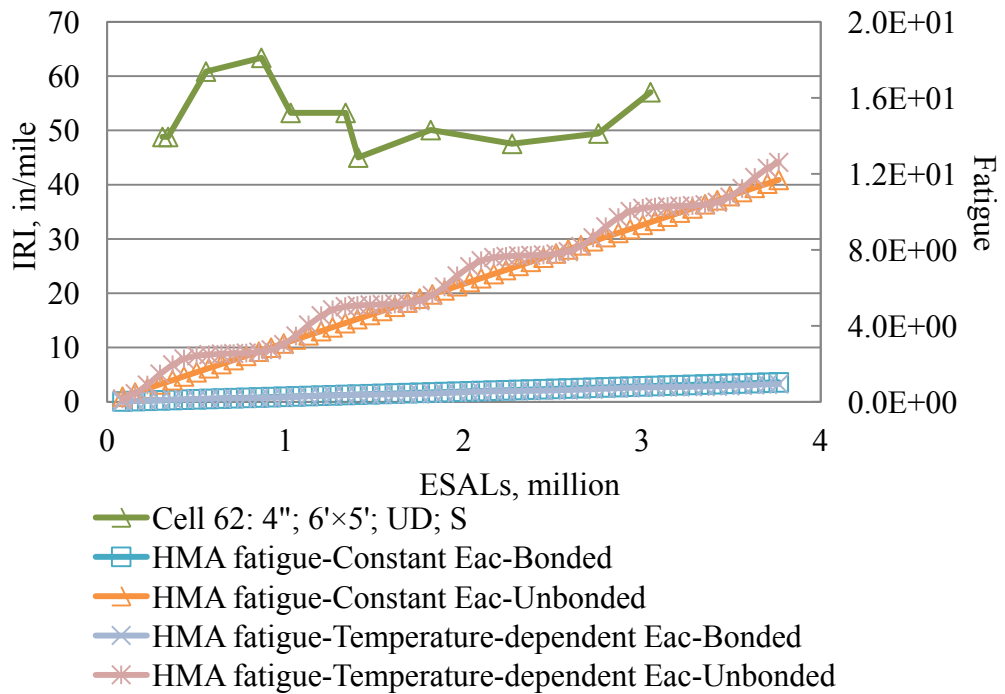


Figure 26. Observed IRI vs. fatigue damage predicted for the HMA of Cell 62 using the NJDOT method.

Table 14. Fatigue summary for Cell 63 using the NJDOT method.

| Date | Constant E_{HMA} | | | | Temperature-dependent E_{HMA} | | | |
|--------|--------------------|---------|----------|---------|---------------------------------|---------|----------|---------|
| | Bonded | | Unbonded | | Bonded | | Unbonded | |
| | PCC | HMA | PCC | HMA | PCC | HMA | PCC | HMA |
| Dec-04 | 0.0E+00 | 8.0E-02 | 3.0E+06 | 9.0E-01 | 0.0E+00 | 9.2E-02 | 2.0E+09 | 1.4E+00 |
| Dec-05 | 0.0E+00 | 2.9E-01 | 1.1E+07 | 3.2E+00 | 5.6E+00 | 2.6E-01 | 2.0E+15 | 3.4E+00 |
| Dec-06 | 0.0E+00 | 5.1E-01 | 1.9E+07 | 5.7E+00 | 1.1E+01 | 4.6E-01 | 4.0E+15 | 5.9E+00 |
| Dec-07 | 0.0E+00 | 7.4E-01 | 2.7E+07 | 8.2E+00 | 1.7E+01 | 6.6E-01 | 6.1E+15 | 8.5E+00 |
| Dec-08 | 0.0E+00 | 9.6E-01 | 3.6E+07 | 1.1E+01 | 2.3E+01 | 8.6E-01 | 8.1E+15 | 1.1E+01 |

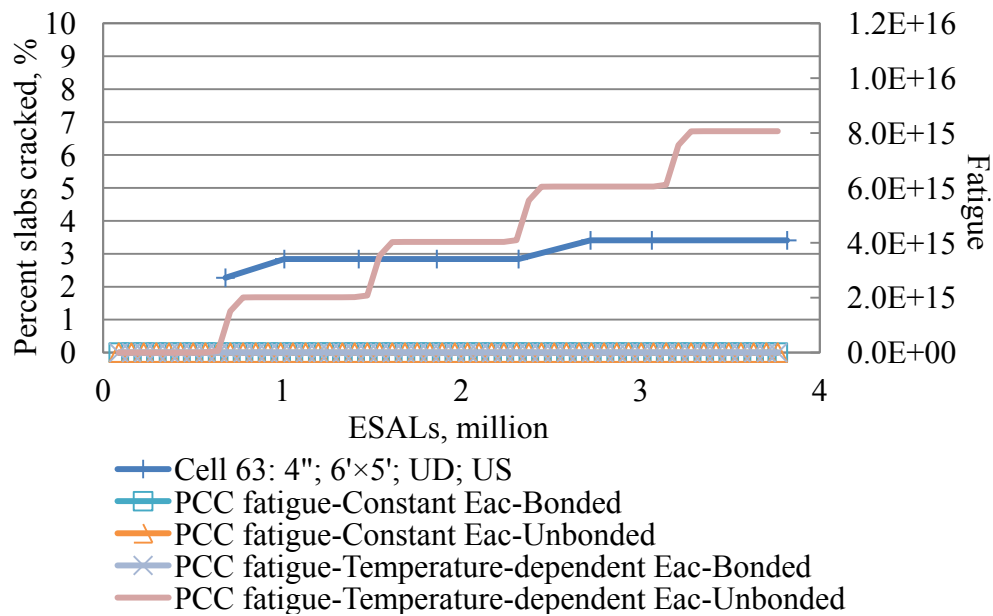


Figure 27. Observed transverse cracking vs. fatigue damage predicted for the PCC of Cell 63 using the NJDOT method.

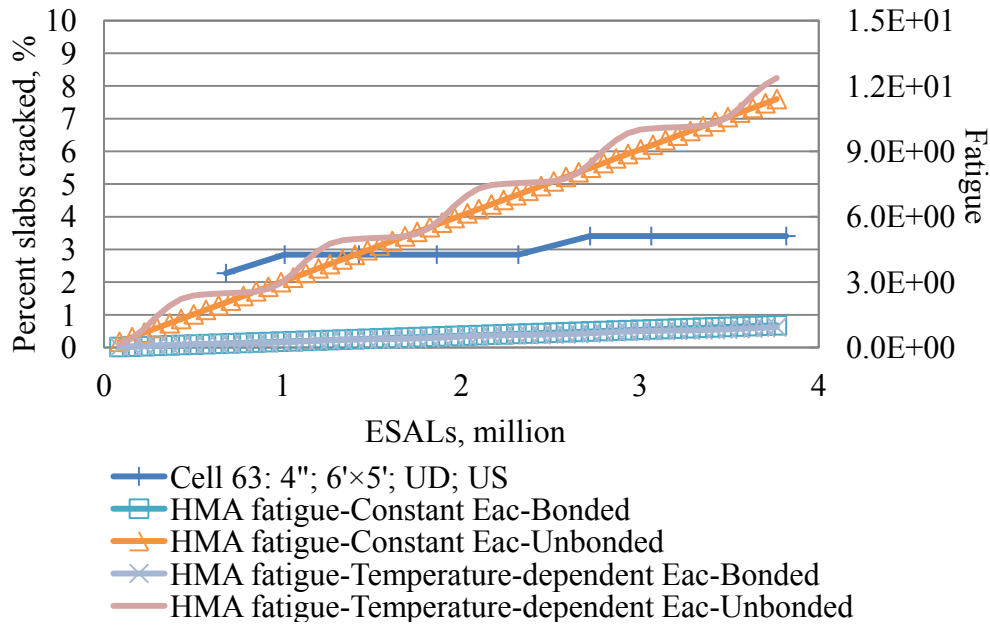


Figure 28. Observed transverse cracking vs. fatigue damage predicted for the HMA of Cell 63 using the NJDOT method.

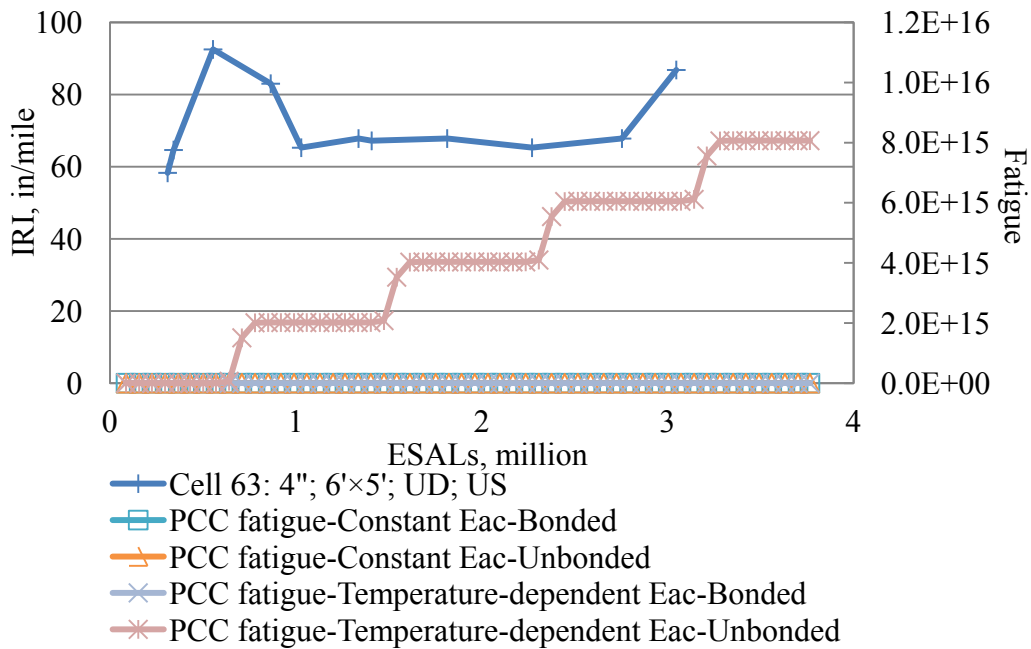


Figure 29. Observed IRI vs. fatigue damage predicted for the PCC of Cell 63 using the NJDOT method.

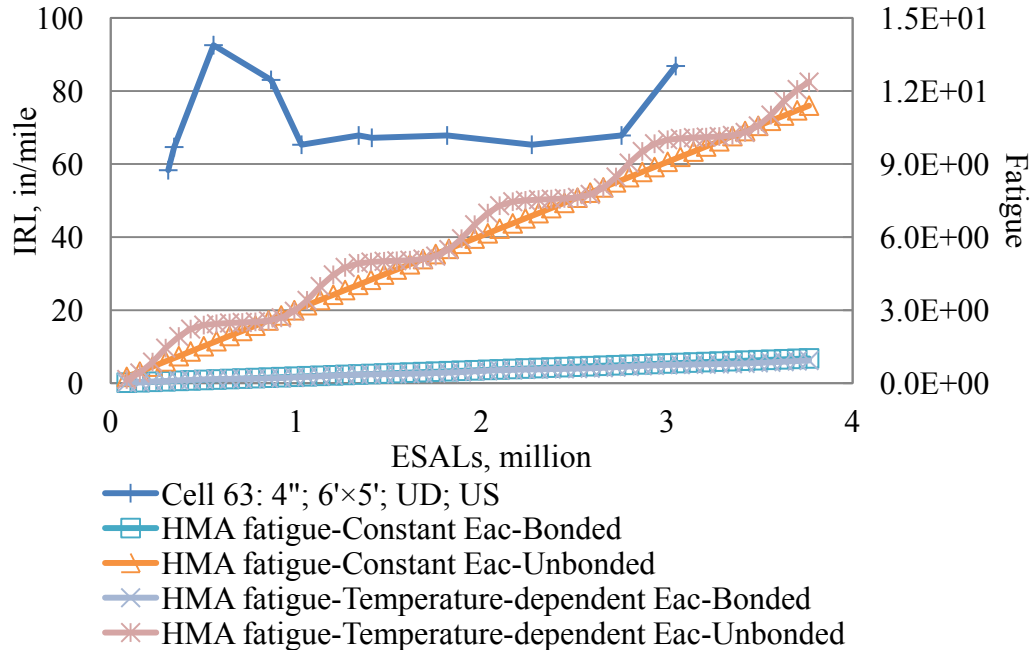


Figure 30. Observed IRI vs. fatigue damage predicted for the HMA of Cell 63 using the NJDOT method.

Table 15. Fatigue summary for Cell 92 using the NJDOT method.

| Date | Constant E_{HMA} | | | | Temperature-dependent E_{HMA} | | | |
|--------|--------------------|---------|----------|---------|---------------------------------|---------|----------|---------|
| | Bonded | | Unbonded | | Bonded | | Unbonded | |
| | PCC | HMA | PCC | HMA | PCC | HMA | PCC | HMA |
| Dec-97 | 0.0E+00 | 5.1E-02 | 6.1E-02 | 1.4E-01 | 0.0E+00 | 1.3E-01 | 0.0E+00 | 3.6E-02 |
| Dec-98 | 0.0E+00 | 1.5E-01 | 1.8E-01 | 4.1E-01 | 0.0E+00 | 1.3E-01 | 2.2E+02 | 5.5E-01 |
| Dec-99 | 0.0E+00 | 2.5E-01 | 3.1E-01 | 6.9E-01 | 0.0E+00 | 2.1E-01 | 3.3E+02 | 9.7E-01 |
| Dec-00 | 0.0E+00 | 3.5E-01 | 4.3E-01 | 9.6E-01 | 0.0E+00 | 3.0E-01 | 4.5E+02 | 1.4E+00 |
| Dec-01 | 0.0E+00 | 4.6E-01 | 5.5E-01 | 1.2E+00 | 0.0E+00 | 3.9E-01 | 5.8E+02 | 1.8E+00 |
| Dec-02 | 0.0E+00 | 5.6E-01 | 6.7E-01 | 1.5E+00 | 0.0E+00 | 4.8E-01 | 7.1E+02 | 2.2E+00 |
| Dec-03 | 0.0E+00 | 6.6E-01 | 8.0E-01 | 1.8E+00 | 0.0E+00 | 5.7E-01 | 8.4E+02 | 2.6E+00 |
| Dec-04 | 0.0E+00 | 7.6E-01 | 9.2E-01 | 2.1E+00 | 0.0E+00 | 1.9E+00 | 9.6E+02 | 3.1E+00 |
| Dec-05 | 0.0E+00 | 8.6E-01 | 1.0E+00 | 2.3E+00 | 0.0E+00 | 2.1E+00 | 1.1E+03 | 3.5E+00 |
| Dec-06 | 0.0E+00 | 9.6E-01 | 1.2E+00 | 2.6E+00 | 0.0E+00 | 2.4E+00 | 1.2E+03 | 3.9E+00 |
| Dec-07 | 0.0E+00 | 1.1E+00 | 1.3E+00 | 2.9E+00 | 0.0E+00 | 2.6E+00 | 1.3E+03 | 4.3E+00 |
| Dec-08 | 0.0E+00 | 1.2E+00 | 1.4E+00 | 3.2E+00 | 0.0E+00 | 2.9E+00 | 1.5E+03 | 4.7E+00 |

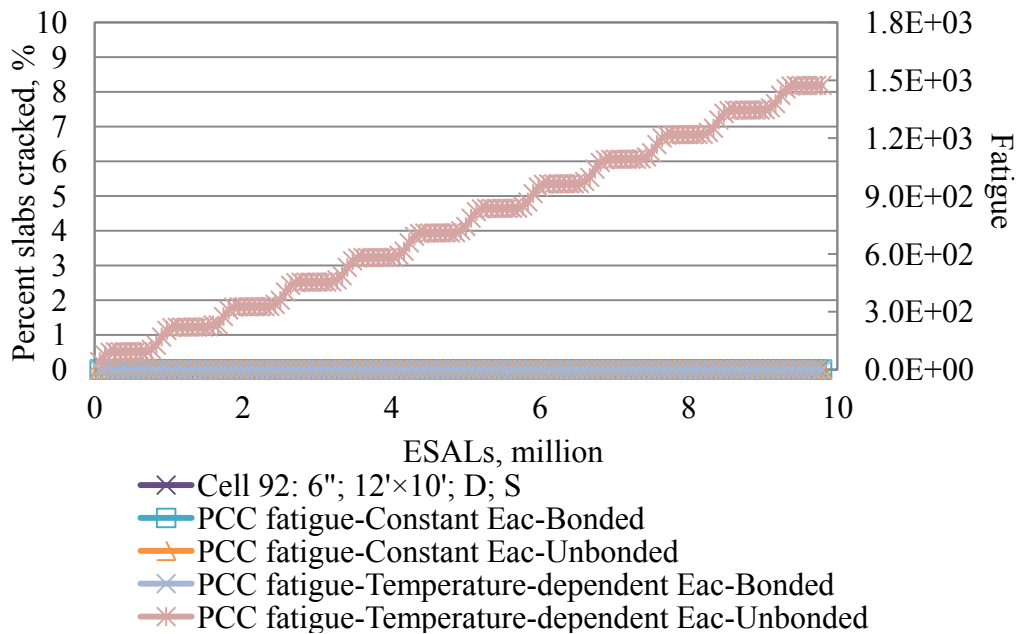


Figure 31. Observed transverse cracking vs. fatigue damage predicted for the PCC of Cell 92 using the NJDOT method.

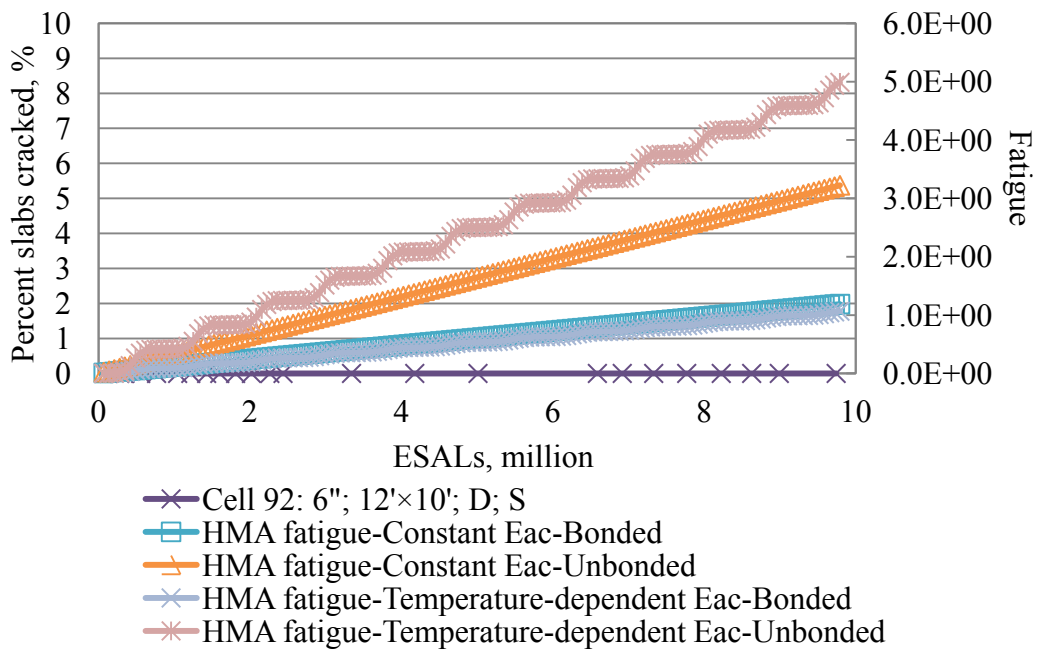


Figure 32. Observed transverse cracking vs. fatigue damage predicted for the HMA of Cell 92 using the NJDOT method.

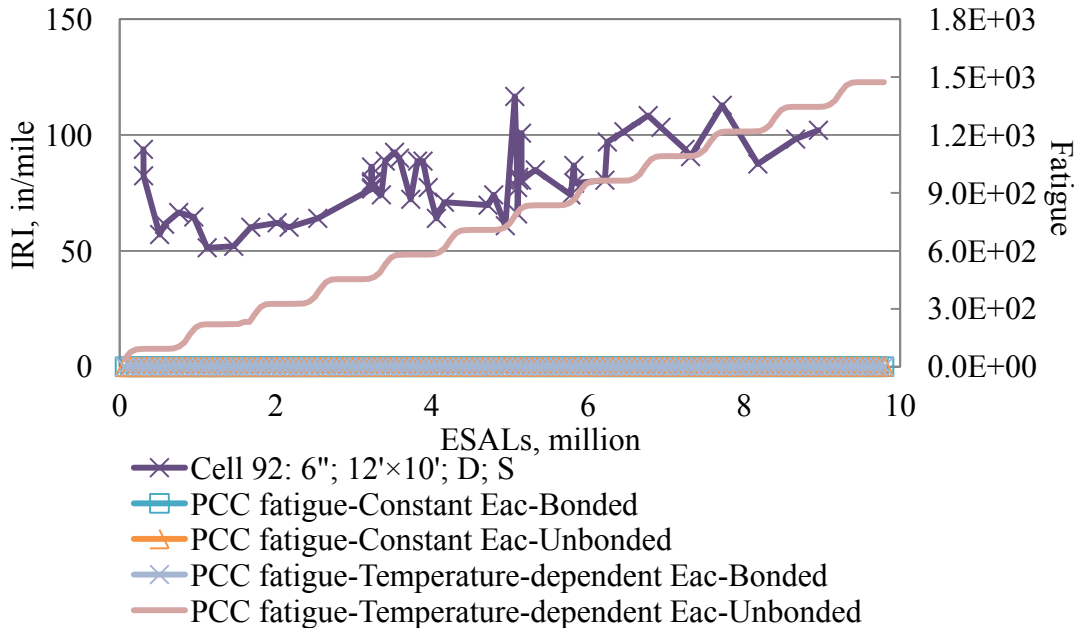


Figure 33. Observed IRI vs. fatigue damage predicted for the PCC of Cell 92 using the NJDOT method.

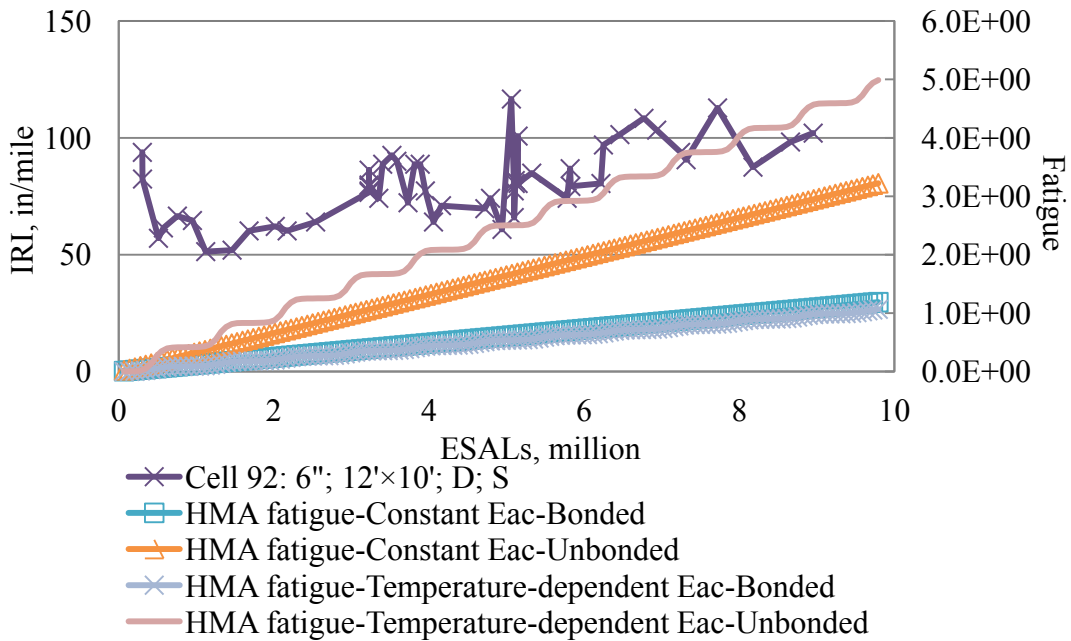


Figure 34. Observed IRI vs. fatigue damage predicted for the HMA of Cell 92 using the NJDOT method.

Table 16. Fatigue summary for Cell 93 using the NJDOT method.

| Date | Constant E_{HMA} | | | | Temperature-dependent E_{HMA} | | | |
|--------|--------------------|---------|----------|---------|---------------------------------|---------|----------|---------|
| | Bonded | | Unbonded | | Bonded | | Unbonded | |
| | PCC | HMA | PCC | HMA | PCC | HMA | PCC | HMA |
| Dec-97 | 0.0E+00 | 7.6E-02 | 4.0E+00 | 1.1E+00 | 0.0E+00 | 1.0E-01 | 2.8E+06 | 9.0E-01 |
| Dec-98 | 0.0E+00 | 2.3E-01 | 1.2E+01 | 3.4E+00 | 0.0E+00 | 2.0E-01 | 6.9E+06 | 3.0E+00 |
| Dec-99 | 0.0E+00 | 3.8E-01 | 2.0E+01 | 5.7E+00 | 0.0E+00 | 3.3E-01 | 1.1E+07 | 5.1E+00 |
| Dec-00 | 0.0E+00 | 5.2E-01 | 2.8E+01 | 7.8E+00 | 0.0E+00 | 4.5E-01 | 1.5E+07 | 6.9E+00 |
| Dec-01 | 0.0E+00 | 6.8E-01 | 3.6E+01 | 1.0E+01 | 0.0E+00 | 6.0E-01 | 1.9E+07 | 9.3E+00 |
| Dec-02 | 0.0E+00 | 8.3E-01 | 4.4E+01 | 1.3E+01 | 0.0E+00 | 7.4E-01 | 2.3E+07 | 1.1E+01 |
| Dec-03 | 0.0E+00 | 9.8E-01 | 5.2E+01 | 1.5E+01 | 0.0E+00 | 8.7E-01 | 2.7E+07 | 1.4E+01 |

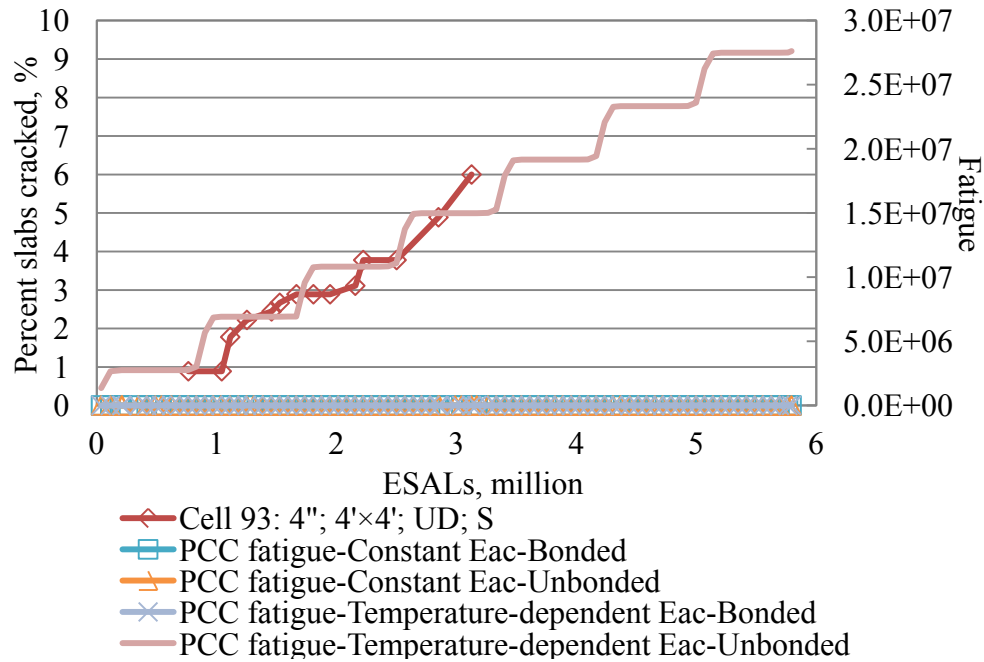


Figure 35. Observed transverse cracking vs. fatigue damage predicted for the PCC of Cell 93 using the NJDOT method.

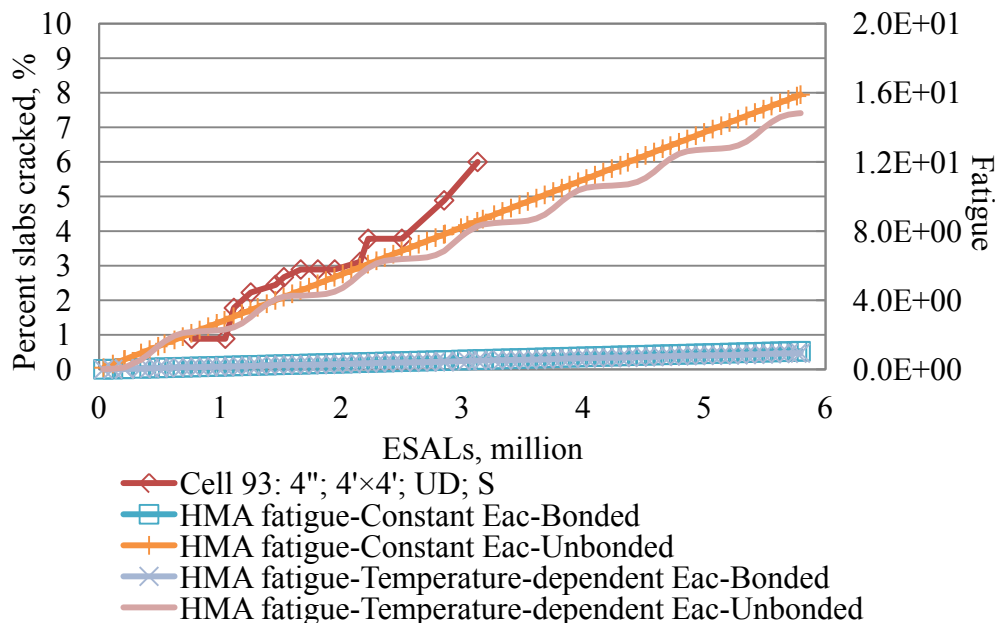


Figure 36. Observed transverse cracking vs. fatigue damage predicted for the HMA of Cell 93 using the NJDOT method.

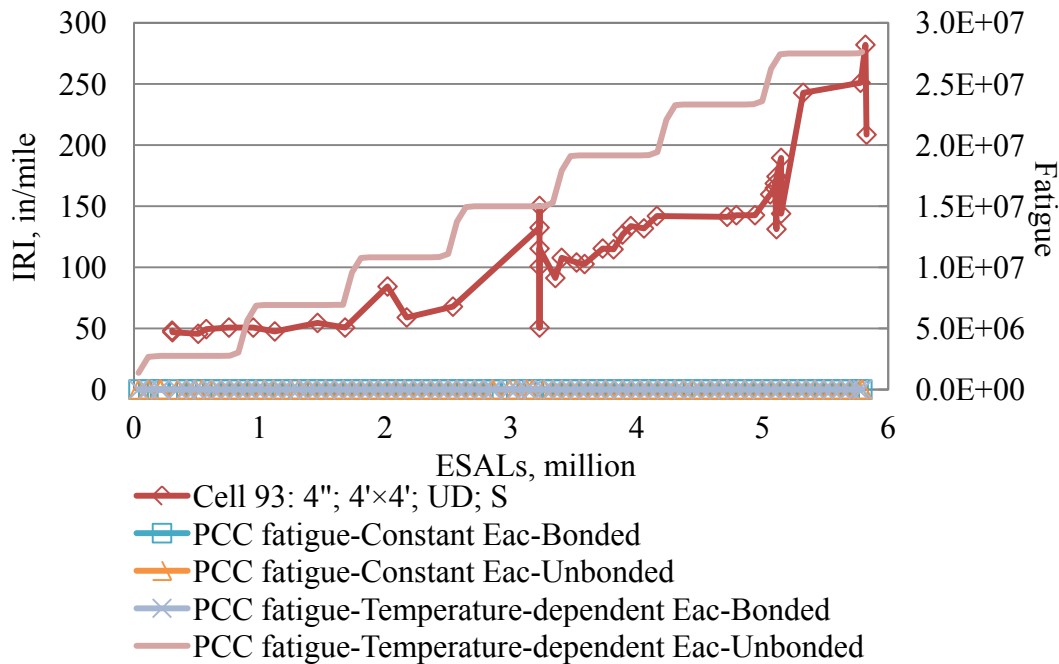


Figure 37. Observed IRI vs. fatigue damage predicted for the PCC of Cell 93 using the NJDOT method.

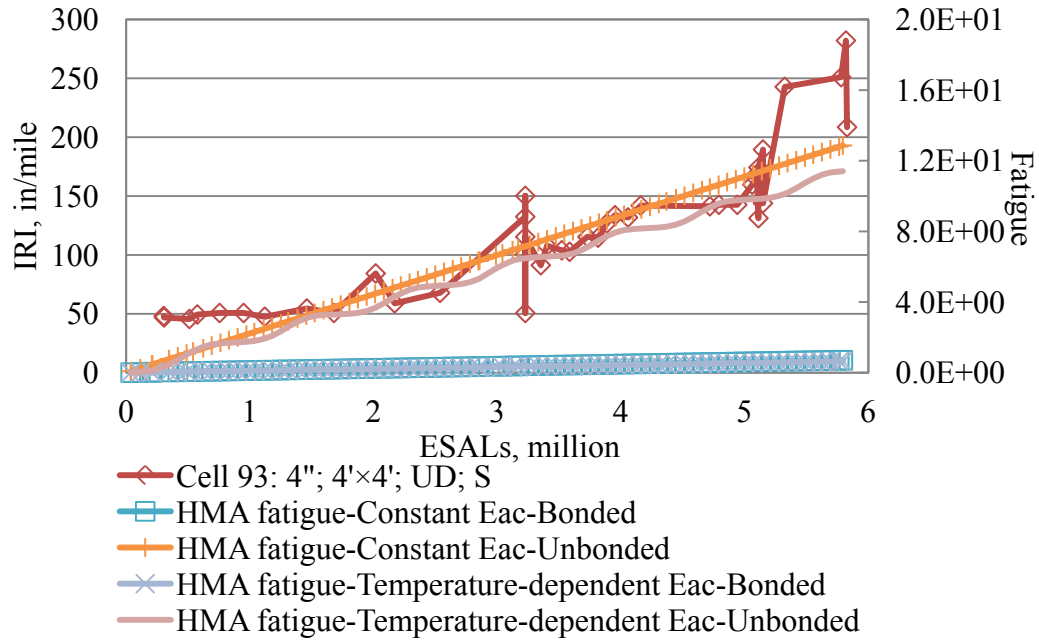


Figure 38. Observed IRI vs. fatigue damage predicted for the HMA of Cell 93 using the NJDOT method.

Table 17. Fatigue summary for Cell 94 using the NJDOT method.

| Date | Constant E_{HMA} | | | | Temperature-dependent E_{HMA} | | | |
|--------|--------------------|---------|----------|---------|---------------------------------|---------|----------|---------|
| | Bonded | | Unbonded | | Bonded | | Unbonded | |
| | PCC | HMA | PCC | HMA | PCC | HMA | PCC | HMA |
| Dec-97 | 0.0E+00 | 7.6E-02 | 3.0E-01 | 1.6E+00 | 0.0E+00 | 6.9E-02 | 2.1E+08 | 1.3E+00 |
| Dec-98 | 0.0E+00 | 2.3E-01 | 8.9E-01 | 4.8E+00 | 0.0E+00 | 2.1E-01 | 5.5E+08 | 4.0E+00 |
| Dec-99 | 0.0E+00 | 3.8E-01 | 1.5E+00 | 8.0E+00 | 0.0E+00 | 3.5E-01 | 8.9E+08 | 6.6E+00 |
| Dec-00 | 0.0E+00 | 5.2E-01 | 2.0E+00 | 1.1E+01 | 0.0E+00 | 4.8E-01 | 1.2E+09 | 9.0E+00 |
| Dec-01 | 0.0E+00 | 6.8E-01 | 2.7E+00 | 1.4E+01 | 0.0E+00 | 6.3E-01 | 1.6E+09 | 1.2E+01 |
| Dec-02 | 0.0E+00 | 8.4E-01 | 3.2E+00 | 1.8E+01 | 0.0E+00 | 7.8E-01 | 1.9E+09 | 1.5E+01 |
| Dec-03 | 0.0E+00 | 9.9E-01 | 3.8E+00 | 2.1E+01 | 0.0E+00 | 9.2E-01 | 2.2E+09 | 1.7E+01 |

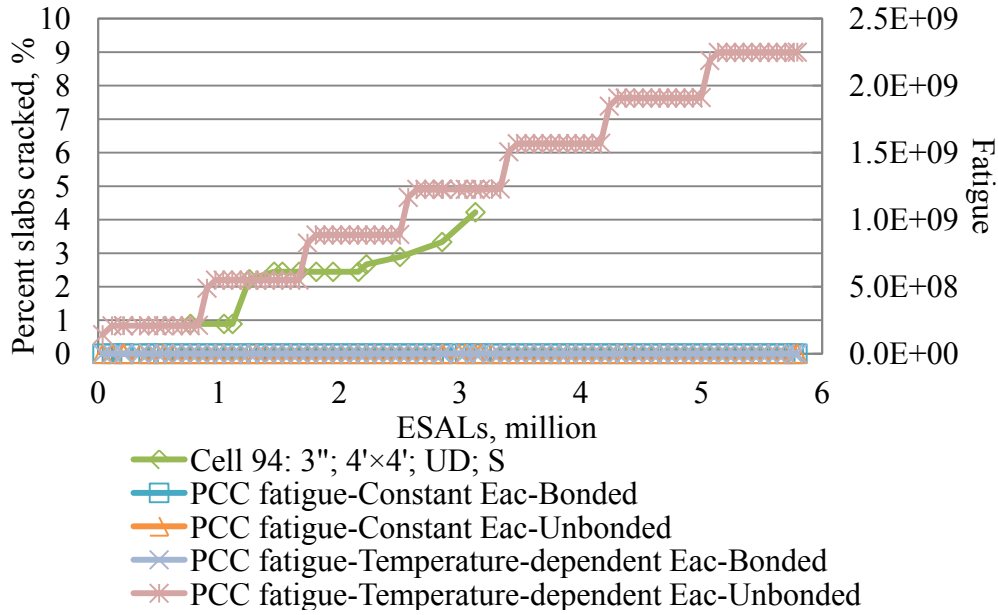


Figure 39. Observed transverse cracking vs. fatigue damage predicted for the PCC of Cell 94 using the NJDOT method.

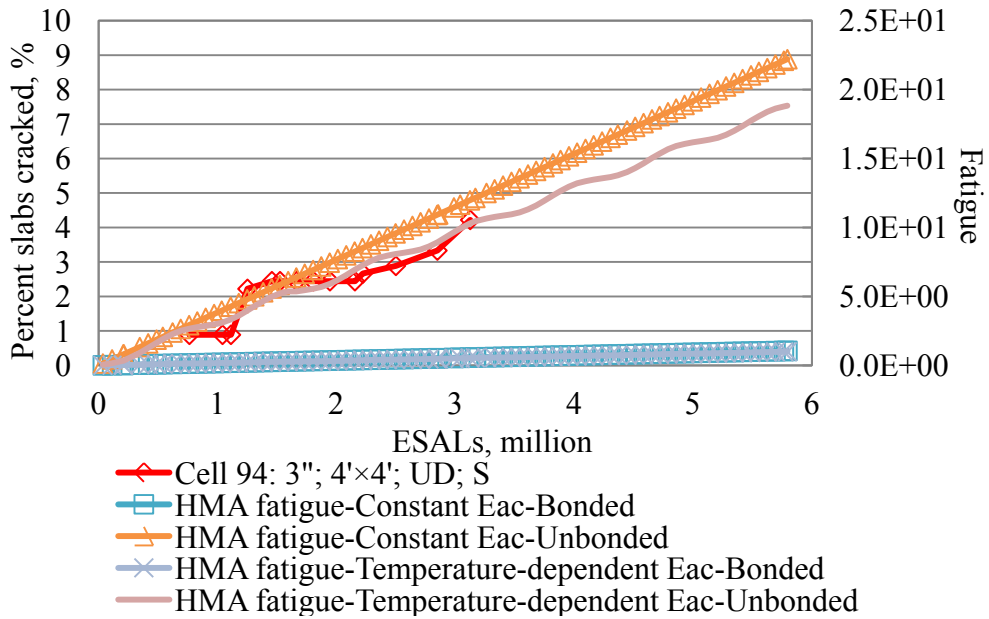


Figure 40. Observed transverse cracking vs. fatigue damage predicted for the HMA of Cell 94 using the NJDOT method.

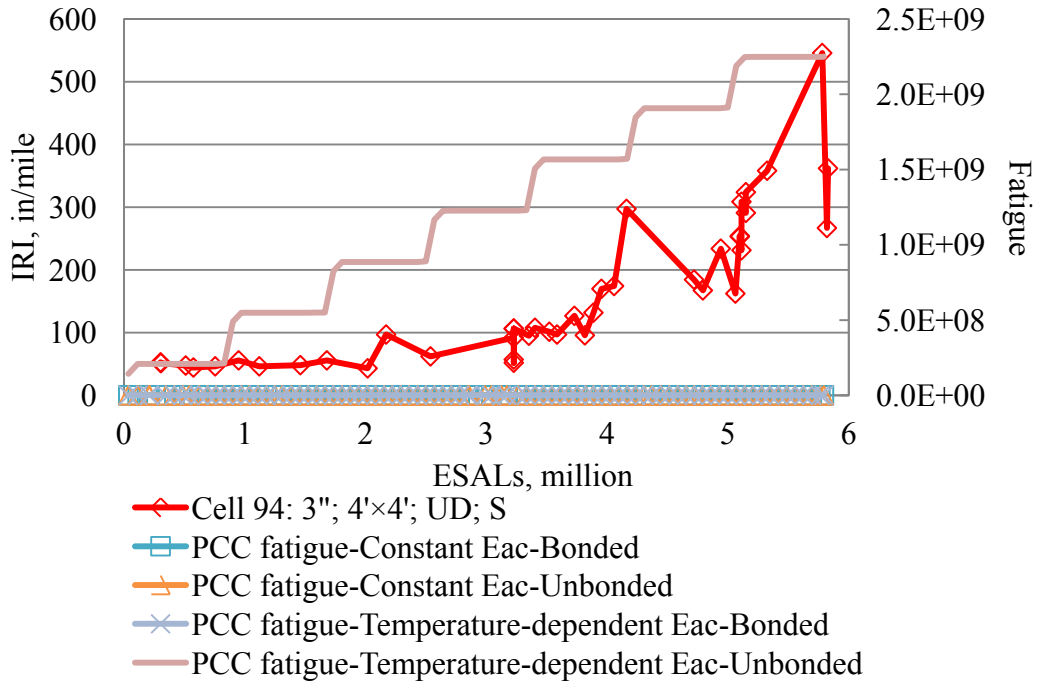


Figure 41. Observed IRI vs. fatigue damage predicted for the PCC of Cell 94 using the NJDOT method.

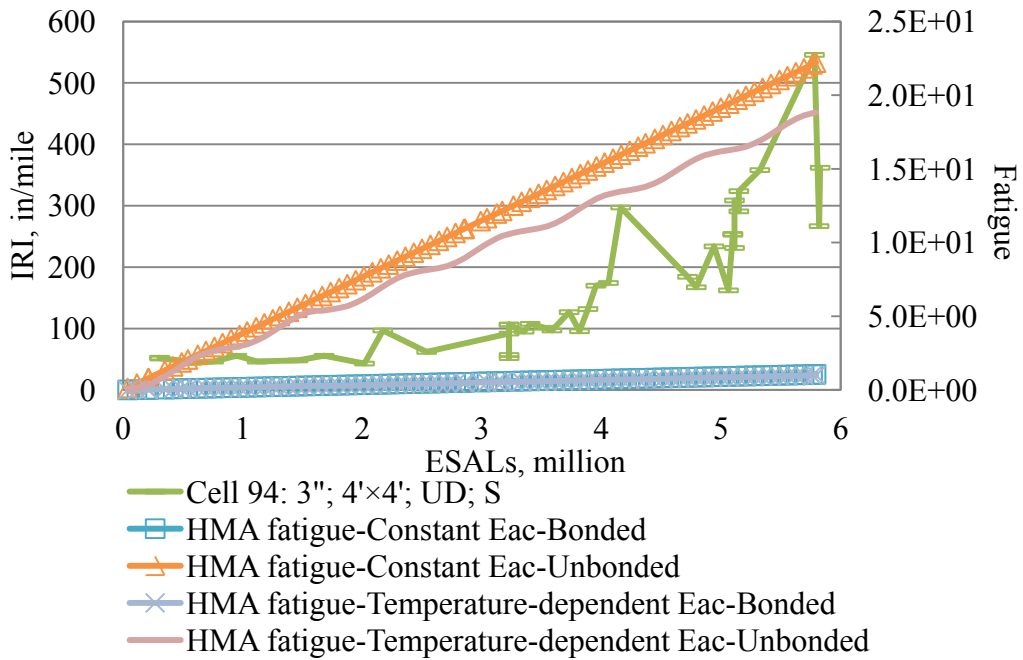


Figure 42. Observed IRI vs. fatigue damage predicted for the HMA of Cell 94 using the NJDOT method.

Table 18. Fatigue summary for Cell 95 using the NJDOT method.

| Date | Constant E_{HMA} | | | | Temperature-dependent E_{HMA} | | | |
|--------|--------------------|---------|----------|---------|---------------------------------|---------|----------|---------|
| | Bonded | | Unbonded | | Bonded | | Unbonded | |
| | PCC | HMA | PCC | HMA | PCC | HMA | PCC | HMA |
| Dec-97 | 0.0E+00 | 7.6E-02 | 0.0E+00 | 1.6E+00 | 0.0E+00 | 6.9E-02 | 9.2E+06 | 1.3E+00 |
| Dec-98 | 0.0E+00 | 2.3E-01 | 0.0E+00 | 4.8E+00 | 0.0E+00 | 2.1E-01 | 2.4E+07 | 4.0E+00 |
| Dec-99 | 0.0E+00 | 3.8E-01 | 0.0E+00 | 8.0E+00 | 0.0E+00 | 3.5E-01 | 3.9E+07 | 6.6E+00 |
| Dec-00 | 0.0E+00 | 5.2E-01 | 0.0E+00 | 1.1E+01 | 0.0E+00 | 4.8E-01 | 5.4E+07 | 9.0E+00 |
| Dec-01 | 0.0E+00 | 6.9E-01 | 0.0E+00 | 1.4E+01 | 0.0E+00 | 6.4E-01 | 6.9E+07 | 1.2E+01 |
| Dec-02 | 0.0E+00 | 8.4E-01 | 0.0E+00 | 1.8E+01 | 0.0E+00 | 7.8E-01 | 8.4E+07 | 1.5E+01 |
| Dec-03 | 0.0E+00 | 9.9E-01 | 0.0E+00 | 2.1E+01 | 0.0E+00 | 9.3E-01 | 9.8E+07 | 1.8E+01 |

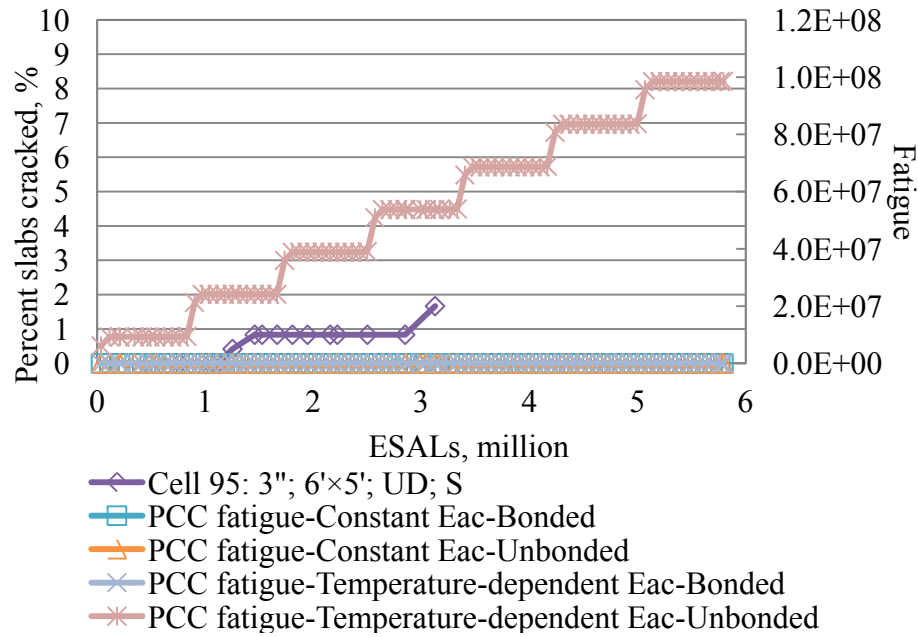


Figure 43. Observed transverse cracking vs. fatigue damage predicted for the PCC of Cell 95 using the NJDOT method.

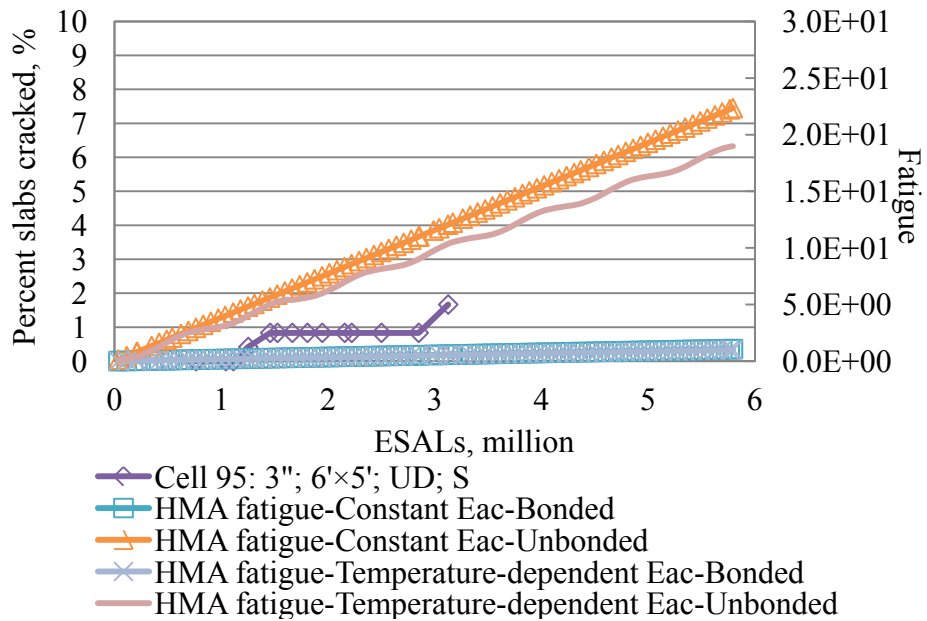


Figure 44. Observed transverse cracking vs. fatigue damage predicted for the HMA of Cell 95 using the NJDOT method.

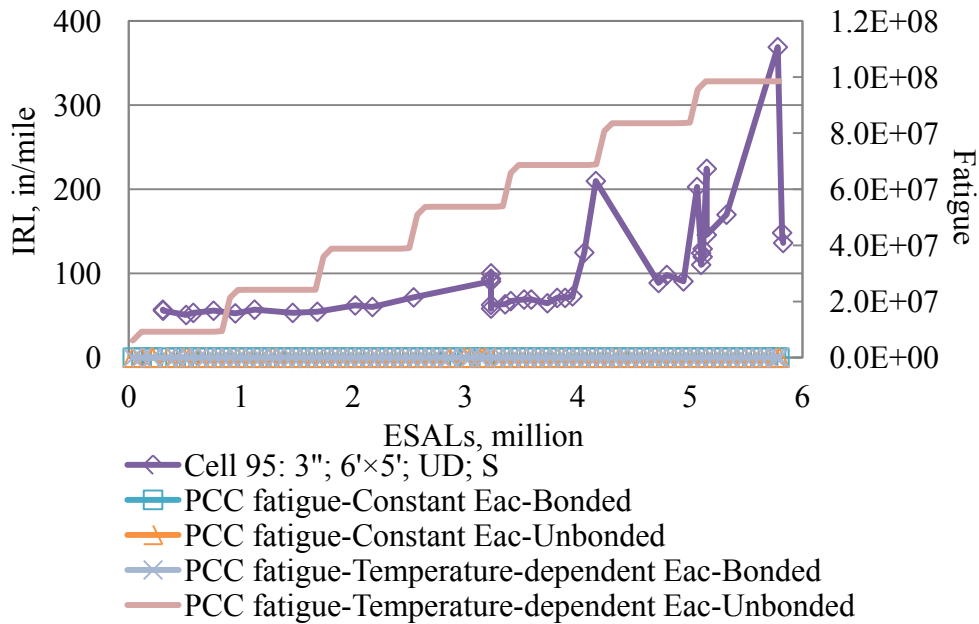


Figure 45. Observed IRI vs. fatigue damage predicted for the PCC of Cell 95 using the NJDOT method.

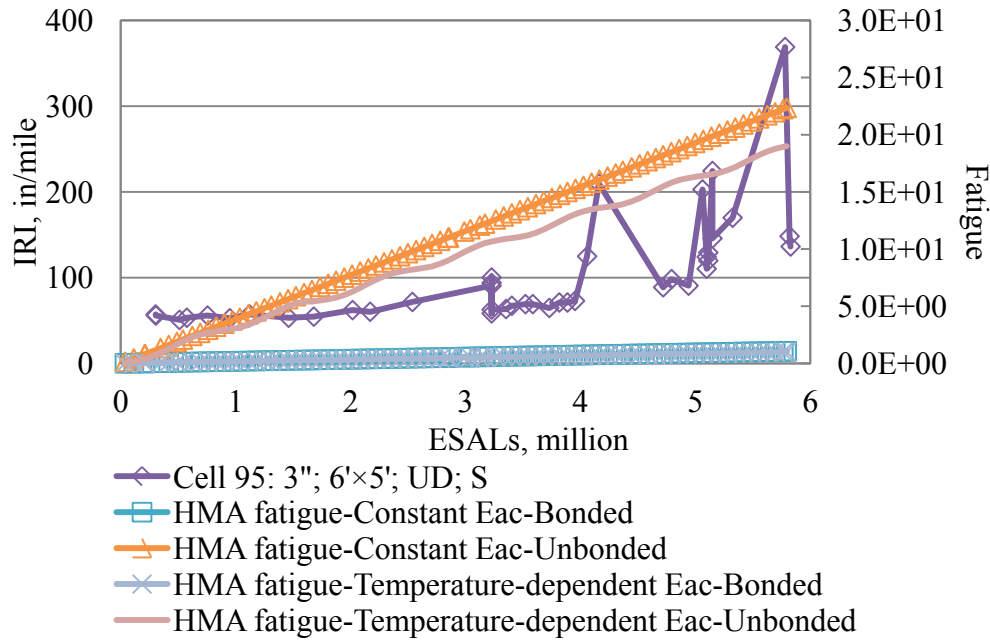


Figure 46. Observed IRI vs. fatigue damage predicted for the HMA of Cell 95 using the NJDOT method.

Table 19. Fatigue summary for Cell 96 using the NJDOT method.

| Date | Constant E_{HMA} | | | | Temperature-dependent E_{HMA} | | | |
|--------|--------------------|---------|----------|---------|---------------------------------|---------|----------|---------|
| | Bonded | | Unbonded | | Bonded | | Unbonded | |
| | PCC | HMA | PCC | HMA | PCC | HMA | PCC | HMA |
| Jan-98 | 0.0E+00 | 5.1E-02 | 0.0E+00 | 1.4E-01 | 0.0E+00 | 3.6E-02 | 2.5E+01 | 1.3E-01 |
| Jan-99 | 0.0E+00 | 1.5E-01 | 0.0E+00 | 4.1E-01 | 0.0E+00 | 1.3E-01 | 6.0E+01 | 5.5E-01 |
| Jan-00 | 0.0E+00 | 2.5E-01 | 0.0E+00 | 6.9E-01 | 0.0E+00 | 2.1E-01 | 8.9E+01 | 9.7E-01 |
| Jan-01 | 0.0E+00 | 3.5E-01 | 0.0E+00 | 9.6E-01 | 0.0E+00 | 3.0E-01 | 1.2E+02 | 1.4E+00 |
| Jan-02 | 0.0E+00 | 4.6E-01 | 0.0E+00 | 1.2E+00 | 0.0E+00 | 3.9E-01 | 1.6E+02 | 1.8E+00 |
| Jan-03 | 0.0E+00 | 5.6E-01 | 0.0E+00 | 1.5E+00 | 0.0E+00 | 4.8E-01 | 1.9E+02 | 2.2E+00 |
| Jan-04 | 0.0E+00 | 6.6E-01 | 0.0E+00 | 1.8E+00 | 0.0E+00 | 5.7E-01 | 2.3E+02 | 2.6E+00 |
| Jan-05 | 0.0E+00 | 7.6E-01 | 0.0E+00 | 2.1E+00 | 0.0E+00 | 6.6E-01 | 2.6E+02 | 3.1E+00 |
| Jan-06 | 0.0E+00 | 8.6E-01 | 0.0E+00 | 2.3E+00 | 0.0E+00 | 7.5E-01 | 3.0E+02 | 3.5E+00 |
| Jan-07 | 0.0E+00 | 9.6E-01 | 0.0E+00 | 2.6E+00 | 0.0E+00 | 8.4E-01 | 3.3E+02 | 3.9E+00 |
| Jan-08 | 0.0E+00 | 1.1E+00 | 0.0E+00 | 2.9E+00 | 0.0E+00 | 9.3E-01 | 3.7E+02 | 4.3E+00 |
| Jan-09 | 0.0E+00 | 1.2E+00 | 0.0E+00 | 3.2E+00 | 0.0E+00 | 1.0E+00 | 4.0E+02 | 4.7E+00 |

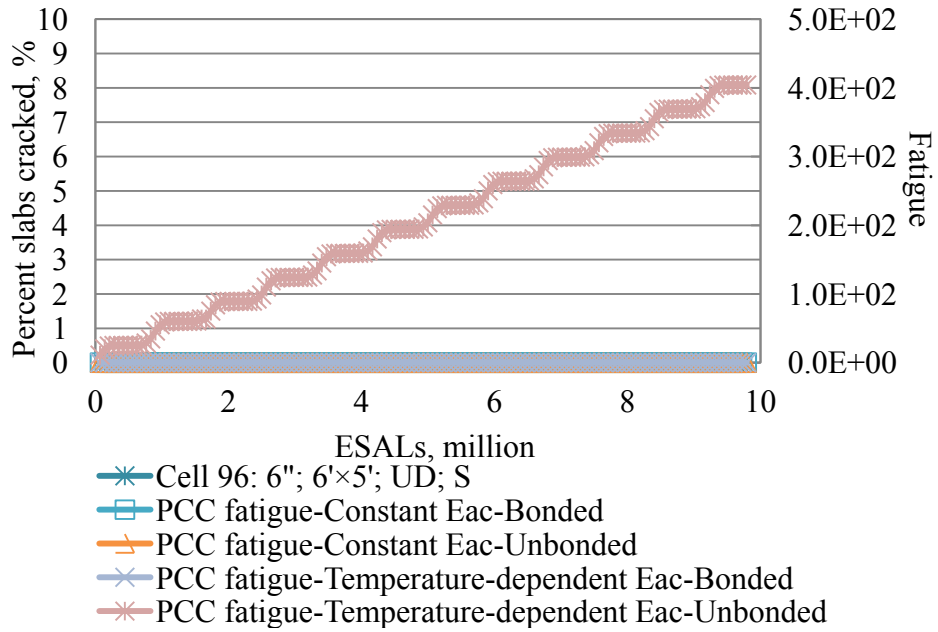


Figure 47. Observed transverse cracking vs. fatigue damage predicted for the PCC of Cell 96 using the NJDOT method.

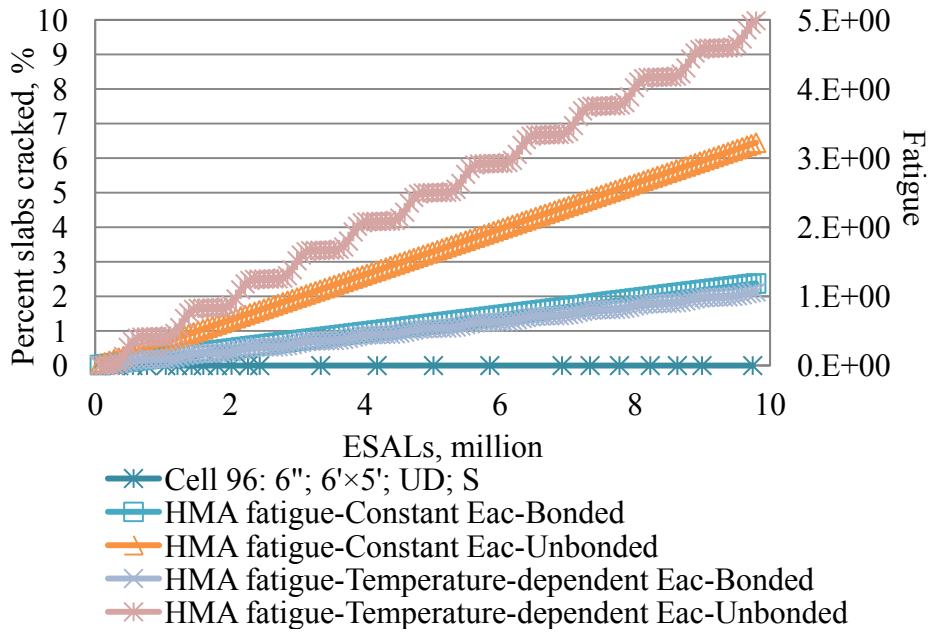


Figure 48. Observed transverse cracking vs. fatigue damage predicted for the HMA of Cell 96 using the NJDOT method.

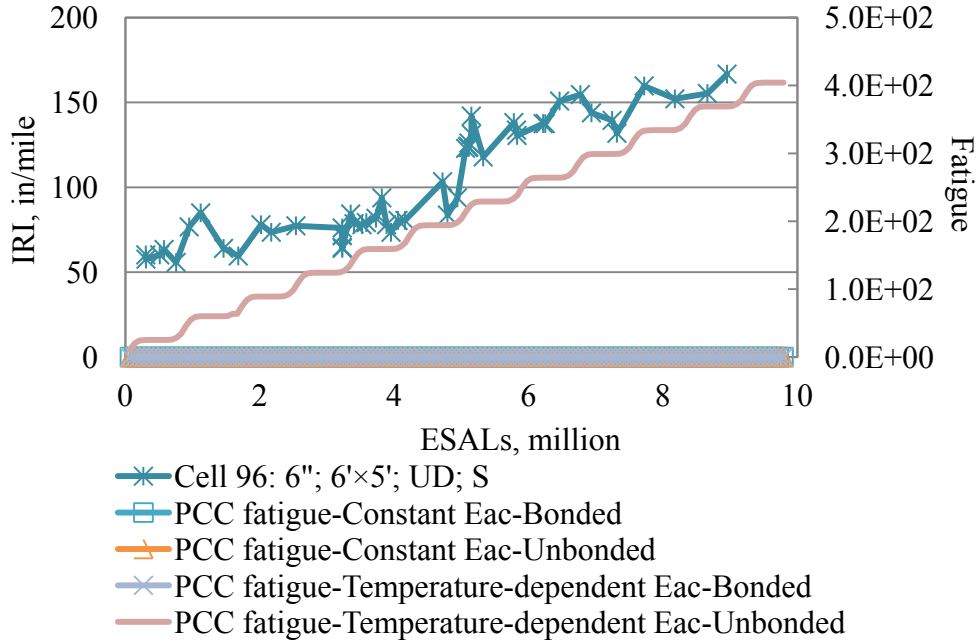


Figure 49. Observed IRI vs. fatigue damage predicted for the PCC of Cell 96 using the NJDOT method.

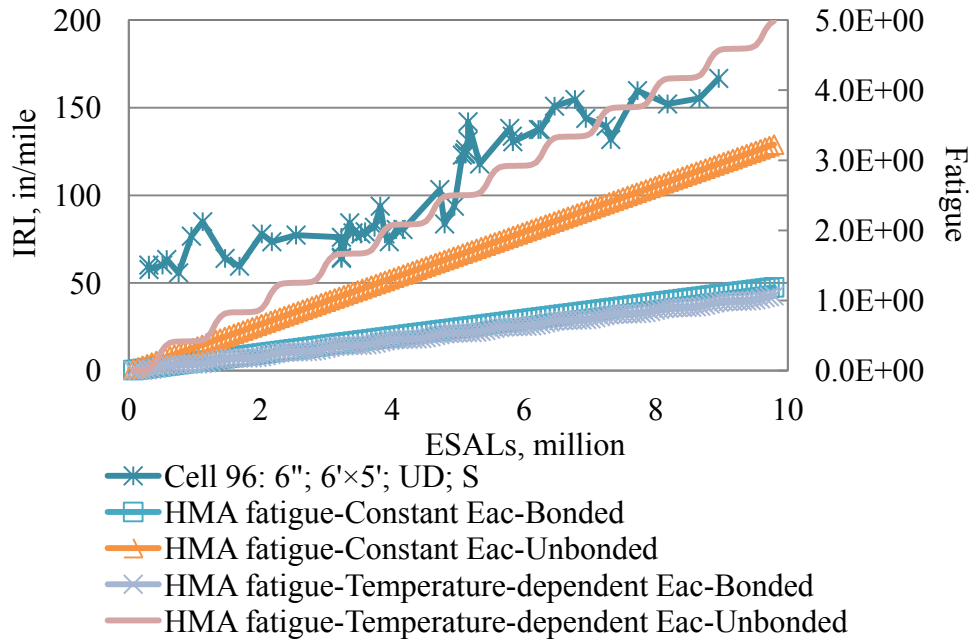


Figure 50. Observed IRI vs. fatigue damage predicted for the HMA of Cell 96 using the NJDOT method.

Table 20. Fatigue summary for Cell 97 using the NJDOT method.

| Date | Constant E_{HMA} | | | | Temperature-dependent E_{HMA} | | | |
|--------|--------------------|---------|----------|---------|---------------------------------|---------|----------|---------|
| | Bonded | | Unbonded | | Bonded | | Unbonded | |
| | PCC | HMA | PCC | HMA | PCC | HMA | PCC | HMA |
| Dec-97 | 0.0E+00 | 5.1E-02 | 6.1E-02 | 1.4E-01 | 0.0E+00 | 3.6E-02 | 9.3E+01 | 1.3E-01 |
| Dec-98 | 0.0E+00 | 1.5E-01 | 1.8E-01 | 4.1E-01 | 0.0E+00 | 1.3E-01 | 2.2E+02 | 5.5E-01 |
| Dec-99 | 0.0E+00 | 2.5E-01 | 3.1E-01 | 6.9E-01 | 0.0E+00 | 2.1E-01 | 3.3E+02 | 9.7E-01 |
| Dec-00 | 0.0E+00 | 3.5E-01 | 4.3E-01 | 9.6E-01 | 0.0E+00 | 3.0E-01 | 4.5E+02 | 1.4E+00 |
| Dec-01 | 0.0E+00 | 4.6E-01 | 5.5E-01 | 1.2E+00 | 0.0E+00 | 3.9E-01 | 5.8E+02 | 1.8E+00 |
| Dec-02 | 0.0E+00 | 5.6E-01 | 6.7E-01 | 1.5E+00 | 0.0E+00 | 4.8E-01 | 7.1E+02 | 2.2E+00 |
| Dec-03 | 0.0E+00 | 6.6E-01 | 8.0E-01 | 1.8E+00 | 0.0E+00 | 5.7E-01 | 8.4E+02 | 2.6E+00 |
| Dec-04 | 0.0E+00 | 7.6E-01 | 9.2E-01 | 2.1E+00 | 0.0E+00 | 6.6E-01 | 9.6E+02 | 3.1E+00 |
| Dec-05 | 0.0E+00 | 8.6E-01 | 1.0E+00 | 2.3E+00 | 0.0E+00 | 7.5E-01 | 1.1E+03 | 3.5E+00 |
| Dec-06 | 0.0E+00 | 9.6E-01 | 1.2E+00 | 2.6E+00 | 0.0E+00 | 8.4E-01 | 1.2E+03 | 3.9E+00 |
| Dec-07 | 0.0E+00 | 1.1E+00 | 1.3E+00 | 2.9E+00 | 0.0E+00 | 9.3E-01 | 1.3E+03 | 4.3E+00 |
| Dec-08 | 0.0E+00 | 1.2E+00 | 1.4E+00 | 3.2E+00 | 0.0E+00 | 1.0E+00 | 1.5E+03 | 4.7E+00 |

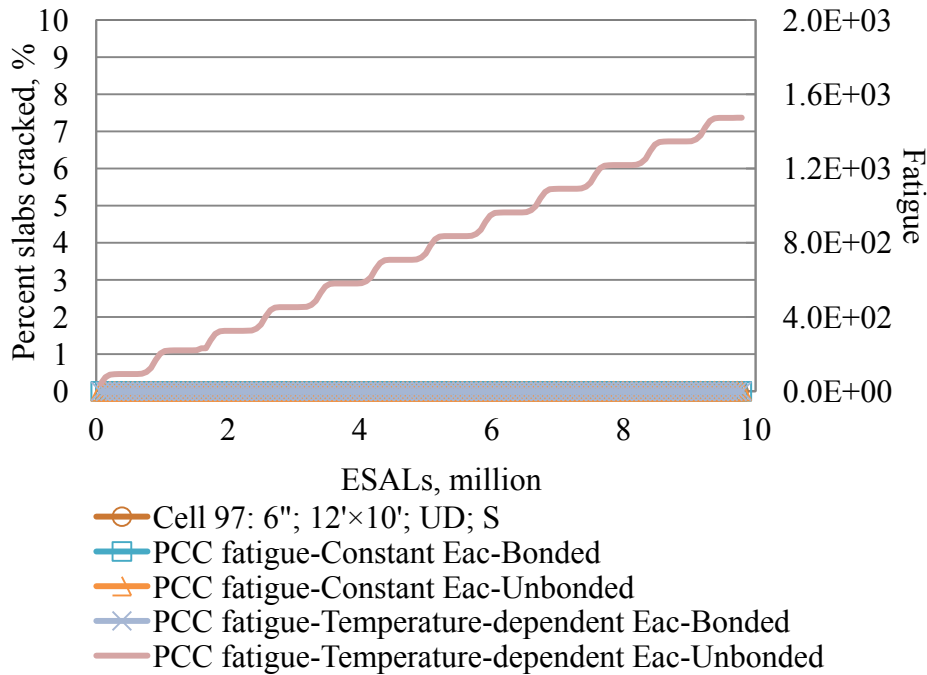


Figure 51. Observed transverse cracking vs. fatigue damage predicted for the PCC of Cell 97 using the NJDOT method.

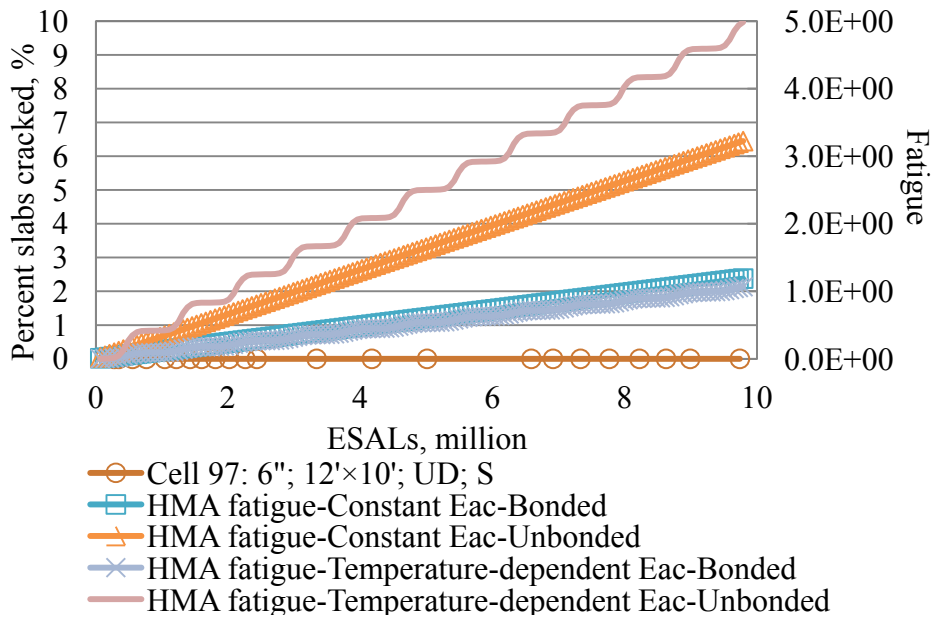


Figure 52. Observed transverse cracking vs. fatigue damage predicted for the HMA of Cell 97 using the NJDOT method.

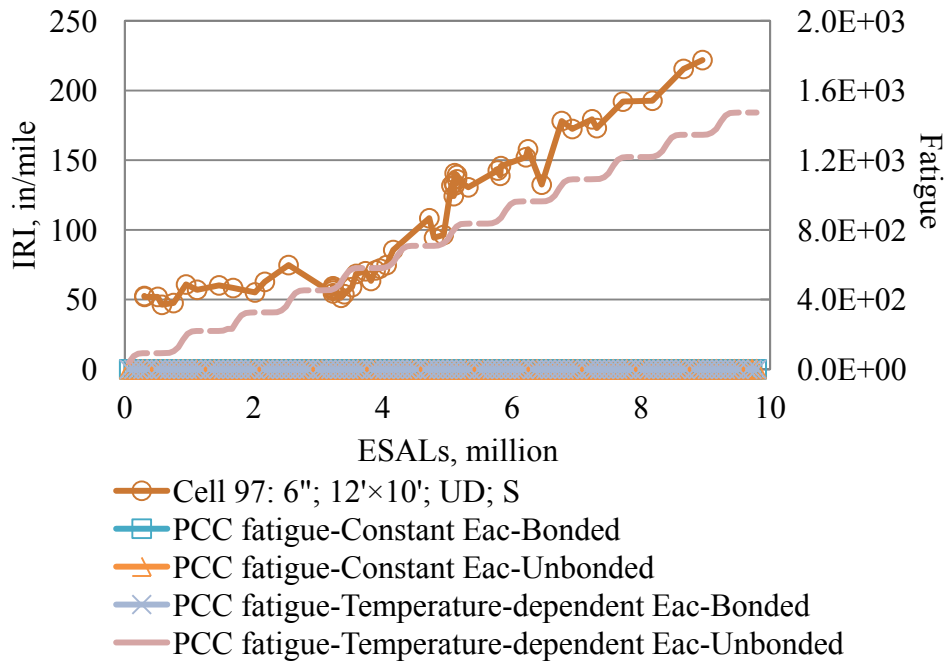


Figure 53. Observed IRI vs. fatigue damage predicted for the PCC of Cell 97 using the NJDOT method.

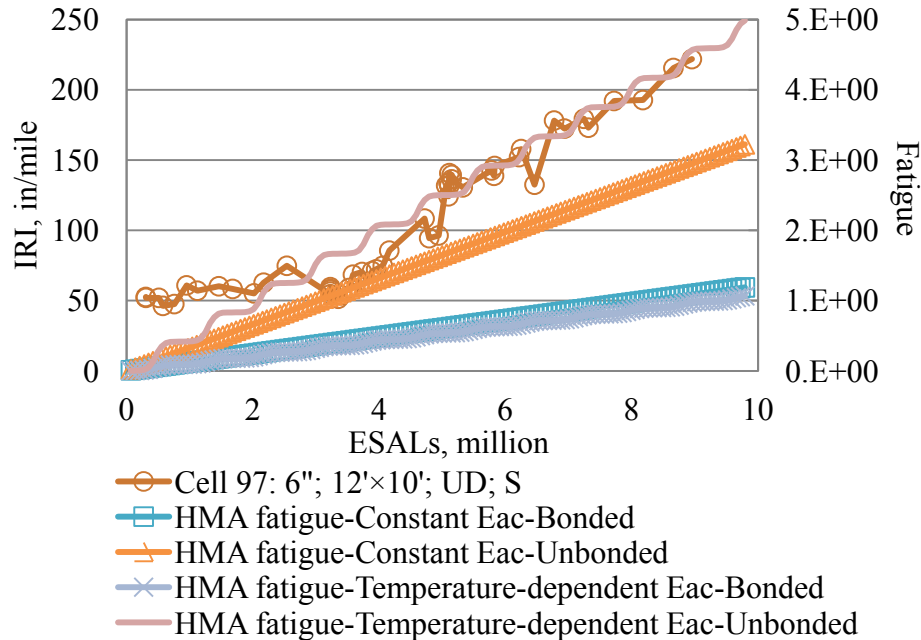


Figure 54. Observed IRI vs. fatigue damage predicted for the HMA of Cell 97 using the NJDOT method.

3.2.1 Conclusion for the NJDOT evaluation

Determining the degree of partial bonding plays an important role in using the NJDOT method to successfully predict the fatigue for the concrete overlay, since it greatly affects the predicted stresses that are significant in the PCA fatigue model. The predicted stresses by the NJDOT structural model are significantly higher for unbonded cases than bonded cases. As can be seen, the trends of the distress development for Cells 93 to 95 agree better with the predictions assuming unbonded layers while the assumption of bonded layers seem to work better for the other cells. Therefore, consistent and successful predictions seem possible to achieve only when the percentage of partial bonding is determined on a cell-to-cell basis.

The low asphalt modulus of elasticity accelerates the PCC fatigue if the overlay is unbonded with the HMA layer. This is indicated by the outstanding predicted PCC damage for cases using a temperature-dependent asphalt modulus of elasticity and the assumption of unbonded layers. Thus, the importance of correctly determining the bonding condition is again addressed in terms of the successful application of the temperature-dependent asphalt modulus of elasticity.

Regarding the HMA fatigue predictions, the employment of a temperature-dependent modulus is only effective for thick whitetopping, i.e. Cells 92, 96 and 97 that are 6 in thick. For the other thinner cells, practically no difference can be observed between predictions using a constant modulus and those with a temperature-dependent modulus.

Lastly, it is important to obtain correct and accurate pavement parameters, namely the overlay thickness and the concrete modulus of rupture. This is because the NJDOT structural model is very sensitive to the overlay thickness in terms of stress prediction; furthermore, the concrete modulus of rupture is a very influential input in the PCA fatigue model.

3.3 Evaluation of the ICT method

In the ICT method, the HMA layer is not considered in the fatigue analysis and thus, fatigue predictions are only made for PCC overlays in this study. The prediction results, as well as their comparisons with the observed transverse cracking and IRI, are presented in this section.

For Cell 60, the predicted fatigue damage using constant and temperature-dependent asphalt moduli of elasticity are compared in Table 21, where cases with a constant asphalt modulus of elasticity yield much lower fatigue predictions. The monthly stress predictions by the ICT method, as shown in Table 22, do not vary as much as those by the NJDOT method (Table 11). For example, the stress predicted in April is only 15 -20 percent lower than that in July. However, when considering the sensitivity of the ACPA concrete fatigue model to the stress ratio, the allowable repetitions in April can be found to be approximately 3,000 times higher than that in July. Therefore, it makes sense to see significantly higher fatigue predictions for the cases where a temperature-dependent asphalt modulus of elasticity is used when there are approximately 0.1 million ESALs each month. The fatigue development shown in Figure 55 also suggests a rapid increase in the summer at 0.6 to 0.8 million ESALs.

Comparisons between the predicted fatigue damage and observed distresses are presented in Figure 55 and Figure 56 for Cell 60. While failure has been suggested by the predictions using a temperature-dependent asphalt modulus of elasticity, the predictions using a constant modulus indicate nearly no damage and thus, better agree with the observation. A similar phenomenon can be found for Cells 61, 62 and 63 in Figure 57 to Figure 62. These cells all have a low concrete modulus of rupture. On the other hand, little damage is predicted for Cells 92 to 97 even using the temperature-dependent asphalt modulus of elasticity as shown in Table 26 to Table 31 and Figure 63 to Figure 74. This does not agree with the observation that Cells 93, 94 and 95 failed due to excessive distresses. A closer examination of the pavement parameters reveals that Cells 92 to 97 present a much higher concrete modulus of rupture than Cells 60 to 63. Therefore, the variation in the predicted stresses for the cells is overcome by the difference in the concrete modulus of rupture so that the predicted damage is much higher for Cells 60 to 63 than Cells 92 to 97.

The last interesting finding is that the predictions of fatigue damage for Cells 92 and 97 are significantly higher than those for Cells 93 to 96. As discussed in Section 2.4.5, the slab length is used in the ICT structural model to substitute an item in the PCA structural model. However, this substitution tends to over predict stresses for long slabs. Cells 92 and 97 are both 144 in long compared with 48 in and 72 in for the other four cells. After checking the predicted stresses, it was found that the stresses for Cells 92 and 97 are 20 to 30 percent higher than the other four cells.

Table 21. Fatigue summary for Cell 60 using the ICT method.

| Date | Constant E_{HMA} | Temperature-dependent E_{HMA} |
|--------|--------------------|---------------------------------|
| Dec-04 | 7.0E-14 | 6.7E-07 |
| Dec-05 | 7.8E-13 | 4.8E-03 |
| Dec-06 | 2.4E-12 | 9.7E-03 |
| Dec-07 | 5.0E-12 | 1.4E-02 |
| Dec-08 | 8.5E-12 | 1.9E-02 |

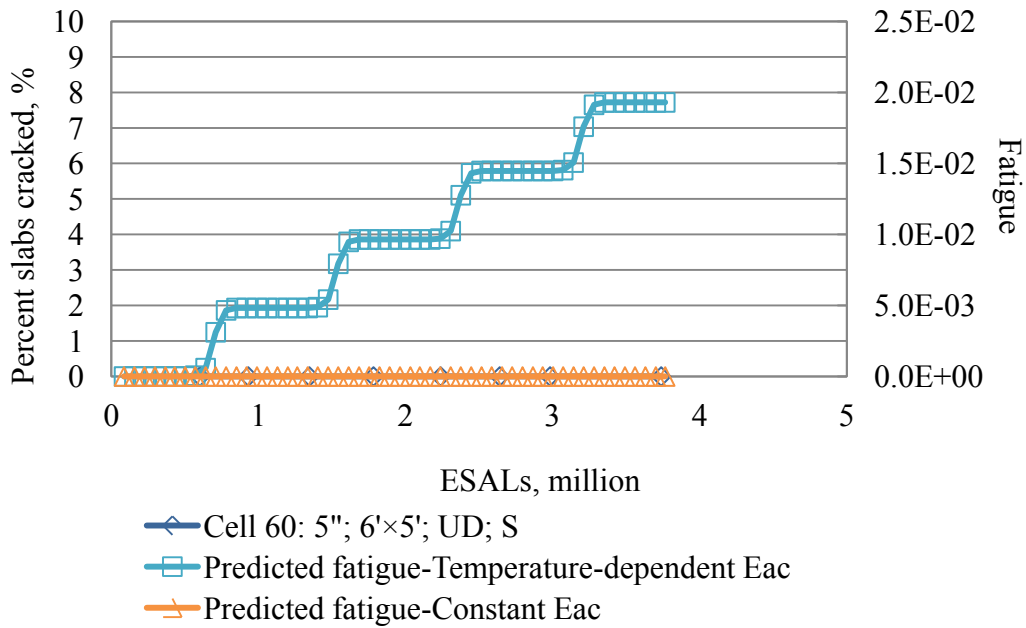


Figure 55. Observed transverse cracking vs. fatigue damage predicted for Cell 60 using the ICT method.

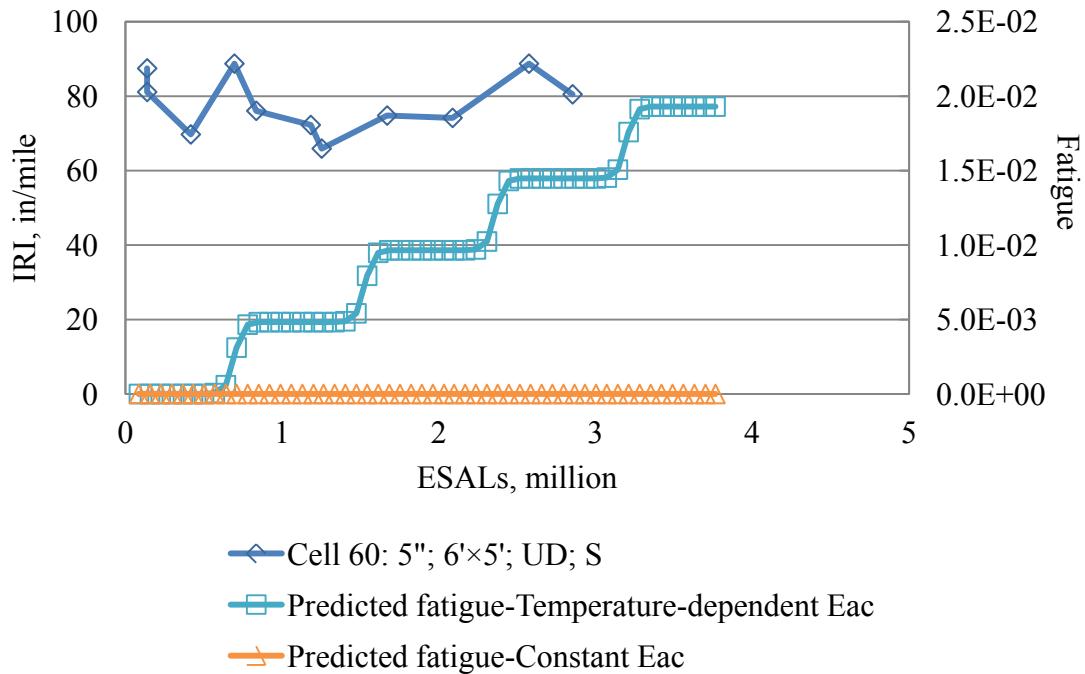


Figure 56. Observed IRI vs. fatigue damage predicted for Cell 60 using the ICT method.

Table 22. Stress predictions for Cell 60 using the ICT method.

| Cell 60 | | Stress in PCC, psi | Stress ratio | Allow load repetitions |
|---------------------------------|-----|--------------------|--------------|------------------------|
| Temperature dependent E_{HMA} | Jan | 195 | 0.33 | 2.3E+14 |
| | Feb | 203 | 0.34 | 1.8E+13 |
| | Mar | 215 | 0.36 | 3.8E+11 |
| | Apr | 240 | 0.40 | 1.2E+09 |
| | May | 272 | 0.46 | 7.3E+06 |
| | Jun | 286 | 0.48 | 1.4E+06 |
| | Jul | 298 | 0.50 | 4.2E+05 |
| | Aug | 294 | 0.49 | 6.3E+05 |
| | Sep | 279 | 0.47 | 3.4E+06 |
| | Oct | 249 | 0.42 | 2.6E+08 |
| | Nov | 223 | 0.38 | 4.5E+10 |
| | Dec | 204 | 0.34 | 1.2E+13 |
| Constant E_{HMA} | | 231 | 0.39 | 7.4E+09 |

Table 23. Fatigue summary for Cell 61 using the ICT method.

| Date | Constant E_{HMA} | Temperature-dependent E_{HMA} |
|--------|--------------------|---------------------------------|
| Dec-04 | 5.8E-11 | 2.0E-04 |
| Dec-05 | 6.5E-10 | 2.6E-01 |
| Dec-06 | 2.0E-09 | 5.2E-01 |
| Dec-07 | 4.1E-09 | 7.8E-01 |
| Dec-08 | 7.0E-09 | 1.0E+00 |

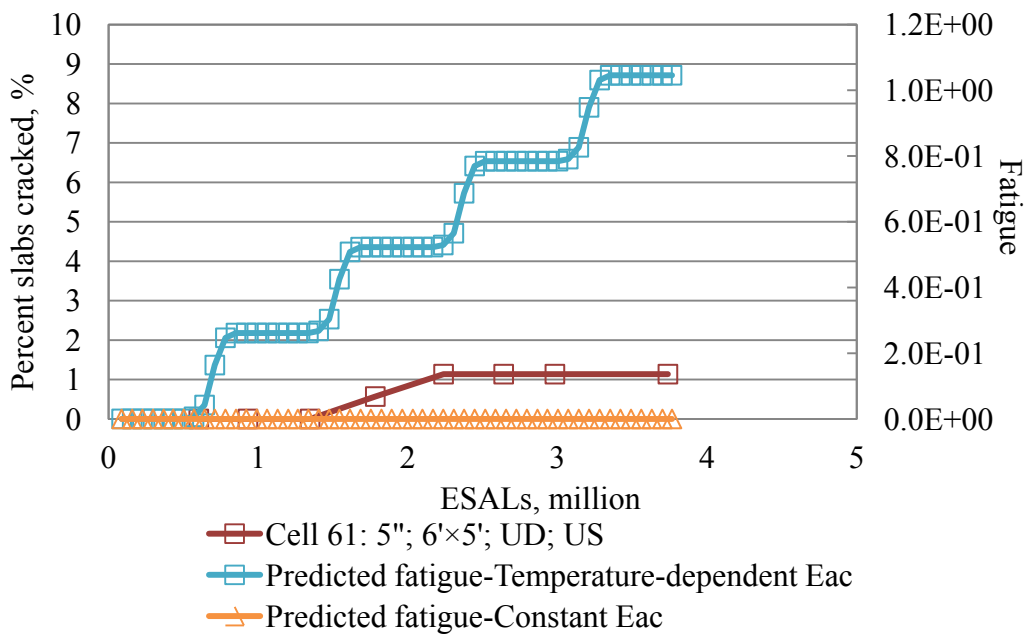


Figure 57. Observed transverse cracking vs. fatigue damage predicted for Cell 61 using the ICT method.

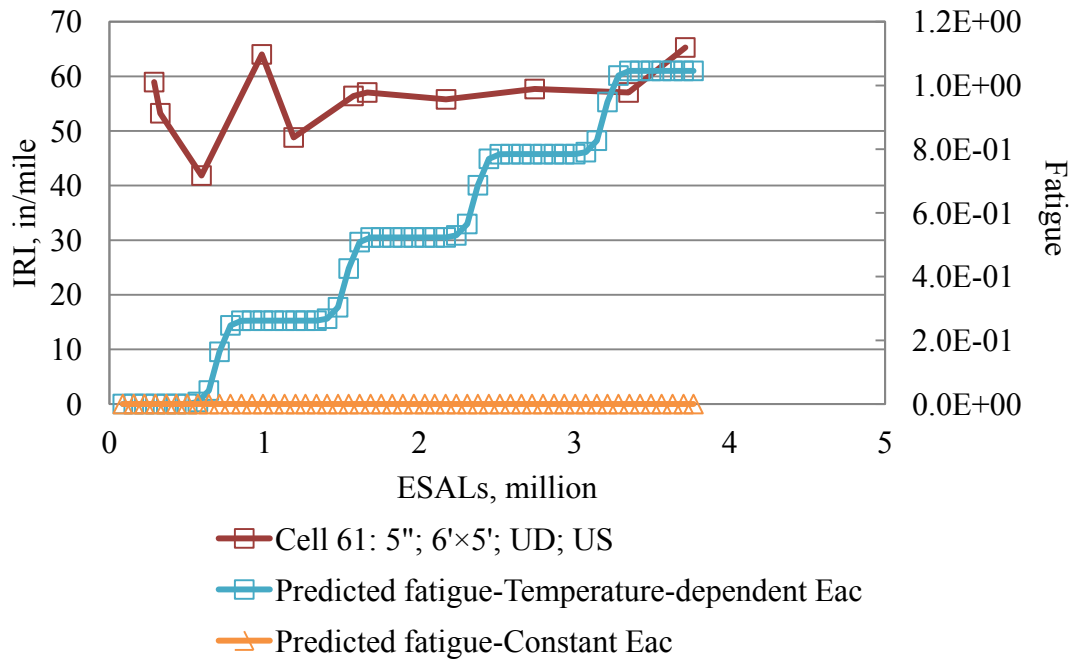


Figure 58. Observed IRI vs. fatigue damage predicted for Cell 61 using the ICT method.

Table 24. Fatigue summary for Cell 62 using the ICT method.

| Date | Constant E_{HMA} | Temperature-dependent E_{HMA} |
|--------|--------------------|---------------------------------|
| Dec-04 | 8.0E-14 | 1.7E-06 |
| Dec-05 | 8.9E-13 | 6.3E-02 |
| Dec-06 | 2.8E-12 | 1.3E-01 |
| Dec-07 | 5.7E-12 | 1.9E-01 |
| Dec-08 | 9.7E-12 | 2.5E-01 |

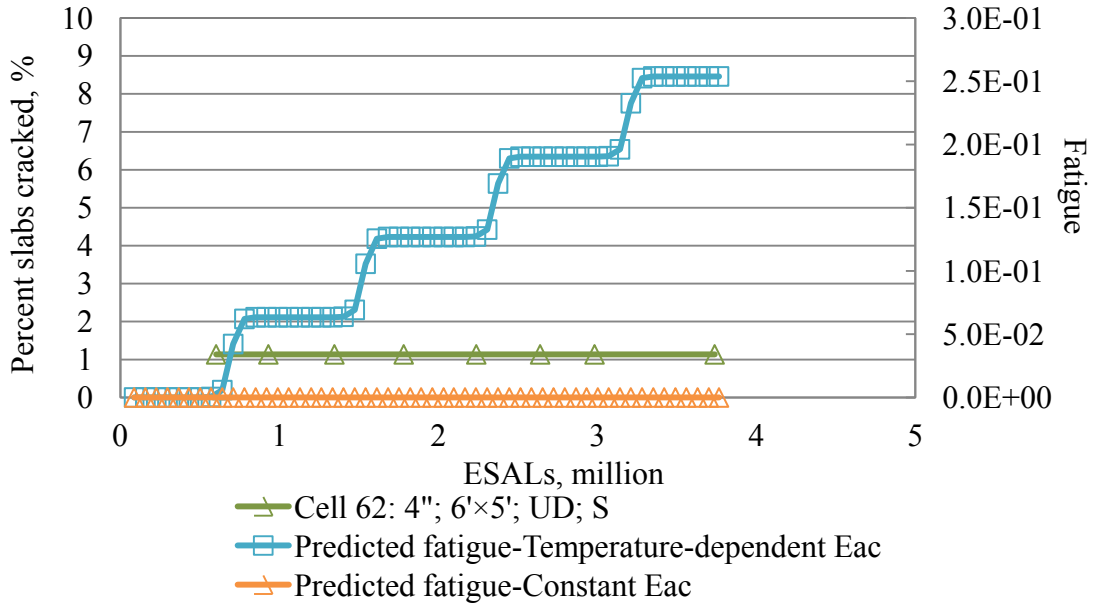


Figure 59. Observed transverse cracking vs. fatigue damage predicted for Cell 62 using the ICT method.

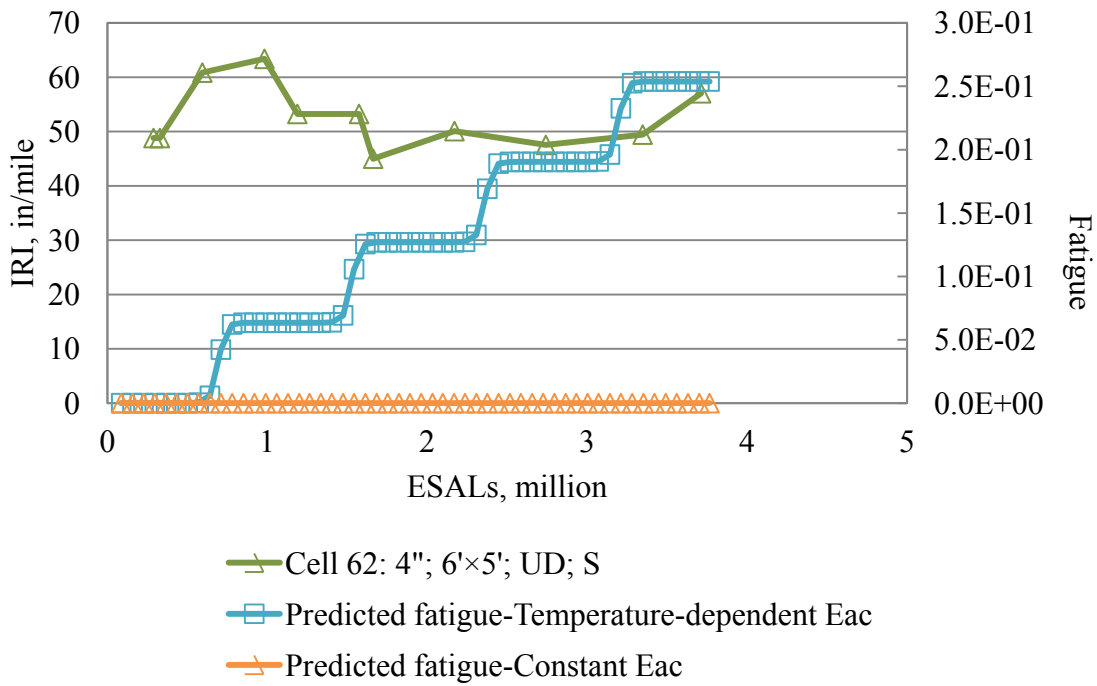


Figure 60. Observed IRI vs. fatigue damage predicted for Cell 62 using the ICT method.

Table 25. Fatigue summary for Cell 63 using the ICT method.

| Date | Constant E_{HMA} | Temperature-dependent E_{HMA} |
|--------|--------------------|---------------------------------|
| Dec-04 | 1.1E-12 | 1.4E-05 |
| Dec-05 | 1.2E-11 | 2.0E-01 |
| Dec-06 | 3.9E-11 | 4.1E-01 |
| Dec-07 | 7.9E-11 | 6.1E-01 |
| Dec-08 | 1.3E-10 | 8.1E-01 |

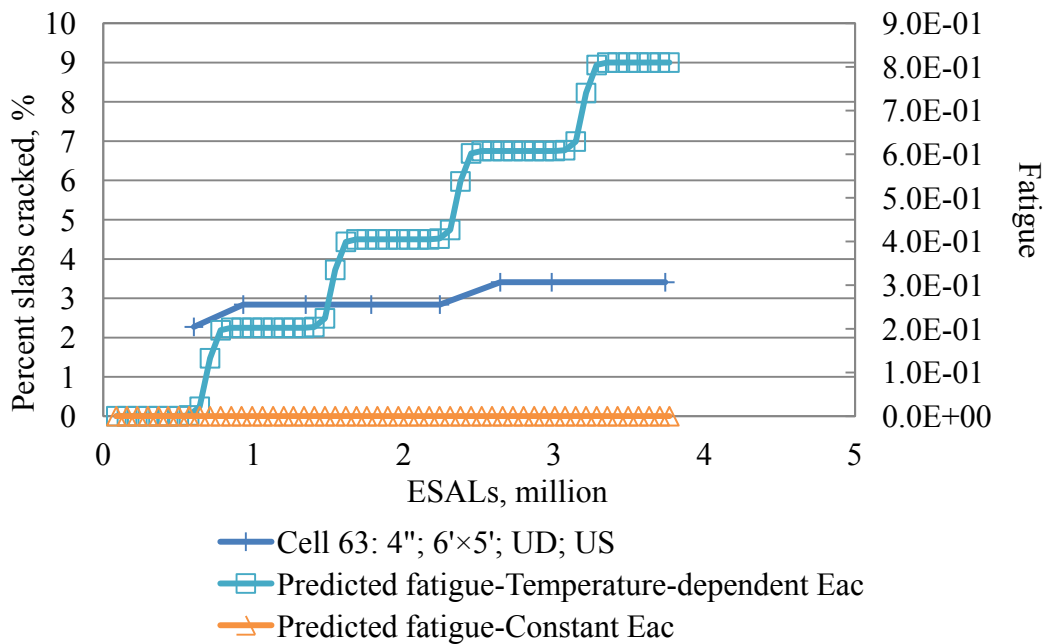


Figure 61. Observed transverse cracking vs. fatigue damage predicted for Cell 63 using the ICT method.

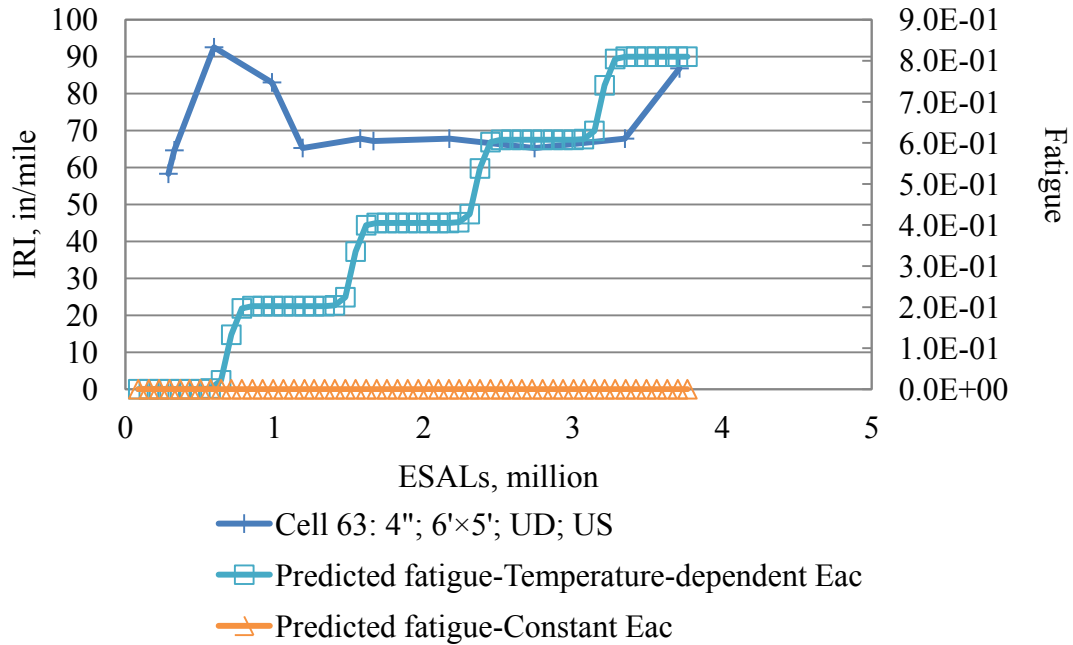


Figure 62. Observed IRI vs. fatigue damage predicted for Cell 63 using the ICT method.

Table 26. Fatigue summary for Cell 92 using the ICT method.

| Date | Constant E_{HMA} | Temperature-dependent E_{HMA} |
|--------|--------------------|---------------------------------|
| Dec-97 | 1.8E-12 | 9.2E-06 |
| Dec-98 | 1.8E-12 | 2.0E-05 |
| Dec-99 | 1.8E-12 | 3.0E-05 |
| Dec-00 | 1.8E-12 | 4.1E-05 |
| Dec-01 | 1.8E-12 | 5.1E-05 |
| Dec-02 | 1.8E-12 | 6.1E-05 |
| Dec-03 | 1.8E-12 | 7.2E-05 |
| Dec-04 | 1.8E-12 | 8.2E-05 |
| Dec-05 | 1.8E-12 | 9.3E-05 |
| Dec-06 | 1.8E-12 | 1.0E-04 |
| Dec-07 | 1.8E-12 | 1.1E-04 |
| Dec-08 | 1.8E-12 | 1.2E-04 |

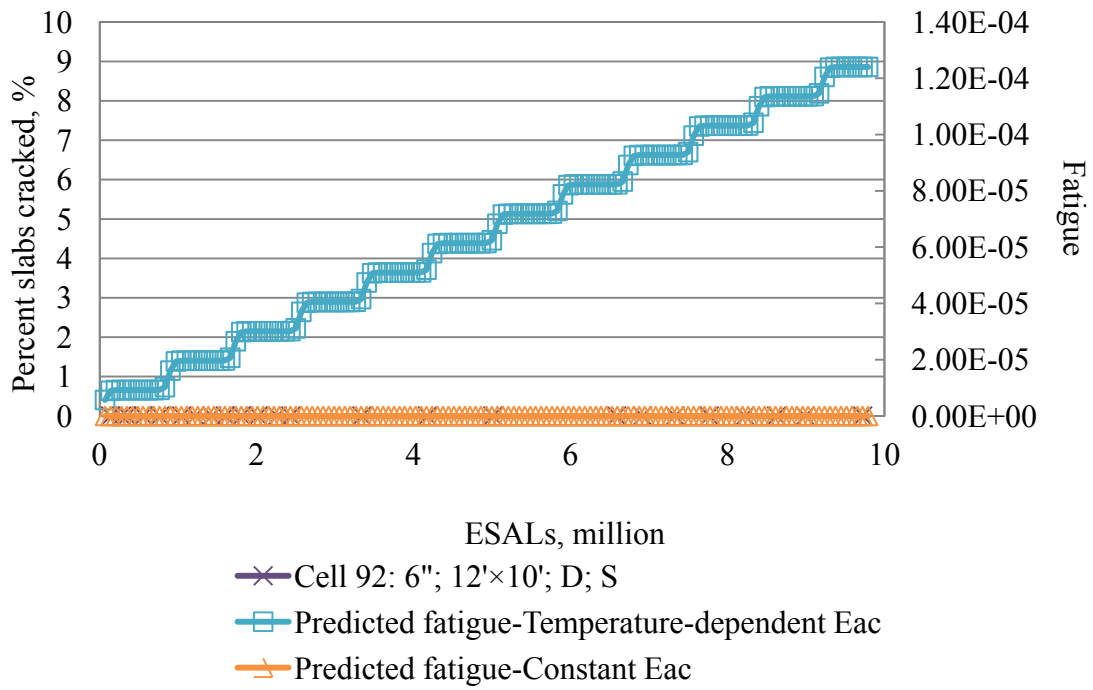


Figure 63. Observed transverse cracking vs. fatigue damage predicted for Cell 92 using the ICT method.

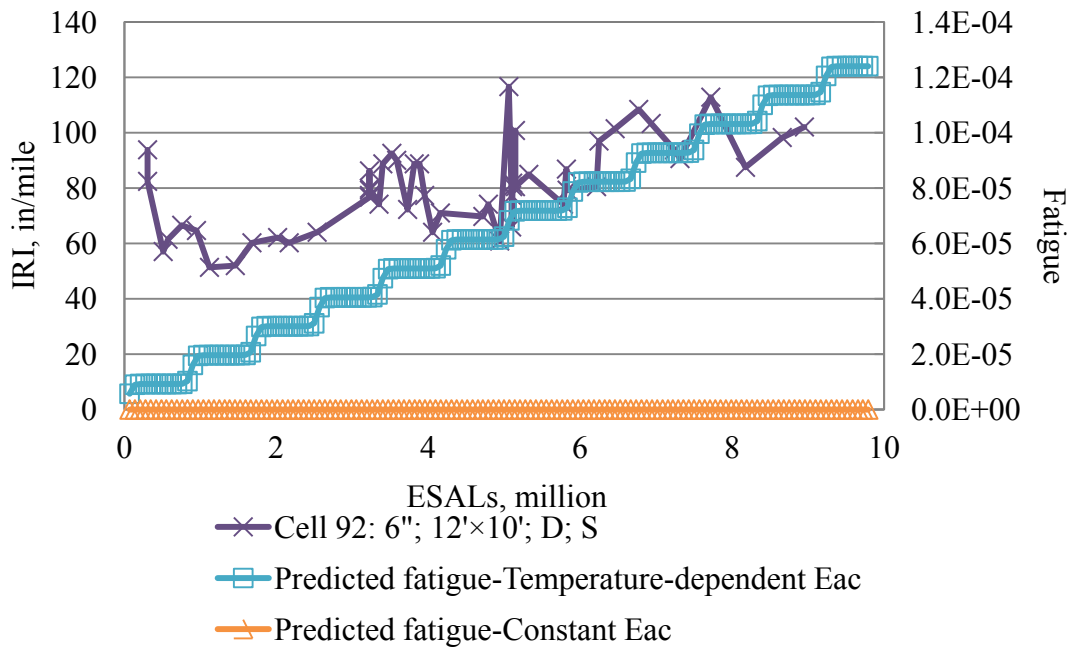


Figure 64. Observed IRI vs. fatigue damage predicted for Cell 92 using the ICT method.

Table 27. Fatigue summary for Cell 93 using the ICT method.

| Date | Constant E_{HMA} | Temperature-dependent E_{HMA} |
|--------|--------------------|---------------------------------|
| Dec-97 | 5.0E-37 | 1.7E-18 |
| Dec-98 | 5.0E-37 | 4.5E-18 |
| Dec-99 | 5.0E-37 | 7.4E-18 |
| Dec-00 | 6.4E-38 | 1.0E-17 |
| Dec-01 | 5.0E-37 | 1.3E-17 |
| Dec-02 | 5.0E-37 | 1.6E-17 |
| Dec-03 | 5.0E-37 | 1.9E-17 |

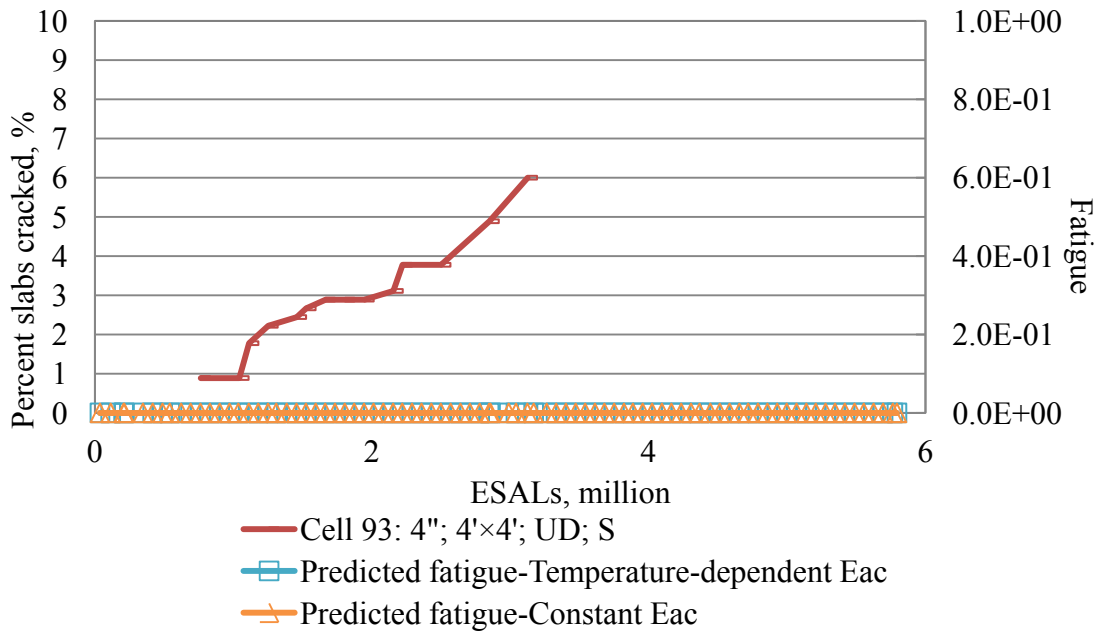


Figure 65. Observed transverse cracking vs. fatigue damage predicted for Cell 93 using the ICT method.

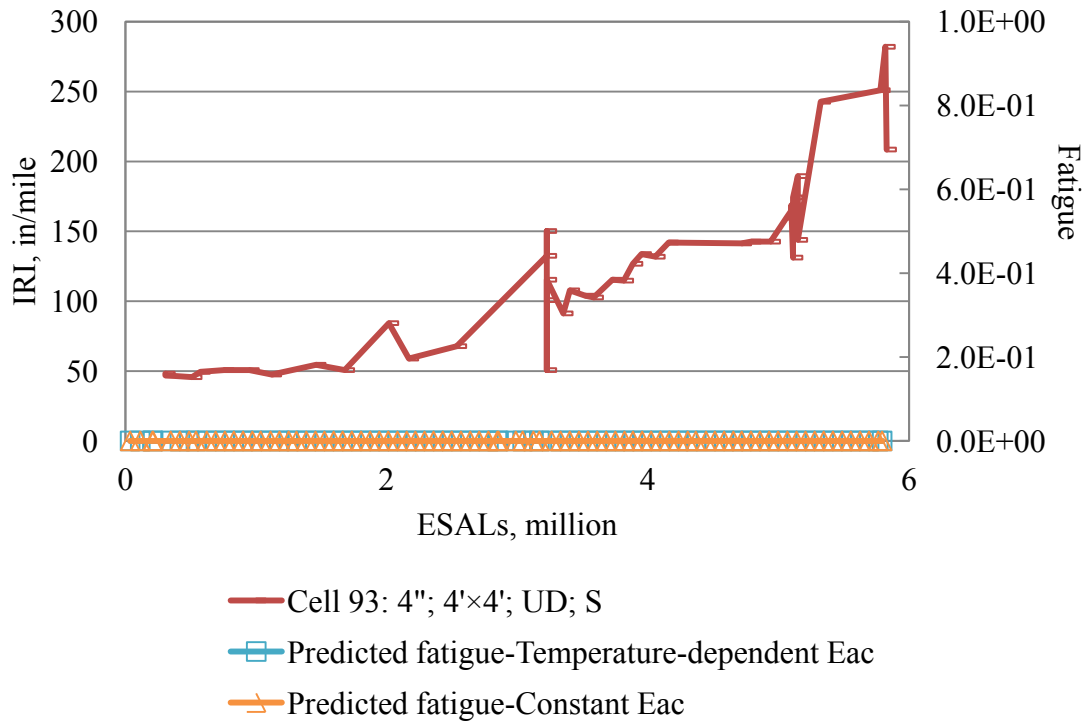


Figure 66. Observed IRI vs. fatigue damage predicted for Cell 93 using the ICT method.

Table 28. Fatigue summary for Cell 94 using the ICT method.

| Date | Constant E_{HMA} | Temperature-dependent E_{HMA} |
|--------|--------------------|---------------------------------|
| Dec-97 | 7.4E-40 | 1.5E-17 |
| Dec-98 | 7.4E-40 | 4.1E-17 |
| Dec-99 | 7.4E-40 | 6.8E-17 |
| Dec-00 | 9.6E-41 | 9.5E-17 |
| Dec-01 | 7.4E-40 | 1.2E-16 |
| Dec-02 | 7.4E-40 | 1.5E-16 |
| Dec-03 | 7.4E-40 | 1.7E-16 |

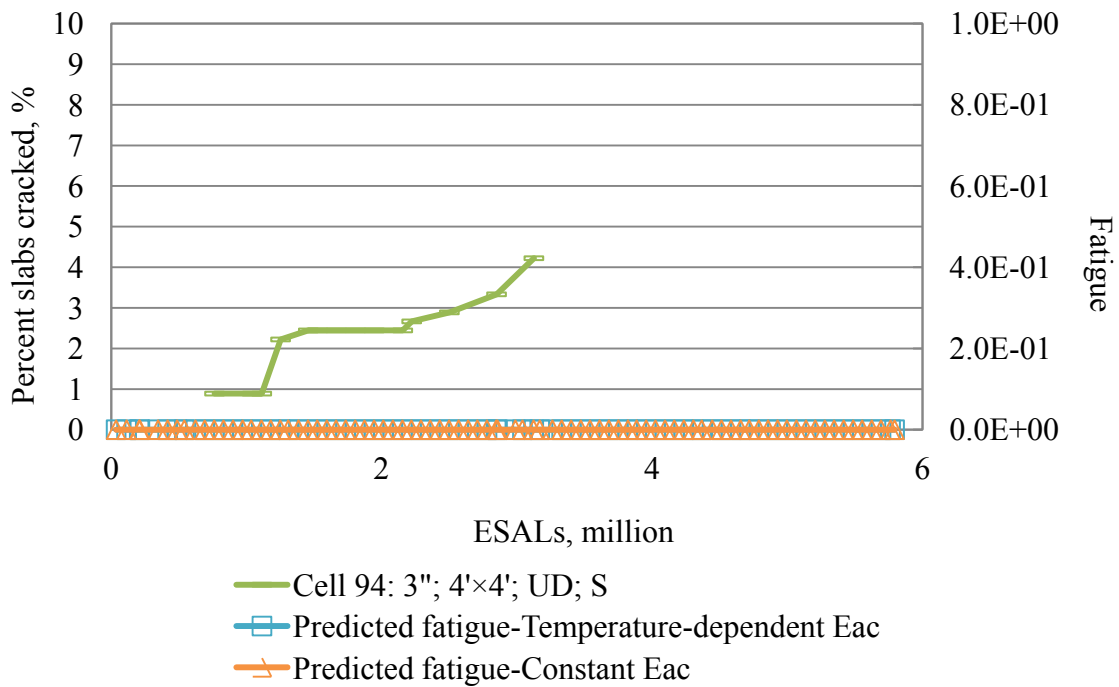


Figure 67. Observed transverse cracking vs. fatigue damage predicted for Cell 94 using the ICT method.

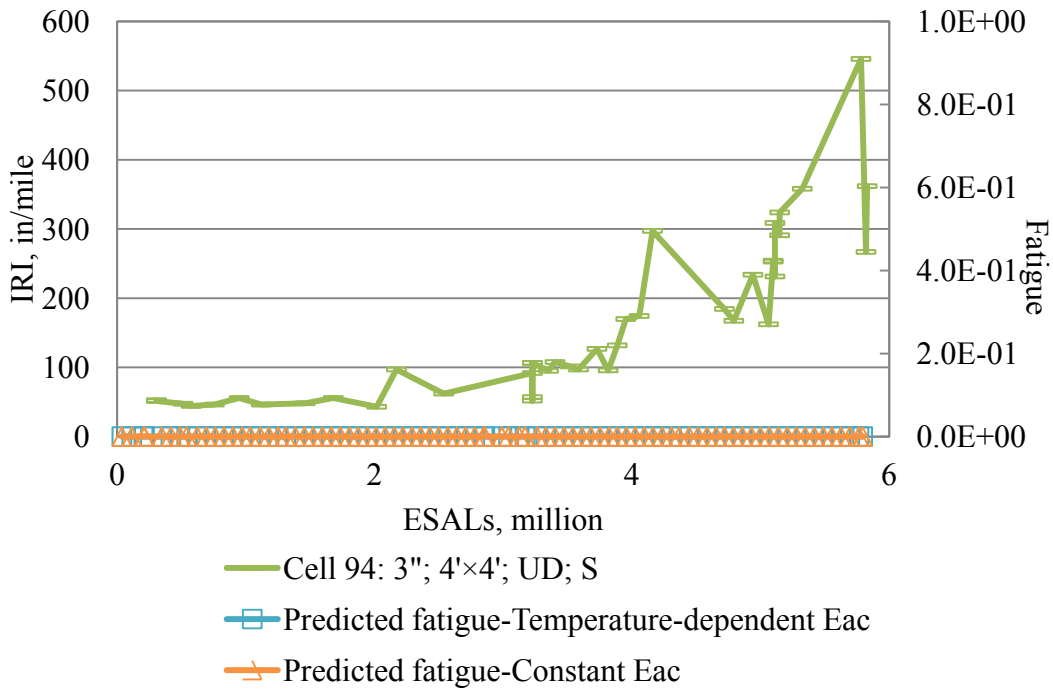


Figure 68. Observed IRI vs. fatigue damage predicted for Cell 94 using the ICT method.

Table 29. Fatigue summary for Cell 95 using the ICT method.

| Date | Constant E_{HMA} | Temperature-dependent E_{HMA} |
|--------|--------------------|---------------------------------|
| Dec-97 | 8.8E-30 | 2.3E-11 |
| Dec-98 | 8.8E-30 | 6.1E-11 |
| Dec-99 | 8.8E-30 | 9.9E-11 |
| Dec-00 | 1.1E-30 | 1.4E-10 |
| Dec-01 | 8.8E-30 | 1.8E-10 |
| Dec-02 | 8.8E-30 | 2.1E-10 |
| Dec-03 | 8.8E-30 | 2.5E-10 |

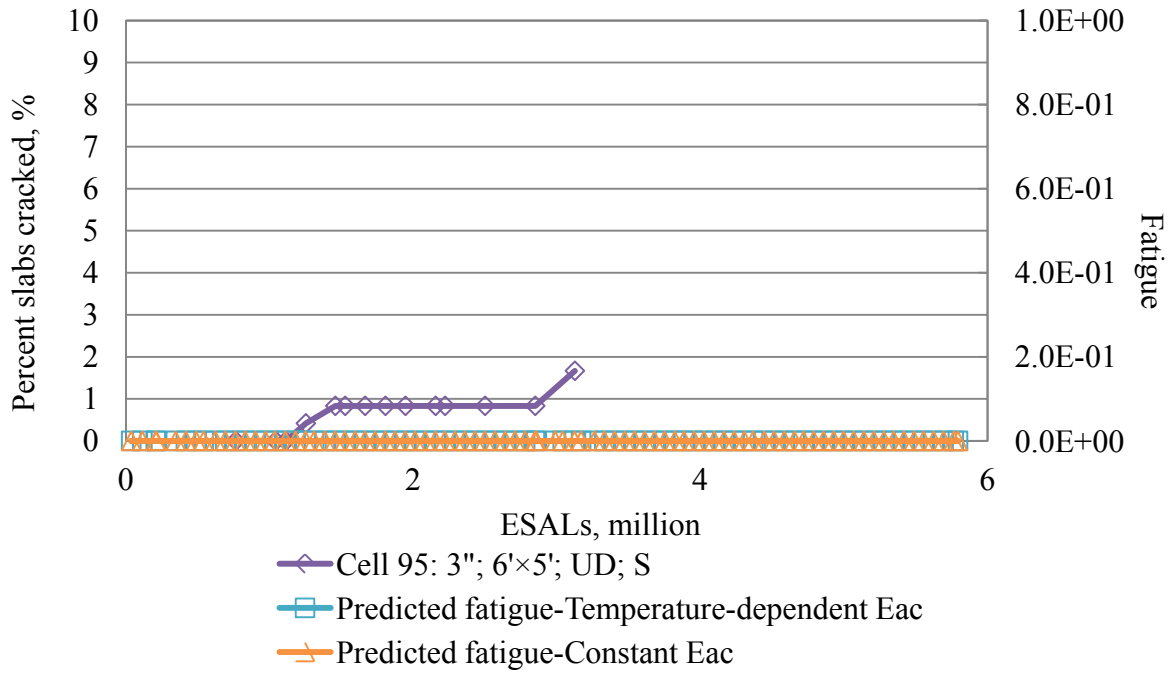


Figure 69. Observed transverse cracking vs. fatigue damage predicted for Cell 95 using the ICT method.

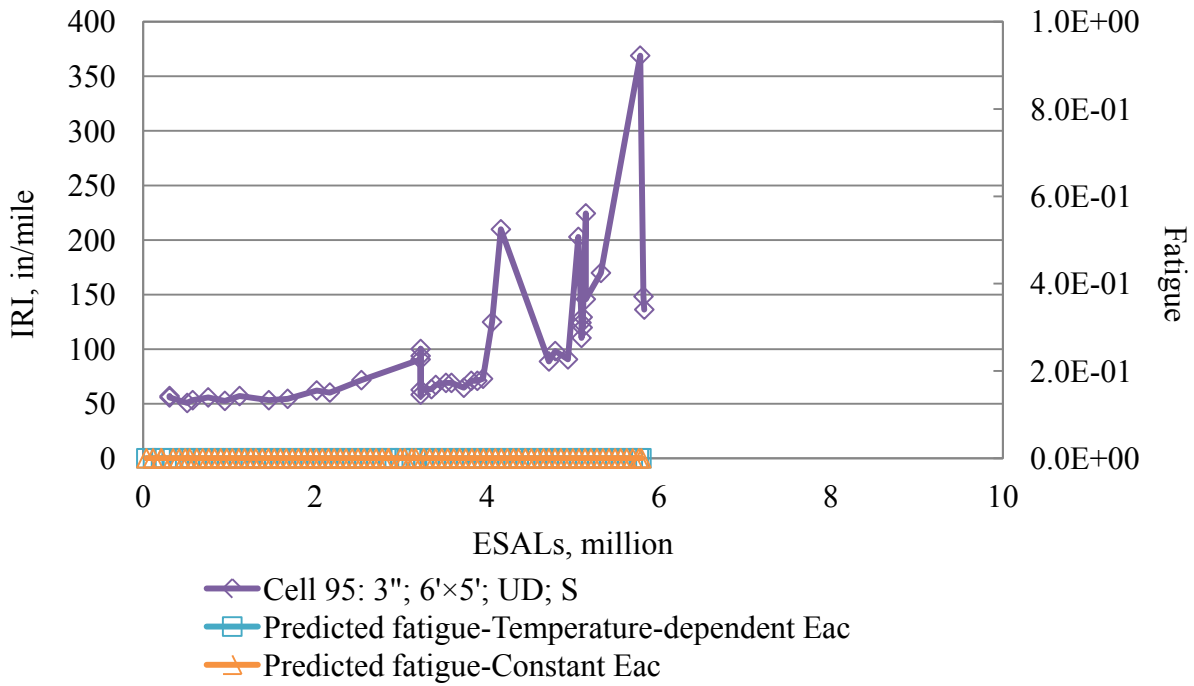


Figure 70. Observed IRI vs. fatigue damage predicted for Cell 95 using the ICT method.

Table 30. Fatigue summary for Cell 96 using the ICT method.

| Date | Constant E_{HMA} | Temperature-dependent E_{HMA} |
|--------|--------------------|---------------------------------|
| Dec-97 | 9.2E-27 | 1.0E-16 |
| Dec-98 | 2.3E-26 | 1.2E-15 |
| Dec-99 | 3.9E-26 | 3.3E-15 |
| Dec-00 | 5.5E-26 | 6.5E-15 |
| Dec-01 | 7.0E-26 | 1.1E-14 |
| Dec-02 | 8.6E-26 | 1.6E-14 |
| Dec-03 | 1.0E-25 | 2.2E-14 |
| Dec-04 | 1.2E-25 | 2.9E-14 |
| Dec-05 | 1.3E-25 | 3.7E-14 |
| Dec-06 | 1.5E-25 | 4.6E-14 |
| Dec-07 | 1.6E-25 | 5.7E-14 |
| Dec-08 | 1.8E-25 | 6.8E-14 |

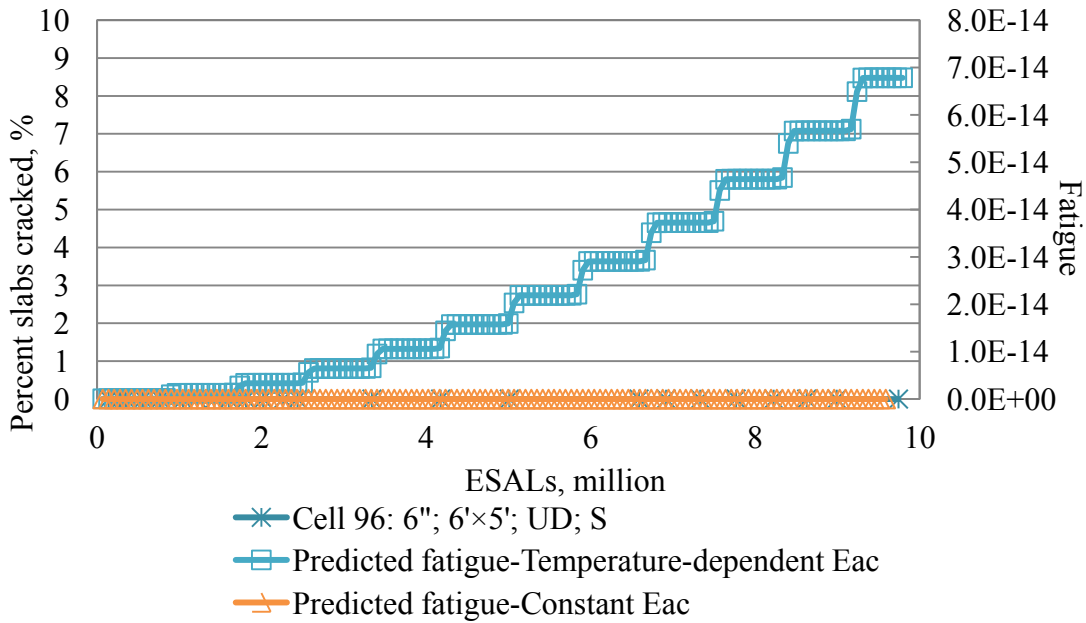


Figure 71. Observed transverse cracking vs. fatigue damage predicted for Cell 96 using the ICT method.

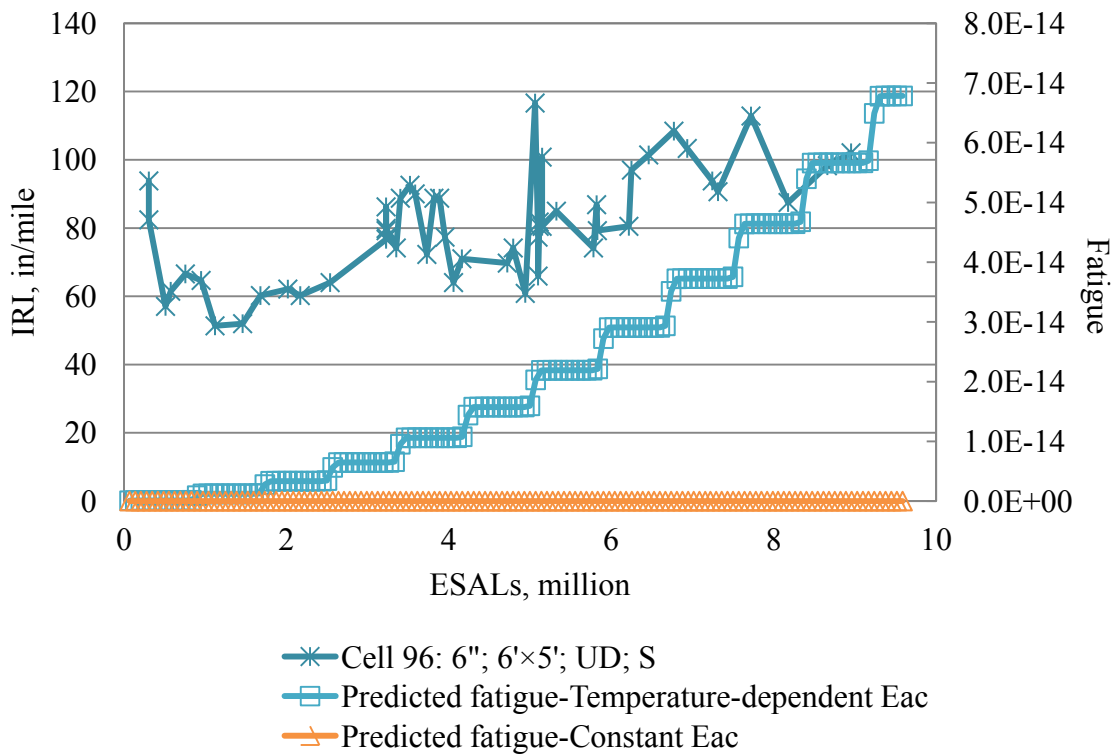


Figure 72. Observed IRI vs. fatigue damage predicted for Cell 96 using the ICT method.

Table 31. Fatigue summary for Cell 97 using the ICT method.

| Date | Constant E_{HMA} | Temperature-dependent E_{HMA} |
|--------|--------------------|---------------------------------|
| Dec-97 | 1.8E-12 | 9.2E-06 |
| Dec-98 | 1.8E-12 | 2.0E-05 |
| Dec-99 | 1.8E-12 | 3.0E-05 |
| Dec-00 | 1.8E-12 | 4.1E-05 |
| Dec-01 | 1.8E-12 | 5.1E-05 |
| Dec-02 | 1.8E-12 | 6.1E-05 |
| Dec-03 | 1.8E-12 | 7.2E-05 |
| Dec-04 | 1.8E-12 | 8.2E-05 |
| Dec-05 | 1.8E-12 | 9.3E-05 |
| Dec-06 | 1.8E-12 | 1.0E-04 |
| Dec-07 | 1.8E-12 | 1.1E-04 |
| Dec-08 | 1.8E-12 | 1.2E-04 |

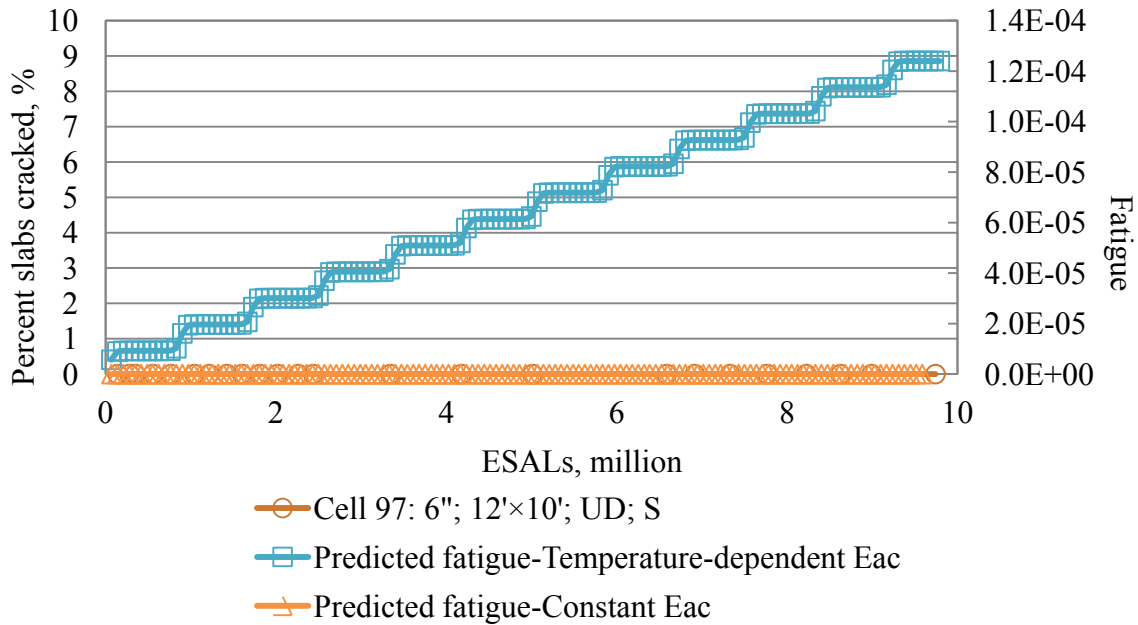


Figure 73. Observed transverse cracking vs. fatigue damage predicted for Cell 97 using the ICT method.

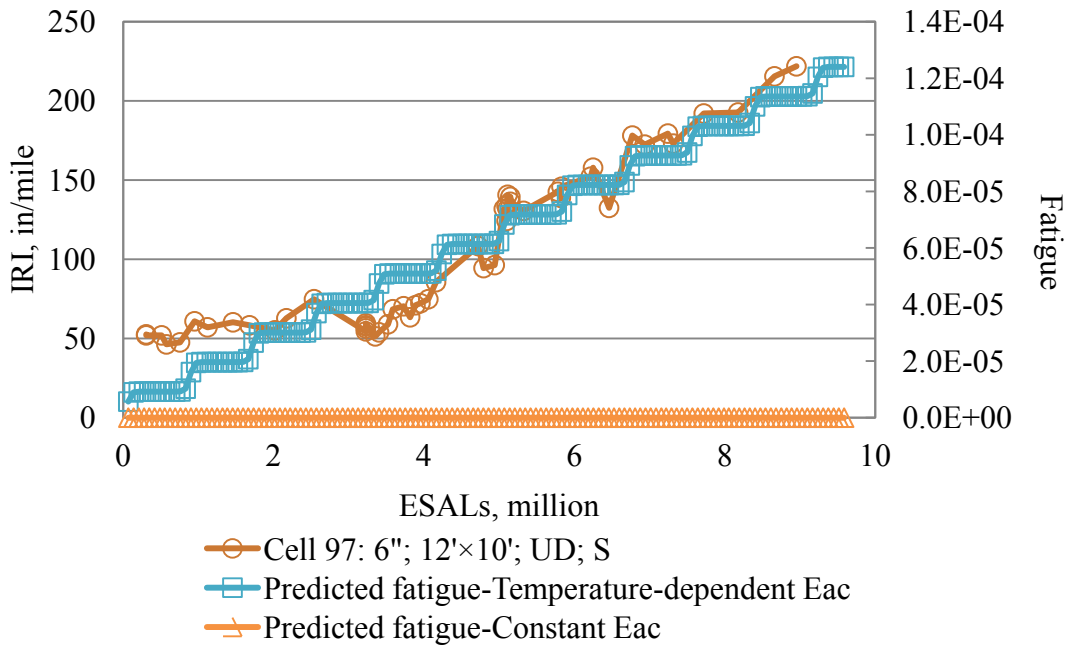


Figure 74. Observed IRI vs. fatigue damage predicted for Cell 97 using the ICT method.

3.3.1 Conclusion for the ICT evaluation

Small fatigue predictions are yielded using the ICT method, especially when the concrete modulus of rupture is high. Other than the concrete modulus of rupture, the ICT method is also sensitive to slab thickness. Comparing the predictions for Cells 60, 61, 62 and 63, reducing the slab thickness by 1 in can result in ten times more fatigue damage. The significance of slab length on predictions seems to be even greater based on the comparison between Cell 92 and Cells 93 to 96. However, this significance cannot be found from the comparison between Cells 93 and 94 (48-in slabs) and Cells 95 and 96 (72-in slabs). This indicates that the use of the ICT structural model might be more appropriate for smaller whitetopping slabs.

The monthly asphalt modulus of elasticity only results in 20 to 30 percent variation in stress predictions. However, it yields thousands of times difference in terms of fatigue predictions. It can be anticipated that the effect of a temperature-dependent asphalt modulus of elasticity would be even greater if the partial interface bonding is taken into account.

3.4 Evaluation of the PCA method

In the PCA method, the fatigue analysis is carried out for each type of axle load. The axle load spectrum used by Vandebossche et al. (2008) in their analysis on MnROAD mainline cells is borrowed and the traffic is adjusted so that the calculated ESALs by the Mechanistic-Empirical Pavement Design Guide (MEPDG) (ARA, 2004) is 0.8 million in 1998 which agrees with the observed ESALs. The axle load repetitions in 1998 are presented for single and tandem axles in Table A1 and Table A2 in the appendix, respectively. Since the accumulated ESALs on MnROAD show a linear trend, it is considered to be appropriate to apply the same axle load repetitions to each year.

The predicted fatigue for Cell 60 is presented in Table 32, where it is found to be lower using a constant asphalt modulus of elasticity than using a temperature-dependent asphalt modulus of elasticity, especially in terms of PCC fatigue. The comparisons between the fatigue predictions and observed transverse cracking and IRIs can be found in Figure 75 and Figure 76, respectively.

It is interesting to see a much larger PCC fatigue predicted by the PCA method than the ICT method. Both methods use almost the same equation, i.e. Equations (35) and (42), to determine stresses in the concrete overlay under 18-kip single axle loading. The stresses for Cell 60 due to an 18-kip single axle loading are 171 psi and 194 psi using PCA and ICT methods, respectively. After considering the temperature-induced stresses, the total stresses using the two methods become 179 psi and 231 psi, respectively. Furthermore, the PCA fatigue model tends to yield more allowable load repetitions than the ACPA model, as shown in Figure 9. It seems that the PCA method would tend to yield smaller PCC predictions. However, it should be noted that the critical stresses in yielding the PCC fatigue damage are not those due to 18-kip single axle loads. The stresses due to other axle loads in the PCA method are interpolated based on the 18-kip and 36-kip stresses for single axles and tandem axles, respectively. As a result, a small increase in the axle load would lead to a large increase in the predicted allowable load repetitions, which can be seen in Table 33 where the stresses are predicted for three tandem axle loads using a constant asphalt modulus of elasticity. This conclusion is further supported by the finding that the majority of the predicted PCC fatigue is caused by tandem axle loads in the summer, as shown in Table 34 where the predicted PCC fatigue is broken down monthly for single and tandem axle loadings using a temperature-dependent asphalt modulus of elasticity. The rapid increase of fatigue damage during the summer can also be seen in Figure 75 and Figure 76, where, 0.7 to 1.0 million ESALs correspond to June through September.

Regarding the HMA fatigue, no significant difference can be found between predictions using the two types of elastic moduli. This might indicate that the asphalt modulus of elasticity determined based on the monthly average temperature is a fair approximation to the temperature-dependent modulus in terms of HMA fatigue predictions using the PCA method.

The results for the other cells are presented in Table 35 to Table 43 and Figure 77 to Figure 94. In general, the PCA method predicts much lower, but more constant HMA fatigue damage.

It is also interesting to see that the fatigue of the HMA dominates when the concrete modulus of rupture is very high for Cells 92 to 97 and thus the predicted PCC fatigue becomes very low.

Table 32. Fatigue summary for Cell 60 using the PCA method.

| Date | Constant E_{HMA} | | Temperature-dependent E_{HMA} | |
|--------|--------------------|---------|---------------------------------|---------|
| | HMA | PCC | HMA | PCC |
| Dec-04 | 4.0E-02 | 5.9E-01 | 5.0E-02 | 2.4E+02 |
| Dec-05 | 1.3E-01 | 2.5E+00 | 1.6E-01 | 4.7E+02 |
| Dec-06 | 2.2E-01 | 4.4E+00 | 2.6E-01 | 7.1E+02 |
| Dec-07 | 3.1E-01 | 6.3E+00 | 3.7E-01 | 9.5E+02 |
| Dec-08 | 4.0E-01 | 8.2E+00 | 4.7E-01 | 1.2E+03 |

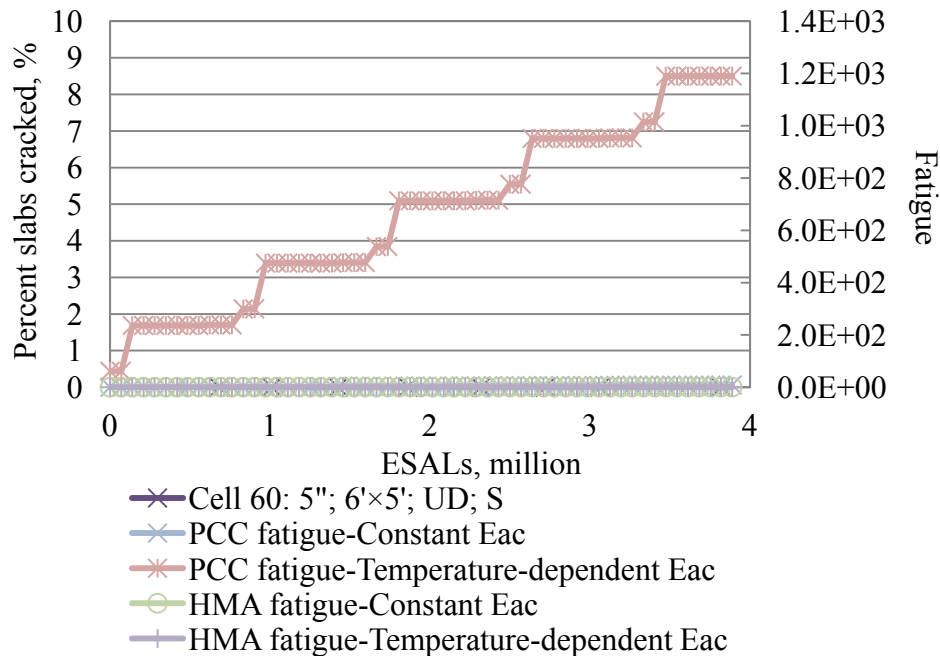


Figure 75. Observed transverse cracking vs. fatigue damage predicted for Cell 60 using the PCA method.

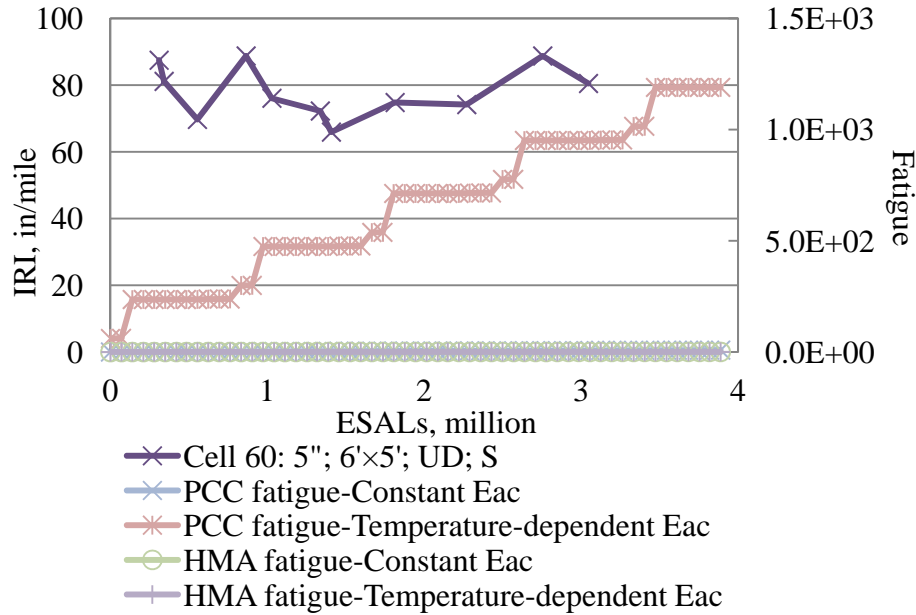


Figure 76. Observed IRI vs. fatigue damage predicted for Cell 60 using the PCA method.

Table 33. Stress predictions for Cell 60 using the PCA method.

| Tandem axle load, kips | Stress, psi | Stress ratio | Allow repetitions |
|------------------------|-------------|--------------|-------------------|
| 36 | 254 | 0.43 | unlimited |
| 38 | 268 | 0.45 | 6.1E+07 |
| 40 | 282 | 0.47 | 4.0E+06 |

Table 34. PCC fatigue predictions based on temperature-dependent asphalt modulus of elasticity for Cell 60 using the PCA method.

| Month | Single axle | Tandem axle |
|-----------|-------------|-------------|
| January | 0.0E+00 | 2.7E-06 |
| February | 1.4E-06 | 5.9E-03 |
| March | 4.5E-05 | 4.2E-02 |
| April | 2.5E-03 | 2.1E+00 |
| May | 4.0E-06 | 8.4E-02 |
| June | 5.7E-06 | 1.3E-01 |
| July | 1.2E+01 | 4.9E+01 |
| August | 1.7E-04 | 3.8E-01 |
| September | 3.6E-03 | 1.7E+02 |
| October | 6.5E-06 | 1.6E-02 |
| November | 0.0E+00 | 8.4E-04 |
| December | 0.0E+00 | 1.0E-04 |

Table 35. Fatigue summary for Cell 61 using the PCA method.

| Date | Constant E_{HMA} | | Temperature-dependent E_{HMA} | |
|--------|--------------------|---------|---------------------------------|---------|
| | HMA | PCC | HMA | PCC |
| Dec-04 | 4.0E-02 | 6.8E+00 | 6.0E-02 | 5.9E+03 |
| Dec-05 | 1.4E-01 | 2.5E+01 | 1.6E-01 | 1.2E+04 |
| Dec-06 | 2.3E-01 | 4.3E+01 | 2.7E-01 | 1.8E+04 |
| Dec-07 | 3.2E-01 | 6.0E+01 | 3.8E-01 | 2.4E+04 |
| Dec-08 | 4.1E-01 | 7.8E+01 | 4.9E-01 | 2.9E+04 |

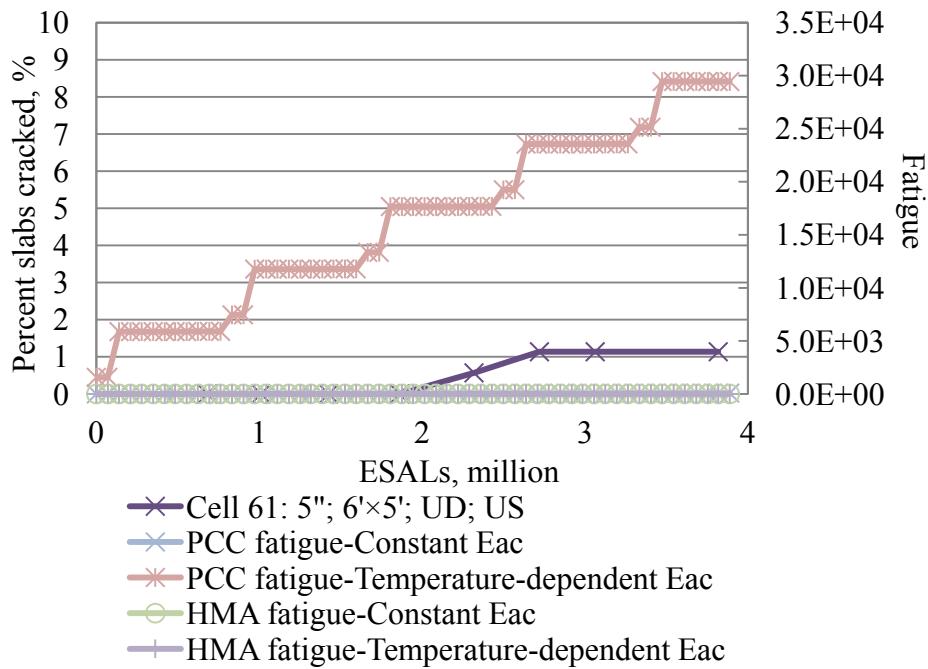


Figure 77. Observed transverse cracking vs. fatigue damage predicted for Cell 61 using the PCA method.

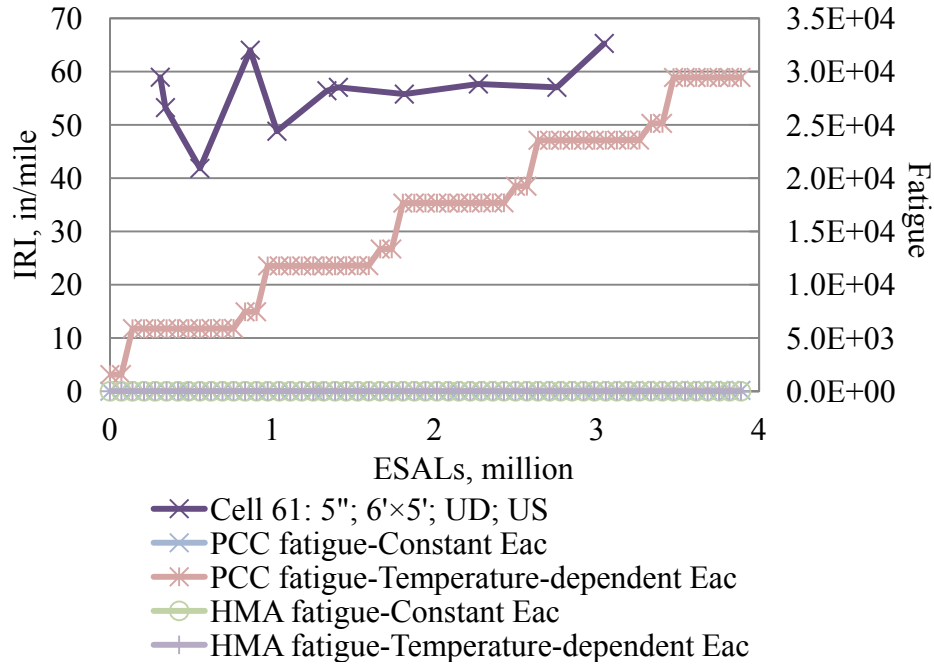


Figure 78. Observed IRI vs. fatigue damage predicted for Cell 61 using the PCA method.

Table 36. Fatigue summary for Cell 62 using the PCA method.

| Date | Constant E_{HMA} | | Temperature-dependent E_{HMA} | |
|--------|--------------------|---------|---------------------------------|---------|
| | HMA | PCC | HMA | PCC |
| Dec-04 | 5.0E-02 | 1.3E+00 | 8.0E-02 | 3.5E+03 |
| Dec-05 | 1.6E-01 | 5.1E+00 | 2.2E-01 | 7.1E+03 |
| Dec-06 | 2.7E-01 | 8.8E+00 | 3.7E-01 | 1.1E+04 |
| Dec-07 | 3.9E-01 | 1.3E+01 | 5.1E-01 | 1.4E+04 |
| Dec-08 | 5.0E-01 | 1.6E+01 | 6.5E-01 | 1.8E+04 |

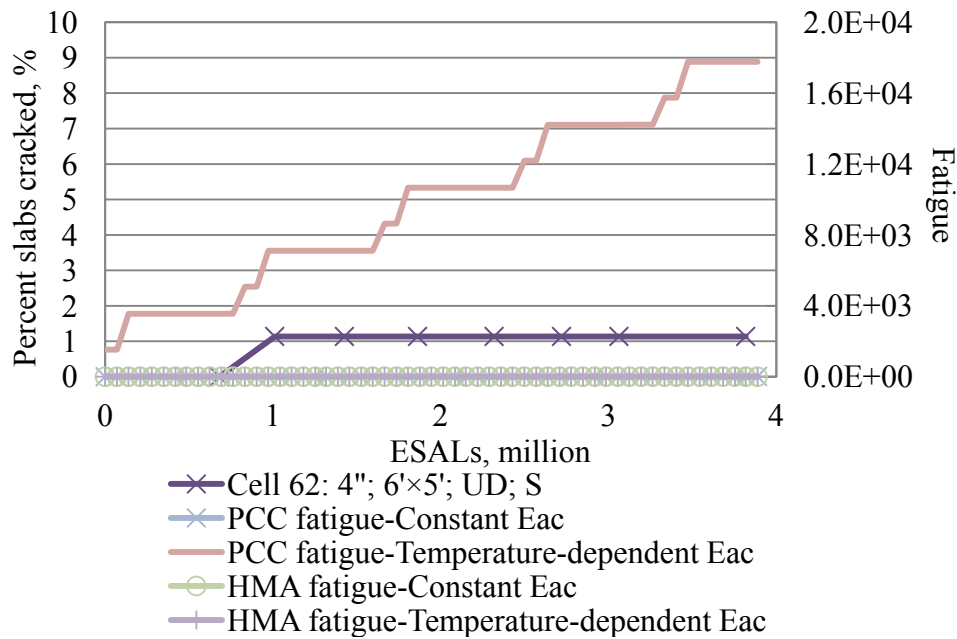


Figure 79. Observed transverse cracking vs. fatigue damage predicted for Cell 62 using the PCA method.

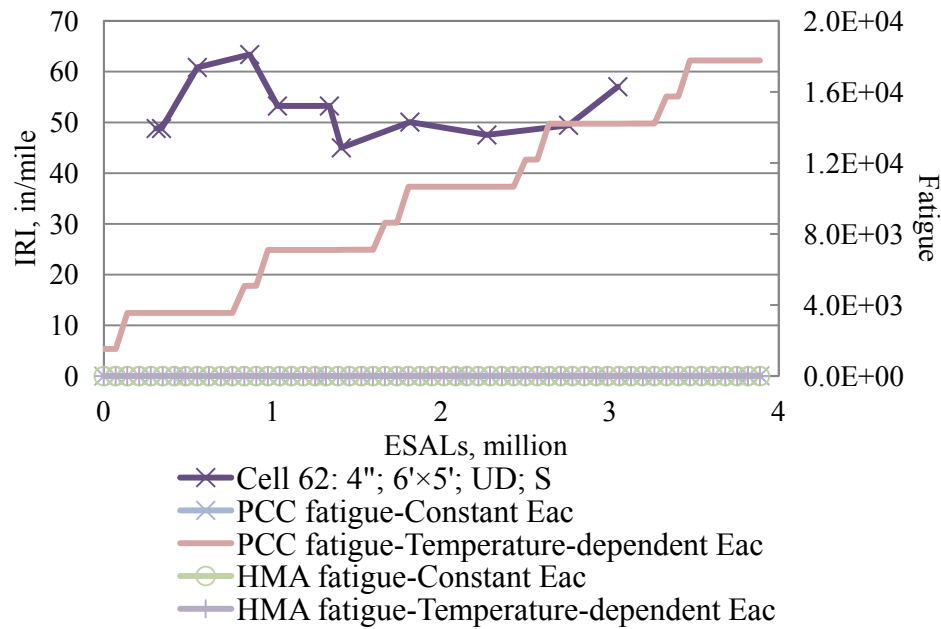


Figure 80. Observed IRI vs. fatigue damage predicted for Cell 62 using the PCA method.

Table 37. Fatigue summary for Cell 63 using the PCA method.

| Date | Constant E_{HMA} | | Temperature-dependent E_{HMA} | |
|--------|--------------------|---------|---------------------------------|---------|
| | HMA | PCC | HMA | PCC |
| Dec-04 | 5.0E-02 | 2.5E+00 | 8.0E-02 | 8.2E+03 |
| Dec-05 | 1.6E-01 | 9.3E+00 | 2.1E-01 | 1.6E+04 |
| Dec-06 | 2.6E-01 | 1.6E+01 | 3.5E-01 | 2.5E+04 |
| Dec-07 | 3.7E-01 | 2.3E+01 | 4.9E-01 | 3.3E+04 |
| Dec-08 | 4.8E-01 | 3.0E+01 | 6.3E-01 | 4.1E+04 |

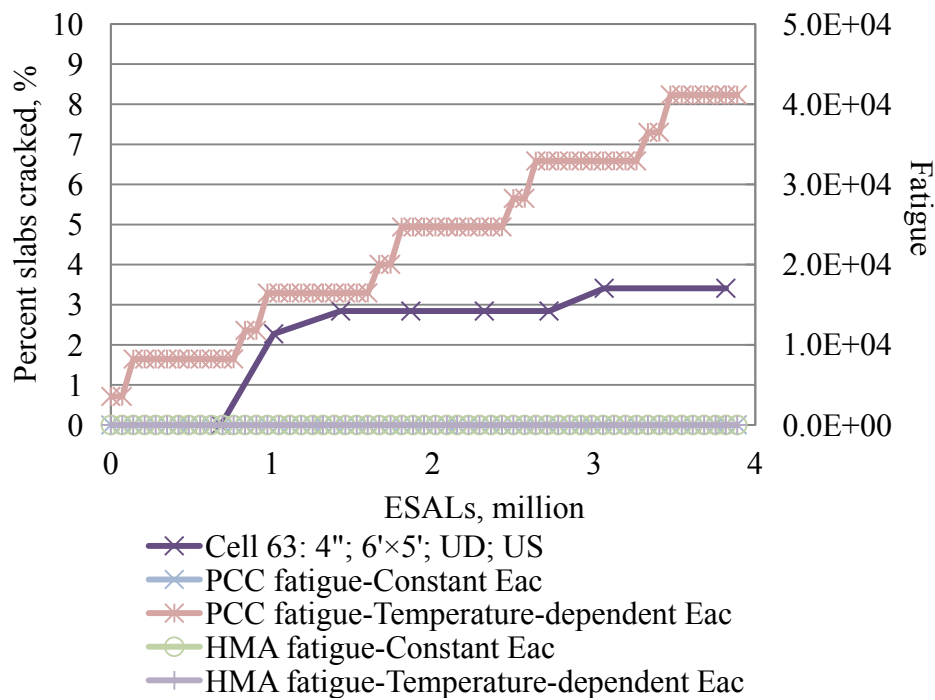


Figure 81. Observed transverse cracking vs. fatigue damage predicted for Cell 63 using the PCA method.

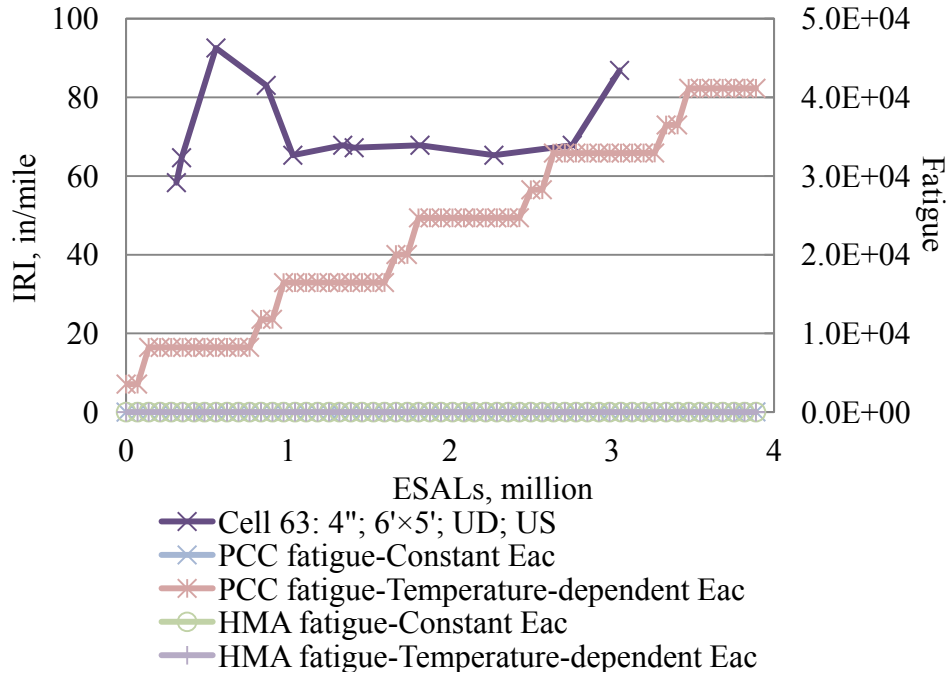


Figure 82. Observed IRI vs. fatigue damage predicted for Cell 63 using the PCA method.

Table 38. Fatigue summary for Cell 92 using the PCA method.

| Date | Constant E_{HMA} | | Temperature-dependent E_{HMA} | |
|--------|--------------------|---------|---------------------------------|---------|
| | HMA | PCC | HMA | PCC |
| Dec-97 | 1.0E-02 | 0.0E+00 | 2.0E-02 | 2.0E-02 |
| Dec-98 | 4.0E-02 | 0.0E+00 | 5.0E-02 | 4.0E-02 |
| Dec-99 | 7.0E-02 | 0.0E+00 | 9.0E-02 | 6.0E-02 |
| Dec-00 | 9.0E-02 | 0.0E+00 | 1.2E-01 | 8.0E-02 |
| Dec-01 | 1.2E-01 | 1.0E-02 | 1.6E-01 | 1.1E-01 |
| Dec-02 | 1.5E-01 | 1.0E-02 | 1.9E-01 | 1.3E-01 |
| Dec-03 | 1.7E-01 | 1.0E-02 | 2.2E-01 | 1.5E-01 |
| Dec-04 | 2.0E-01 | 1.0E-02 | 2.6E-01 | 1.7E-01 |
| Dec-05 | 2.2E-01 | 1.0E-02 | 2.9E-01 | 1.9E-01 |
| Dec-06 | 2.5E-01 | 1.0E-02 | 3.3E-01 | 2.1E-01 |
| Dec-07 | 2.8E-01 | 1.0E-02 | 3.6E-01 | 2.3E-01 |
| Dec-08 | 3.0E-01 | 1.0E-02 | 4.0E-01 | 2.6E-01 |

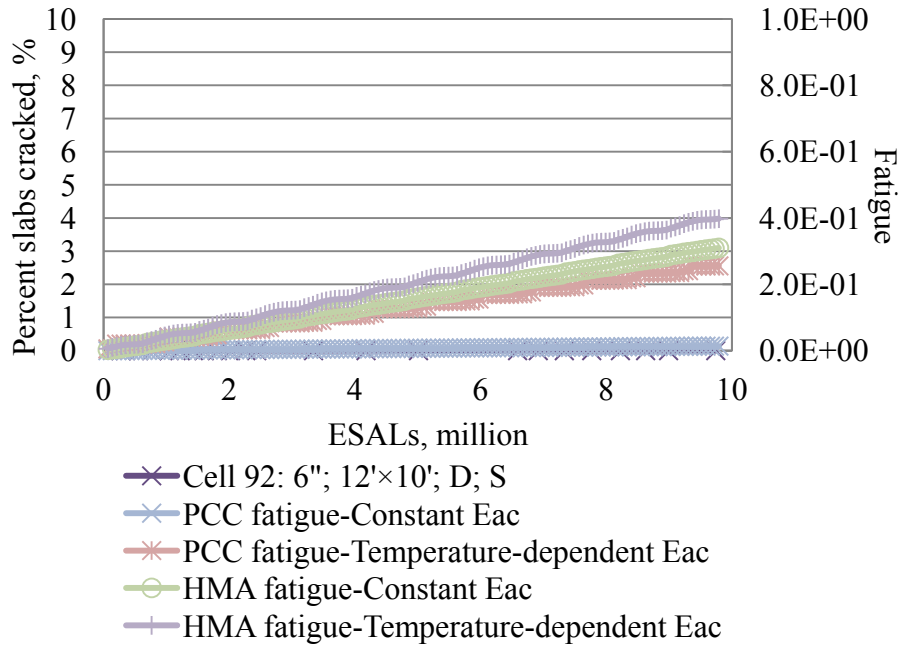


Figure 83. Observed transverse cracking vs. fatigue damage predicted for Cell 92 using the PCA method.

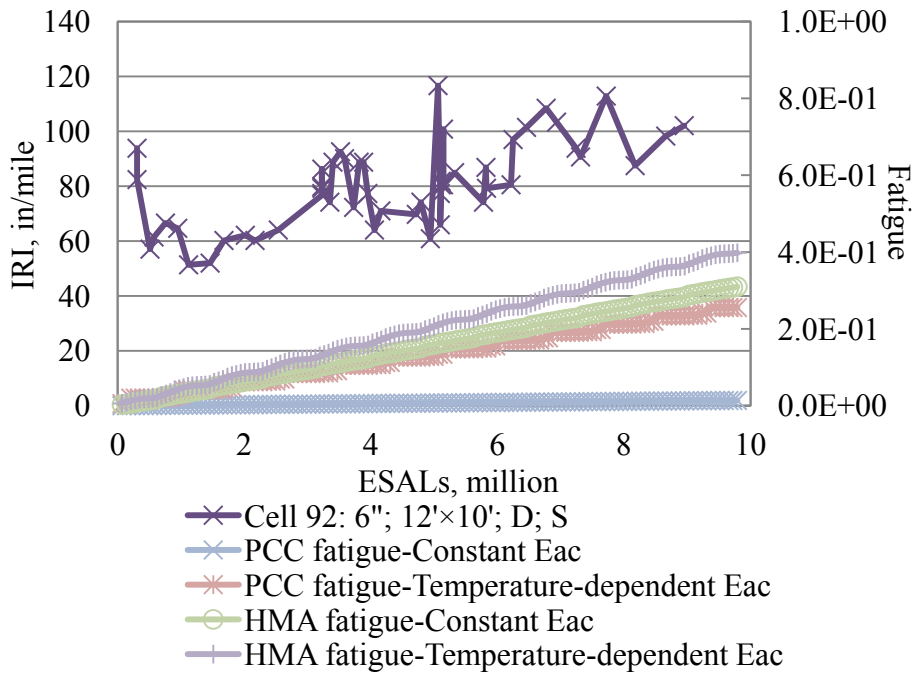


Figure 84. Observed IRI vs. fatigue damage predicted for Cell 92 using the PCA method.

Table 39. Fatigue summary for Cell 93 using the PCA method.

| Date | Constant E_{HMA} | | Temperature-dependent E_{HMA} | |
|--------|--------------------|---------|---------------------------------|---------|
| | HMA | PCC | HMA | PCC |
| Dec-97 | 1.0E-02 | 0.0E+00 | 2.0E-02 | 0.0E+00 |
| Dec-98 | 2.0E-02 | 0.0E+00 | 5.0E-02 | 0.0E+00 |
| Dec-99 | 4.0E-02 | 0.0E+00 | 7.0E-02 | 0.0E+00 |
| Dec-00 | 5.0E-02 | 0.0E+00 | 1.0E-01 | 0.0E+00 |
| Dec-01 | 7.0E-02 | 0.0E+00 | 1.3E-01 | 0.0E+00 |
| Dec-02 | 8.0E-02 | 0.0E+00 | 1.6E-01 | 0.0E+00 |
| Dec-03 | 1.0E-01 | 0.0E+00 | 1.9E-01 | 0.0E+00 |

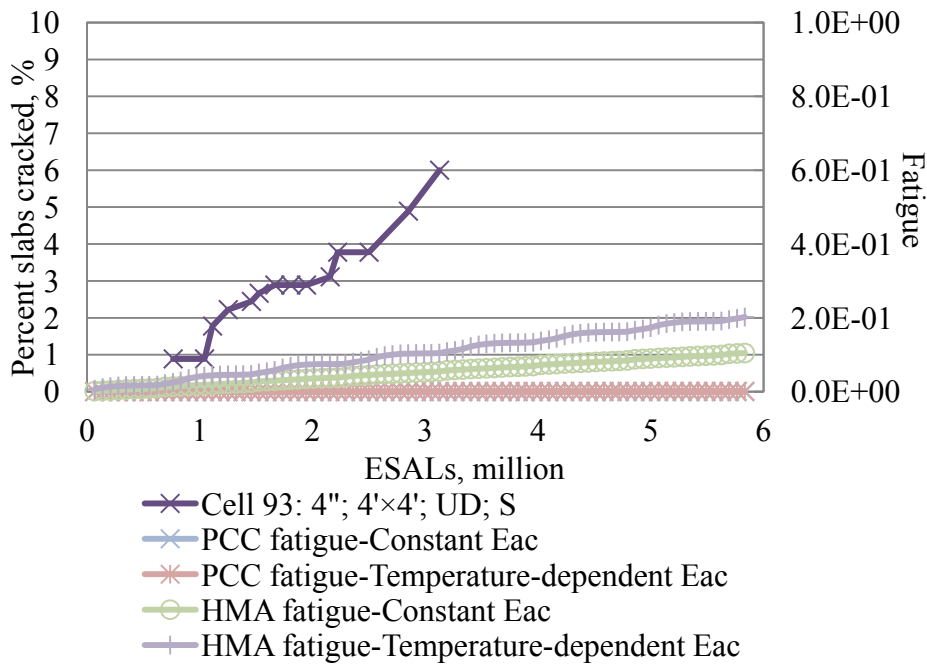


Figure 85. Observed transverse cracking vs. fatigue damage predicted for Cell 93 using the PCA method.

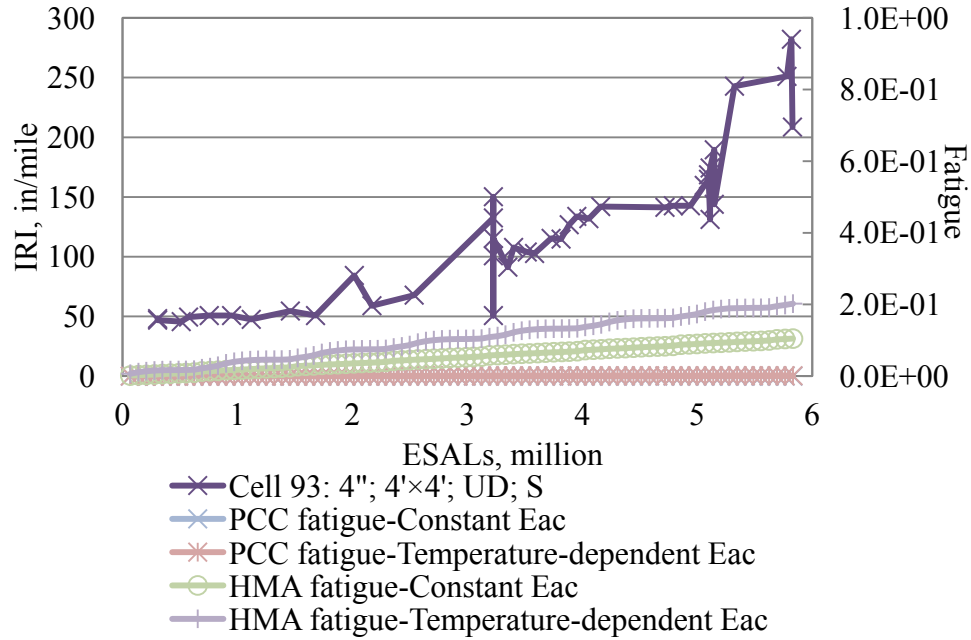


Figure 86. Observed IRI vs. fatigue damage predicted for Cell 93 using the PCA method.

Table 40. Fatigue summary for Cell 94 using the PCA method.

| Date | Constant E_{HMA} | | Temperature-dependent E_{HMA} | |
|--------|--------------------|---------|---------------------------------|---------|
| | HMA | PCC | HMA | PCC |
| Dec-97 | 1.0E-02 | 0.0E+00 | 2.0E-02 | 0.0E+00 |
| Dec-98 | 3.0E-02 | 0.0E+00 | 6.0E-02 | 0.0E+00 |
| Dec-99 | 5.0E-02 | 0.0E+00 | 1.0E-01 | 0.0E+00 |
| Dec-00 | 7.0E-02 | 0.0E+00 | 1.4E-01 | 0.0E+00 |
| Dec-01 | 9.0E-02 | 0.0E+00 | 1.7E-01 | 0.0E+00 |
| Dec-02 | 1.1E-01 | 0.0E+00 | 2.1E-01 | 0.0E+00 |
| Dec-03 | 1.3E-01 | 0.0E+00 | 2.5E-01 | 0.0E+00 |

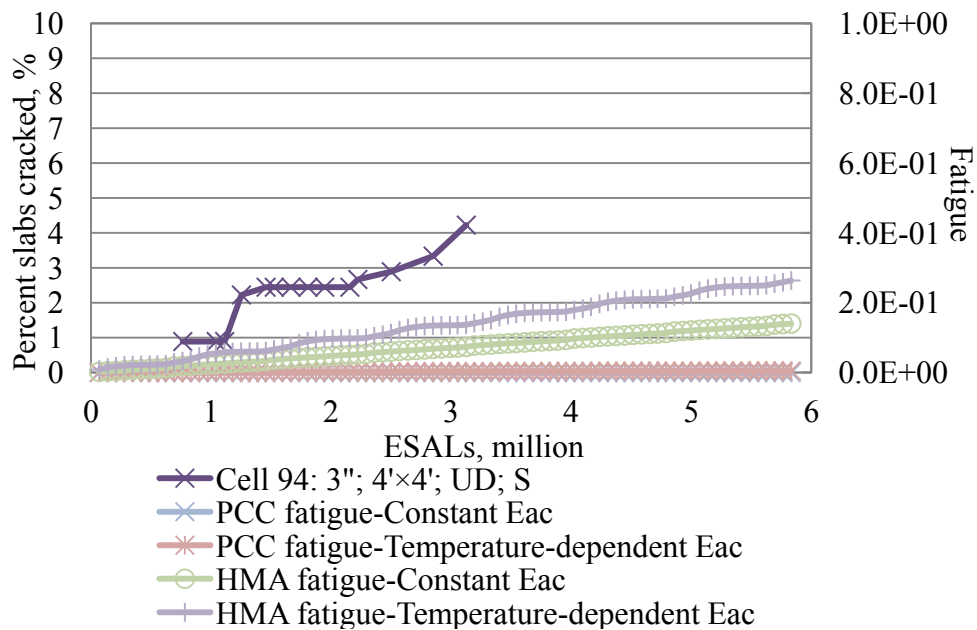


Figure 87. Observed transverse cracking vs. fatigue damage predicted for Cell 94 using the PCA method.

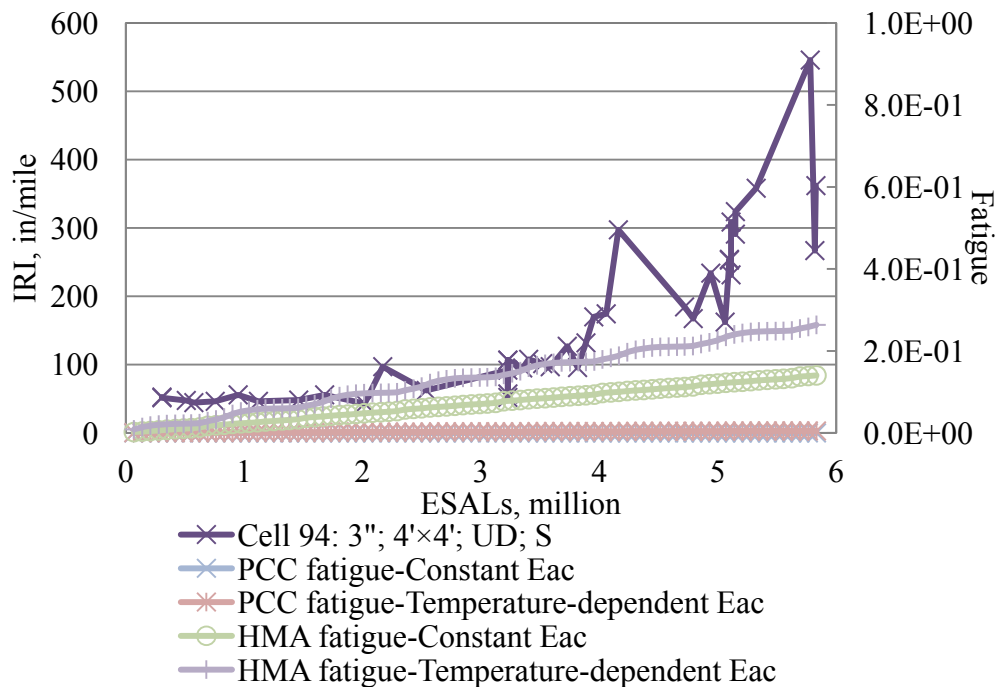


Figure 88. Observed IRI vs. fatigue damage predicted for Cell 94 using the PCA method.

Table 41. Fatigue summary for Cell 95 using the PCA method.

| Date | Constant E_{HMA} | | Temperature-dependent E_{HMA} | |
|--------|--------------------|---------|---------------------------------|---------|
| | HMA | PCC | HMA | PCC |
| Dec-97 | 2.0E-02 | 0.0E+00 | 4.0E-02 | 1.0E-02 |
| Dec-98 | 5.0E-02 | 0.0E+00 | 1.0E-01 | 2.0E-02 |
| Dec-99 | 9.0E-02 | 0.0E+00 | 1.6E-01 | 3.0E-02 |
| Dec-00 | 1.3E-01 | 0.0E+00 | 2.2E-01 | 4.0E-02 |
| Dec-01 | 1.6E-01 | 0.0E+00 | 2.8E-01 | 5.0E-02 |
| Dec-02 | 2.0E-01 | 0.0E+00 | 3.4E-01 | 6.0E-02 |
| Dec-03 | 2.3E-01 | 0.0E+00 | 4.0E-01 | 7.0E-02 |

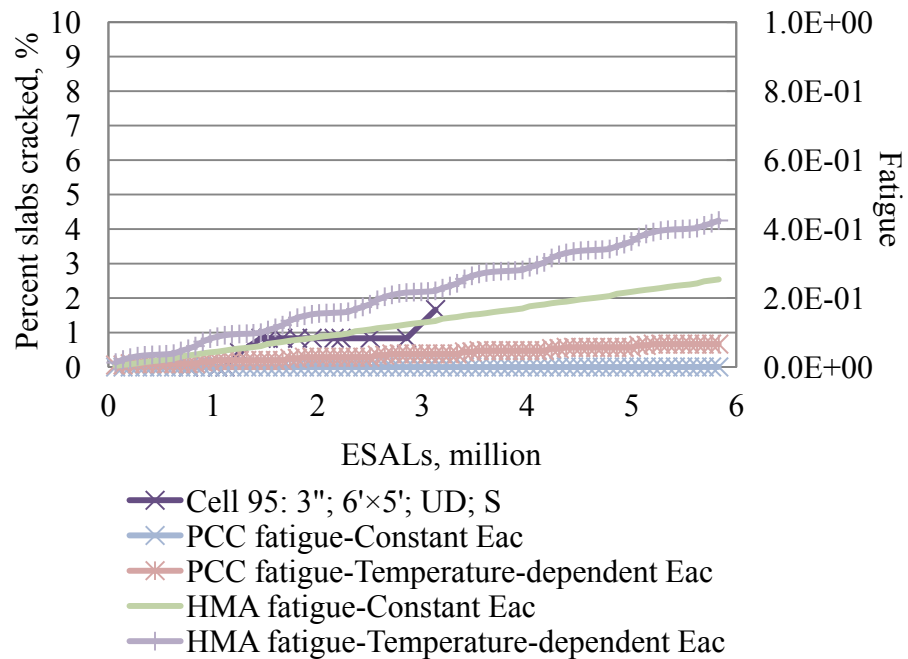


Figure 89. Observed transverse cracking vs. fatigue damage predicted for Cell 95 using the PCA method.

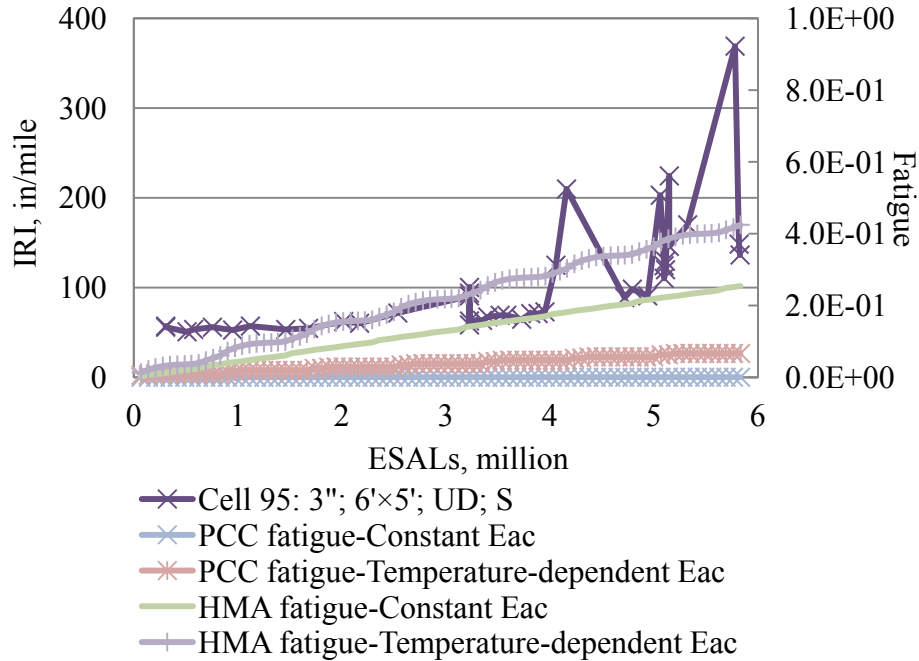


Figure 90. Observed IRI vs. fatigue damage predicted for Cell 95 using the PCA method.

Table 42. Fatigue summary for Cell 96 using the PCA method.

| Date | Constant E_{HMA} | | Temperature-dependent E_{HMA} | |
|--------|--------------------|---------|---------------------------------|---------|
| | HMA | PCC | HMA | PCC |
| Dec-97 | 1.0E-02 | 0.0E+00 | 1.0E-02 | 0.0E+00 |
| Dec-98 | 2.0E-02 | 0.0E+00 | 3.0E-02 | 0.0E+00 |
| Dec-99 | 3.0E-02 | 0.0E+00 | 5.0E-02 | 0.0E+00 |
| Dec-00 | 5.0E-02 | 0.0E+00 | 7.0E-02 | 0.0E+00 |
| Dec-01 | 6.0E-02 | 0.0E+00 | 9.0E-02 | 0.0E+00 |
| Dec-02 | 7.0E-02 | 0.0E+00 | 1.1E-01 | 0.0E+00 |
| Dec-03 | 9.0E-02 | 0.0E+00 | 1.3E-01 | 0.0E+00 |
| Dec-04 | 1.0E-01 | 0.0E+00 | 1.5E-01 | 0.0E+00 |
| Dec-05 | 1.1E-01 | 0.0E+00 | 1.7E-01 | 0.0E+00 |
| Dec-06 | 1.3E-01 | 0.0E+00 | 1.8E-01 | 0.0E+00 |
| Dec-07 | 1.4E-01 | 0.0E+00 | 2.0E-01 | 0.0E+00 |
| Dec-08 | 1.5E-01 | 0.0E+00 | 2.2E-01 | 1.0E-02 |

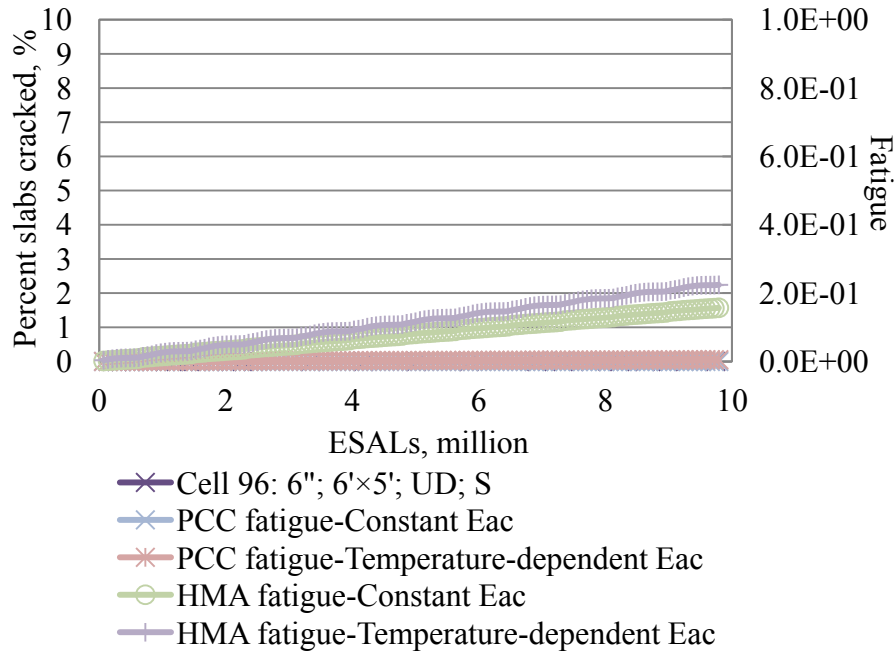


Figure 91. Observed transverse cracking vs. fatigue damage predicted for Cell 96 using the PCA method.

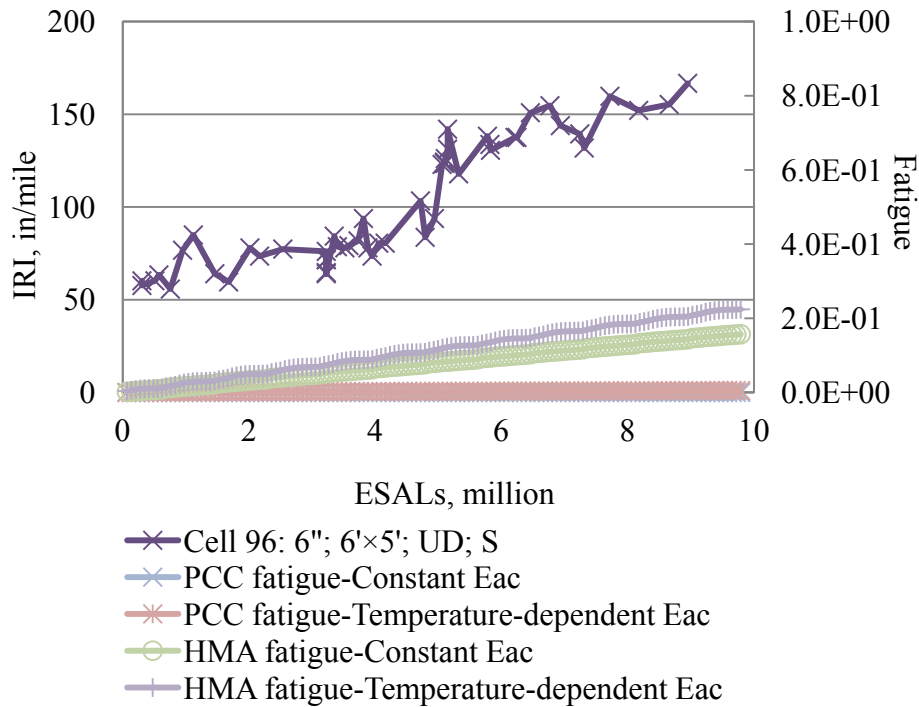


Figure 92. Observed IRI vs. fatigue damage predicted for Cell 96 using the PCA method.

Table 43. Fatigue summary for Cell 97 using the PCA method.

| Date | Constant E_{ac} | | Temperature-dependent E_{ac} | |
|--------|-------------------|---------|--------------------------------|---------|
| | HMA | PCC | HMA | PCC |
| Dec-97 | 1.0E-02 | 0.0E+00 | 2.0E-02 | 4.0E-02 |
| Dec-98 | 4.0E-02 | 0.0E+00 | 5.0E-02 | 9.0E-02 |
| Dec-99 | 7.0E-02 | 1.0E-02 | 9.0E-02 | 1.4E-01 |
| Dec-00 | 9.0E-02 | 1.0E-02 | 1.2E-01 | 1.9E-01 |
| Dec-01 | 1.2E-01 | 1.0E-02 | 1.6E-01 | 2.4E-01 |
| Dec-02 | 1.5E-01 | 2.0E-02 | 2.0E-01 | 2.8E-01 |
| Dec-03 | 1.8E-01 | 2.0E-02 | 2.3E-01 | 3.3E-01 |
| Dec-04 | 2.0E-01 | 2.0E-02 | 2.7E-01 | 3.8E-01 |
| Dec-05 | 2.3E-01 | 2.0E-02 | 3.0E-01 | 4.3E-01 |
| Dec-06 | 2.6E-01 | 3.0E-02 | 3.4E-01 | 4.7E-01 |
| Dec-07 | 2.9E-01 | 3.0E-02 | 3.7E-01 | 5.2E-01 |
| Dec-08 | 3.1E-01 | 3.0E-02 | 4.1E-01 | 5.7E-01 |

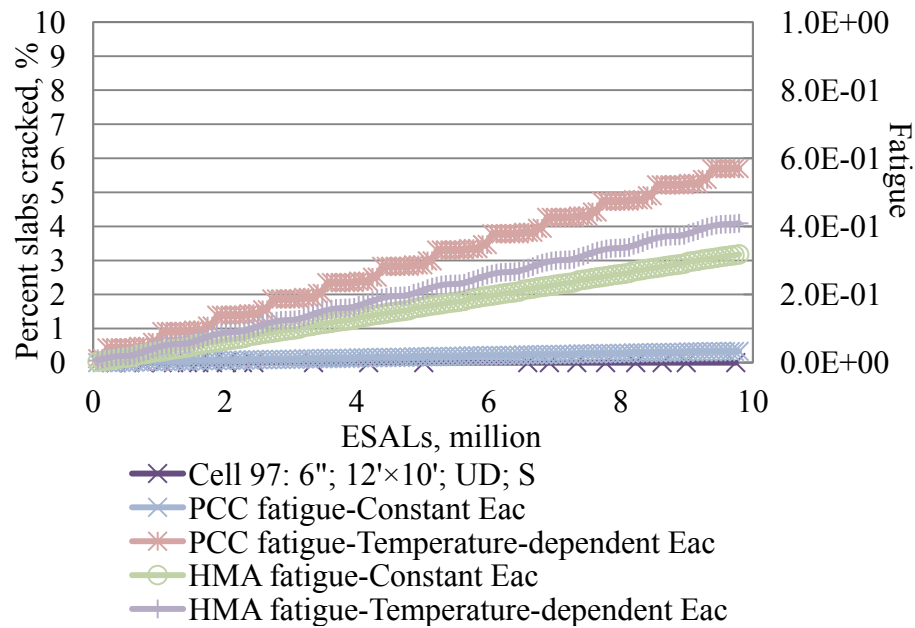


Figure 93. Observed transverse cracking vs. fatigue damage predicted for Cell 97 using the PCA method.

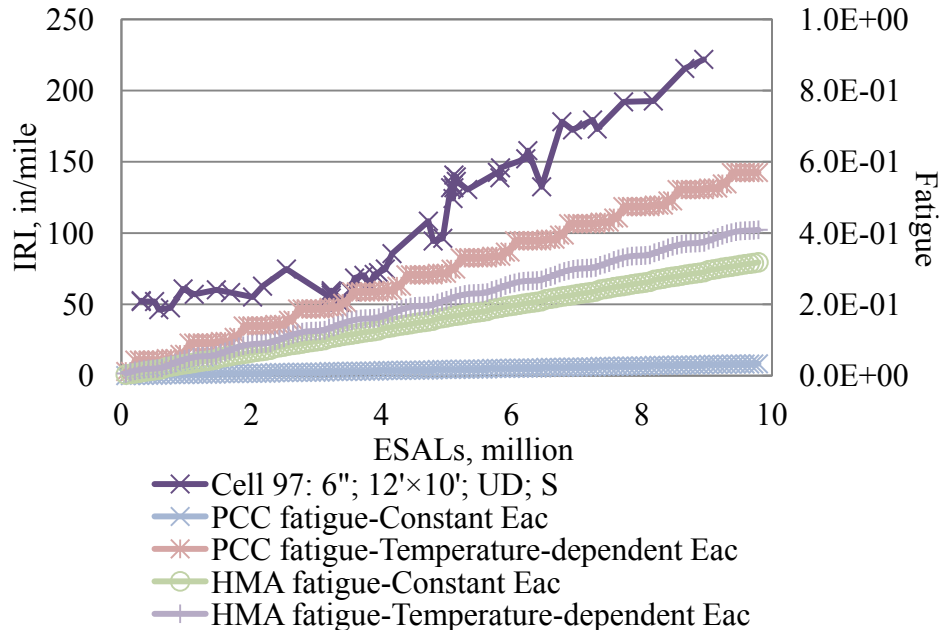


Figure 94. Observed IRI vs. fatigue damage predicted for Cell 97 using the PCA method.

3.4.1 Conclusion for the PCA evaluation

Both PCC and HMA predictions by the PCA method do not seem to capture the observed distress development for MnROAD cells. On one hand, the HMA predictions are relatively constant for all the cells. The PCC predictions are extremely higher than the observations for Cells 60 to 63 and extremely lower than the observations for Cells 93 to 95. This again suggests the importance of accurately determining the concrete modulus of rupture, which is a very sensitive input in the PCA fatigue model. The assumption of a constant bonding condition may also be responsible for the inability to predict the performance, since the influence of pavement parameters, such as PCC thickness and stiffness and HMA thickness and stiffness, on the stress predictions would be more significant for unbonded whitetopping.

Based on the PCA evaluation, it can also be concluded that the use of load spectrum as a traffic input would result in more PCC fatigue predictions than ESALs, especially when the asphalt is less stiff during summer.

3.5 Evaluation of the CDOT method

Similar to the PCA method, the monthly axle spectra in Tables A1 and A2 are used in the evaluation of the CDOT method. Although a modified procedure was introduced in the CDOT method that employs the 18-kip ESALs as the traffic input, the correlation between the axle loading and ESALs is only valid for 6-in whitetopping and thus, cannot be used in this study.

The predicted fatigue damage for Cell 60 are presented in Table 44, where the fatigue prediction can be found for both HMA and PCC layers using both constant and temperature-dependent asphalt moduli of elasticity. The comparisons between the fatigue predictions and the field

observations can be found in Figure 95 and Figure 96 for transverse cracking and IRI, respectively.

Compared with the predictions by the ICT and PCA methods, the difference between PCC fatigue predictions using constant and temperature-dependent asphalt moduli of elasticity, as shown in Table 44, is as large as hundreds of times. This is because the asphalt modulus of elasticity is explicitly considered in the CDOT stress predictions as shown in Equations (4) and (5). Therefore, much larger stresses are predicted for the PCC when the asphalt is less stiff during the summer time.

A similar analysis is carried out for all of the other cells and the results are presented in Table 45 to Table 53 and Figure 97 to Figure 114.

It is interesting to see that the predicted fatigue damage using a constant modulus is greater for Cell 61 than for Cell 62, while the predictions with a temperature-dependent modulus are lower for Cell 61 than for Cell 62. The constant modulus is determined based on an annual average temperature that is more representative to the temperature in March or April, as shown in Table 9. In March or April, the asphalt is relatively stiff and therefore thicker whitetopping slabs, i.e. Cell 61 will present more stresses. However, fatigue damage mainly occurs during the summer using the temperature-dependent asphalt modulus of elasticity. When the asphalt is soft, more fatigue would be predicted for thinner slabs. Therefore, the above finding may suggest that thinner slabs are more critical in terms of fatigue prediction when the temperature is high and the asphalt is soft and vice versa.

It is also interesting to see that the CDOT method successfully predicts that more distresses developed at Cells 93, 94 and 95 than Cells 92, 96 and 97. The thin slabs of Cells 93, 94 and 95 are believed to be responsible for the increase in PCC fatigue damage predicted.

Over 100 percent of HMA fatigue damage is predicted for Cell 92. However, the overall HMA fatigue predictions were kept relatively constant for all the cells. The stress and strain are both corrected for the effect of partial bonding in the CDOT method. Therefore, for Cell 92, which presents the lowest PCC stresses, the highest HMA strain would definitely occur.

Significantly higher PCC fatigue is predicted for Cells 60 to 63 than for Cells 92 to 97 in the CDOT evaluation, which is also believed to be due to the lower modulus of rupture for Cells 60 to 63.

Table 44. Fatigue summary for Cell 60 using the CDOT method.

| Date | Constant E_{HMA} | | Temperature-dependent E_{HMA} | |
|--------|--------------------|---------|---------------------------------|---------|
| | PCC | HMA | PCC | HMA |
| Dec-04 | 8.4E+00 | 1.2E-02 | 6.5E+03 | 2.0E-02 |
| Dec-05 | 1.3E+04 | 3.8E-02 | 8.7E+08 | 5.6E-02 |
| Dec-06 | 2.6E+04 | 6.3E-02 | 1.7E+09 | 9.2E-02 |
| Dec-07 | 3.8E+04 | 8.9E-02 | 2.6E+09 | 1.3E-01 |
| Dec-08 | 5.1E+04 | 1.1E-01 | 3.5E+09 | 1.6E-01 |

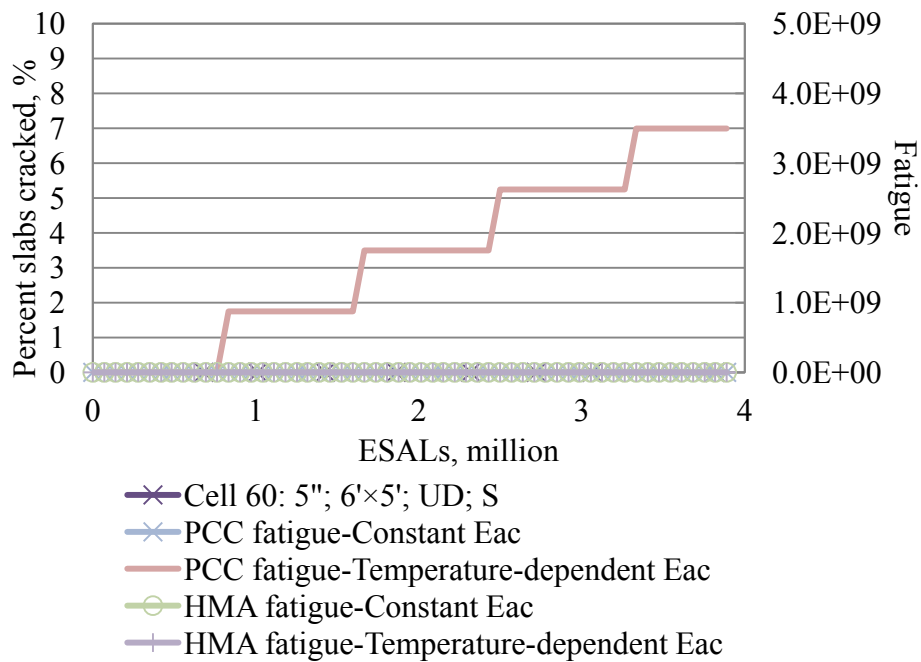


Figure 95. Observed transverse cracking vs. fatigue damage predicted for Cell 60 using the CDOT method.

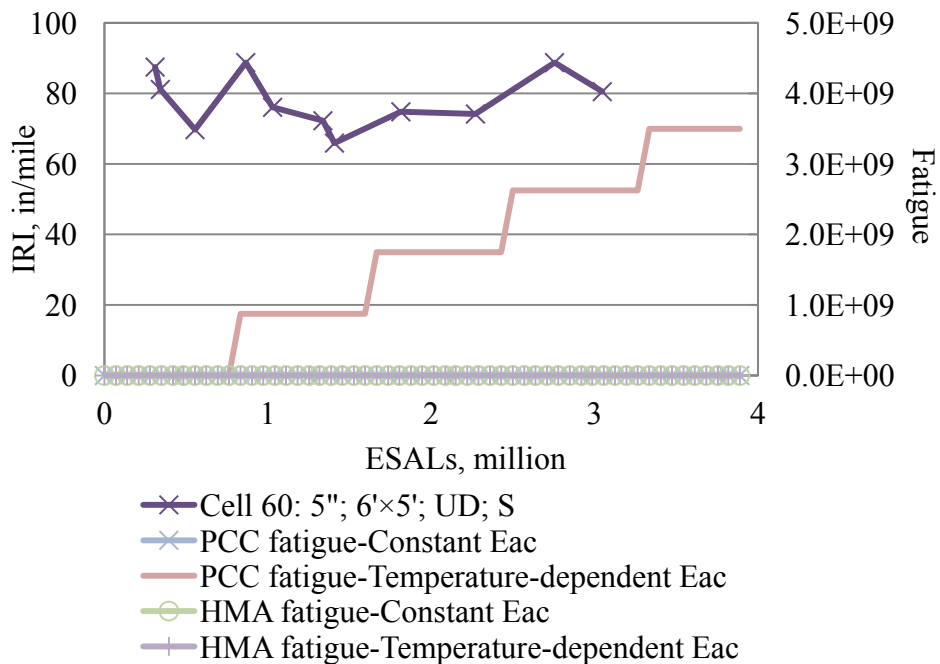


Figure 96. Observed IRI vs. fatigue damage predicted for Cell 60 using the CDOT method.

Table 45. Fatigue summary for Cell 61 using the CDOT method.

| Date | Constant E_{HMA} | | Temperature-dependent E_{HMA} | |
|--------|--------------------|---------|---------------------------------|---------|
| | PCC | HMA | PCC | HMA |
| Dec-04 | 1.8E+02 | 1.2E-02 | 3.4E+05 | 2.0E-02 |
| Dec-05 | 4.1E+05 | 3.8E-02 | 1.3E+11 | 5.7E-02 |
| Dec-06 | 8.2E+05 | 6.4E-02 | 2.6E+11 | 9.4E-02 |
| Dec-07 | 1.2E+06 | 8.9E-02 | 3.9E+11 | 1.3E-01 |
| Dec-08 | 1.6E+06 | 1.2E-01 | 5.2E+11 | 1.7E-01 |

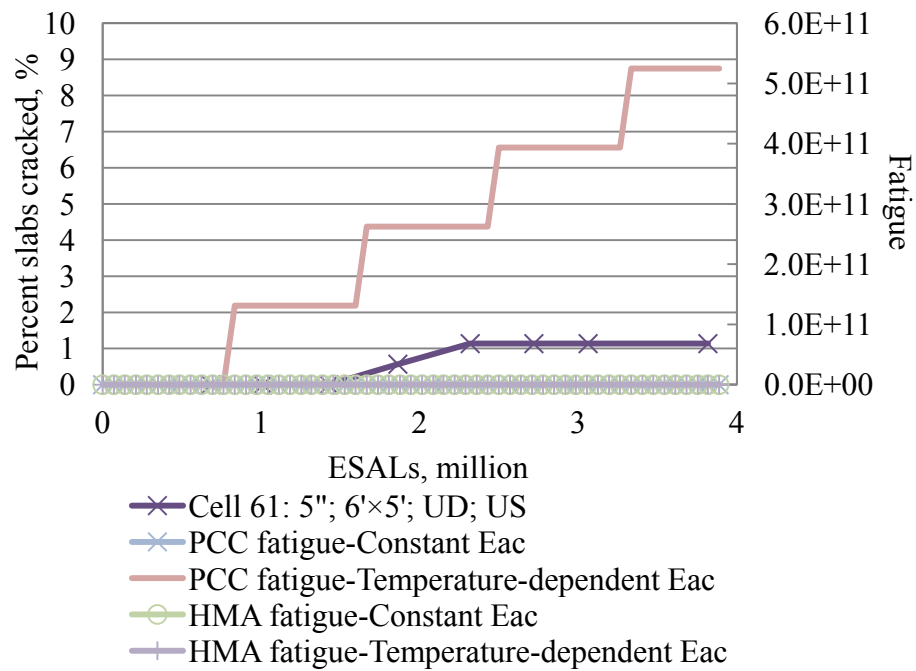


Figure 97. Observed transverse cracking vs. fatigue damage predicted for Cell 61 using the CDOT method.

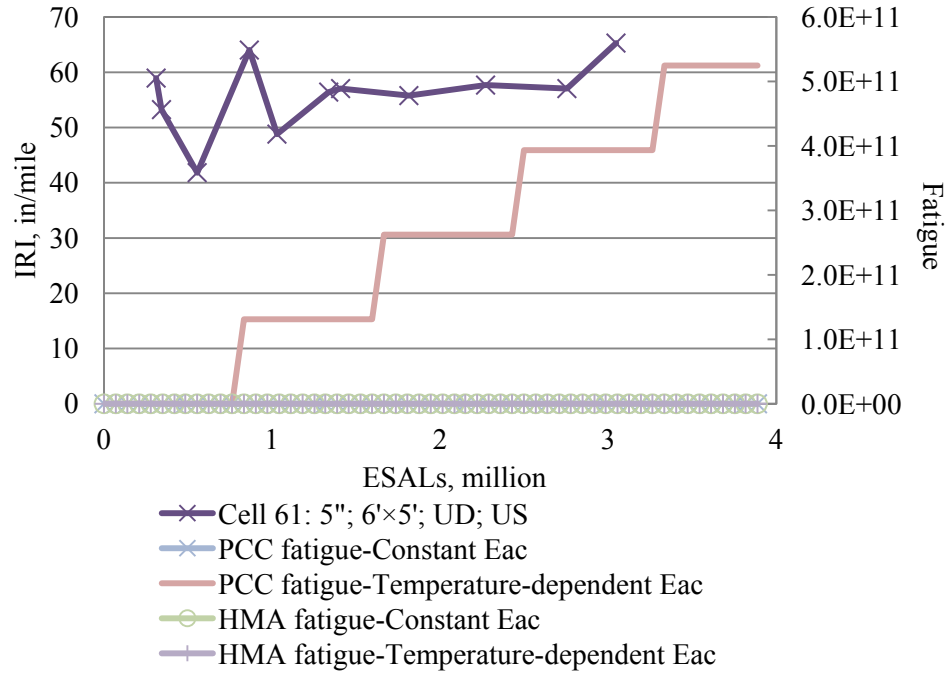


Figure 98. Observed IRI vs. fatigue damage predicted for Cell 61 using the CDOT method.

Table 46. Fatigue summary for Cell 62 using the CDOT method.

| Date | Constant E_{HMA} | | Temperature-dependent E_{HMA} | |
|--------|--------------------|---------|---------------------------------|---------|
| | PCC | HMA | PCC | HMA |
| Dec-04 | 3.4E+01 | 1.2E-02 | 4.3E+05 | 2.1E-02 |
| Dec-05 | 6.2E+04 | 3.8E-02 | 7.3E+11 | 6.0E-02 |
| Dec-06 | 1.2E+05 | 6.4E-02 | 1.5E+12 | 9.8E-02 |
| Dec-07 | 1.9E+05 | 9.0E-02 | 2.2E+12 | 1.4E-01 |
| Dec-08 | 2.5E+05 | 1.2E-01 | 2.9E+12 | 1.7E-01 |

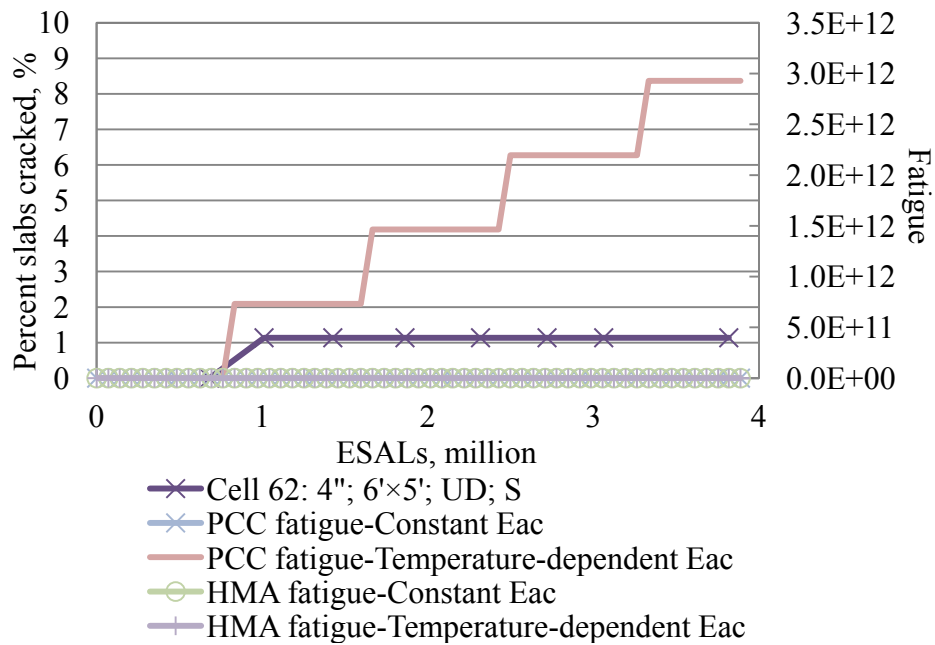


Figure 99. Observed transverse cracking vs. fatigue damage predicted for Cell 62 using the CDOT method.

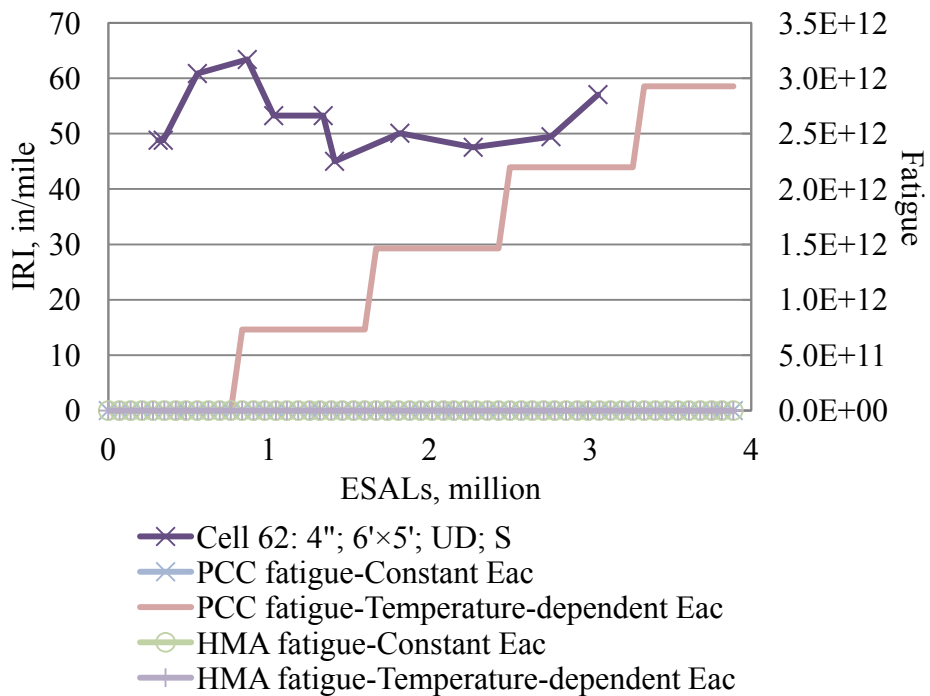


Figure 100. Observed IRI vs. fatigue damage predicted for Cell 62 using the CDOT method.

Table 47. Fatigue summary for Cell 63 using the CDOT method.

| Date | Constant E_{HMA} | | Temperature-dependent E_{HMA} | |
|--------|--------------------|---------|---------------------------------|---------|
| | PCC | HMA | PCC | HMA |
| Dec-04 | 6.6E+01 | 1.2E-02 | 1.1E+06 | 2.1E-02 |
| Dec-05 | 1.3E+05 | 3.8E-02 | 2.3E+12 | 6.0E-02 |
| Dec-06 | 2.7E+05 | 6.4E-02 | 4.6E+12 | 9.8E-02 |
| Dec-07 | 4.0E+05 | 8.9E-02 | 6.9E+12 | 1.4E-01 |
| Dec-08 | 5.3E+05 | 1.2E-01 | 9.2E+12 | 1.7E-01 |

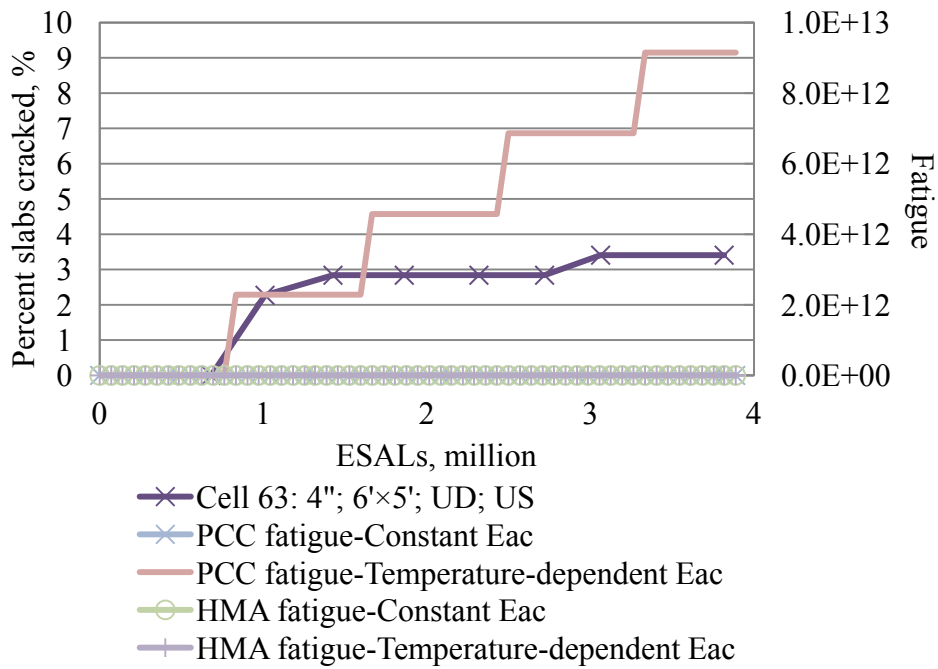


Figure 101. Observed transverse cracking vs. fatigue damage predicted for Cell 63 using the CDOT method.

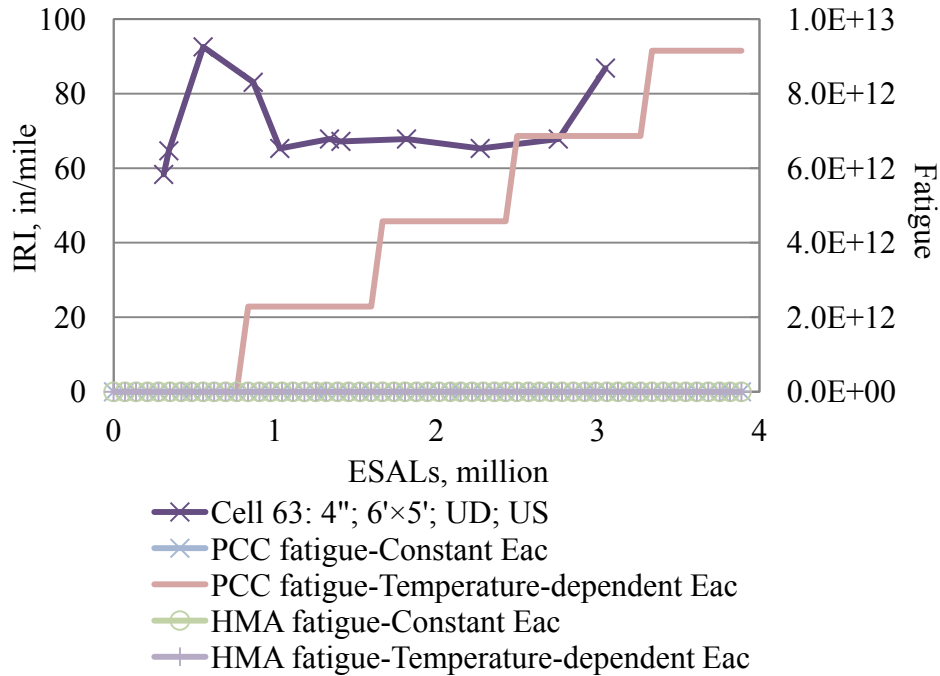


Figure 102. Observed IRI vs. fatigue damage predicted for Cell 63 using the CDOT method.

Table 48. Fatigue summary for Cell 92 using the CDOT method.

| Date | Constant E_{HMA} | | Temperature-dependent E_{HMA} | |
|--------|--------------------|---------|---------------------------------|---------|
| | PCC | HMA | PCC | HMA |
| Dec-97 | 1.6E-02 | 2.6E-02 | 2.7E+00 | 5.9E-02 |
| Dec-98 | 3.4E-02 | 8.1E-02 | 5.4E+00 | 1.6E-01 |
| Dec-99 | 5.1E-02 | 1.4E-01 | 8.1E+00 | 2.6E-01 |
| Dec-00 | 6.8E-02 | 1.9E-01 | 1.1E+01 | 3.6E-01 |
| Dec-01 | 8.5E-02 | 2.4E-01 | 1.3E+01 | 4.6E-01 |
| Dec-02 | 1.0E-01 | 3.0E-01 | 1.6E+01 | 5.6E-01 |
| Dec-03 | 1.2E-01 | 3.5E-01 | 1.9E+01 | 6.6E-01 |
| Dec-04 | 1.4E-01 | 4.1E-01 | 2.2E+01 | 7.7E-01 |
| Dec-05 | 1.5E-01 | 4.6E-01 | 2.4E+01 | 8.7E-01 |
| Dec-06 | 1.7E-01 | 5.2E-01 | 2.7E+01 | 9.7E-01 |
| Dec-07 | 1.9E-01 | 5.7E-01 | 3.0E+01 | 1.1E+00 |
| Dec-08 | 2.1E-01 | 6.3E-01 | 3.2E+01 | 1.2E+00 |

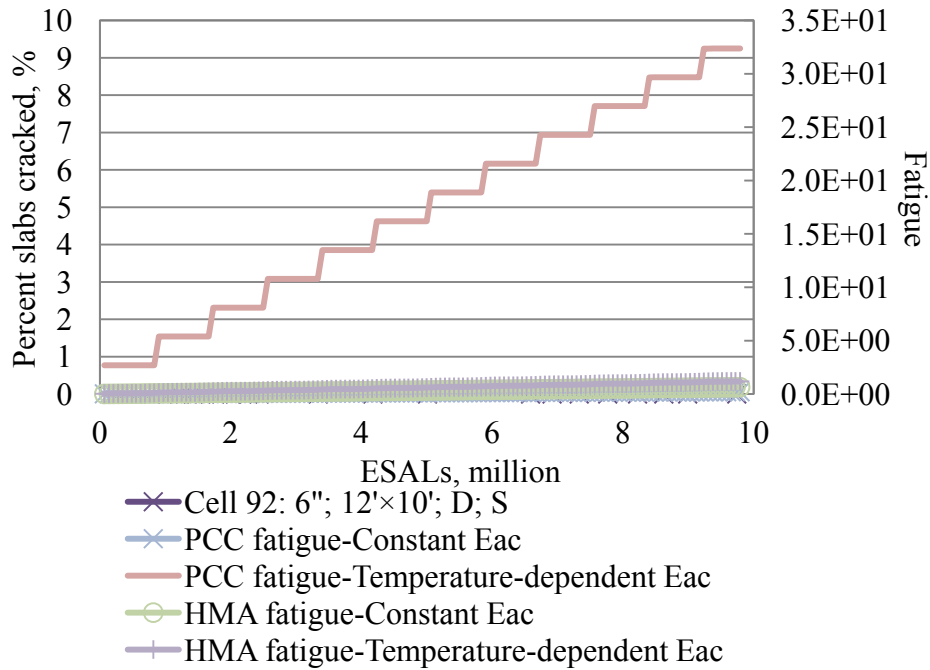


Figure 103. Observed transverse cracking vs. fatigue damage predicted for Cell 92 using the CDOT method.

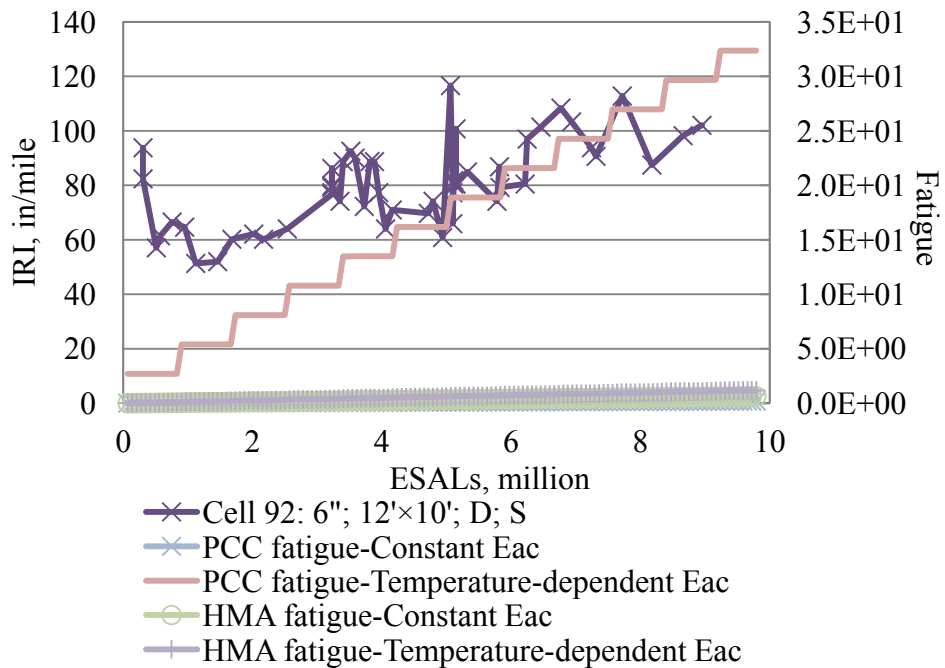


Figure 104. Observed IRI vs. fatigue damage predicted for Cell 92 using the CDOT method.

Table 49. Fatigue summary for Cell 93 using the CDOT method.

| Date | Constant E_{HMA} | | Temperature-dependent E_{HMA} | |
|--------|--------------------|---------|---------------------------------|---------|
| | PCC | HMA | PCC | HMA |
| Dec-97 | 2.9E-02 | 5.7E-03 | 1.2E+03 | 8.0E-03 |
| Dec-98 | 5.9E-02 | 1.8E-02 | 2.4E+03 | 2.3E-02 |
| Dec-99 | 9.0E-02 | 3.0E-02 | 3.6E+03 | 3.8E-02 |
| Dec-00 | 1.2E-01 | 4.1E-02 | 4.8E+03 | 5.3E-02 |
| Dec-01 | 1.5E-01 | 5.3E-02 | 5.9E+03 | 6.8E-02 |
| Dec-02 | 1.8E-01 | 6.5E-02 | 7.1E+03 | 8.3E-02 |
| Dec-03 | 2.1E-01 | 7.7E-02 | 8.3E+03 | 9.8E-02 |

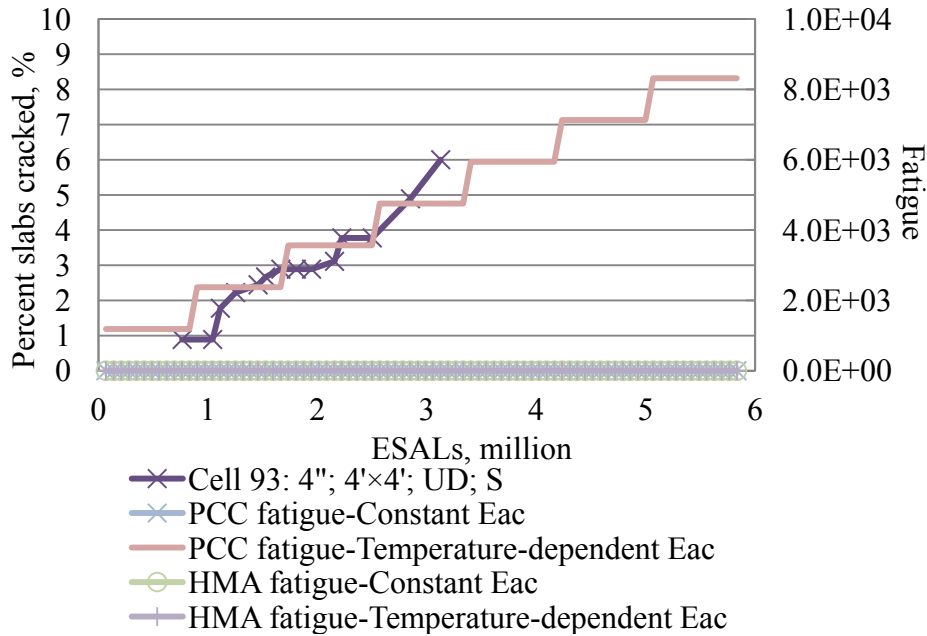


Figure 105. Observed transverse cracking vs. fatigue damage predicted for Cell 93 using the CDOT method.

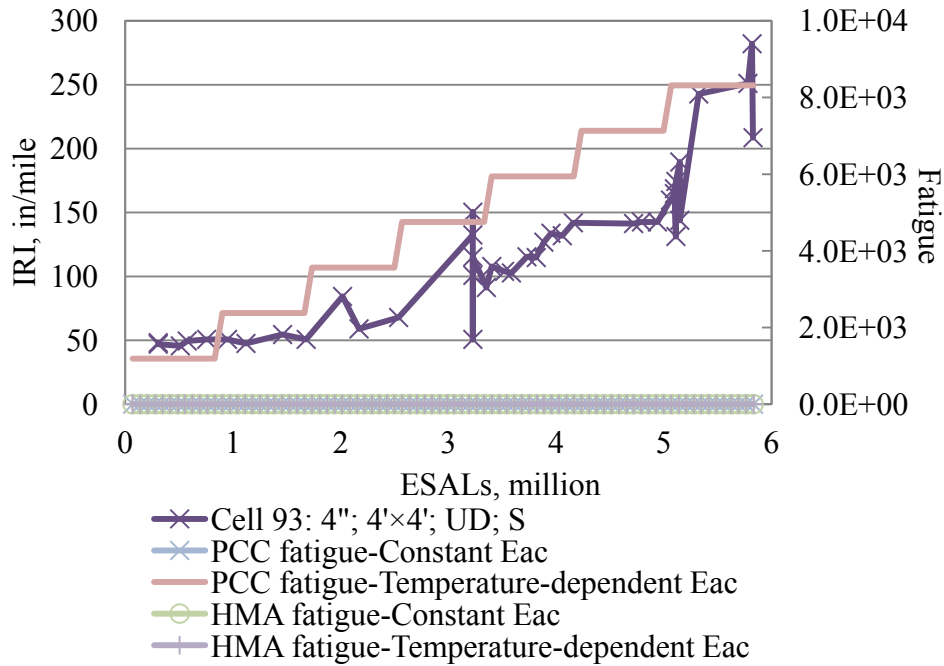


Figure 106. Observed IRI vs. fatigue damage predicted for Cell 93 using the CDOT method.

Table 50. Fatigue summary for Cell 94 using the CDOT method.

| Date | Constant E_{HMA} | | Temperature-dependent E_{HMA} | |
|--------|--------------------|---------|---------------------------------|---------|
| | PCC | HMA | PCC | HMA |
| Dec-97 | 9.1E-02 | 5.7E-03 | 3.6E+04 | 8.3E-03 |
| Dec-98 | 1.9E-01 | 1.8E-02 | 7.1E+04 | 2.4E-02 |
| Dec-99 | 2.8E-01 | 3.0E-02 | 1.1E+05 | 3.9E-02 |
| Dec-00 | 3.8E-01 | 4.2E-02 | 1.4E+05 | 5.4E-02 |
| Dec-01 | 4.8E-01 | 5.3E-02 | 1.8E+05 | 7.0E-02 |
| Dec-02 | 5.7E-01 | 6.5E-02 | 2.1E+05 | 8.5E-02 |
| Dec-03 | 6.7E-01 | 7.7E-02 | 2.5E+05 | 1.0E-01 |

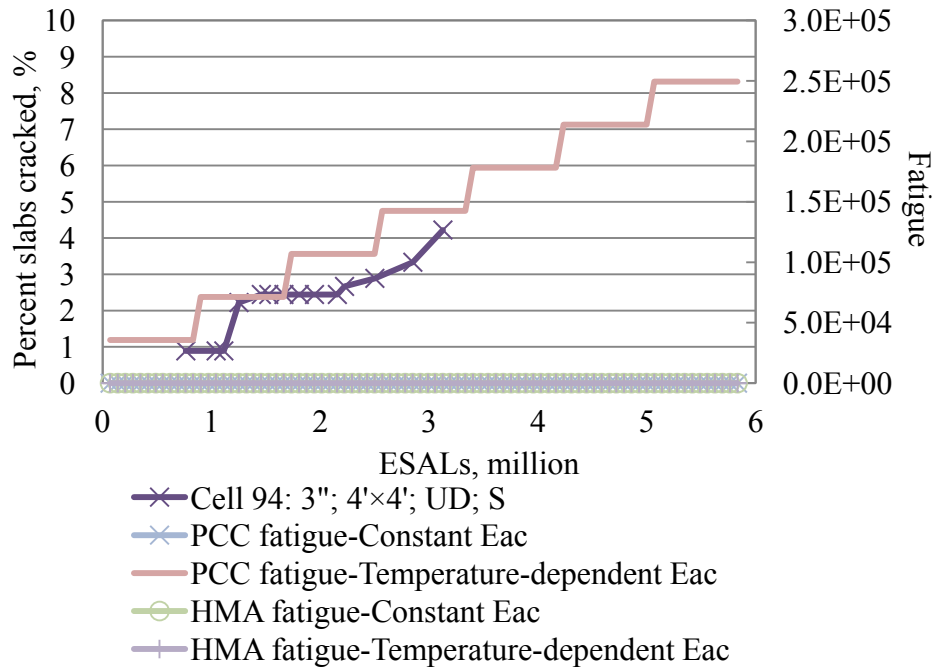


Figure 107. Observed transverse cracking vs. fatigue damage predicted for Cell 94 using the CDOT method.

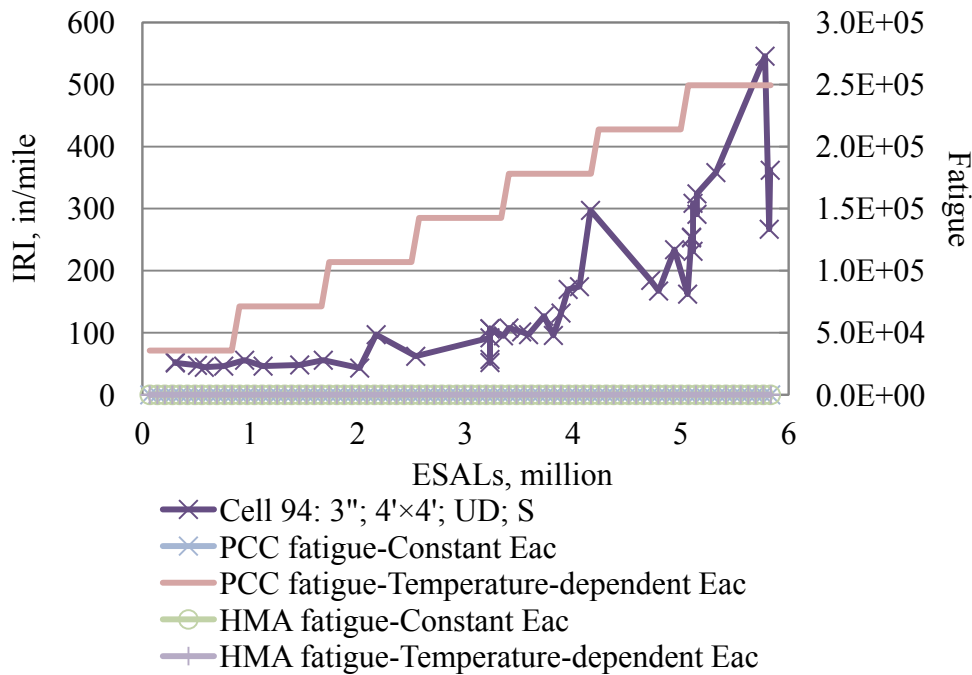


Figure 108. Observed IRI vs. fatigue damage predicted for Cell 94 using the CDOT method.

Table 51. Fatigue summary for Cell 95 using the CDOT method.

| Date | Constant E_{HMA} | | Temperature-dependent E_{HMA} | |
|--------|--------------------|---------|---------------------------------|---------|
| | PCC | HMA | PCC | HMA |
| Dec-97 | 7.3E-02 | 1.1E-02 | 1.9E+04 | 2.0E-02 |
| Dec-98 | 1.5E-01 | 3.5E-02 | 3.8E+04 | 5.6E-02 |
| Dec-99 | 2.3E-01 | 5.9E-02 | 5.7E+04 | 9.1E-02 |
| Dec-00 | 3.0E-01 | 8.3E-02 | 7.6E+04 | 1.3E-01 |
| Dec-01 | 3.8E-01 | 1.1E-01 | 9.5E+04 | 1.6E-01 |
| Dec-02 | 4.6E-01 | 1.3E-01 | 1.1E+05 | 2.0E-01 |
| Dec-03 | 5.4E-01 | 1.5E-01 | 1.3E+05 | 2.3E-01 |

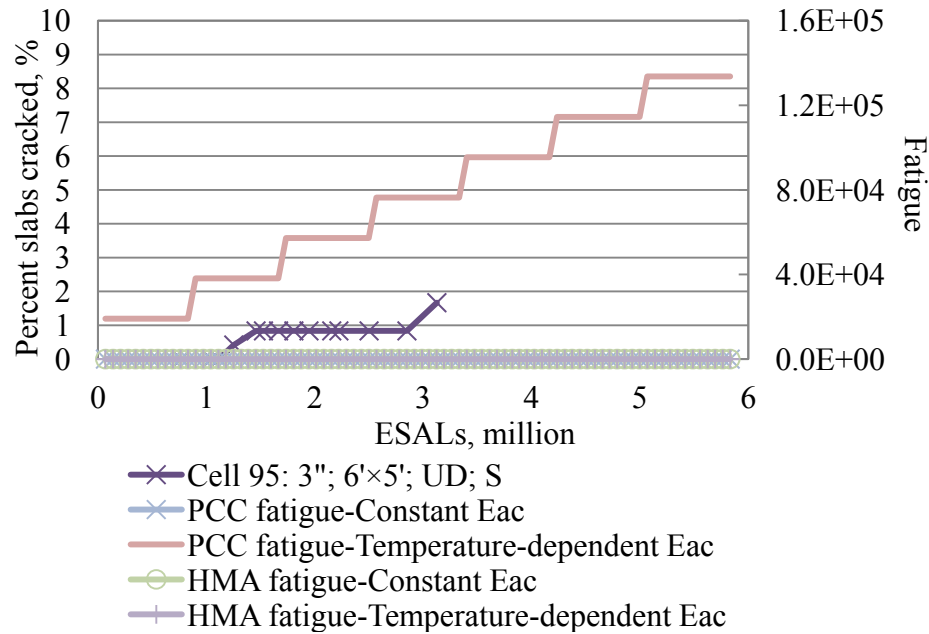


Figure 109. Observed transverse cracking vs. fatigue damage predicted for Cell 95 using the CDOT method.

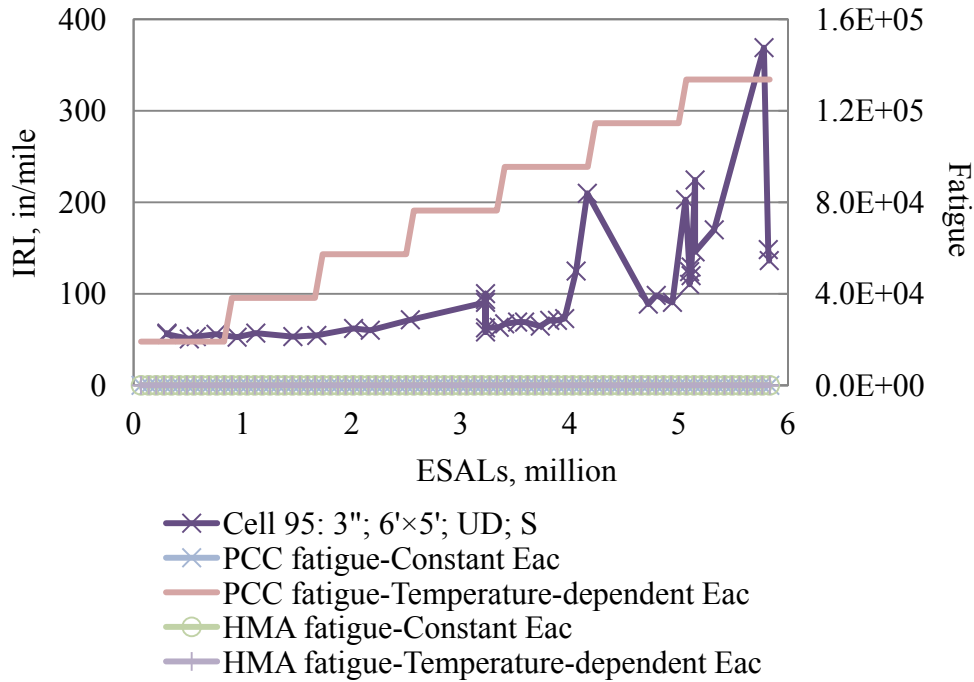


Figure 110. Observed IRI vs. fatigue damage predicted for Cell 95 using the CDOT method.

Table 52. Fatigue summary for Cell 96 using the CDOT method.

| Date | Constant E_{HMA} | | Temperature-dependent E_{HMA} | |
|--------|--------------------|---------|---------------------------------|---------|
| | PCC | HMA | PCC | HMA |
| Dec-97 | 5.0E-03 | 1.1E-02 | 6.0E-01 | 1.7E-02 |
| Dec-98 | 1.0E-02 | 3.4E-02 | 1.2E+00 | 4.7E-02 |
| Dec-99 | 1.5E-02 | 5.7E-02 | 1.8E+00 | 7.8E-02 |
| Dec-00 | 2.1E-02 | 7.9E-02 | 2.4E+00 | 1.1E-01 |
| Dec-01 | 2.6E-02 | 1.0E-01 | 3.0E+00 | 1.4E-01 |
| Dec-02 | 3.1E-02 | 1.3E-01 | 3.6E+00 | 1.7E-01 |
| Dec-03 | 3.6E-02 | 1.5E-01 | 4.2E+00 | 2.0E-01 |
| Dec-04 | 4.2E-02 | 1.7E-01 | 4.8E+00 | 2.3E-01 |
| Dec-05 | 4.7E-02 | 1.9E-01 | 5.4E+00 | 2.6E-01 |
| Dec-06 | 5.2E-02 | 2.2E-01 | 6.0E+00 | 2.9E-01 |
| Dec-07 | 5.7E-02 | 2.4E-01 | 6.6E+00 | 3.2E-01 |
| Dec-08 | 6.2E-02 | 2.6E-01 | 7.2E+00 | 3.5E-01 |

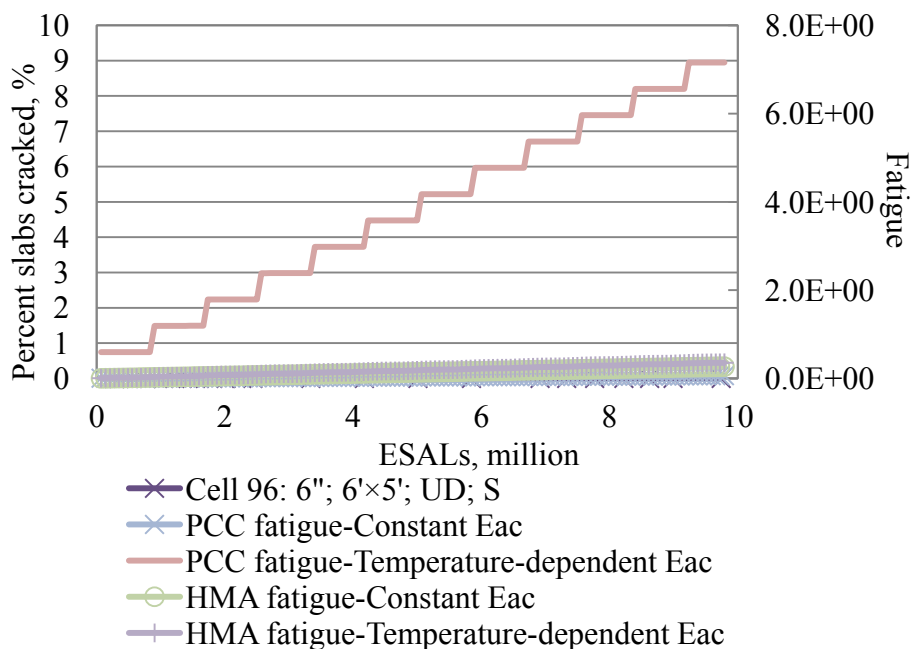


Figure 111. Observed transverse cracking vs. fatigue damage predicted for Cell 96 using the CDOT method.

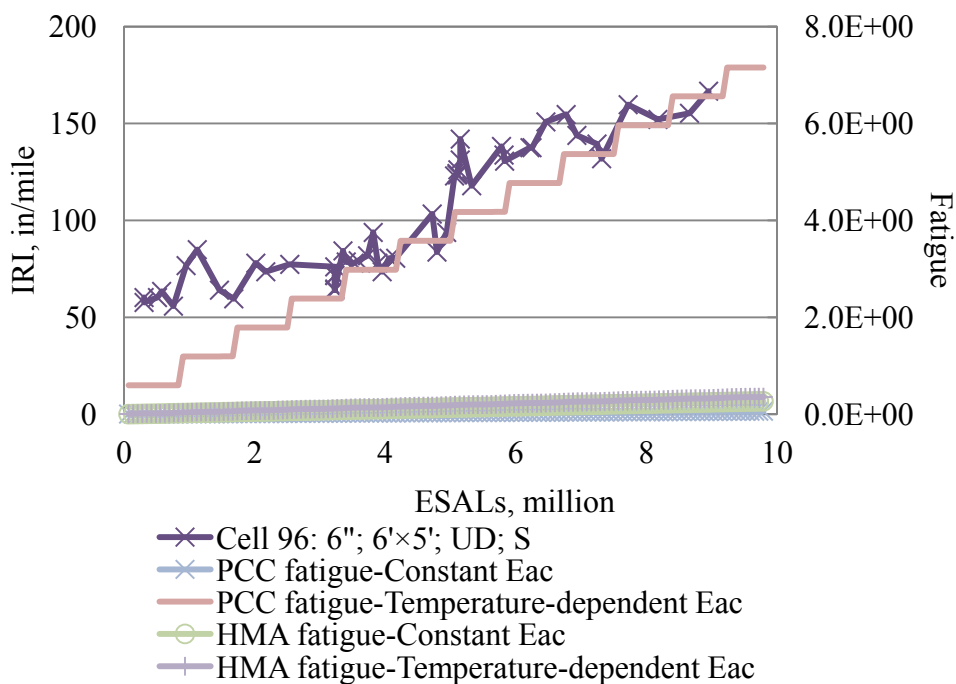


Figure 112. Observed IRI vs. fatigue damage predicted for Cell 96 using the CDOT method.

Table 53. Fatigue summary for Cell 97 using the CDOT method.

| Date | Constant E_{HMA} | | Temperature-dependent E_{HMA} | |
|--------|--------------------|---------|---------------------------------|---------|
| | PCC | HMA | PCC | HMA |
| Dec-97 | 1.6E-02 | 2.6E-02 | 2.7E+00 | 5.9E-02 |
| Dec-98 | 3.4E-02 | 8.1E-02 | 5.4E+00 | 1.6E-01 |
| Dec-99 | 5.1E-02 | 1.4E-01 | 8.1E+00 | 2.6E-01 |
| Dec-00 | 6.8E-02 | 1.9E-01 | 1.1E+01 | 3.6E-01 |
| Dec-01 | 8.5E-02 | 2.4E-01 | 1.3E+01 | 4.6E-01 |
| Dec-02 | 1.0E-01 | 3.0E-01 | 1.6E+01 | 5.6E-01 |
| Dec-03 | 1.2E-01 | 3.5E-01 | 1.9E+01 | 6.6E-01 |
| Dec-04 | 1.4E-01 | 4.1E-01 | 2.2E+01 | 7.7E-01 |
| Dec-05 | 1.5E-01 | 4.6E-01 | 2.4E+01 | 8.7E-01 |
| Dec-06 | 1.7E-01 | 5.2E-01 | 2.7E+01 | 9.7E-01 |
| Dec-07 | 1.9E-01 | 5.7E-01 | 3.0E+01 | 1.1E+00 |
| Dec-08 | 2.1E-01 | 6.3E-01 | 3.2E+01 | 1.2E+00 |

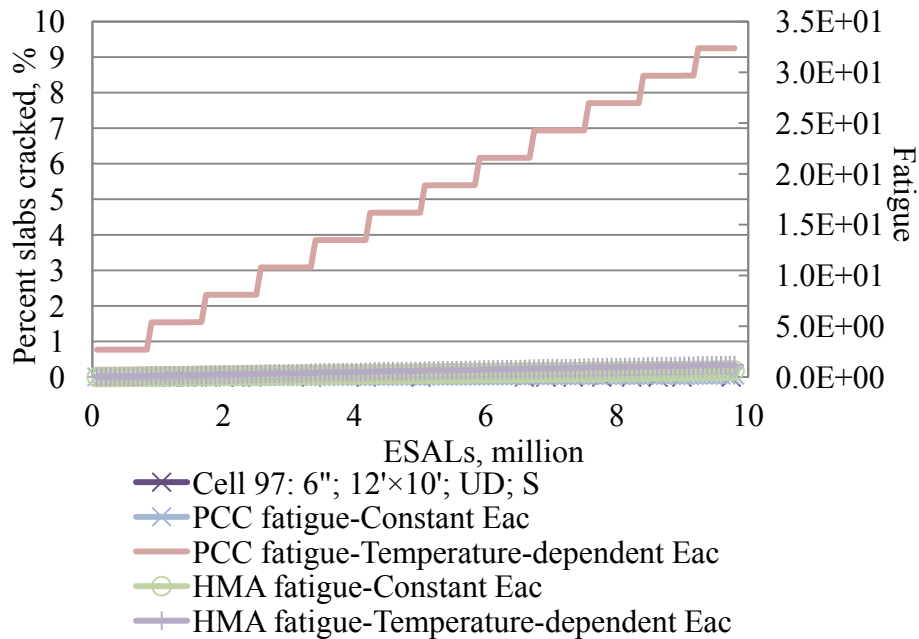


Figure 113. Observed transverse cracking vs. fatigue damage predicted for Cell 97 using the CDOT method.

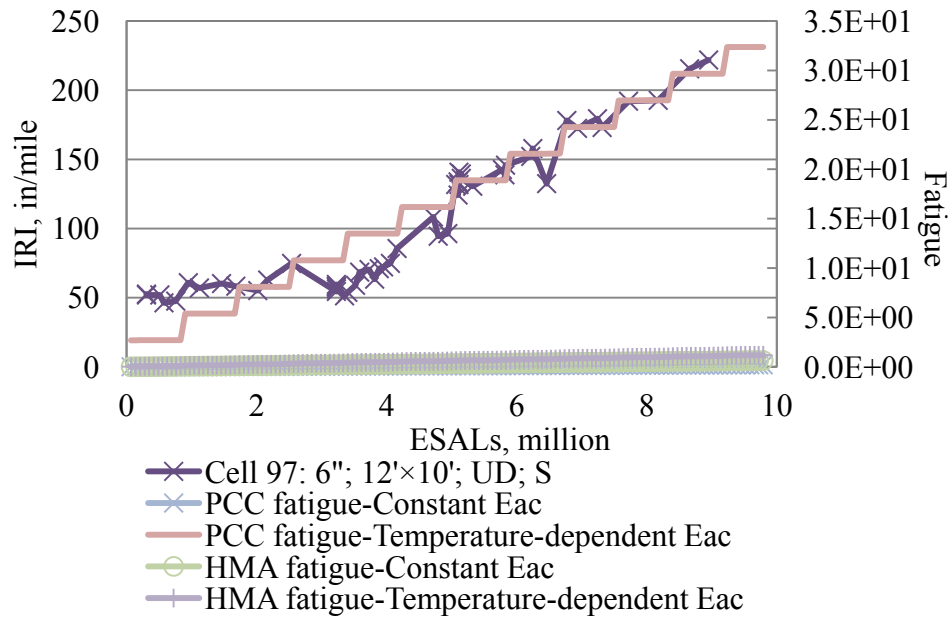


Figure 114. Observed IRI vs. fatigue damage predicted for Cell 97 using the CDOT method.

3.5.1 Conclusion for the CDOT evaluation

The CDOT method is the only one out of the four methods that successfully predicts much more fatigue damage for Cells 93 to 95 than Cells 92, 96 and 97. However, the high dependency of the concrete modulus of rupture impairs the sensitivity of the method to the pavement parameters in the stress and subsequent fatigue predictions.

The asphalt modulus of elasticity is such a significant input in the CDOT method that the difference in PCC fatigue predictions using constant and temperature-dependent moduli is the largest among the four methods. Furthermore, it was found that the critical pavement structure, in terms of stress predictions, shifts with the temperature of the asphalt.

Both PCC stress and HMA strain are corrected for partial bonding resulting in the phenomenon where larger HMA strains can be found in the cell where the PCC stress is the lowest.

3.6 Conclusions made base on the evaluations

Evaluations were made on four of the methods currently available for whitetopping design, on which the following conclusions can be made.

The NJDOT method predicts tremendous PCC and HMA fatigue damage for unbonded conditions and nearly zero fatigue damage for fully bonded conditions, as can be seen in Table 54. The prediction for the degree of bonding condition is supposed to lie in between the two extreme scenarios. However, a new problem arises when trying to determine the percentage of partial bonding.

The ICT method yields the lowest predictions for the PCC fatigue damage among the four methods as shown in Table 54. This can be explained by the fact that the ICT method predicts

the lowest stresses, as shown in Table 55, considering that the stresses due to an 18-kip single axle loading are not the most critical stresses in the fatigue analysis of the PCA method. The ICT method is sensitive to pavement parameters, namely pavement thickness and slab size. However, Cell 92 and 97, which are 144-in slabs, have significantly over predicted stresses, as shown in Table 55. This is believed to be due to the difference between the ICT stress equations, Equations (42) and (43), and the PCA stress equations, Equations (35) and (38). The difference between the PCA stresses and the ICT stresses becomes more significant as the joint spacing increases, as shown in Figure 8. As long as typical whitetopping slab dimensions, 36-72 in, are used, it is appropriate to use either equation.

Among the four methods, the PCA and the CDOT methods seem to be able to yield the most reasonable fatigue predictions for both PCC and HMA, as shown in Table 54. Both methods have taken partial bonding into account through calibrating the structural response models based on field observations. Furthermore, the CDOT method is the only one that captures more fatigue damage in Cells 93, 94 and 95 than Cells 92, 96 and 97. As shown in Table 55, the CDOT method predicts lower stresses for Cells 93 to 95, which are thinner than Cells 92, 96 and 97, while the PCA method is not very sensitive to the slab thickness.

The use of a temperature-dependent asphalt modulus of elasticity results in significantly higher fatigue damage for all four methods, since a monthly asphalt modulus of elasticity is better able to capture the critical stresses generated in the overlay when asphalt is soft in the summer. This effect is found to be more significant for whitetopping with unbonded layers. The other advantage of using a temperature-dependent asphalt modulus of elasticity is that it can capture the shift in the critical pavement thickness in terms of stress prediction. Based on both the PCA and CDOT evaluations, it is found that a thicker concrete overlay will present more stresses when the asphalt is stiffer and vice versa.

Regarding the traffic input, it was identified that the use of axle repetitions instead of ESALs results in more fatigue damage. Furthermore, it was found that the majority of the fatigue is predicted due to heavy tandem axle loadings occurring during the summer time.

It is extremely important to accurately determine the concrete modulus of rupture since it is a very sensitive input in the PCC fatigue analysis. In Table 54, significantly higher fatigue predictions can be found for Cells 60 to 63, which have a much lower modulus of rupture than Cells 92 to 97. However, the variation in stress predictions among the cells, as shown in Table 55, is so small that it is not statistically significant. Instead, it is the sensitivity of fatigue models to the stress ratio, as shown in Table 56 that leads to the exponential increase of fatigue with tiny changes in the stress ratio.

The thermal stresses due to the temperature differentials in the slab are considered in all four methods. Depending where the critical tensile stress is located in the overlay, the thermal stress would be added or subtracted from the load-induced tensile stress. For the MnROAD cells, negative temperature differentials exist. In the ICT and PCA methods, the critical stresses are assumed to be at the top of the overlay, so positive tensile stresses are added to the total stress, as shown in Table 57. On the other hand, the tensile stress is alleviated due to the temperature differential in the CDOT and NJDOT methods, since the critical stress is assumed to be at the bottom of the slabs. It can also be found that the thermal stresses make up a large percent of the

total predicted stresses in the ICT and NJDOT method (bonded cases). Therefore, to successfully apply these two methods, the determination of the concrete CTE and temperature differential becomes very critical.

Compared with the fatigue predictions for the PCC, the predictions for the HMA are consistently low as long as the assumed bond condition is reasonable. This is believed to be due to the fact that the Asphalt Institute fatigue model is not as sensitive to the asphalt strain as the PCA and ACPA concrete fatigue model is to the stress ratio. Therefore, the employment of the inactive asphalt fatigue analysis into design might not always be helpful.

Table 54. Summary of fatigue damage predictions at 3 million ESALs for MnROAD cells using a constant asphalt modulus of elasticity.

| | PCC fatigue | | | | | HMA fatigue | | | | |
|---------|-------------|-----|--------|----------|-------|-------------|------|--------|----------|-----|
| | CDOT | ICT | NJDOT | | PCA | CDOT | ICT | NJDOT | | PCA |
| | | | Bonded | Unbonded | | | | Bonded | Unbonded | |
| Cell 60 | 3.8E+04 | 0% | 0% | 1.8E+05 | 652% | 9% | N.A. | 69% | 335% | 32% |
| Cell 61 | 1.2E+06 | 7% | 0% | 1.8E+05 | 6362% | 9% | N.A. | 69% | 335% | 33% |
| Cell 62 | 1.9E+05 | 0% | 0% | 1.2E+07 | 1317% | 9% | N.A. | 82% | 932% | 40% |
| Cell 63 | 4.0E+05 | 0% | 0% | 3.0E+07 | 2407% | 9% | N.A. | 81% | 909% | 38% |
| Cell 92 | 7% | 0% | 0% | 44% | 1% | 20% | N.A. | 36% | 98% | 10% |
| Cell 93 | 12% | 0% | 0% | 2890% | 0% | 4% | N.A. | 54% | 820% | 5% |
| Cell 94 | 38% | 0% | 0% | 212% | 0% | 4% | N.A. | 55% | 1146% | 7% |
| Cell 95 | 30% | 0% | 0% | 0% | 0% | 9% | N.A. | 55% | 1153% | 13% |
| Cell 96 | 2% | 0% | 0% | 0% | 0% | 8% | N.A. | 36% | 98% | 5% |
| Cell 97 | 7% | 0% | 0% | 44% | 1% | 20% | N.A. | 36% | 98% | 10% |

Table 55. Summary of structural response predictions due to 18-kip single axle loading for MnROAD cells using a constant asphalt modulus of elasticity.

| | PCC stress, psi | | | | | HMA microstrain | | | | |
|---------|-----------------|-----|--------|----------|-----|-----------------|------|--------|----------|-----|
| | CDOT | ICT | NJDOT | | PCA | CDOT | ICT | NJDOT | | PCA |
| | | | Bonded | Unbonded | | | | Bonded | Unbonded | |
| Cell 60 | 307 | 194 | 106 | 518 | 179 | 102 | N.A. | 136 | 219 | 105 |
| Cell 61 | 312 | 196 | 96 | 503 | 182 | 103 | N.A. | 137 | 224 | 106 |
| Cell 62 | 312 | 196 | 45 | 587 | 175 | 103 | N.A. | 143 | 299 | 110 |
| Cell 63 | 310 | 196 | 45 | 591 | 176 | 103 | N.A. | 143 | 297 | 109 |
| Cell 92 | 240 | 270 | 103 | 388 | 173 | 129 | N.A. | 112 | 151 | 75 |
| Cell 93 | 257 | 132 | -4 | 480 | 138 | 81 | N.A. | 126 | 288 | 61 |
| Cell 94 | 258 | 133 | -44 | 396 | 131 | 81 | N.A. | 127 | 319 | 66 |
| Cell 95 | 262 | 177 | -43 | 364 | 144 | 100 | N.A. | 127 | 320 | 79 |
| Cell 96 | 240 | 168 | 103 | 388 | 160 | 99 | N.A. | 112 | 151 | 62 |
| Cell 97 | 240 | 270 | 103 | 388 | 174 | 129 | N.A. | 112 | 151 | 76 |

Table 56. Summary of stress ratios due to 18-kip single axle loading for MnROAD cells using a constant asphalt modulus of elasticity.

| | CDOT | ICT | NJDOT | | PCA |
|---------|------|------|--------|----------|------|
| | | | Bonded | Unbonded | |
| Cell 60 | 0.52 | 0.33 | 0.18 | 0.87 | 0.30 |
| Cell 61 | 0.52 | 0.33 | 0.16 | 0.85 | 0.31 |
| Cell 62 | 0.52 | 0.33 | 0.08 | 0.99 | 0.29 |
| Cell 63 | 0.52 | 0.33 | 0.08 | 0.99 | 0.29 |
| Cell 92 | 0.40 | 0.45 | 0.17 | 0.65 | 0.29 |
| Cell 93 | 0.43 | 0.22 | -0.01 | 0.81 | 0.23 |
| Cell 94 | 0.43 | 0.22 | -0.07 | 0.66 | 0.22 |
| Cell 95 | 0.44 | 0.30 | -0.07 | 0.61 | 0.24 |
| Cell 96 | 0.40 | 0.28 | 0.17 | 0.65 | 0.27 |
| Cell 97 | 0.40 | 0.45 | 0.17 | 0.65 | 0.29 |

Table 57. Summary of thermal stress/strain predictions for MnROAD cells using a constant asphalt modulus of elasticity.

| | PCC stress, psi | | | | | HMA microstrain | | | | |
|---------|-----------------|-----|--------|----------|-----|-----------------|------|--------|----------|-----|
| | CDOT | ICT | NJDOT | | PCA | CDOT | ICT | NJDOT | | PCA |
| | | | Bonded | Unbonded | | | | Bonded | Unbonded | |
| Cell 60 | -12 | 37 | -40 | -54 | 8 | N.A. | N.A. | N.A. | N.A. | -2 |
| Cell 61 | -12 | 41 | -41 | -55 | 9 | N.A. | N.A. | N.A. | N.A. | -3 |
| Cell 62 | -13 | 28 | -36 | -47 | 2 | N.A. | N.A. | N.A. | N.A. | 2 |
| Cell 63 | -13 | 32 | -40 | -52 | 3 | N.A. | N.A. | N.A. | N.A. | 1 |
| Cell 92 | -8 | 20 | -57 | -78 | 16 | N.A. | N.A. | N.A. | N.A. | -6 |
| Cell 93 | -11 | 67 | -52 | -66 | 19 | N.A. | N.A. | N.A. | N.A. | -13 |
| Cell 94 | -11 | 50 | -39 | -49 | 12 | N.A. | N.A. | N.A. | N.A. | -9 |
| Cell 95 | -11 | 34 | -36 | -45 | 4 | N.A. | N.A. | N.A. | N.A. | -2 |
| Cell 96 | -8 | 64 | -57 | -78 | 25 | N.A. | N.A. | N.A. | N.A. | -15 |
| Cell 97 | -8 | 20 | -57 | -78 | 16 | N.A. | N.A. | N.A. | N.A. | -6 |

4 RECOMMENDATION FOR NEW GUIDE

In this task, the structural and performance models for whitetopping pavements, concrete pavements and asphalt pavements were reviewed, with special attention paid to the modeling effort of the interface bonding.

The mechanistic-empirical approach that has been used in most of the currently available whitetopping structural models shows the merit in combining the advantages of both analytical and numerical models. Such an approach is usually implemented in three steps, namely calculating the stress and strain by finite element methods, correlating the FEM calculated stresses and strains to typical pavement parameters and finally calibrating the established correlations based on field observations. Three models have been identified using such an approach during the development, namely the CDOT model, the NJDOT model, and the PCA model (ICT method employs the PCA model). During the development of the CDOT and the NJDOT models, a 2-D FEM analysis was employed and the so-called '2.5-D' FEM was used to develop the PCA model. The 2.5-D FEM analysis for developing the analytical stress/strain equations is more capable to capture the unique features of whitetopping due to the employment of 3-D FEM. The performance of the NJDOT, the ICT, the PCA and the CDOT methods were evaluated using field observations. None of the methods yield perfect predictions for the fatigue development of the MnROAD cells. The PCA and the CDOT methods seem to be able to yield the most reasonable predictions for the PCC fatigue. This might be because of the consideration of partial bonding. Therefore, the PCA structural model seems to be the most favorable model for which the new design guide can be developed.

With respect to the concrete performance model, the PCA and ACPA models were the most-widely borrowed ones by the current whitetopping design methods. The PCA model only employs the stress ratio as an input and yields an average fatigue prediction among the fatigue models. The modified ACPA model not only considers the stress ratio but also takes into account the design probability and failure criterion; furthermore, it yields similar predictions to the PCA model. Therefore, either one would be a good candidate in modeling the fatigue performance for PCC.

The Asphalt Institute fatigue model is the only model used in the current whitetopping designs, except for the ICT method where the asphalt fatigue is not considered as a failure criterion. However, it is worth noting that the Asphalt Institute model was not developed for a flexible layer underlying a concrete overlay. Therefore, a research effort is still needed to validate the employment of the Asphalt Institute model into whitetopping design.

Based on the literature review and the evaluation of the current design methods, the following models are believed the best candidates to develop the new UTW design guide, namely the PCA structural model, the PCA/ACPA PCC fatigue model, and the Asphalt Institute asphalt fatigue model.

No model is currently available for the interface bonding. Based on the review, more laboratory and field work is still needed to characterize the interface debonding, which contributes greatly to the failure of whitetopping, especially UTWs. This issue will be addressed in Task 3.

During the evaluation, it was also identified that the asphalt modulus of elasticity is such an important parameter in stress predictions that a monthly based asphalt modulus of elasticity should be used. To achieve this goal, a nationwide characterization for climate in terms of ambient temperature and temperature gradient should be carried out. This issue will be addressed in Task 4. Furthermore, the condition of the existing asphalt layer has to be characterized, possibly in terms of its stiffness, so that the regions where reflective cracking/distress is most likely to occur can be predicted and repairs can be suggested in advance.

REFERENCES

- AASHTO. (1993). *AASHTO Guide for Design of Pavement Structures*, American Association of State Highway and Transportation Officials, Washington, D.C.
- ARA, Inc., ERES Division. (2004). *Guide for Mechanistic-Empirical Design of New and Rehabilitated Pavement Structures*, Transportation Research Board, Washington, D.C.
- Asphalt Institute. (1982). *Research and Development of the Asphalt Institute's Thickness Design Manual (MS-1) Ninth Edition*, Report No. 82-2, Asphalt Institute, Lexington, KY.
- Burnham, T.R. (2005). *Forensic Investigation Report for MnROAD Ultrathin Whitetopping Test Cells 93, 94 and 95*, Report No. MN/RC-2005-45, Minnesota Department of Transportation, St. Paul, MN.
- Burnham, T.R. (2006). *Construction Report for MnROAD Thin Whitetopping Test Cells 60-63*, Report No. MN/RC 2006-18, Minnesota Department of Transportation, St. Paul, MN.
- Cown, R.M. (1997). "Pavement Condition Survey of Ultra-thin Whitetopping Projects." *6th International Conference on Concrete Pavement Design and Rehabilitation*, Vol. 2, pp. 175, Purdue University, Lafayette, IN.
- Darter, M.I., and Barenberg, E.J. (1977). *Design of Zero-Maintenance Plain Jointed Plain Concrete Pavements Volume-I Development of Design Procedure*, Report No. FHWA-RD-77-111, Federal Highway Administration, Washington, D.C.
- Darter, M.I. (1988). *A comparison between Corps of Engineers and ERES Consultants, Inc. Rigid Pavements Design Procedure*, Technical Report, United States Air Force SAC, Urbana, IL.
- Gucunski, N. (1998). *Development of a Design Guide for Ultra Thin Whitetopping (UTW)*, Report No. 2001-018, Federal Highway Administration, Washington, D.C.
- PCA. (1984). *Thickness Design for Concrete Highway and Street Pavements*, Portland Cement Association, Skokie, IL.
- Riley, R.C., Titus-Glover, L., Mallela, J., Waalkes, S., and Darter, M. (2005). "Incorporation of Probabilistic Concepts into Fatigue Analysis of Ultrathin Whitetopping as Developed for the American Concrete Pavement Association." *Proceedings from the Best Practices in Ultra Thin and Thin Whitetopping*, pp. 288-317, Denver, CO.
- Roesler, J., Bordelon, A., Ioannides, A., Beyer, M., and Wang, D. (2008). *Design and Concrete Material Requirement for Ultra-Thin Whitetopping*, Report No. FHWA-ICT-08-016. Federal Highway Administration, Washington, D.C.
- Salsilli, R.A., Barenberg, E.J., and Darter, M.I. (1993). "Calibrated Mechanistic Design Procedure to Prevent Transverse Cracking of Jointed Plain Concrete Pavements." *Proceedings of*

the 5th International Conference on Concrete Pavement Design and Rehabilitation, Purdue University, Lafayette, IN.

Speakman, J., and Scott III, H.N. (1996). "Ultra-thin, Fiber-reinforced Concrete Overlays for Urban Intersections." *Transportation Research Record*, No. 1532, pp. 15-20.

Tarr, S.M., Sheehan, M., and Okamoto, P.A. (1998). *Guidelines for the Thickness Design of Bonded Whitetopping Pavement in the State of Colorado*, Report No. CDOT-DTD-R-98-10, Colorado Department of Transportation, Denver, CO.

Treybig, H.J., McCullough, B.F., Smith, P., and Von Quintus, H. (1977). *Overlay Design and Reflection Cracking Analysis for Rigid Pavements Volume 2, Design Procedures*, Report No. FHWA-RD-77-67, Federal Highway Administration, Washington, D.C.

Vandenbossche, J.M., and Rettner, D.L. (1998). *The Construction of US-169 and I-94 Experimental Thin and Ultra-thin Whitetopping Sections in Minnesota*, Report No. MN/RC 2001-07, Minnesota Department of Transportation, St. Paul, MN.

Vandenbossche, J.M. (2001). "The Measured Response of Ultrathin and Thin Whitetopping to Environmental Loads." *7th International Conference on Concrete Pavements*, Orlando, FL.

Vandenbossche, J.M., and Fagerness, A.J. (2002). "Performance, Analysis, and Repair of Ultrathin and Thin Whitetopping at Minnesota Road Research Facility." *Transportation Research Record*, No. 1809, pp. 191–198.

Vandenbossche, J.M., Mu, F., and Gutierrez, J.J. (2009). "Evaluating the Built-in Temperature Difference in the JPCP Cracking Model of the Mechanistic-Empirical Pavement Design Guideline." *International Journal of Pavement Engineering*, First published on 01 June 2010 (iFirst).

Westergaard, H.M. (1926). "Analysis of Stresses in Concrete Pavements Due to Variations of Temperature." *Proceedings of the Highway Research Board*, Vol. 6, pp. 201-215, Highway Research Board, Washington, D.C.

Westergaard, H.M. (1948). "New Formulas for Stresses in Concrete Pavements of airfields." *Transactions of the American Society of Civil Engineers*, Vol. 113, pp. 425-439.

Wu, C.L., Tarr, S.M., Refai, T.M., Nagi, M.A., and Sheehan, M.J. (1999). *Development of Ultra-Thin Whitetopping Design Procedure*, Portland Cement Association, Skokie, IL.

**APPENDIX A: LOAD SPECTRUM FOR SINGLE AND TANDEM AXLES AT
THE MNROAD CELL**

Table A1. Load spectrum for single axle loads at the MnROAD cells.

| Axle Load, kips | January | February | March | April | May | June | July | August | September | October | November | December |
|-----------------|---------|----------|-------|-------|------|------|-------|--------|-----------|---------|----------|----------|
| 3 | 530 | 551 | 759 | 385 | 684 | 744 | 539 | 692 | 1017 | 578 | 323 | 599 |
| 4 | 1767 | 1685 | 1952 | 1173 | 1572 | 1609 | 1341 | 1636 | 2382 | 1766 | 1328 | 1848 |
| 5 | 1611 | 1582 | 2175 | 1516 | 1797 | 1865 | 1733 | 1871 | 5116 | 1974 | 1775 | 1969 |
| 6 | 2002 | 2165 | 6004 | 3870 | 1763 | 1836 | 1955 | 2066 | 6274 | 2438 | 2158 | 1968 |
| 7 | 1870 | 2066 | 7203 | 2028 | 1678 | 1755 | 1353 | 1585 | 2312 | 1751 | 1610 | 1847 |
| 8 | 3571 | 3518 | 8525 | 1960 | 2963 | 2938 | 2258 | 3067 | 3015 | 3145 | 2431 | 2889 |
| 9 | 4716 | 4813 | 2815 | 1839 | 3746 | 3797 | 2719 | 3802 | 3104 | 3967 | 2767 | 4416 |
| 10 | 9554 | 9627 | 2573 | 3381 | 7425 | 7574 | 5641 | 7416 | 5517 | 8139 | 5715 | 9226 |
| 11 | 9342 | 9417 | 2766 | 3669 | 8575 | 8765 | 7423 | 8281 | 6567 | 8837 | 7115 | 10459 |
| 12 | 7525 | 7375 | 3751 | 4128 | 9515 | 9532 | 10761 | 9323 | 6656 | 9894 | 11360 | 10280 |
| 13 | 2317 | 2172 | 2399 | 2461 | 3958 | 3263 | 6020 | 3894 | 2566 | 5281 | 9288 | 3407 |
| 14 | 999 | 957 | 1204 | 1930 | 1216 | 1118 | 1573 | 1222 | 1098 | 1804 | 2896 | 1260 |
| 15 | 1038 | 1042 | 1586 | 3397 | 1181 | 1107 | 1170 | 1138 | 1082 | 1333 | 1392 | 1137 |
| 16 | 818 | 712 | 1520 | 3691 | 831 | 930 | 827 | 837 | 819 | 948 | 1084 | 990 |
| 17 | 964 | 908 | 1871 | 5155 | 1034 | 1091 | 1026 | 1048 | 923 | 1086 | 999 | 903 |
| 18 | 691 | 718 | 1148 | 3319 | 819 | 937 | 901 | 833 | 645 | 783 | 755 | 764 |
| 19 | 613 | 666 | 794 | 2423 | 886 | 882 | 1021 | 887 | 574 | 800 | 1170 | 689 |
| 20 | 272 | 259 | 311 | 851 | 433 | 404 | 675 | 448 | 287 | 462 | 625 | 426 |

Table A1. Load spectrum for single axle loads at the MnROAD cells (continued).

| Axle Load, kips | January | February | March | April | May | June | July | August | September | October | November | December |
|-----------------|---------|----------|-------|-------|-----|------|------|--------|-----------|---------|----------|----------|
| 21 | 173 | 168 | 215 | 545 | 262 | 204 | 499 | 272 | 196 | 326 | 499 | 282 |
| 22 | 66 | 58 | 131 | 351 | 84 | 85 | 174 | 94 | 108 | 108 | 161 | 105 |
| 23 | 33 | 20 | 136 | 385 | 50 | 33 | 140 | 52 | 92 | 76 | 66 | 63 |
| 24 | 16 | 9 | 143 | 407 | 18 | 20 | 57 | 20 | 67 | 28 | 35 | 10 |
| 25 | 7 | 5 | 102 | 285 | 8 | 5 | 24 | 9 | 32 | 9 | 0 | 8 |
| 26 | 5 | 4 | 121 | 309 | 4 | 7 | 48 | 3 | 23 | 10 | 0 | 9 |
| 27 | 0 | 1 | 75 | 286 | 0 | 0 | 26 | 3 | 18 | 6 | 0 | 0 |
| 28 | 1 | 1 | 80 | 303 | 0 | 0 | 32 | 2 | 4 | 2 | 0 | 0 |
| 29 | 0 | 0 | 52 | 173 | 0 | 0 | 28 | 0 | 4 | 0 | 0 | 0 |
| 30 | 1 | 0 | 35 | 121 | 0 | 0 | 39 | 0 | 1 | 0 | 0 | 0 |
| 31 | 0 | 0 | 21 | 67 | 0 | 0 | 35 | 0 | 0 | 0 | 0 | 0 |
| 32 | 0 | 0 | 17 | 43 | 0 | 0 | 37 | 0 | 0 | 0 | 0 | 0 |
| 33 | 0 | 0 | 9 | 23 | 0 | 0 | 30 | 0 | 3 | 0 | 0 | 0 |
| 34 | 0 | 0 | 5 | 13 | 0 | 0 | 51 | 0 | 0 | 0 | 0 | 0 |
| 35 | 0 | 0 | 3 | 9 | 0 | 0 | 51 | 0 | 3 | 0 | 0 | 0 |
| 36 | 0 | 1 | 1 | 4 | 0 | 0 | 53 | 0 | 0 | 0 | 0 | 0 |
| 37 | 0 | 0 | 0 | 1 | 0 | 0 | 62 | 0 | 0 | 0 | 0 | 0 |
| 38 | 0 | 0 | 0 | 0 | 0 | 0 | 54 | 0 | 0 | 0 | 0 | 0 |
| 39 | 0 | 0 | 0 | 0 | 0 | 0 | 81 | 0 | 0 | 0 | 0 | 0 |
| 40 | 0 | 0 | 0 | 0 | 0 | 0 | 43 | 0 | 0 | 0 | 0 | 0 |
| 41 | 0 | 0 | 0 | 0 | 0 | 0 | 0 | 0 | 0 | 0 | 0 | 0 |

Table A2. Load spectrum for tandem axle loads at the MnROAD cells.

| Axle Load, kips | January | February | March | April | May | June | July | August | September | October | November | December |
|-----------------|---------|----------|-------|-------|------|------|------|--------|-----------|---------|----------|----------|
| 6 | 358 | 366 | 1247 | 311 | 377 | 439 | 289 | 468 | 3292 | 386 | 371 | 314 |
| 8 | 1010 | 1187 | 3162 | 504 | 848 | 1041 | 776 | 1114 | 3068 | 1081 | 964 | 901 |
| 10 | 2900 | 3227 | 4551 | 1127 | 2348 | 2344 | 1874 | 2396 | 3651 | 2468 | 2731 | 2830 |
| 12 | 4446 | 4514 | 4137 | 2010 | 3925 | 4078 | 3251 | 3758 | 4335 | 4223 | 4270 | 4209 |
| 14 | 4771 | 4772 | 3947 | 2572 | 4500 | 4524 | 4867 | 4685 | 4361 | 4976 | 5044 | 4541 |
| 16 | 3843 | 3932 | 3942 | 2645 | 3610 | 3522 | 4135 | 3744 | 5059 | 4235 | 4715 | 4083 |
| 18 | 3417 | 3386 | 3735 | 3105 | 2989 | 2870 | 3263 | 3140 | 3647 | 3568 | 3874 | 3537 |
| 20 | 3230 | 3373 | 3912 | 3398 | 2852 | 3054 | 2858 | 2940 | 2482 | 3406 | 3171 | 3864 |
| 22 | 3088 | 3376 | 5282 | 2995 | 2891 | 3036 | 2889 | 2910 | 2374 | 3572 | 3009 | 3669 |
| 24 | 3002 | 3197 | 4772 | 2962 | 3186 | 3167 | 3152 | 3243 | 2598 | 3657 | 3231 | 3852 |
| 26 | 2651 | 2662 | 1772 | 2339 | 2631 | 2729 | 2586 | 2853 | 2239 | 3012 | 2821 | 3557 |
| 28 | 2694 | 2839 | 1215 | 2320 | 2575 | 2691 | 2464 | 2893 | 2396 | 2934 | 2285 | 3212 |
| 30 | 3558 | 3762 | 1243 | 2445 | 2922 | 3087 | 2495 | 3083 | 2886 | 3225 | 2199 | 3748 |
| 32 | 4708 | 4887 | 1523 | 2791 | 3833 | 4246 | 3134 | 3793 | 3674 | 4278 | 3466 | 4772 |
| 34 | 4524 | 4237 | 1761 | 3064 | 5061 | 5208 | 4382 | 4839 | 3444 | 4825 | 5143 | 4944 |
| 36 | 2774 | 2104 | 1368 | 2659 | 4826 | 4314 | 5092 | 4160 | 1808 | 4454 | 5578 | 3782 |
| 38 | 1261 | 790 | 719 | 1875 | 2559 | 1980 | 3496 | 2154 | 720 | 2805 | 3681 | 1787 |
| 40 | 553 | 319 | 518 | 1300 | 826 | 556 | 1291 | 666 | 303 | 953 | 1328 | 499 |

Table A2. Load spectrum for tandem axle loads at the MnROAD cells (continued).

| Axle Load, kips | January | February | March | April | May | June | July | August | September | October | November | December |
|-----------------|---------|----------|-------|-------|-----|------|------|--------|-----------|---------|----------|----------|
| 42 | 197 | 98 | 469 | 1163 | 216 | 136 | 408 | 169 | 211 | 242 | 326 | 177 |
| 44 | 65 | 33 | 507 | 1195 | 59 | 40 | 126 | 49 | 170 | 66 | 130 | 51 |
| 46 | 22 | 8 | 684 | 1618 | 32 | 20 | 88 | 21 | 127 | 25 | 45 | 30 |
| 48 | 12 | 3 | 716 | 1730 | 12 | 7 | 68 | 7 | 94 | 6 | 16 | 6 |
| 50 | 3 | 2 | 700 | 2033 | 5 | 1 | 32 | 0 | 54 | 0 | 0 | 26 |
| 52 | 1 | 0 | 519 | 1957 | 5 | 1 | 34 | 1 | 29 | 0 | 0 | 3 |
| 54 | 0 | 5 | 380 | 1505 | 0 | 0 | 22 | 0 | 12 | 0 | 0 | 2 |
| 56 | 0 | 0 | 174 | 832 | 0 | 0 | 15 | 3 | 7 | 0 | 0 | 3 |
| 58 | 0 | 0 | 78 | 379 | 0 | 0 | 1 | 0 | 5 | 0 | 0 | 0 |
| 60 | 0 | 1 | 25 | 142 | 0 | 0 | 1 | 0 | 6 | 2 | 0 | 0 |
| 62 | 0 | 0 | 17 | 68 | 0 | 0 | 0 | 0 | 5 | 0 | 0 | 0 |
| 64 | 0 | 5 | 10 | 30 | 0 | 0 | 1 | 0 | 6 | 0 | 0 | 0 |
| 66 | 0 | 0 | 5 | 11 | 0 | 0 | 0 | 0 | 5 | 0 | 0 | 0 |
| 68 | 0 | 0 | 0 | 5 | 0 | 0 | 0 | 0 | 6 | 0 | 0 | 0 |
| 70 | 0 | 0 | 0 | 0 | 0 | 0 | 1 | 0 | 5 | 0 | 0 | 0 |
| 72 | 0 | 0 | 0 | 0 | 0 | 0 | 0 | 0 | 5 | 0 | 0 | 0 |
| 74 | 0 | 5 | 0 | 0 | 0 | 0 | 0 | 0 | 5 | 0 | 0 | 0 |
| 76 | 0 | 0 | 0 | 0 | 0 | 0 | 0 | 0 | 0 | 0 | 0 | 0 |
| 78 | 0 | 0 | 0 | 0 | 0 | 0 | 0 | 0 | 0 | 0 | 0 | 0 |
| 80 | 0 | 0 | 0 | 0 | 0 | 0 | 0 | 0 | 0 | 0 | 0 | 0 |
| 82 | 0 | 0 | 0 | 0 | 0 | 0 | 0 | 0 | 0 | 0 | 0 | 0 |